Satellite radar interferometry: estimation of atmospheric delay

Shizhuo Liu

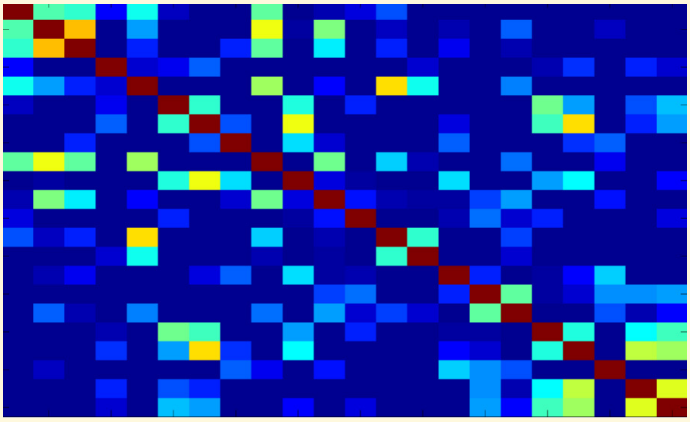

NCG KNAW

Nederlandse Commissie voor Geodesie Netherlands Geodetic Commission 80

Satellite radar interferometry: estimation of atmospheric delay

Satellite radar interferometry: estimation of atmospheric delay

Shizhuo Liu

Publications on Geodesy 80

NCG Nederlandse Commissie voor Geodesie Netherlands Geodetic Commission

Delft, January 2013

Satellite radar interferometry: estimation of atmospheric delay
Shizhuo Liu
Publications on Geodesy 80
ISBN: 978 90 6132 340 2
ISSN 0165 1706

Published by: NCG, Nederlandse Commissie voor Geodesie, Netherlands Geodetic Commission, Delft, the Netherlands

NCG, Nederlandse Commissie voor Geodesie, Netherlands Geodetic Commission
P.O. Box 5030, 2600 GA Delft, the Netherlands
T: +31 (0)15 278 21 03
F: +31 (0)15 278 17 75
E: info@ncg.knaw.nl
W: www.ncg.knaw.nl

The NCG, Nederlandse Commissie voor Geodesie, Netherlands Geodetic Commission is part of the Royal Netherlands Academy of Arts and Sciences (KNAW).

Contents

Preface

As a remote sensing technique, SAR Interferometry (InSAR) belongs to the active and microwave remote sense category. Unlike the passive and optical remote sensing techniques InSAR is capable of providing measurements under all weather conditions during day and night. The earliest space-borne InSAR experiments can be traced back to the SEASAT mission operated by JPL (Jet Propulsion Laboratory) in late 1970s. In the beginning, the main purpose of InSAR was to measure land topography. With the achievements made by scientists and engineers (such as Zebker et al. (1994), Massonnet et al. (1995) and Hanssen (2001), just to name a few), nowadays, InSAR has been approved and accepted as an ideal tool for monitoring earth surface deformation. Thanks to the advance in space technology since 1990s, surface deformation can be detected and monitored from space by satellites (e.g., ERS1/2, RadarSat1/2, Envisat, TerraSAR-X and COSMO-SkyMed) with remarkable precision (sub-centimeter level) and unprecedented spatial resolution (down to 1 m).

One of the biggest uncertainties in InSAR measurement is the so-called atmospheric phase screen (APS) which is the result of the signal propagation delay caused by the earth's atmosphere. Without knowing the exact delay, it is difficult to measure low-rate land deformation with acceptable accuracy (e.g., sub-centimeter). The difficulty in removing APS from InSAR measurements comes from the high spatio-temporal dynamics of water vapor in the lower troposphere. The most straightforward way to correct APS is to use delay measurements from other sources such as GPS networks, space-borne spectroradiometers (MODIS and MERIS) and meteorological observations (e.g., weather balloon), see Williams et al. (1998), Li et al. (2004) and Onn and Zebker (2006). However, these independent sources of delay have their own limitations such as spatial density and coverage, and weather and sunlight dependency. Therefore, a generic solution for mitigating APS cannot be based on these sources.

Alternatively, APS can be estimated from InSAR measurement itself by utilizing the difference in temporal characteristics between APS and ground deformation. The former has a high variability (high frequency), whereas the latter very often shows a strong temporal correlation (low-frequency). A temporal low-pass filtering approach was originally proposed by Ferretti et al. (2000) for InSAR time series analysis using persistent scatterers InSAR (PSInSAR). In such approach APS is treated as a temporally uncorrelated signal which is filtered out by the low-pass filter. However,

the approach does not provide quality assessment for the APS estimate and requires a user to construct the low-pass filter, which often results in different deformation estimates from different InSAR processors and makes the estimated deformation not falsifiable.

Till now, APS is regarded as noise for surface deformation monitoring. From the meteorology point of view, however, APS could be a valuable source for weather analysis and climate study. The distinctive features of InSAR for atmosphere study from other remote sensing techniques are its high spatial resolution and all weather capability. But, one of the difficulties that prevents its meteorological applications is the so called acquisition ambiguity (Hanssen and Kampes, 2004) in which only the temporal difference of delay between two SAR acquisitions is observed. Therefore, the delay during each acquisition is not directly measurable.

At first, this book reviews the cause of APS and its spatio-temporal characteristics. Then, it assesses the feasibility of mitigating APS using numerical weather forecast. Afterwards, the book presents a new method for estimating APS as well as the precision of the estimate based on InSAR time series analysis. Finally, the book also provides a method for resolving the acquisition ambiguity to obtain APS at single SAR acquisitions.

Acknowledgements

Isaac Newton once said:"*If I have seen further, it is by standing on the shoulders of giants*". Scientific research like other human activities in modern society, in one way or another, visible or invisible, is a collaborative and joint work based on other's experience and findings.

Foremost, I would like to express my greatest gratitude to my supervisor Prof. Ramon Hanssen for his patience and long-term vision which helped to secure my PhD project from the very beginning. I still remember that, at the end of the first year, it was a difficult decision for both of us to continue the project which was short of funding and had a gloomy prospect at the time. The successful completion of the project may not be a great leap for InSAR but absolutely an indispensable step for me as an individual who grew up in a non-western culture to climb the career ladder in the European society. It was his support, encouragement and patience that enabled me to accomplish the ESA's METAWAVE (Mitigation of Electromagnetic Transmission Errors induced by atmospheric Water VApour Effects) project from which I learned effective collaboration in a multinational team. It was his support and encouragement that made the trips to Cape Town and Vancouver for IGARSS (International Geoscience and Remote Sensing Symposium) and to ESA's satellite data storage center ESRIN at Frascati (Italy) for training possible. Thanks to these exposures, my scientific vision was broadened and a primitive network in academia was established. Although I have moved to the industrial world, most of the lessons learned from my academic experience are still applicable. The most important one he taught me is:"*always take the initiative and make a difference*".

Furthermore, I would like to thank all (former) colleagues at the InSAR group for their supports to my PhD work: Andy Hooper, Freek van Leijen, Petar Marinkovic,

Gini Ketelaar, Zbigniew Perski, Rossen Grebenitcharsky, Liu Guang, Yue Huanyin, Mahmut Arikan, Miguel Caro Cuenca, Gert Jan van Zwieten, Sami Samiei Esfahany, Anneleen Oyen, Pooja Mahapatra, Prabu Dheenathayalan, Joana Esteves Martins, Jose Manuel Delgado Blasco and Ling Chang. Special thanks go to Freek van Leijen, Petar Marinkovic, Mahmut Arikan and Miguel Caro Cuenca for maintaining the group's Linux cluster and inventing the Matlab and Bash scripts which greatly increased the efficiency of my daily work at TUDelft. I am also very grateful to Andy Hooper and Roderik Lindenbergh for their interest in my work and the valuable discussions we had during my PhD. My appreciation also goes to other former colleagues at DEOS (Department of Earth Observation and Space Systems) of TUDelft: Xianglin Liu, Mark Willem Janson, Jasper van Loon, Bas Alberts for the joyful non-technical discussions we had during lunch time and coffee breaks.

I also appreciate very much all members who participated in the MEWAVE project for their patience and dedication: Bjorn Rommen, Ágnes Mika, Leslie Gale, Urs Wegmuller, Maurizio Santoro, Charles Werner, Charistian Matzler, Wenyu Gong and Franz Meyer. Special thanks go to Ágnes Mika for reviewing my proceeding and journal papers. I am also very grateful to ESA for freely providing worldwide SAR images for my PhD research.

I would also like to thank Lammert Zeijlmaker, Maarten Bomers, Neil Hodgson, Roel Nicolai, Robert Everts, Leen Boer and Jack Verouden from Shell for their mentoring and coaching during my internship at Shell. Their patience and understanding encouraged me to finish the thesis writing without significant delay. I am also grateful to Shell Global Solutions for jointly (with TUDelft) providing funds for printing my thesis.

I express my thanks to all the committee members for reviewing my thesis and traveling to Netherlands for my defense.

It is obvious to see the efforts made by PhD candidates on their researches, but it is less obvious to notice the efforts made by their families and partners who support them behind the scenes. I am highly indebted to my wife Sijia Rong who gave up her job in her hometown and joined me in 2009. Like me, she is the only child in her family and I am very grateful to my parents-in-law Rong Zhongming and Liu Yixian for their love and support. It is our Chinese tradition to stay close to our parents and look after them when they get old. I know my father Liu Xin and mother Zhang Wenfang have such a wish but they have never asked me to do so because they know what is best for their son. Thank you father and mother for everything you have done for me.

Finally, I want to devote this thesis to my former supervisor Prof. Liangming Liu who passed away in a car accident in 2011. His death was a great loss to Wuhan University as well as to the international remote sensing community. It was his encouragement and recommendation letter which enabled me to obtain the admission from TUDelft to pursue my master degree.

Shizhuo Liu
Den Haag, September 2012

Summary

Satellite SAR Interferometry (InSAR) is frequently promoted as an active, all-weather technique in comparison to optical remote sensing techniques that need solar illumination and cloud free conditions. However, the earth's atmospheric refractivity plays an important role in delaying the radar signal, resulting in a spatio-temporal phase shift in repeat-pass InSAR measurements (i.e., interferograms). The phase shift is also referred to as an atmospheric phase screen (APS). Therefore, repeat-pass InSAR is not weather independent.

For C-band and X-band interferometry APS is mainly driven by the earth's troposphere. The difficulty of correcting APS for surface deformation monitoring largely comes from the highly dynamic behavior of water vapor located in the lower (< 2 km) troposphere. In this study we develop two methods for the APS correction and one method for the usage of APS for meteorological purposes. The first correction method is based on numerical weather models (NWM) and the second relies on InSAR time series analysis. The method for meteorological purposes aims at retrieving water vapor spatial distributions at single SAR acquisitions from interferograms.

In the first correction method, we use the weather research and forecast (WRF) model to simulate delay at SAR acquisitions. To evaluate the simulation, we use atmosphere-only interferograms over different climatic regions varying from tropic to semi-arid. Some of the regions have strong topography variations and the others have flat terrains. We find that significant APS correction can be achieved only in mountainous regions. This is mainly the result of correcting the delay correlated with topography. However, the simulated topography dependent delay is not always reliable with a success rate of 80% (1 out of 5 cases in which the model failed).

In flat regions the correction hardly leads to APS mitigation and very often deteriorates the original interferograms. This is because the model is not able to simulate the realistic water vapor lateral distribution at fine scales (between 1 and 50 km). We also assess the feasibility of using the model to simulate stochastic properties of APS such as spatial variograms. Unfortunately, we find the model constantly underestimates the real variability of APS at all spatial scales between 1 and 50 km.

Therefore, we conclude that contemporary weather models are useful for correcting the topography dependent delay but should not be considered reliable at all times. For flat regions, the value of the models is very limited and we recommend not to use them for delay correction.

The second correction method, based on InSAR time series, utilizes least-squares collocation (LSC) and variance-covariance estimation to separate APS and ground deformation. The LSC method regards the deformation as a temporally correlated stochastic signal and models it by its temporal variance-covariance function. APS is also modeled as a stochastic signal. In time, APS is assumed uncorrelated and modeled by a diagonal variance-covariance matrix. In space, APS is correlated and modeled by a variance-covariance function from the Mátern-family. Given the stochastic modeling, the optimal separation of APS and deformation can be achieved by least-squares collocation which not only gives the best estimates in terms of their precisions but also provides the precision estimation. We implement the method for PSInSAR. The evaluation of the method is performed over different climatic regions with and without strong topography variations. We find that the method can better separate APS and ground deformation than the APS filter in conventional PSInSAR, especially when there are significant acquisition gaps in the time series and for acquisitions taken during turbulent weather. This is because the temporal variance-covariance matrix of APS incorporates the time-varying magnitude of APS disturbance to achieve the largest suppression of APS. Moreover, the stochastic modeling of deformation is capable of estimating complex deformation that is difficult to be modeled deterministically by a functional model. Therefore, we conclude that the method provides an optimal way to separate ground deformation and APS for PSInSAR in terms of the result precision and its quality assessment.

The third and last objective is InSAR based water vapor mapping for meteorological applications. The main difficulty of the mapping comes from the so-called acquisition ambiguity in which only the spatio-temporal differences of water vapor (instead of spatial distributions at one specific epoch we observe the difference between two satellite acquisitions) are observed. To resolve the ambiguity a constrained least-squares approach is used assuming APS between acquisitions are temporally uncorrelated. Moreover, to prevent phase decorrelation we form a network of interferograms with favorable temporal and geometric baselines. The network not only permits least-squares adjustment for the retrieving but also allows hypothesis testing to reject incoherent pixels (i.e., outliers) in the interferograms. The APS at the incoherent pixels can be later spatially interpolated using kriging. To evaluate the method we choose a non-urban area over southwest Australia and obtain the water vapor spatial distributions with 1 km lateral resolution during 22 ASAR acquisitions over the area. The evaluation suggests that the retrieved distributions are realistic and accurate.

In this study we have assessed the feasibility of mitigating APS for InSAR using numerical weather models. We develop a method to separate APS and surface deformation based on InSAR time series for PSInSAR. For meteorological purposes, we develop a method to retrieve water vapor spatial distributions at single SAR acquisitions. Future work should focus on improving the reliability of numerical weather simulation by incorporating high spatial resolution water vapor maps as inputs for weather analysis. InSAR water vapor products can play an important role in such aspect. In return, the improved simulation will have a higher success rate in mitigating APS for events such as earthquakes and volcano eruptions in which

the time series based method is no longer applicable.

Samenvatting (Summary in Dutch)

Satelliet SAR Interferometrie (InSAR) wordt vaak neergezet als een actieve techniek werkend onder alle weersomstandigheden. Dit in vergelijking met optische remote sensing technieken die zonlicht en bewolkingsvrije omstandigheden nodig hebben. De refractiviteit van de aardse atmosfeer speelt echter een belangrijke rol in het vertragen van het radarsignaal, resulterend in een ruimtelijk-temporele faseverschuiving in InSAR metingen gebaseerd op herhaalde overkomsten (dat wil zeggen, interferogrammen). De faseverschuiving wordt ook aangeduid als een atmosferisch fasebeeld (APS). Daarom is InSAR gebaseerd op herhaalde overkomsten niet weersonafhankelijk.

Voor C-band en X-band interferometrie wordt het APS vooral veroorzaakt door de aardse troposfeer. De moeilijkheid van het corrigeren van het APS voor oppervlaktedeformatie monitoring is grotendeels afkomstig van het zeer dynamische gedrag van waterdamp in de onderste (¡2 km) troposfeer. In deze studie ontwikkelen we twee methoden voor de APS correctie en een methode voor het gebruik van APS voor meteorologische doeleinden. De eerste correctiemethode is gebaseerd op numerieke weermodellen (NWM) en de tweede berust op InSAR tijdreeksanalyse. De methode voor meteorologische doeleinden beoogt het reconstrueren van de ruimtelijke distributie van waterdamp voor individuele SAR opnamen uit interferogrammen.

Bij de eerste correctiemethode gebruiken we het Weather Research and Forcast (WRF) model om de vertraging gedurende SAR opnamen te simuleren. Om de simulatie te evalueren gebruiken we interferogrammen met uitsluitend atmosfeer in verschillende klimatologische regio's varirend van tropisch tot semi-aride. Een deel van de regio's hebben sterke hoogtevariaties en de anderen hebben een vlak oppervlak. We ondervinden dat significante APS correctie alleen kan worden bereikt in bergachtige gebieden. Dit is voornamelijk het gevolg van het corrigeren van de vertraging die gecorreleerd is met de topografie. De gesimuleerde topografie afhankelijke vertraging is echter niet altijd betrouwbaar met een slagingspercentage van 80% (1 van de 5 gevallen waarin het model faalde).

In vlakke gebieden leidt de correctie nauwelijks tot APS reductie en verslechteren heel vaak de oorspronkelijke interferogrammen. Dit komt omdat het model niet in staat is de realistische ruimtelijke waterdampverdeling op kleine schaal te simuleren (tussen 1 en 50 km). Ook hebben we de haalbaarheid beoordeeld van het gebruik van het model om stochastische eigenschappen van APS te simuleren, zoals ruimtelijke

variogrammen. Helaas vinden we dat het model de werkelijke variabiliteit van APS voortdurend onderschat op alle ruimtelijke schalen tussen 1 en 50 km.

Daarom concluderen we dat de hedendaagse weermodellen bruikbaar zijn voor het corrigeren van de topografie afhankelijke vertraging, maar niet altijd als betrouwbaar moet worden beschouwd. Voor vlakke gebieden is de waarde van de modellen zeer beperkt en we raden aan ze niet te gebruiken voor vertragingscorrectie.

De tweede correctiemethode, gebaseerd op InSAR tijdreeksen, maakt gebruik van kleinste-kwadraten collocatie (LSC) en variantie-covariantie schatting om APS en deformatie van de ondergrond te onderscheiden. De LSC methode beschouwt de deformatie als een in tijd gecorreleerd stochastisch signaal en modelleert dat door zijn temporele variantie-covariantie functie. Het APS wordt ook gemodelleerd als een stochastisch signaal. APS worden ongecorreleerd in tijd verondersteld en gemodelleerd door een diagonale variantie-covariantie matrix. In ruimte is een APS gecorreleerd en wordt gemodelleerd door een variantie-covariantie functie uit de Mtern-familie. Gebaseerd op de stochastische modellering kan het optimale onderscheid tussen APS en deformatie worden bereikt door kleinste-kwadraten collocatie, dat niet alleen de beste schattingen geeft in termen van precisie, maar ook de schatting van de precisie zelf. We hebben de methode voor PSInSAR gemplementeerd. De evaluatie van de methode is uitgevoerd voor verschillende klimatologische gebieden met en zonder sterke topografische variaties. We vinden dat de methode APS en deformatie beter kan onderscheiden vergeleken met het APS-filter in conventionele PSInSAR, vooral wanneer er significante onderbrekingen zitten in de opname tijdreeksen en voor opnamen gedurende turbulent weer. Dit komt doordat de temporele variantie-covariantie matrix van APS de in tijd varirende sterkten van APS verstoring bevat, om zodoende de sterkste onderdrukking van APS te bereiken. Bovendien is de stochastische modellering van deformatie in staat om complexe deformaties te schatten, die moeilijk te deterministisch te modeleren zijn door een functioneel model. Daarom concluderen we dat de methode zorgt voor een optimale manier om deformatie en APS te onderscheiden in PSInSAR, zowel in termen van de precisie van het resultaat als de kwaliteitsbeschrijving.

De derde en laatste doelstelling is het op InSAR gebaseerd in kaart brengen van waterdamp voor meteorologische toepassingen. De grootste moeilijkheid voor het in kaart brengen wordt veroorzaakt door de zogenaamde opname meerduidigheid waarmee de ruimtelijk-temporele variaties in waterdamp worden waargenomen (in plaats van ruimtelijke verdelingen op een specifiek epoch worden verschillen tussen twee satellietopnamen geobserveerd). Om de meerduidigheid op te lossen wordt een geconditioneerde kleinste-kwadraten methode toegepast, waarbij aangenomen wordt dat de APS van verschillende opnamen ongecorreleerd zijn in tijd. Bovendien vormen we een netwerk van interferogrammen met gunstige temporele en geometrische basislijnen, ter voorkoming van fase decorrelatie. Het netwerk staat niet alleen een kleinste-kwadraten vereffening voor het oplossen toe, maar maakt het ook mogelijk hypothese testen uit te voeren om incoherente pixels (dat wil zeggen, blunders) in de interferogrammen te verwerpen. De APS waarde voor de incoherente pixels kan later ruimtelijk genterpoleerd worden met behulp van kriging. Om de methode te evalueren kiezen we een niet-stedelijk gebied in zuidwest Australi en verkrijgen we

de ruimtelijke verdeling van waterdamp met 1 km ruimtelijke resolutie gedurende 22 ASAR opnamen van het gebied. De evaluatie suggereert dat de gevonden verdelingen realistisch en nauwkeurig zijn.

In deze studie hebben we de haalbaarheid onderzocht van het reduceren van APS voor InSAR met behulp van numerieke weermodellen. We ontwikkelen een methode om APS en deformatie van het oppervlak te onderscheiden op basis van InSAR tijdreeksen voor PSInSAR. Voor meteorologische doeleinden ontwikkelen we een methode om ruimtelijke verdelingen van waterdamp te bepalen voor individuele SAR acquisities. Toekomstige werkzaamheden moeten worden toegespitst op het verbeteren van de betrouwbaarheid van numerieke weer simulatie door het toevoegen van een ruimtelijk hoge resolutie waterdampkaarten als invoer voor weeranalyse. InSAR waterdamp producten kunnen in die zin een belangrijke rol spelen. In ruil daarvoor zal de verbeterde simulatie een hoger slagingspercentage hebben in het reduceren van APS voor gebeurtenissen zoals aardbevingen en vulkaanuitbarstingen, waarvoor de tijdreeks gebaseerde methode niet meer toepasbaar is.

Nomenclature

List of acronyms

ABL	Atmospheric Boundary Layer
APS	Atmospheric Phase Screen
ASAR	Advanced SAR
BLUE	Best Linear Unbiased Estimation
BLUP	Best Linear Unbiased Prediction
DD	Double Difference
DEM	Digital Elevation Model
DIA	Detection, Identification and Adaptation
Envisat	ENVironment SATellite
ERS	European Remote Sensing Satellite
ESA	European Space Agency
GDAS	Global Data Assimilation System
GPS	Global Positioning System
InSAR	SAR INterferometry
IWV	Integrated Water Vapor
LOS	Line Of Sight
LSC	Least-Squares Collocation
MERIS	MEdium spectral Resolution Imaging Spectrometer
MODIS	MODerate resolution Imaging Spectroradiometer
MVUQE	Minimum Variance Unbiased Quadratic Estimator
NCEP	National Center for Environmental Prediction
NWM	Numerical Weather Model
NWP	Numerical Weather Prediction
OMT	Overal Model Test
PDF	Probability Density Function

PS	Persistent Scatterers
PSC	Persistent Scatterer Candidate
PSD	Power Spectral Density
PSP	Persistent Scatterer Potential
RMLE	Restricted Maximum Likelihood Estimator
RMS	Root Mean Square
SAR	Synthetic Aperture Radar
SLC	Single Look Complex
SNR	Signal to Noise Ratio
SRTM	Shuttle Radar Topography Mission
USGS	U.S. Geological Survey
VCE	Variance-Covariance Estimation
VCM	Variance-Covariance Matrix
VLBI	Very Long Baseline Interferometry
WLS	Weighted Least-Squares
WRF	Weather Research and Forecast

List of distance units

cm	centimeter
km	kilometer
m	meter
mm	millimeter

List of symbols

Γ	Gamma function
γ	variogram; phase coherence
ρ_w	liquid water density
θ_i	local incidence angle
ε_0	permittivity of water
$\{.\}^{-1}$	inversion
$\{.\}^T$	transposition
A	design matrix
$B_\perp$	perpendicular baseline

$chol$	Cholesky factorization
D	signal propagation delay
$D\{.\}$	dispersion
D_A	amplitude dispersion
e	water vapor partial pressure
$E\{.\}$	expectation
g_m	local gravity at the center of the atmospheric column
K_τ	modified Bessel function of the second kind
L	excess path length
M_d	molar mass of dry air
N	refractivity
P	pressure
P_s	surface pressure
Q_{cloud}	cloud water mixing ratio
R	ideal gas constant
R_d	specific gas constant
S	distance between signal source and receiver
T	temperature; transformation matrix
W_{cloud}	liquid water cntent

Chapter 1

Introduction

Satellite synthetic aperture radar interferometry is a global, all-weather and active remote sensing technique that is capable of imaging land surface topography and monitoring ground deformation with high spatial resolution (down to 1-meter) and on frequent basis (e.g., 8-day). Raw InSAR measurements consist of phase differences between two SAR images and are the combination of phases due to possible ground deformation, land topography, atmospheric delay, earth curvature and instrumental noise. Among these phase components the atmospheric delay that is often referred to as an atmospheric phase screen (APS) poses a great challenge on InSAR for surface deformation monitoring.

1.1 Background

For radio signals, the atmospheric delay is introduced by the earth's troposphere and ionosphere during the signal propagation. Although the observed atmospheric delay in InSAR is the sum of the delays caused by these two mediums, the challenge for ground deformation monitoring mainly comes from the tropospheric delay that has a high spatio-temporal variability. The high variability is due to a so-called turbulent mixing process (Stull, 1995) in which water vapor in the lower troposphere plays an important role. Without knowing the fine scale spatial distribution of water vapor, the delay can be easily interpreted as a ground deformation that is measured as a distance change from satellite to ground surface between two satellite acquisitions. For general concepts of radar, SAR and InSAR, readers are referred to Massonnet (1997), Bamler and Hartl (1998), Hanssen (2001) and Rosen et al. (2000).

The earliest report of the atmospheric delay (APS) in InSAR measurements can be traced back to the mid-nineties, see Goldstein (1995), Massonnet and Feigl (1995), Tarayre and Massonnet (1996), Hanssen and Feijt (1996) and Zebker et al. (1997). APS not only affects ground deformation monitoring but also contaminates land topography mapping in case of repeat-pass InSAR, see Dupont et al. (1997), Hanssen (1998), Hanssen and Feijt (1996), Mattar et al. (1999), Hanssen and Klees (1997) and Hanssen and Klees (1999). Moreover, the stochastic analyses made by Goldstein (1995), Williams et al. (1998), Hanssen (1998), Hanssen (2001), Di-Bisceglie et al. (2001), Emardson et al. (2003), Yun et al. (2010), Knospe and Jonsson (2010) and

Liu et al. (2011) reveal that APS has a power-law behavior as predicted by the Kolmogorov turbulence theory (Kolmogorov, 1941). All the studies have reached a consensus upon the idea that APS in InSAR measurements cannot be characterized as a single isolated anomaly. It affects the total interferogram and the disturbance increases with the increase of spatial distance (Goldstein, 1995; Ferretti et al., 1999; Hanssen, 2001).

On the other hand, we should not limit our focus only on the negative side of APS. One man's trash could be another man's treasure, which is particularly true for APS if water vapor distribution rather than ground deformation is the signal of interest. So far no earth observation techniques other than InSAR can provide water vapor mapping at fine scales ($\sim 100\,\mathrm{m}$), globally under all weather conditions (Hanssen et al., 1999). The spatial distribution of water vapor is strongly correlated with the turbulent mixing process occurring in the lower part of troposphere and affecting our day-to-day weather (Stull, 1995). Therefore, APS opens a door to InSAR for meteorological applications, i.e., InSAR meteorology.

We will discuss the possibilities of mitigating APS for ground deformation modeling in section 1.1.1 and InSAR meteorology in section 1.1.2.

1.1.1 Mitigation of APS for ground deformation modeling

In general, the approaches for the mitigation of APS can be divided into two categories: 1. using ancillary delay measurements, 2. internal adjustment using InSAR time series.

Mitigation based on ancillary measurements

Attempts to mitigate APS by using ancillary measurements of delay from meteorological observations, optical remote sensing, GPS networks and their integrations have been reported by Delacourt et al. (1998), Hanssen et al. (1998), Williams et al. (1998), Beauducel et al. (2000), van der Hoeven et al. (2002), Li et al. (2004), Li et al. (2005), Onn and Zebker (2006), Li et al. (2006), Li et al. (2006) and Li et al. (2009). The advantages of these methods are their straightforwardness, no need for a-priori knowledge of surface deformation and assumptions regarding temporal correlation of APS. However, these methods are usually hampered by practical limitations such as data spatial coverage, temporal coincidence, full vertical profile (related with stratification), spatial resolution and clouds (weather conditions). Therefore, we will not investigate these methods in this thesis.

Following recent advances in numerical weather modeling, delay simulated by numerical weather models is now regarded as the most promising ancillary data for APS mitigation, see Wadge et al. (2002), Webley et al. (2002), Foster et al. (2006), Puyssegur et al. (2007), Jolivet et al. (2011), Liu et al. (2009), Rommen et al. (2009) Hobiger et al. (2010), Gong et al. (2010), Jolivet et al. (2011), Nico et al. (2010), Liu et al. (2011), Gong et al. (2011) and Cimini et al. (2012). The distinctive features of the simulated delay include its availability under all weather conditions, relatively high spatial resolution ($\sim 1\,\mathrm{km}$) and perfect temporal coincidence with SAR acquisitions. Nevertheless, the key research question for the simulated delay is its success

rate and reliability.

Mitigation based on InSAR time series

The methods that utilize the temporal and spatial characteristics of APS and attempt to separate it from gradual and low-rate ground deformation have been reported by Ferretti et al. (2001), Shimada et al. (2001), Crosetto et al. (2002), Emardson et al. (2003), Li et al. (2009), Heleno et al. (2010) and Liu et al. (2011). It is a commonly accepted assumption that two APS fields become temporally uncorrelated if the time interval between them is larger than 1-day (Ferretti et al., 2000; Hanssen, 2001). Under such an assumption APS can be treated as a high frequency noise in time and eliminated by a temporal low-pass filtering (Ferretti et al., 2000; Berardino et al., 2002) or averaging a larger number of interferograms (Sandwell and Price, 1998). Obviously, these approaches do not suffer the practical limitations as mentioned for the ancillary data based approaches. They are however only applicable when there are sufficient number of images available. With the advance in space SAR missions such as ERS-1/2, Envisat, Radarsat-2, TerraSAR-X and Cosmo-SkyMed the global achieve of SAR images has been enriched tremendously and the time cost for building up a time series of SAR images has been significantly reduced. As a result, the internal adjustment approaches are widely used nowadays in mitigating APS. However, the performance of the methods has not yet been fully understood and assessed.

In this thesis we will focus on improving the accuracy and reliability of separating APS and ground deformation under PSInSAR framework (Ferretti et al., 2000) which is the most widely used method in InSAR time series analysis. Given a good spatial density of coherent targets and a short satellite repeat orbit the filtering method used in the standard PSInSAR (see Ferretti et al. (2000)) provides a simple and fast means to separate APS from temporally correlated deformation signal. However, the separation is usually not optimal and can be erroneous when there are acquisition gaps in the time series or for acquisitions taken under extreme weather conditions such as thunderstorms. This is because the approach weights APS equally for all acquisitions and remove it by a window-based (e.g., triangle, Gaussian) temporal low-pass filter. The filter is not adaptive and its parameters (e.g., temporal correlation length) are up to the users to specify. A good filter, however, should weight APS per acquisition differently according to its significance and be self-adjustable based on the input data to optimize its parameters towards an optimal filtering.

1.1.2 InSAR meteorology

The potential of using InSAR for meteorological studies, e.g., fine scale water vapor mapping, has been investigated by Hanssen et al. (1999), Hanssen et al. (2000), Hanssen et al. (2001) and Liu et al. (2009). The water vapor maps may be incorporated into advanced weather and climate analyses via weather and climate models to improve the quality of weather and climate forecasts. However, APS is so far widely regarded as a by-product of InSAR analysis and its value for the meteorology applications is underestimated. This is mainly because InSAR is only sensitive to the spatio-temporal variation of delay instead of absolute delay, i.e., a so-called *acqui-*

sition ambiguity (Hanssen and Kampes, 2004). The first step toward the potential meteorology applications is to retrieve the spatial variation of APS per acquisition from the measured spatio-temporal variation. The challenge mainly comes from the acquisition ambiguity as well as the rapid interferometric phase decorrelation (Zebker and Villasenor, 1992) over non-urban areas. In this thesis, we will try to find a way to resolve the acquisition ambiguity and overcome the phase decorrelation problem without compromising the spatial resolution of water vapor distribution.

1.2 Research objectives and thesis outline

Given the above discussion the research objectives of this thesis can be summarized as follows:

- Investigate the feasibility of using high resolution numerical weather predictions (NWP) from numerical weather models (NWM) for mitigating APS in space-borne SAR Interferometry.
- Develop an algorithm based on geodetic methodologies to improve the precision and reliability of separating APS and ground deformation using InSAR time series.
- Develop an algorithm to map high spatial resolution water vapor lateral variation at SAR acquisitions.

In chapter 2 we review the cause of the tropospheric delay for microwave signals. The spatio-temporal characteristics of APS are discussed. In chapter 3 we use the WRF (Weather Research and Forecasting) (Wang et al., 2009) model to predict tropospheric delay during SAR acquisitions and compare the model predictions at 1 km spatial resolution with atmosphere-only interferograms (≤ 70 days baseline) formed from SAR images acquired by ENVISAT in descending orbit. We choose four regions with different climatic conditions for case studies. Cloud-free MERIS water vapor measurements from ENVISAT are used for cross validation and comparison when available.

In chapter 4 we develop an algorithm based on least-squares collocation (LSC) and variance-covariance components estimation to achieve an optimal separation of ground deformation and APS. The advantages of the developed algorithm are highlighted. Moreover, the original spatio-temporal filtering method proposed by Ferretti et al. (2000) is re-formalized from a weighted least-squares point of view and its characteristics are discussed. Chapter 5 is dedicated to assessing the developed algorithm based on simulated time series in which the ground truth of each signal component (e.g., ground deformation, APS, noise, etc.) is perfectly known. In this chapter the simulation strategies for ground deformation, APS, satellite orbit errors and phase noise are given followed by the result of evaluation for each signal estimate. The sensitivity of the algorithm to the functional and stochastic models chosen for ground deformation modeling as well as the image acquisition rate (minimum satellite repeat-orbit) is also assessed in this chapter. Finally, in chapter 6

the algorithm is evaluated using real InSAR time series from four regions in which the climate varies from tropical to semiarid. For assessing the APS estimate from the developed algorithm we compare them to cloud-free MERIS measurements (if available), atmosphere-only interferograms (short baselines) and the APS estimates from the standard filtering method.

In chapter 7 we develop an algorithm to retrieve spatial variation of APS for each single SAR acquisition. The algorithm is based on the so-called free network adjustment approach (Teunissen, 2000a). The network is formed by small baseline interferograms and designed to be redundant for least-squares adjustment. The approach is applied to ASAR interferograms over Southwest Australia in which phase coherence is well reserved for a relatively long period ($\sim$ 180 days). The good phase coherence allows to retrieve APS per acquisition at 1 km resolution.

Finally, conclusions and recommendations are given in chapter 8.

Chapter 2

Tropospheric delay and its effects on InSAR measurements

Spatio-temporal variation in atmospheric refractivity can significantly influence wave propagation in repeat-pass InSAR observations, leading to errors known as atmospheric phase screen (APS) in derived products such as digital elevation models (DEMs) or deformation maps. This chapter provides a review of tropospheric delay mechanisms for microwave signals and the delay spatio-temporal characteristics in InSAR observations (i.e., interferograms). In section 2.1 the causes of the delay is reviewed and its numerical evaluation is given based on atmospheric refractivity. Section 2.2 elaborates on the spatio-temporal characteristics of the delay observed in InSAR. Based on the characteristics modeling of the delay is given in section 2.3. To read this chapter as well as the rest thesis basic concepts of SAR and conventional SAR interferometric processing are indispensable. Readers who are not familiar with those concepts are recommended to get acquainted with the technical basics from for example Massonnet (1997), Bamler and Hartl (1998) and Hanssen et al. (2000).

2.1 Signal propagation delay and refractivity

The propagation delay of a radio signal caused by the Earth's atmosphere depends on the refractivity along the path traveled by the signal. If we denote the electromagnetic (or optical) distance between the source and receiver by S and the geometric distance by L, the excess path length D reads (Hall et al., 1996):

$$D = S - L = \underbrace{\int_s (n(s) - 1) ds}_{\text{delay}} + \underbrace{(\int_s ds - \int_l dl)}_{\text{bending}}, \tag{2.1.1}$$

where s and l are the electro-magnetic path and geometric path respectively, n is the dimensionless refraction index which is the ratio between the speed of light in vacuum and the actual signal propagation speed through the atmosphere. The first integral in Eq. (2.1.1) accounts for the excess path length caused by the propagation delay, whereas the second term is the excess path length caused by ray bending. The

bending effect is negligible (<1 mm) for measurements made with elevation angles (θ_e) larger than 15° (Mendes, 1999) which corresponds to an incidence angle (θ_i) of 75° for radar. Therefore the bending effect can be safely ignored for all space-borne SAR systems. Since the value of n is nearly equal to one for the atmosphere, the refractivity $N = (n-1) \times 10^6$ is often used instead of n. The refractivity N of the troposphere can be expressed as (Davis et al., 1985):

$$N = \underbrace{k_1 \frac{P}{T}}_{\text{hydro}} + \underbrace{(k_2' \frac{e}{T} + k_3 \frac{e}{T^2})}_{\text{wet}} + \underbrace{k_4 W_{\text{cloud}}}_{\text{droplet}}, \tag{2.1.2}$$

where P is total air pressure (hPa), T is air temperature (K), e is water vapor partial pressure (hPa) and W_{cloud} denotes the cloud liquid water content (g/m^3). The first term on the right-hand side of Eq. (2.1.2) is often called hydrostatic refractivity (N_{hydro}) which results from the induced molecular polarizations of dry air and water vapor (Davis et al., 1985). The second term (between brackets) is often referred to as wet refractivity (N_{wet}) and represents the effect of the permanent dipole moment of the water vapor molecule (Thayer, 1974). The last term is due to liquid water (droplets) within clouds. The constant coefficients $k_1 = 71.6\,\text{K hPa}^{-1}$, $k_2' = 23.3\,\text{K hPa}^{-1}$ and $k_3 = 3.75 \times 10^5\,\text{K}^2\,\text{hPa}^{-1}$ are taken from Smith and Weintraub (1953) while $k_4 = 1.45$ from Solheim et al. (1997).

Using the refractivities defined above and assuming a homogeneous and isotropic troposphere, the one-way slant range delay for radar in meters can be expressed as:

$$\begin{aligned} D &= \frac{1}{\cos\theta_i}(D^z_{\text{hydro}} + D^z_{\text{wet}} + D^z_{\text{droplet}}) \\ &= \frac{10^{-6}}{\cos\theta_i}(\int_h^H N_{\text{hydro}} dz + \int_h^H N_{\text{wet}} dz + \int_h^H N_{\text{droplet}} dz), \end{aligned} \tag{2.1.3}$$

where H is the effective height of the troposphere and h is the elevation of the ground surface. The factor 10^{-6} is due to the conversion between refractivity index n and refractivity N. The hydrostatic delay is of the order of a few meters (Bevis et al., 1996) and the wet delay is usually not larger than 0.3 m (Elgered, 1982). The delay caused by droplets depends on the cloud type and will be discussed in section 2.2.3.

2.2 Characteristics of delay in InSAR

The delay of interest for InSAR is the so-called double difference (DD) delay caused by the spatio-temporal variations of the atmosphere instead of the point-wise absolute delay expressed by Eq. (2.1.3). The actual atmospheric delay observed by InSAR reads:

$$\Delta D_{p,q}^{t_1,t_2} = \overbrace{\underbrace{(D_p - D_q)^{t_1}}_{\text{spatio-temporal}} - (D_p - D_q)^{t_2}}^{\text{spatial}}, \tag{2.2.1}$$

where p and q denote two arbitrary pixels of an interferogram and t_1 and t_2 denote the SAR acquisition times. Obviously, the relative delay $\Delta D_{p,q}^{t_1,t_2}$ makes InSAR blind to point-wise absolute delay. Using Eq. (2.1.3) the DD delay can be decomposed into:

$$\Delta D_{p,q}^{t_1,t_2} = \Delta D_{\text{hydro}} + \Delta D_{\text{wet}} + \Delta D_{\text{cloud}}. \tag{2.2.2}$$

The impact of the components in Eq. (2.2.2) are assessed in the following.

2.2.1 Hydrostatic delay

Under the condition of hydrostatic equilibrium, the zenith hydrostatic delay in Eq. (2.1.3) can be re-parameterized as a function of surface pressure P_{s} (Kleijer, 2004):

$$D_{\text{h}}^{z} = 10^{-6} k_1 \frac{R_{\text{d}}}{g_{\text{m}}} P_{\text{s}}, \tag{2.2.3}$$

where $R_{\text{d}} = 287.053\,\text{J}\,\text{K}^{-1}\text{kg}^{-1}$ is the specific gas constant of dry air and g_{m} (m/s^2) is the local gravity at the center of the atmospheric column (Saastamoinen, 1972), which is a function of latitude and surface elevation. Given the surface pressure P_{s} measured with an accuracy of 0.4 hPa the hydrostatic delay can be estimated with an accuracy of 1 mm (Bevis et al., 1996). For relatively flat regions, standard observations of surface pressure within a typical interferogram area ($100\times100\,\text{km}^2$) show a smooth behavior with variations typically below 1 hPa, which is the result of the large spatial extent of high and low pressure zones. Therefore, the hydrostatic component in Eq. (2.2.2) usually manifests itself as a surface trend of maximally a few millimeters over an entire interferogram (Hanssen, 2001).

2.2.2 Wet delay

Although the wet delay is usually much smaller in magnitude than the hydrostatic delay ($< 10\%$), its fluctuations in both space and time are significantly larger. The fluctuation known as atmospheric turbulence is driven by the turbulent mixing of heat and humidity within the atmospheric boundary layer (Stull, 1995). The life time of a turbulence is proportional to its spatial extent: $\tau \approx aD$ (Stull, 1995), where $a \cong 1\,\text{s/m}$, and D and τ denote the horizontal extent and life time of the turbulence respectively. For instance, the lifetime of a turbulence with a horizontal scale less than 1 km is usually less than 15 minutes. The small spatial scale and short life time of turbulence result in a great challenge on delay mitigation based on external measurements. In general, turbulence is stronger during the summer and during day-time than in winter and during night due to the annual and diurnal variations of solar heating of ground surfaces (Stull, 1995).

Due to its large spatio-temporal variability, turbulence is often modeled stochastically rather than deterministically. We consider the total wet delay as the sum of a mean delay and a delay fluctuation (turbulence) around the mean:

$$D_{\text{wet}} = E\{D_{\text{wet}}\} + \upsilon = \overline{D}_{\text{wet}} + \upsilon, \tag{2.2.4}$$

where E denotes the ensemble average. Like the hydrostatic delay, the mean wet delay $\overline{D}_{\text{wet}}$ can be modeled as a constant or a surface trend over a $100\times100\,\text{km}^2$ area . The turbulent (stochastic) component υ can be modeled stochastically using a variogram γ, also known as structure function. Based on the Kolmogorov turbulence theory (Kolmogorov, 1941) the variogram which describes a homogeneous and isotropic turbulent medium has the form (Tatarski, 1961):

$$\begin{aligned}\gamma(\upsilon) &= E\{[\upsilon(\vec{r}+\Delta\vec{r}) - \upsilon(\vec{r})]^2\} \\ &= C(|\Delta r|)^{\nu},\end{aligned} \tag{2.2.5}$$

where $\vec{r}$ denotes a position vector in 3D space, $\Delta\vec{r}$ is a spatial displacement vector and $|\Delta r|$ denotes the length of the displacement, C defines the power or strength of the turbulence and the exponent ν indicates the smoothness of the turbulence, also called the correlation dimension (a higher correlation dimension indicates a more homogenous medium (Handcock and Wallis, 1994; Hanssen, 2001)). A random signal which has a structure function of the form Eq. (2.2.5) is said to have a power-law behavior. Earlier observations made by e.g., very long baseline interferometry (VLBI) (Treuhaft and Lanyi, 1987) and GPS (Williams et al., 1998) suggest a value of $\frac{2}{3}$ for ν which is also the value predicted by Tatarski (1961) for the elementary turbulence. Due to the low spatial resolution ($>$10 km) of these measurements they only reveal the turbulence at wavelengths much larger than the thickness of the ABL ($\leq$2 km), therefore the measured turbulence is effectively 2-dimensional (2D) turbulence. By analyzing a number of tandem interferograms at fine resolution ($\sim$100 m) over the Netherlands which has a flat terrain, Hanssen (2001) reveals that the turbulence-induced delay has a scale-variant power law behavior and a transition region is observed at wavelengths of approximately 1.5 km. Below this wavelength the correlation dimension is increased by one to $\nu = \frac{5}{3}$ which corresponds to a 3D turbulence. Therefore, the complete form of the variogram describing the atmospheric turbulence is:

$$\gamma(\upsilon) = \begin{cases} C^2(|\Delta r|)^{2/3} & \text{if } |\Delta r| > H_{\text{ABL}}, \\ C^2(|\Delta r|)^{5/3} & \text{if } |\Delta r| \leq H_{\text{ABL}}, \end{cases} \tag{2.2.6}$$

where H_{ABL} is the thickness of the ABL.

Given Eq. (2.2.1) and the decomposition in Eq. (2.2.4), the DD wet delay between points p and q taken at the same altitude can be written as:

$$\begin{aligned}\Delta D_{p,q}^{t_1,t_2} &= [(\overline{D}_p - \overline{D}_q)^{t_1} + (\upsilon_p - \upsilon_q)^{t_1}] - [(\overline{D}_p - \overline{D}_q)^{t_2} + (\upsilon_p - \upsilon_q)^{t_2}] \\ &= \underbrace{\Delta\overline{D}_{pq}^{\Delta t_{12}}}_{\text{mean}} + \underbrace{\Delta\upsilon_{pq}^{\Delta t_{12}}}_{\text{turbulence}}.\end{aligned} \tag{2.2.7}$$

Table 2.1. Liquid water content (W) for different types of clouds (taken from Hanssen (2001)). W is obtained from Hall et al. (1996) and Bean and Dutton (1968). The slant delay in mm per km is evaluated using Eq. (2.2.10) with $\theta_{\text{i}} = 23°$.

Type	Altitude [km]	Liquid water content [g/m^3]	Slant delay [mm/km]
Ice clouds (e.g. Cirrus, Cirrostratus)	> 6	< 0.1	0.1
Stratiform clouds (e.g. Altostratus)	2-6	0.05-0.25	0.1-0.4
Cumulus (e.g. Cumulus humilis)	< 2	0.5	0.7
Comulus congestus and cumulonimbus	≤ 10	0.5-2.0	0.7-3.1

Therefore, the DD wet delay can be written as the sum of the difference between the mean wet delays at t_1 and t_2 and a random term which has a variogram of the form given in Eq. (2.2.6). Here we assume that the two turbulent fields at t_1 and t_2 are uncorrelated. This decorrelation condition is satisfied when the time interval between t_1 and t_2 is sufficiently large, e.g., $\Delta t_{12} > 1$ day (Stull, 1995; Hanssen, 2001).

2.2.3 Cloud droplets

The phase delay caused by clouds is due to the interaction of the radar waves with the cloud droplets. The wave induces a dipole moment in the droplet which results in a secondary wave front. After passing the droplet, the original undisturbed wave front interferes with the secondary wave front and cause a phase shift (Hanssen et al., 2000). The delay due to clouds is proportional to the liquid water content W (g/m^3) of the cloud (Solheim et al., 1999). Since air at a lower temperature can hold less water vapor, low-altitude clouds such as Cumulus usually contain more liquid water than clouds at high altitudes such as Cirrus. Table 2.1 lists the liquid water contents for different types of clouds. Given the liquid water content W, the refractivity of cloud droplets can be obtained using the Clausius-Mossotti equation (Solheim et al., 1999):

$$N_{\text{cloud}} = \frac{3W(\varepsilon_0 - 1)}{2\rho_{\text{w}}(\varepsilon_0 + 2)} \approx 1.45W \tag{2.2.8}$$

and

$$W = 100\frac{Q_{\text{cloud}}(P - e)M_{\text{d}}}{R\,T}, \tag{2.2.9}$$

where ε_0 is the permittivity of water, ρ_{w} is the density (kg/m^3) of liquid water, $R = 8.314\,\text{J}\,\text{K}^{-1}\text{kg}^{-1}$ is the ideal gas constant, $M_{\text{d}} = 28.966\,\text{g}\,\text{mol}^{-1}$ is the molar mass of dry air and Q_{cloud} (kg kg^{-1}) is the cloud water mixing ratio. The relative error caused by the approximation in Eq. (2.2.8) is below 1% (Solheim et al., 1999). Therefore, the one-way slant delay (in millimeters) caused by the liquid water in clouds can be estimated as:

$$D_{\text{cloud}} = \frac{1.45}{\cos\theta_i} WL, \tag{2.2.10}$$

where L is the thickness of the cloud in km. According to Eq. (2.2.10) and the values of W listed in Tab. 2.1, significant delay up to 3 cm can be caused by the liquid water in vertical clouds, i.e., cumulonimbus (thunder clouds), which usually have a relatively limited horizontal size (< 10 km) and a large vertical extent and liquid water content. These clouds are typically generated by thermal convection or frontal lifting (Stull, 1995; Hanssen, 2001).

2.2.4 Height-dependent delay (vertical stratification)

Let us assume the troposphere to be composed of an infinite number of thin layers in which the refractivity can be regarded constant (i.e., turbulence-free) at altitudes h_i (where i is an integer index). Given the refractivity $N(h_i)$ of each layer, the DD zenith delay between points p and q, at altitudes h_p and h_q respectively, can be written as:

$$\begin{aligned} \Delta D_{p,q}^{t_1,t_2}(h) &= \int_{h_p}^{h_q} N^{t_1}(h)dh - \int_{h_p}^{h_q} N^{t_2}(h)dh \\ &= \int_{h_p}^{h_q} \Delta N^{t_1,t_2}(h)dh, \end{aligned} \tag{2.2.11}$$

where $\Delta N^{t_1,t_2}(h)$ is the refractivity difference between times t_1 and t_2 at height $h \in [h_p,\, h_q]$. When $h_p \neq h_q$ and $\Delta N^{t_1,t_2} \neq 0$, Eq. (2.2.11) represents an effect called delay vertical stratification which is a function of height and therefore strongly correlated with land topography. For regions with significant topography, $\Delta D_{p,q}^{t_1,t_2}(h)$ might be comparable to, or even larger than, the lateral delay gradients in the interferogram whereas in flat areas the vertical stratification is "invisible". One way to evaluate $\Delta D_{p,q}^{t_1,t_2}(h)$ is to use radiosonde profiles to compute $N^{t_1}(h)$ and $N^{t_2}(h)$ followed by integrating their difference with height using Eq. (2.2.11) (Hanssen, 2001). Alternatively, since the average profile of wet refractivity can be assumed to have a linear or exponential form (Davis et al., 1991), some authors (e.g., Elosegui et al. 1998; Delacourt et al. 1998; Onn and Zebker 2006) propose to use a linear or exponential model to estimate the delay as a function of height from the observed total delay.

2.3 Delay re-parameterization

One one hand, the DD delay in InSAR can be formulated as a combination of delays due to different driving sources, i.e., dry air, water vapor, droplets (see Eq. (2.2.1)). Under such formulation, the delay can be numerically calculated based on the standard meteorological quantities in Eqs. (2.1.2) and (2.1.3). On the other hand, based on the spatial delay characteristics discussed in section 2.2, the DD delay can be re-parameterized as:

$$\Delta D = M(x, y, h_{\mathrm{m}}) + \upsilon(x, y) + V(h), \tag{2.3.1}$$

where the terms on the right-hand side represent the spatial mean, the turbulence and the height-dependent (vertical stratification) component of the DD delay, respectively. M is equivalent to the mean (zenith) delay due to the air between the mean topographic elevation of the area of interest, h_{m}, and the top of the troposphere. Due to its spatial smoothness, M can be often modeled as a constant or a surface trend within the typical size of an interferogram. Meanwhile, V accounts for the vertical stratification effect which is of importance in mountainous regions. It can be modeled as an analytical function (e.g., linear, exponential) of the surface elevation which is available from a global digital elevation model (DEM) such as the Shuttle Radar Topography Mission (SRTM). The middle term υ represents the delay fluctuation around the mean (turbulence) caused by the spatio-temporal variations of water vapor, cloud droplets and possible precipitation among which water vapor is the dominant contributor.

2.4 Summary

In this chapter we have discussed the cause of the signal propagation delay for microwaves. The one-way absolute delay can be evaluated numerically provided the air temperature, air pressure, water vapor pressure and the signal propagation length. The delay observed in interferograms is however a spatio-temporal variation of the absolute delay and the largest contribution to the variation is caused by turbulent mixing of water vapor within the atmospheric boundary layer. The turbulent mixing is usually regarded as a stochastic process which can be modeled by its spatial variogram. In addition, in mountainous regions the delay in interferograms is often correlated with land topography and the phenomenon is known as vertical stratification. Based on the spatio-temporal characteristics of delay in interferograms we model it as a spatial trend due to dry air and mean water vapor content, a spatial variation caused by turbulent mixing of water vapor and a height dependent term which can be modeled as a function of height. Such modeling of delay forms the basis for comparing the delay observed by InSAR and the delay predicted by weather models which will be discussed in next chapter.

Chapter 3

Delay mitigation using numerical weather prediction (NWP)

Advance in numerical weather predictions, in terms of spatial resolution and success rate as well as recent publications suggest the feasibility of correcting APS in InSAR products using numerical weather model (NWM) outputs. In this chapter we use the state-of-the-art Weather Research and Forecasting (WRF) model to evaluate its usefulness for the pixel-wise correction of InSAR images as well as for a stochastic approximation of the expected variability of APS. A short overview of the recent advance in correcting APS using high resolution weather models is given in section 3.1. The generation of atmosphere-only interferograms, the WRF setup as well as the calculation of tropospheric delays from WRF simulations are presented in section 3.2. Section 3.3 gives details of repeat-pass InSAR processing to generate atmosphere-only interferograms. In section 3.4 the case studies are described and the results are analyzed. The tuning of model settings and its consequences are discussed in section 3.5. Conclusions are drawn and an outlook is provided in section 3.6.

3.1 Introduction

Following recent advances in numerical weather modeling (Wadge et al., 2002; Foster et al., 2006; Puyssegur et al., 2007), atmospheric models are regarded a promising tool for mitigating the atmospheric effect haunting InSAR for decades. The main advantages of these models are that they can be applied to any are of the globe, are not hampered by cloudiness or the availability of daylight in contrast to many external measurements, they have a relatively high spatial resolution and that they can simulate the atmospheric conditions at the SAR acquisition time. Previous studies conducted by e.g., Wadge et al. (2002) using NH3 (Non-Hydrostatic) model, Foster et al. (2006) and Puyssegur et al. (2007) using MM5 (PSU/NCAR Mesoscale Model) have shown encouraging results. The authors found a strong correlation between their model results and the APS observed in interferograms. However, the regions chosen for demonstration exhibit strong elevation changes (i.e., mount Etna, Hawaii and mount Lebanon). In these mountainous regions differences in the vertical stratification of refractivity cause delay patterns in the interferograms

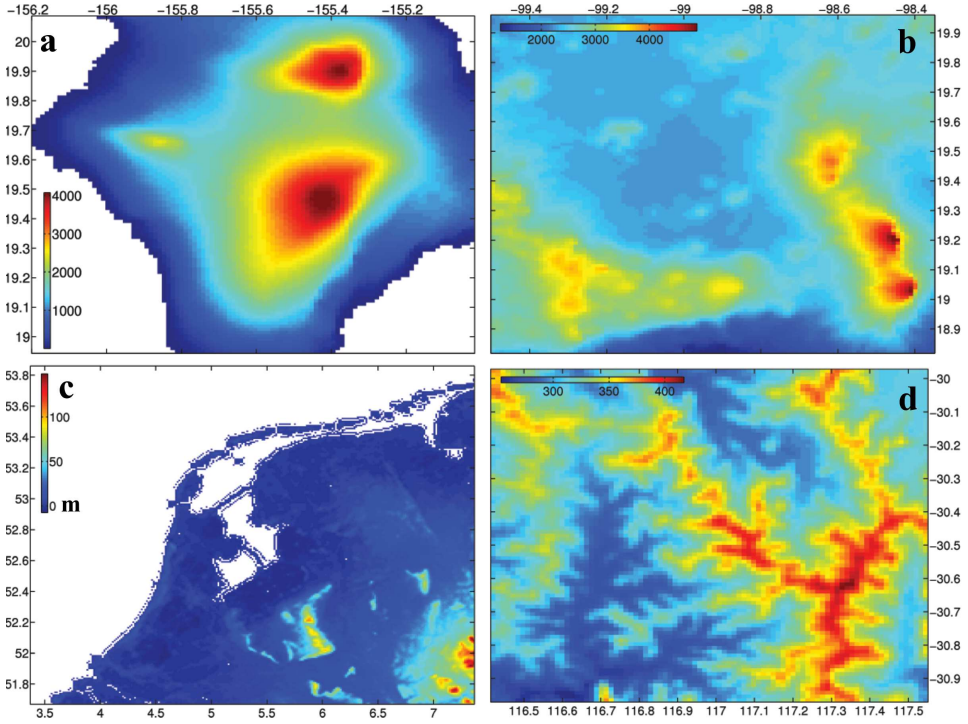

Fig. 3.1. Regional land topography from SRTM, re-sampled to radar coordinates (i.e., azimuth and range). Strong elevation variations are found in (a) Hawaii and (b) Mexico City whereas (c) the Netherlands and (d) Southwest Australia (sub-area) have almost flat terrains. The colorbar unit is meters.

that show a strong correlation with the topography. In many application areas of InSAR (e.g., subsidence, tectonics, infrastructure), the limiting factor is mainly the lateral variability of the APS. To effectively mitigate lateral variation, however, requires not only the modeling of the elevation-dependent delay but also of the lateral delay variation driven by tropospheric turbulence in the atmospheric boundary layer (ABL) with a typical depth of $\sim$2 km above the ground surface.

In this study, we use the WRF (Weather Research and Forecasting) (Wang et al., 2009) model to predict tropospheric delay during SAR acquisitions and compare the model predictions at 1 km spatial resolution with atmosphere-only interferograms ($\leq$ 70 days baseline) formed from SAR images acquired by ENVISAT in descending orbit. We choose four regions with different climatic conditions for case studies (i.e., Hawaii, Mexico City, the Netherlands and Southwest Australia). Strong topography is present in Hawaii and Mexico City, whereas the terrains over the other two regions are relatively flat (see Fig. 3.1). Cloud-free MERIS water vapor measurements from ENVISAT are used for cross validation and comparison when available.

3.2 Delay simulation using numerical weather models

Numerical weather models, generally speaking, use mathematical and physical models of the atmosphere and oceans to predict the weather based on current and past weather conditions. The first attempt can be traced back to the 1920s (Richardson, 2007) and it was not practically feasible until the advent of computer simulation in the 1950s. Typical inputs for weather models representing the current and historical weather conditions are atmospheric data (e.g., air pressure, temperature, etc.) collected from ground launched radiosondes and space-borne weather satellites. Factors affecting the performance of the weather models are the spatio-temporal density and quality of the inputs as well as the complexities of the models themselves. The outputs of weather models vary with applications and in our study the outputs are air temperature, pressure, water vapor pressure and cloud liquid water content in a three-dimension space from ground surface till the top of troposphere.

3.2.1 Model setup

In this study we use Weather Research and Forecasting (WRF) model (release version 3.1.1) to simulate tropospheric delays during SAR acquisitions. WRF is a state-of-the-art numerical weather forecasting model suitable for meso-scale applications (Wang et al., 2009; Skamarock et al., 2008). The WRF model allows the user to choose from a number of different dynamics options and physics parameterization schemes. It can be applied on the continental to local scales with resolutions from hundreds of kilometers down to under a kilometer. The model has two "dynamics cores", a hydrostatic and a non-hydrostatic one. For the purposes of our study, the non-hydrostatic core is chosen since it is capable of representing convection and the associated water vapor processes with higher reliability.

The WRF model requires input data (initial and boundary conditions) from a global model. A global model is also a numerical weather model which incorporates and reanalyzes (this is also known as *data assimilation*) both ground based and remotely sensed data before and after a weather event of interest to generate the input data. The spatial density of the input data for the global model is usually sparse and meant to provide boundary conditions for a local model. In this study we used the NCEP (National Center for Environmental Prediction) Final Analyses (FNL) from the Global Data Assimilation System (GDAS) which are available at 6-hour intervals with a horizontal resolution of 1-degree ($\approx 100\,\mathrm{km}$). The FNL is the starting point for the WRF model to simulate atmospheric process at mesoscale below 100 km. The model is run with 28 vertical levels out of which about 10 are situated in the lowest 2 km of the atmosphere in order to better model the water vapor fluctuation. A nested set-up (Wang et al., 2009) is used to ensure a smooth transition from the coarse resolution of the FNL data to a fine, 1-km horizontal resolution. Four WRF domains are nested into the global fields with successively increasing resolutions of 27 km, 9 km, 3 km, and 1 km. Each coarser domain serves as the parent domain for the one step finer nested domain, providing it with initial and boundary conditions.

The model is started 7 to 10 hours before the SAR acquisition time, in order to allow for the fine scale features to appear and the processes related to water vapor

Table 3.1. Physical parameterizations used with the WRF model.

Physics	Scheme
Microphysics	Morrison 2-moment
Longwave radiation	RRTMG
Shortwave radiation	RRTMG
Surface-layer option	MYNN
Land surface	Noah
Urban physics	single-layer UCM
PBL physics	MYNN 3$^{\text{rd}}$ level TKE
Cumulus option (only for domains 1 and 2)	Kain-Fritsch (new Eta)

to properly initialize (called spin-up time (Wang et al., 2009)). The properties of the land surface (e.g. , albedo, roughness length, topography height, vegetation type, etc.) can substantially impact the heat, moisture and momentum fluxes in the lowest layers of the atmosphere. Therefore, it is important to use as accurate land-use and topography databases as possible. We choose the 20-category MODIS-based land-cover classification of the International Geosphere-Biosphere Program modified for use with WRF (Wang et al., 2009). This proves to be more accurate in most areas than the other option, the 24-category United States Geological Survey (USGS) database. Both datasets are available at resolutions down to 30 seconds ($\approx$ 1 km). The USGS topography data which is readily available for use with WRF is replaced by terrain elevation data from the Shuttle Radar Topography Mission (SRTM). In contrary to the USGS topography data which is available at a maximum resolution of 30 seconds, the SRTM data has a 3-second (about 90 m) resolution. As mentioned before, WRF comes with a large number of physics parameterizations. The physics settings selected for the simulations discussed in this paper are summarized in Tab. 3.1.

3.2.2 Delay computation

Given the model output variables: air temperature T (K), total air pressure P (hPa), water vapor partial pressure e (hPa), cloud liquid water content W (g/m^3) and cloud water mixing ratio Q_{cloud} (kg kg^{-1}) for each model grid box, the refractivity N can be determined using Eqs. (2.1.2) and (2.2.9). Due to the spatial heterogeneity of N_{wet} and N_{cloud} we do not use Eq. (2.1.3) in which the zenith delay is computed first followed by mapping to the radar line-of-sight. Instead, we integrate the computed N along the exact propagation path of the radar wave determined by the SAR orbit geometry. The temporal differential delay is computed as:

$$\Delta D_{\text{NWP}}^{t_1,t_2} = \int_L N(t_1)dl - \int_L N(t_2)dl, \tag{3.2.1}$$

where L denotes the propagation path of the radar wave. Since the delay observed by InSAR is a double-difference delay, InSAR is insensitive to the image-wide delay bias. To eliminate the bias between NWP and InSAR we apply the same de-trending

procedure to $\Delta D_{\mathrm{NWP}}^{t_1,t_2}$ as we do for InSAR (see section 3.3). This de-trended delay can be directly compared to the InSAR delay given by Eq. (3.3.4).

3.3 Repeat-pass InSAR processing

To exclude possible low-rate land deformation and to suppress phase noise due to temporal and geometric decorrelation (Zebker and Villasenor, 1992), all interferograms formed in this study have short temporal baselines (≤ 70 days) and small perpendicular baselines (≤ 300 m). Hence, the dominant signal in the interferograms should be the result of atmospheric disturbance during SAR acquisitions. Our InSAR processing starts with SLC (single look complex) images acquired by ENVISAT in descending orbit. Interferograms are generated using the DORIS software (Kampes, 1999) using ESA's precise orbits. The topographic phase in the interferograms is modeled and removed using 3-arc second SRTM data and phase unwrapping is carried out using the SNAPHU software (Chen and Zebker, 2000). In order to speed up the phase unwrapping and to suppress phase unwrapping errors and phase noise, all interferograms are multi-looked (i.e., spatially average or low-pass filtered) from the original ASAR pixel size of 20 m in range and 4 m in azimuth to 100 m both in range and azimuth using a rectangular window (25 in azimuth and 5 in range) after removing the topography phase. A larger multi-look window may cause unwrapping errors in areas with strong topography since phase gradients between nearby pixels may be significant due to possible strong vertical delay stratification. After the phase unwrapping we further multi-look the unwrapped interferograms to 1 km by 1 km which is the spatial resolution of the WRF model simulations. To avoid biases which might be caused by the large spatial size of the multi-look window (from 100 m to 1 km) we use the coherence γ (ranging from 0 to 1) between the complex signals of master (s_{m}) and slave (s_{s}) SLCs to guide the multi-looking:

$$\phi' = \frac{1}{\sum_{i=1}^{m}\sum_{j=1}^{n} w_{i,j}} \sum_{i=1}^{m}\sum_{j=1}^{n} w_{i,j}\phi(i,j), \tag{3.3.1}$$

where

$$w_{i,j} = \begin{cases} 1 & \text{if } |\gamma|(i,j) > |\gamma|_{\min} \\ 0 & \text{otherwise,} \end{cases} \tag{3.3.2}$$

$$\gamma = \frac{E\{s_{\mathrm{m}} s_{\mathrm{s}}\}}{\sqrt{E\{|s_{\mathrm{m}}|^2\}E\{|s_{\mathrm{s}}|^2\}}} \tag{3.3.3}$$

and ϕ is the unwrapped phase while $|\gamma|_{\min}$ is a pre-defined coherence threshold (0.35 is used in this study).

Since inaccurate satellite orbits may result in phase trends in interferograms (Hanssen, 2001) which are usually not distinguishable from the phase trends caused by the atmosphere, we model the possible surface trends in the interferograms using a least-squares fit based on the unwrapped phases using a linear trend model in range and azimuth. The phase residue after de-trending has a zero mean and represents delay fluctuations due to turbulent mixing for areas with flat terrain and it consists of turbulent mixing and vertical stratification for mountainous areas. The corresponding

Table 3.2. Mitigation results for Hawaii. Global RMS error (mm) of the original interferograms, WRF predictions and mitigation residues are denoted as σ_{InSAR}, σ_{WRF} and σ_{res} respectively. γ indicates the pixel-wise delay correlations between the original interferograms and the WRF simulations. The track and frame for the SAR acquisitions are 200 and 3213 respectively. The acquisition time is 20:23 UTC.

Index	Date	σ_{InSAR}	σ_{WRF}	σ_{res}	γ
1	20030617/20030721	11.5	10.2	14.9	0.07
2	20030721/20030825	12.3	9.1	12.6	0.34
3	20030929/20031103	19.4	23.8	11.4	0.88
4	20041227/20050130	12.0	6.8	13.3	0.37
5	20050130/20050307	12.8	6.8	14.1	0.06
6	20080331/20080505	11.2	10.5	13.9	0.18
7	20081027/20081201	8.2	5.9	9.1	0.20
8	20081201/20090105	16.9	14.2	10.5	0.79

one-way double-difference slant range delay reads:

$$\Delta D_{\text{InSAR}}^{\text{res}} = -\frac{\lambda}{4\pi}\phi_{\text{res}}, \text{ where } E\{\phi_{\text{res}}\} = 0 \tag{3.3.4}$$

and λ is the radar wavelength, ϕ_{res} is the phase residue and the negative sign is due to a phase increase corresponding to a range decrease (Rosen et al., 2000).

3.4 Evaluation of the delays simulated by WRF

In this section we first evaluate the performance of WRF for delay mitigation by subtracting the predicted delay during SAR acquisitions from the ASAR interferograms. To make the evaluation globally representative, four climatic regions are chosen: Hawaii (maritime and tropical), Mexico City (continental and tropical), the Netherlands (marine time and temperate) and Southwest Australia (continental and semi-arid). Among these regions, the Netherlands and Southwest Australia have flat terrains, whereas significant topography is present in the others. Fig. 3.1 shows the ground elevation maps for these regions. The effectiveness of delay mitigation is assessed by global (i.e., image-wide) delay root mean square (RMS) error and pixel-wise delay correlation between the interferograms and the WRF predictions. We expect a high delay correlation and a small delay RMS error after mitigation if WRF performs well. For the mountainous regions we separate the total observed delay into a part due to turbulent mixing (lateral variation) and a delay component which is strongly correlated with land topography (vertical stratification). In section 3.4.2 we further evaluate the statistics of the WRF simulations using variograms which reveal the turbulence strength turbulence at different spatial scales.

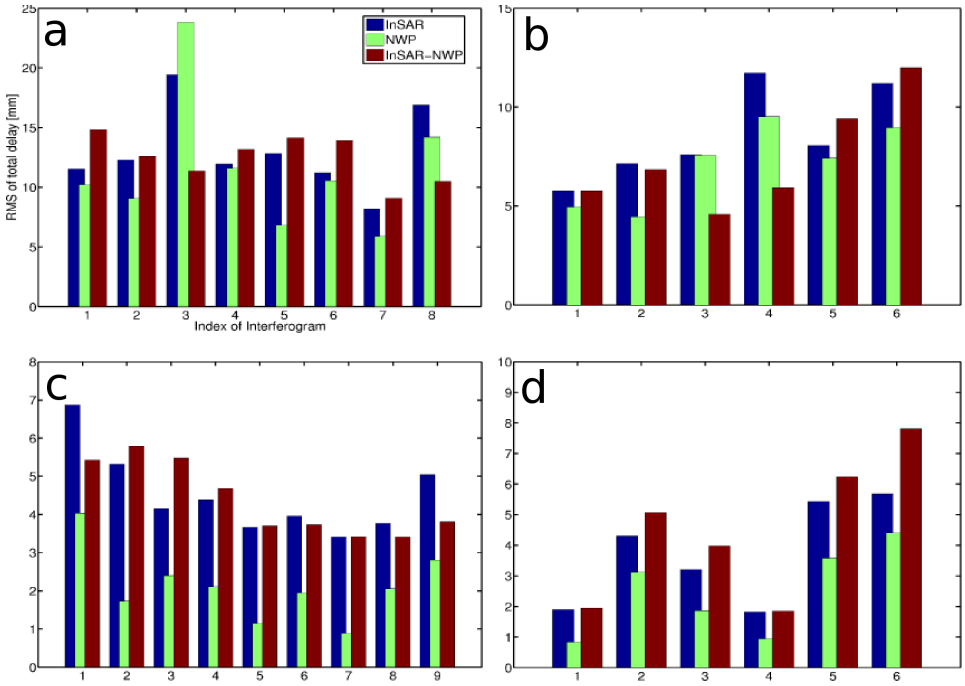

Fig. 3.2. Global delay RMS error in millimeters for (a) Hawaii, (b) Mexico City, (c) the Netherlands, (d) Southwest Australia. The RMS errors of the original interferograms, WRF predictions and residues after mitigation are shown as blue, green and red bars, respectively.

3.4.1 Pixel-wise comparison

Island of Hawaii

The climate of Hawaii is dominated by a moist and heterogeneous tropical atmosphere. Its terrain height ranges from sea level to more than 4 km at the summits of the Mauna Loa and Mauna Kea volcanoes, see Fig. 3.1a. We correct 8 interferograms with 35-day temporal baselines using WRF model results. The overall RMS errors are displayed in Fig. 3.2a and quantified in Tab. 3.2. After correction, interferograms 3 and 8 (see Tab. 3.2) show reduced delay RMS errors of 11 from 19 mm and 10 from 17 mm respectively, which corresponds to about 40% reduction in the delay RMS error. The delay correlations between InSAR and WRF are 0.9 and 0.8 respectively for these two cases. In the other 6 cases, however, deterioration is observed rather than mitigation. The mean delay RMS error for these cases increases from 11 to 13 mm after correction and the pixel-wise delay correlations do not exceed 0.4.

The considerable delay reductions in interferograms 3 and 8 are largely due to the removal of delays which are strongly correlated with height. This can be visualized by plotting the delay against the local DEM as shown in Fig. 3.3. Strong height-dependent delays can be observed both in InSAR and WRF for these two cases. To

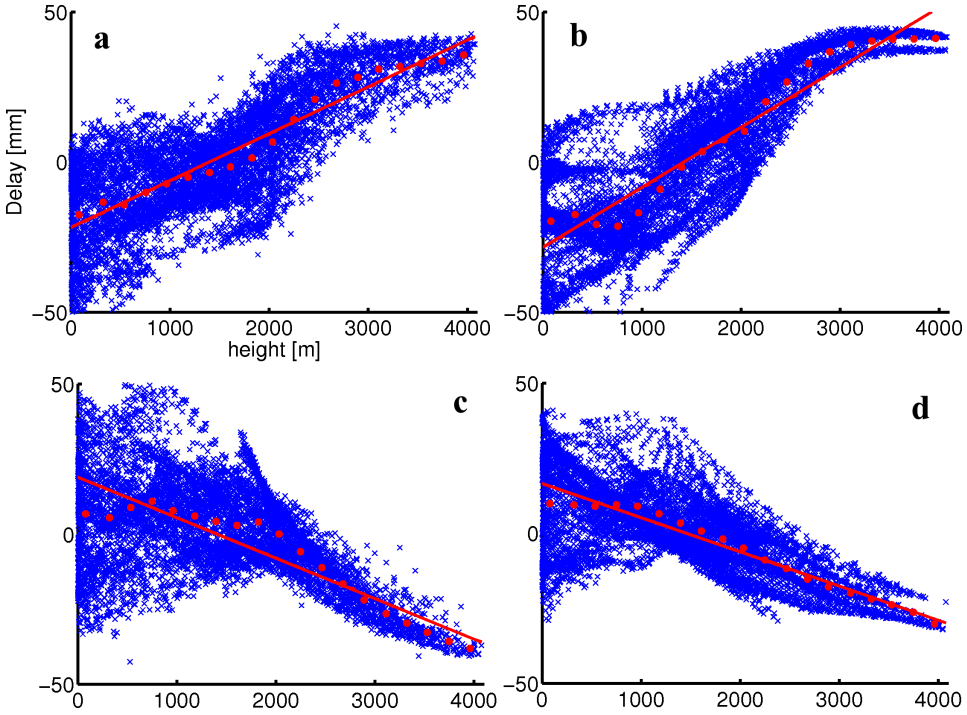

Fig. 3.3. Delay (millimeters) with respect to the local DEM (meters) for Hawaii. (a) and (c) are delays (denoted by crosses) obtained from the original interferograms 3 and 8 in Tab. 3.2 respectively. (b) and (d) are delays obtained from the corresponding WRF simulations. The full altitude range is divided into 20 bins and in each of the bins a mean delay is calculated (marked by a red dot). The red line is the least-squares fit to the mean delay.

model the delays we equally divide the full height range (i.e., 0 to 4 km) into 20 bins and calculate the mean delay (red dots in Fig. 3.3) of the group of pixels within each bin followed by fitting the mean delays along height using a linear trend model (red lines in Fig. 3.3). After the trend is determined, the delay caused by turbulent mixing is isolated by taking the difference between the original delay and the modeled height-dependent delay. By subtracting the modeled height-dependent delays only, the delay RMSs of the original interferograms 3 and 8 reduce to 12 mm and 13 mm respectively. As a demonstration, Fig. 3.4 shows the delay maps of the total delay, the modeled height-dependent delay and the delay caused by turbulent mixing in the original interferogram and in the WRF simulation, respectively and the residue (difference) for interferogram 3. As can be seen from the figure, the height-dependent delay is almost completely removed after mitigation but the turbulent mixing part largely remains. We calculate the correlation between InSAR and WRF for the delays due to turbulent mixing which reveals that in both cases (interferograms 3 and 8) they decrease to 0.5. The decrease of correlation implies that the height-

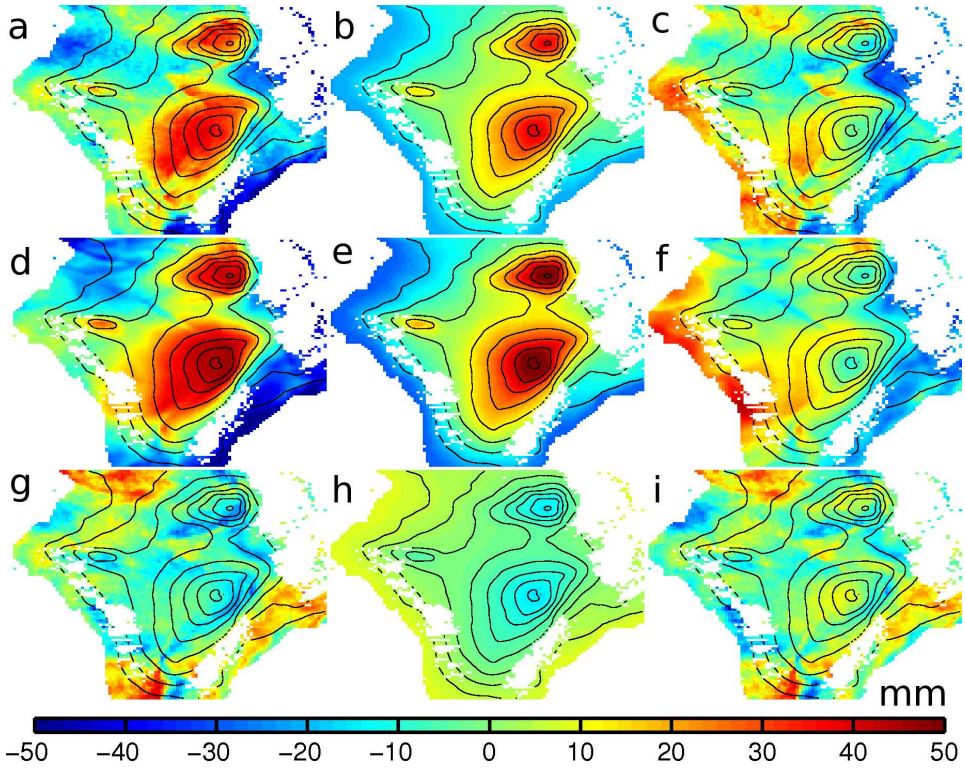

Fig. 3.4. Delay decompositions for case 3 of Hawaii (see Tab. 3.2). The first column (a,d,g) represents (top-to-bottom) the total delay obtained from the interferogram (100 by 100 km), the WRF simulations and their difference respectively. The second column (b,e,h) represents (top-to-bottom) the modeled height-dependent delays from the interferogram, the WRF simulations and their difference respectively. The last column (c,f,i) represents (top-to-bottom) the modeled turbulent mixings from the interferogram, the WRF simulations and their difference respectively. The colorbar unit is millimeters. Similar results from MM5 for this case can be found in Fig. 2 of Foster et al. (2006)

dependent delays present in the interferograms are better modeled by WRF than the delays caused by turbulent mixing. In the other 6 cases neither InSAR nor WRF show noticeable height-dependent delays thus these cases are dominated by turbulent mixing. Therefore, for this region WRF is only successful in correcting the height-dependent delays which exhibit much less spatio-temporal variations than the delays driven by turbulent mixing.

Mexico City

The region of Mexico City has a subtropical climate which is the result of the interaction between tropical air masses from the south and cold northerly fronts. The urban area of the city with a mean elevation of 2200 m is surrounded by mountains

Table 3.3. Mitigation results for Mexico City (see the caption of Tab. 3.2 for the meanings of the symbols). The track and frame for the SAR acquisitions are 255 and 3216 respectively. The acquisition time is 16:36 UTC.

Index	Date	σ_{InSAR}	σ_{WRF}	σ_{res}	γ
1	20031107/20031212	5.8	4.9	5.8	0.43
2	20031212/20040220	7.1	4.4	6.9	0.38
3	20041126/20041231	7.6	7.6	4.6	0.82
4	20041231/20050204	11.7	9.5	5.9	0.86
5	20041231/20050311	8.0	7.4	9.4	0.26
6	20050311/20050415	11.2	9.0	12.0	0.31

with elevations up to 5000 m in the east and the southwest, see Fig. 3.1b. The lowest area is located in the south where the elevation decreases rapidly from 2000 to 1300 m. High-rate ($\sim$1 cm/month) land subsidence in the urban area due to extensive ground water withdrawal has been observed in a number of interferograms. To avoid the mixing of the atmospheric signal with land deformation, we mask out the subsiding region from all the interferograms. Moreover, coherence loss in non-urban areas of the region is significant and results in noisy interferograms during seasons other than winter. To avoid this, we only use SAR images acquired during winter. Note that air is normally less turbulent in winter than in warmer seasons (Stull, 1995).

We correct 6 interferograms using WRF model simulations. The overall RMS errors are displayed in Fig. 3.2b and quantified in Tab. 3.3. Similarly to the Hawaii region, only 2 out of 6 interferograms experience delay reduction after correction (see interferograms 3 and 4 in Tab. 3.3) with delay RMS error reductions from 8 to 5 mm and 12 to 6 mm respectively (i.e., $\sim$40-50% reduction). The delay correlations between InSAR and WRF for these two cases are 0.8 and 0.9 respectively. The worst case is interferogram 5 in which the delay RMS error is increased by 2 mm after correction. This case shows the lowest delay correlation as well (0.3). By plotting the delay against the local DEM for this case we observe that WRF indicates a significant height-dependent delay (Fig. 3.5b) which is, however, not present in the corresponding interferogram (Fig. 3.5a). To find out which picture is the realistic one, we carry out a cross-validation using two cloud-free water vapor measurements by MERIS which were acquired simultaneously with the SAR images. In these data water vapor is expressed in terms of integrated water vapor (IWV) along the zenith with a reduced horizontal resolution of 1.2 km which is comparable to the resolution of the WRF simulations (1 km). The theoretical accuracy of the MERIS IWV over land is 0.17 g/m^2 at full resolution ($\sim$300 m) (Bennartz and Fischer, 2001), which corresponds to 1 cm accuracy in range delay. The accuracy of the reduced resolution product is expected to be substantially higher due to the spatial averaging applied (ESA, 2006). To obtain delay from the IWV along slant range we apply the following widely used approximation:

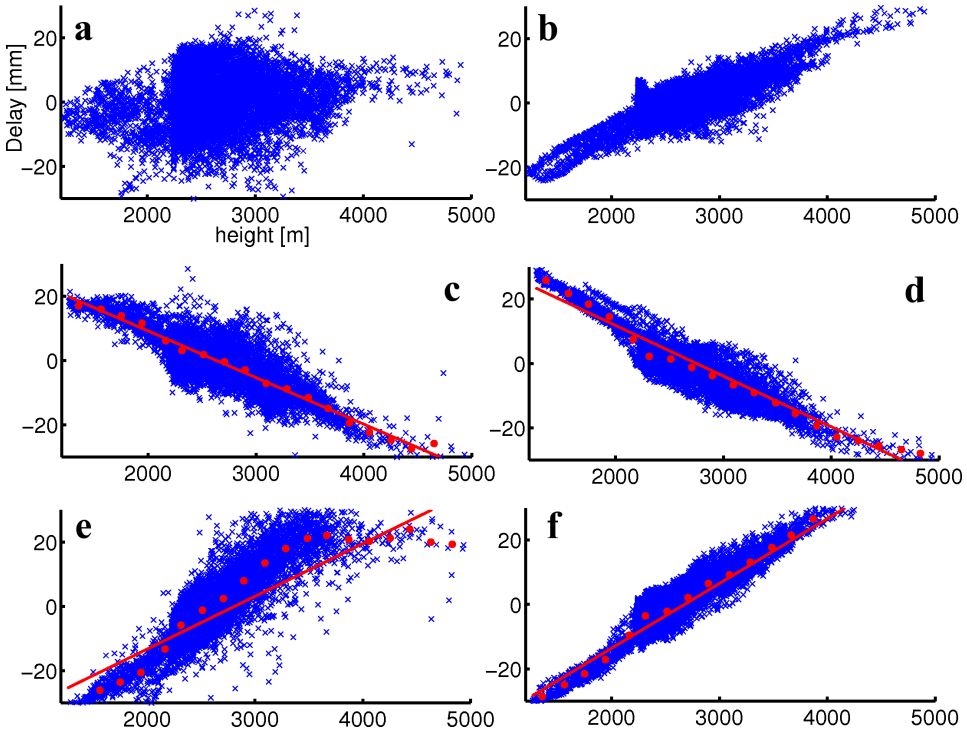

Fig. 3.5. Delay with respect to the local DEM for the Mexico City area. (a) and (b) are delays (denoted by crosses) obtained from interferogram 5 and the corresponding WRF simulations respectively (see Tab. 3.3). WRF indicates a strong but non-existent height-dependent delay (see Fig. 3.6). (c) and (d) are delays obtained from interferogram 3 and the corresponding WRF simulations respectively. (e) and (f) show the results interferogram 4 and the corresponding WRF simulations respectively.

$$\Delta D_{\text{slant}} \approx \frac{\text{IWV}_\text{m} - \text{IWV}_\text{s}}{\Pi \cdot \cos\theta_\text{i}}, \tag{3.4.1}$$

where the indices m and s denote the master and slave acquisitions respectively, Π is a dimensionless factor with a typical value of 0.15 (Bevis et al., 1996). The delay derived from MERIS is shown in Fig. 3.6b which confirms the InSAR observation shown in Fig. 3.6a. Thus in this case WRF predicts a strong but non-existent height-dependent delay which is largely responsible for the serious deterioration of the original interferogram.

Similarly to the Hawaii cases, the considerable delay reductions in interferograms 3 and 4 are the result of the removal of the height-dependent delay. To illustrate this we model the height-dependent delay and turbulent mixing in the same way as for the Hawaii cases. The results are shown in Fig. 3.5(c-f). After removing the height-dependent delays, the delay correlations between InSAR and WRF substantially

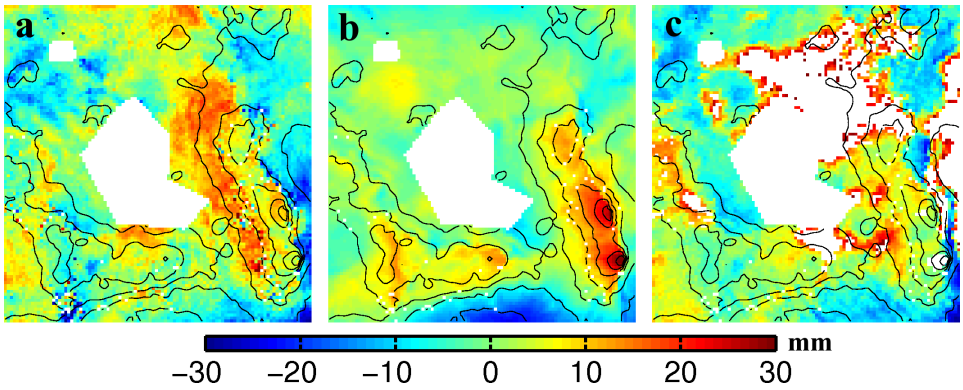

Fig. 3.6. Validation of the WRF simulations for interferogram 5 of Mexico City. (a) delay map from the original interferogram (100 by 100 km), (b) from the WRF simulation, (c) from the MERIS acquisition taken simultaneously with the ASAR image. Cloud pixels in the MERIS image are masked out using the cloud flag provided by ESA. The subsiding urban area of Mexico City has been masked out manually.

decrease to 0.4 and 0.3 respectively. As a demonstration, we plot the total delay, the modeled height-dependent delay and the delay caused by turbulent mixing for interferogram 3 in Fig. 3.7. The delay correlated with land topography is almost perfectly represented by the WRF results, whereas the turbulent mixing part is poorly modeled and is much smoother than the real delay in the interferogram. In the other three cases (interferograms 1, 2 and 6) neither InSAR nor WRF show noticeable height-dependent delay and the mean delay correlation between InSAR and WRF is less than 0.4.

The results from this region are largely consistent with what we have found for Hawaii. Both of them reveal that turbulent mixing is poorly modeled by WRF and the considerable delay mitigations are achieved mainly due to the removal of the height-dependent delay. However, interferogram 5 from this region further warns us that the height-dependent delays modeled by WRF are not always reliable and subtracting them from the interferograms without caution may result in misinterpretations of geophysical phenomena such as co-/post-/or inter-eruptive activities.

The Netherlands

The Netherlands have a maritime climate and flat terrain. Clouds appear virtually every day and rainfall occurs throughout the year. Land deformation rates are less than 1 mm/year for most land surfaces within the region. Since vegetation causes significant temporal decorrelation for C-band interferometry even within 35 days, we only use ASAR images acquired during winter when the land surface is relatively barren. The chosen SAR images come from 5 frames in 2 orbit tracks which cover the whole country.

We correct 9 interferograms with 35-day temporal baselines. Due to the flat terrain, the height-dependent delay is negligible in all interferograms and delay variations

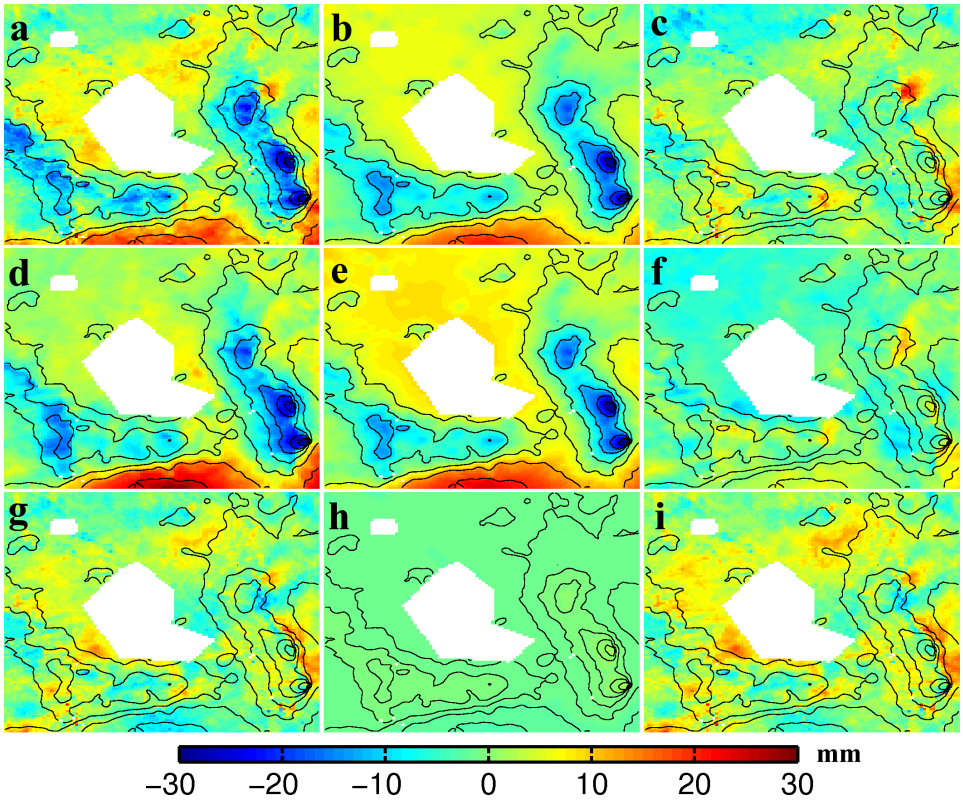

Fig. 3.7. Delay decompositions for case 3 (see Tab. 3.3) of Mexico City. The first column (a,d,g) represents (top-to-bottom) the total delay obtained from the interferogram (100 by 100 km), the WRF simulations and their difference respectively. The second (b,e,h) and the last columns (c,f,i) represent the modeled height-dependent delays and the delays driven by turbulent mixing respectively.

are solely caused by turbulent mixing. The overall mitigation results are displayed in Fig. 3.2c and quantified in Tab. 3.4. Seven out of nine cases show no considerable delay reduction after mitigation. Only interferograms 1 and 9 show a global delay RMS error reduction from 7 to 5 mm and from 5 to 4 mm respectively (about 25% reduction). Figure. 3.8 shows the delay maps obtained from InSAR and WRF as well as their difference for these two cases. Although the spatial delay patterns in the interferograms and the WRF simulations are similar at relatively large spatial scales (i.e., along the diagonal from southwest to northeast and in the southeast and northwest corners), the modeled lateral delay variations are much smoother than the ones in the interferograms. This implies that the strength of turbulent mixing is underestimated by WRF in these two cases. A possible reason for the poor performance of WRF is a prediction timing error which may manifest itself as a horizontal delay shift in space with respect to the real delay at the acquisition

Table 3.4. Mitigation results for the Netherlands (see the caption of Tab. 3.2 for the meanings of the symbols). The chosen acquisitions are from 5 frames (2533, 2576, 2542 2544 2550) and 2 tracks (380, 423) covering the whole of the Netherlands. The data acquisition varies between 10:00 and 10:10 UTC. The last 4 columns show the results of a search for prediction timing errors. The maximum pixel-wise correlation between InSAR and WRF is searched for within ±2 hours around the acquisition epoch. Δt_{m} and Δt_{s} are the times in the modelled master and slave acquisition with respect to the SAR acquisition epoch. $\sigma_{\mathsf{res}}^{\mathsf{min}}$ is the delay residue RMS error corresponding to γ_{max}.

Index	Date	σ_{InSAR}	σ_{WRF}	σ_{res}	γ	Δt_{m}	Δt_{s}	γ_{max}	$\sigma_{\mathrm{res}}^{\mathrm{min}}$
1^{2533}	20041031/20041205	6.9	4.0	5.4	0.61	-120	60	0.78	4.6
2^{2533}	20051120/20051225	5.3	1.7	5.8	-0.12	-90	120	0.23	5.3
3^{2576}	20041031/20041205	4.2	2.4	5.5	-0.35	0	-30	0.75	3.1
4^{2576}	20051120/20051224	4.4	2.1	4.7	0.1	30	120	0.53	4.1
5^{2542}	20041103/20041208	3.7	1.1	3.7	0.12	-120	-30	0.34	3.5
6^{2542}	20050112/20050216	4.0	2.0	3.7	0.36	30	-30	0.43	3.6
7^{2554}	20041103/20041208	3.4	0.9	3.4	0.12	90	120	0.35	3.2
8^{2554}	20050112/20050216	3.8	2.1	3.4	0.44	30	-60	0.55	3.4
9^{2550}	20041031/20041205	5.0	2.8	3.8	0.66	-30	0	0.79	3.3

epoch. Depending on the local wind conditions, a large mass of water vapor can be transported a substantial distance within a relatively short period. Therefore, we do not only calculate the delay from the simulations at the acquisition epoch but within 2 hours before and after the epoch. The results are reported in Tab. 3.4 and suggest that there is probably a simulation timing error in the modeling of the delays in interferogram 3. Without taking the timing error into account the delay correlation between InSAR and WRF is as low as -0.35 and the RMS error of the delay residue after mitigation (6 mm) is even larger than the RMS error in the original interferogram (4 mm). The maximum delay correlation (0.8) for this case is found using the model results from 30 minutes before the slave acquisition epoch, see Fig. 3.9. After correcting for the timing error, the RMS error of the delay residue reduces to 3 mm ($\sim$ 25% RMS error reduction). Nevertheless, even accounting for the timing error WRF significantly underestimates the lateral delay variations. No apparent timing error is found for the other eight cases. Since only two out of nine cases show delay RMS error reductions ($\sim$ 25%), we come to the same conclusion as for the mountainous regions, namely, that the WRF simulations, in general, are not able to mitigate satisfactorily the delay due to turbulent mixing in interferograms.

Southwest Australia

The center of the region is located at -30°27′ S 116°57′ E, approximately 220 km away from the city Perth in southwest Australia. It has a semi-arid climate and the terrain is nearly barren in all seasons. The average terrain height is approximately 300 m above sea level and height differences are less than 200 m, see Fig. 3.1d. We correct 6 interferograms with short temporal baselines to avoid possible local surface deformation. The mitigation results are visualized in Fig. 3.2d and quantified

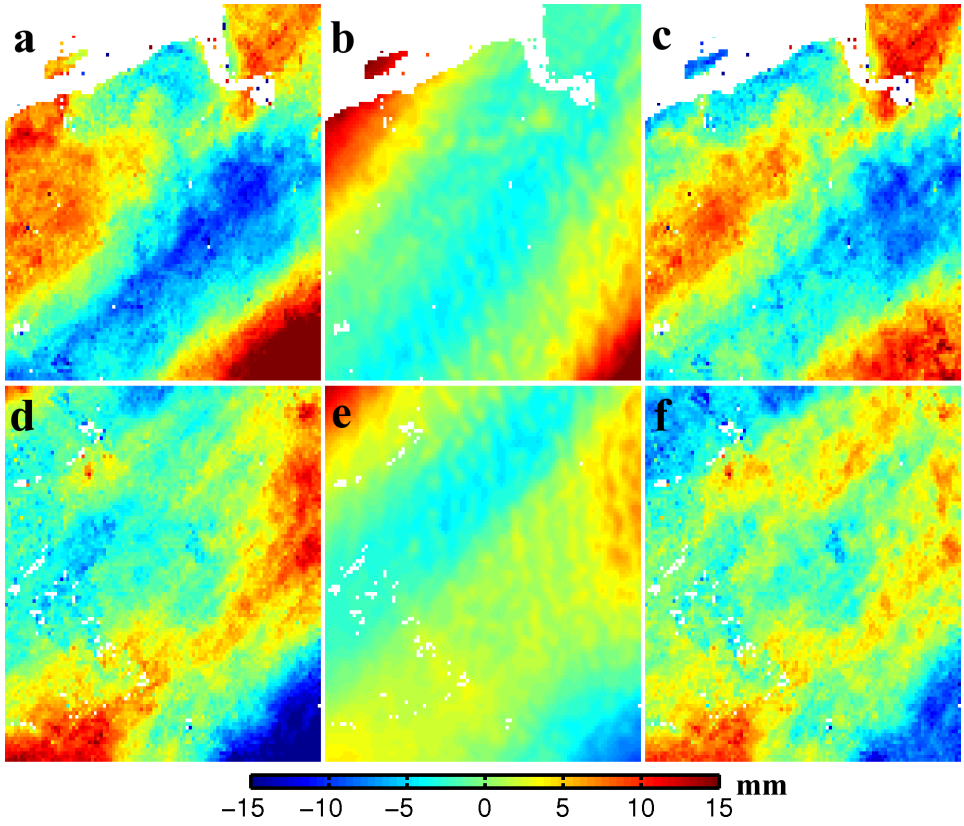

Fig. 3.8. Delay mitigation results for interferograms 1 and 9 from the Netherlands, see Tab. 3.4. The first row from left to right (a,b,c) represents delay maps (100 by 100 km) obtained from interferogram 1, the corresponding WRF simulations and their difference respectively. The second row (d,e,f) is the same but for interferogram 9. The water bodies in the figures are masked out.

in Tab. 3.5. None of the interferograms show noticeable delay reduction after correction. The mean delay RMS error of the interferograms is increased by 1 mm from the original 4 mm and the delay correlation between InSAR and WRF ranges from -0.2 (interferogram 6 shown in Fig. 3.10a) to 0.2 (interferogram 4 shown in Fig. 3.10d) with an average value of 0.04. A search for possible simulation timing errors as done for the Netherlands did not lead to improvements.

Due to the semi-arid climate there are 13 mostly cloud-free MERIS acquisitions spanning 4 years over the region available. This provides us an opportunity to evaluate the absolute wet delays modeled by WRF during single acquisitions instead of the double differential delays which only represent spatio-temporal delay variation. We compute the mean and the variability of the MERIS measurements and of the WRF simulations along with their differences. The results are summarized

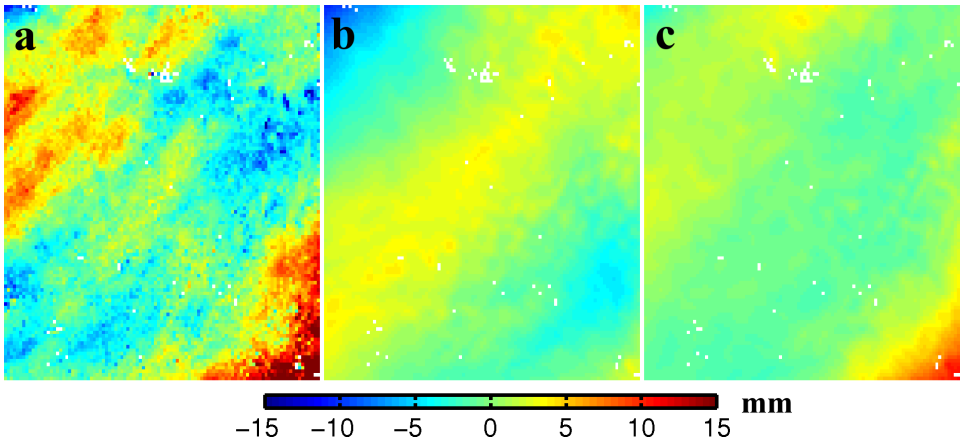

Fig. 3.9. Visualization of the timing error found in the 3rd Netherlands case (see Tab. 3.4). Delay maps (100 by 100 km) obtained from (a) the original interferogram; (b) the WRF simulations at the master and slave acquisition epochs; (c) the simulations at the master acquisition epoch and 30 minutes (i.e., timing error) prior to the slave acquisition epoch.

in Fig. 3.11. The mean and the RMS errors of the delays represent the mean water vapor content and the strength of turbulent mixing respectively. The mean of the difference indicates the mean content bias between WRF and MERIS and the RMS error of the difference is a measure of the pixel-wise correspondence between the modeled and measured turbulent mixings. The comparison reveals that (i) in terms of the mean water vapor content (which ranges from 35 mm under dry conditions to 166 mm under wet conditions) WRF agrees reasonably well with MERIS albeit WRF shows a slight overestimation (8 mm on average, corresponding to $\sim 1.2\,\mathrm{kg/m^2}$ IWV); (ii) WRF significantly underestimates the water vapor variability in all cases; (iii) WRF does not simulate a realistic water vapor distribution as evidenced by the large RMS errors of the differences. In summary, the comparison suggests that WRF

Table 3.5. Mitigation results for Southwest Australia (see the caption of Tab. 3.2 for the meanings of the symbols). The track and frame for the SAR acquisitions are 203 and 4221 respectively. The acquisition time is 01:39 UTC. No evident timing error has been found in the WRF simulations.

Index	Date	σ_{InSAR}	σ_{WRF}	σ_{res}	γ
1	20050621/20050726	1.9	0.8	1.9	0.16
2	20051004/20051108	4.3	3.1	5.1	0.10
3	20060919/20061024	3.2	1.9	4.0	-0.17
4	20070522/20070626	1.8	0.9	1.9	0.23
5	20070626/20070731	5.4	3.6	6.2	0.09
6	20070731/20070904	5.7	4.4	7.8	-0.19

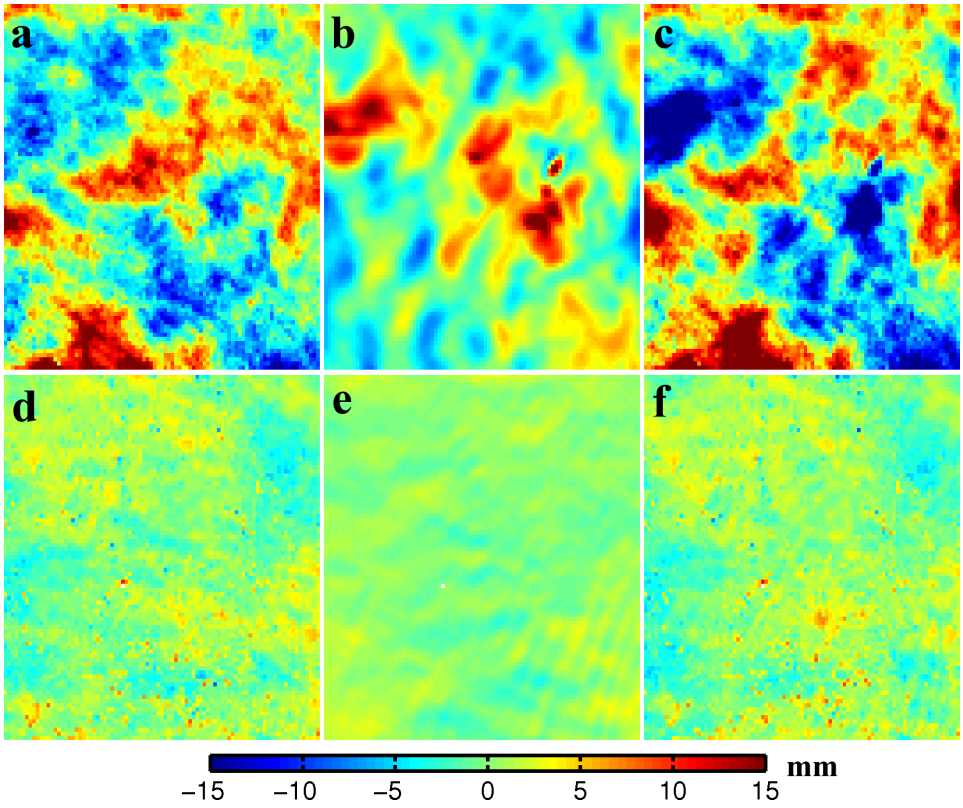

Fig. 3.10. Delay mitigation for cases 4 and 6 from Southwest Australia, see Tab. 3.5. The first row (a,b,c) from left to right represents the delay maps (100 by 100 km) obtained from interferogram 6, the corresponding WRF simulations and their difference respectively. This is the worst case from the region. After mitigation the delay RMS error is increased by 2 mm. The second row (d,e,f) displays the same for interferogram 4. This is the best case from Southwest Australia in terms of delay correlation between InSAR and WRF albeit no delay reduction is achieved.

can predict the total water vapor content reasonably well, but it fails to simulate the lateral water vapor distribution and its overall variability realistically.

3.4.2 Comparison in terms of turbulence statistics

The global model data (i.e., FNL) used to initialize the WRF simulations have a coarse horizontal resolution of 1 degree ($\approx$ 100 km). Water vapor fields are interpolated to the higher-resolution (27, 9, 3 and 1 km) WRF domains during the model initialization step. As the simulation progresses, more details appear in the water vapor field as the adjustment to the high-resolution orography and land-use takes place and the physical processes develop in the model. The coarse initialization of the water vapor fields together with the fact that the turbulent mixing of water

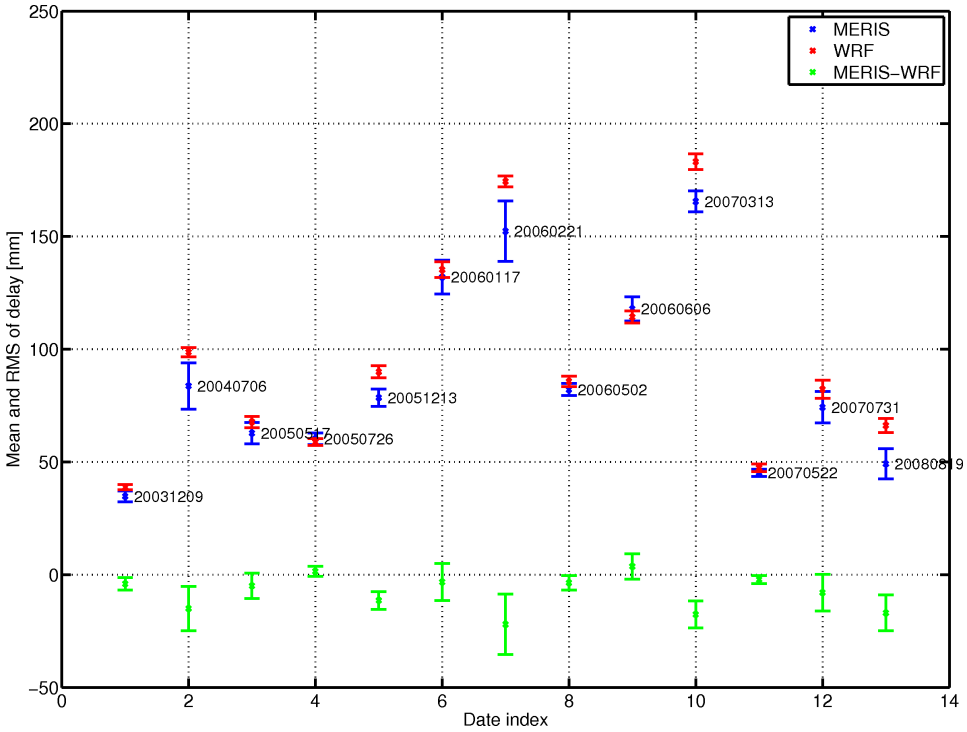

Fig. 3.11. Wet delay comparison between MERIS and WRF. Thirteen cloud-free MERIS water vapor measurements are compared to the corresponding WRF simulations. Blue, red and green crosses denote the mean delays from MERIS, WRF and their difference (residue) respectively. The error bars represent the delay RMS error around the mean which indicates the strength of turbulent mixing. The mean delays of MERIS and WRF agree reasonably well, ranging from 35 mm under dry condition to 166 mm in wet weather with WRF slightly overestimating the mean. However, the turbulence strength is underestimated by WRF in each case. Furthermore, the RMS errors of the residues (green error bars) are comparable to or larger than the RMS errors of the original MERIS measurements. This implies that the turbulent mixing modeled by WRF is unrealistic.

vapor is a chaotic process (Lorenz, 1963; Stull, 1995) are likely responsible for the poor performance of WRF at predicting realistic turbulence at fine scales, which may even lead to a deteriorated result after correction. Hence, it might not be a reasonable approach to mitigate delay in interferograms using WRF in a deterministic manner, i.e., to perform a pixel-wise correction. Note that independent of possible realizations of turbulent mixing at an arbitrary location and time their spatial statistics should obey a power law behavior according to the Kolmogorov turbulence theory (Tatarski, 1961). This implies that the predicted delays should have variograms of the form of Eq. (2.2.5) but with varying magnitudes due to different weather conditions (Hanssen, 2001). If NWMs would be able to predict the power law variograms, even if they are not capable of simulating the actual water

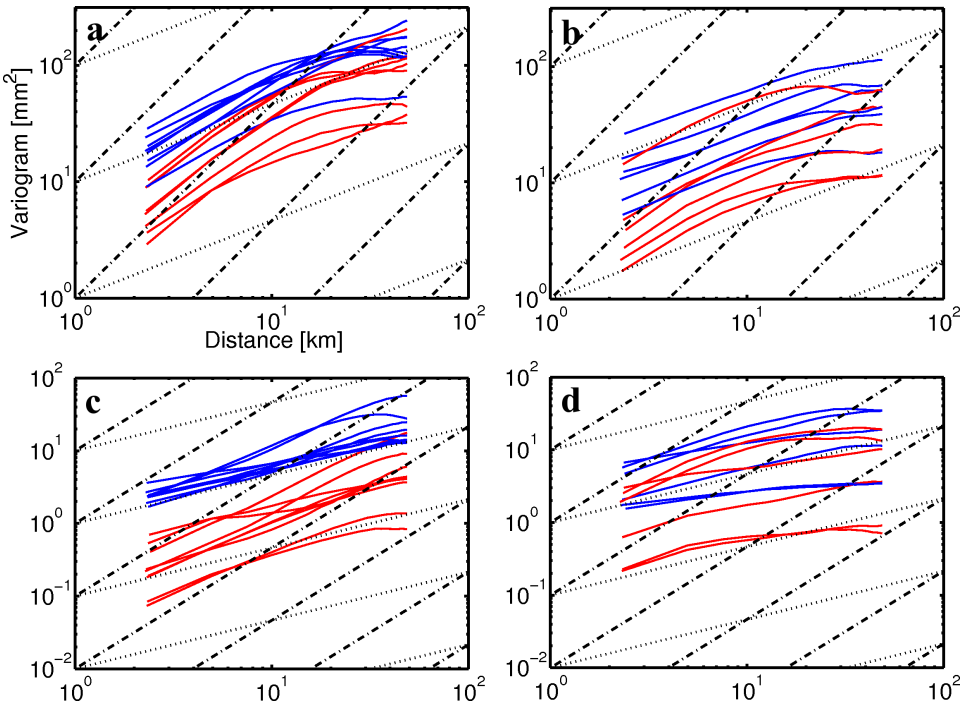

Fig. 3.12. Statistical comparison between WRF and InSAR. The delay variograms (log-log) of the interferograms and WRF simulations are shown in blue and red respectively. (a) Hawaii, (b) Mexico City, (c) the Netherlands, (d) Southwest Australia. WRF considerably underestimates the turbulence strength at all spatial scales ranging from 1 to 50 km. The dashed and dotted lines follow a 5/3 (3D isotropic turbulence) and a 2/3 (2D isotropic turbulence) slope for reference.

vapor distribution, such statistical information may still be very valuable to the internal adjustment based approaches such as low-pass filtering used in persistent scatterers InSAR (Ferretti et al., 2000) and the small baseline subset method (Berardino et al., 2002) or interferogram stacking (Sandwell and Price, 1998; Hooper, 2006). In these methods, atmospheric delays during different SAR acquisitions are currently equally weighted regardless of their varying strengths and are eliminated as a high-frequency component using a low-pass filter. This encourages us to further examine the capabilities of WRF and to compute the experimental variograms of the interferograms and the WRF simulations, shown in Fig. 3.12 for each region. For Hawaii and Mexico City the variograms are computed from the delays driven by turbulent mixing only (see section 3.4.1). The statistical analysis reveals that WRF significantly underestimates the turbulence strength (by approximately one order of magnitude) at all spatial scales between 1 and 50 km (see Fig. 3.12) in all cases. The underestimation results in rather smooth delay maps compared to InSAR or MERIS as also seen before in section 3.4.1. Therefore the WRF simulations neither represent

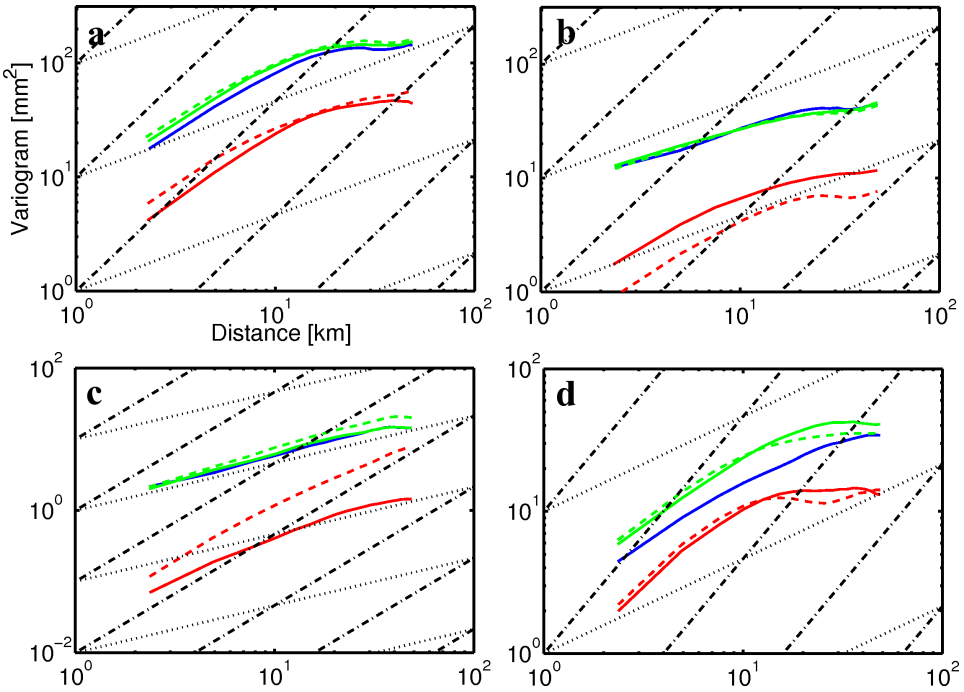

Fig. 3.13. Variograms computed from WRF model results before and after tuning. (a) case 5 of Hawaii, (b) case 4 of Mexico City, (c) case 5 of the Netherlands (d) case 5 of Southwest Australia. The variograms represented by the dashed lines are computed from the simulations with more than 24 hours of spin-up time and 70 vertical levels. The variograms shown as solid lines are computed from simulations with less than 10 hours of spin-up time and 28 vertical levels. Blue, red and green variograms are computed from the interferograms, the WRF model results and their differences respectively. Possible height-dependent delays in the Hawaii and Mexico City cases were removed before computing the variograms.

the turbulent mixing in a realistic manner deterministically nor statistically in any of the cases. However, the variograms computed from the model results shown in Fig. 3.12 do obey the power-law of turbulence, although they are all down-scaled. In section 3.5 we tune a number of model parameters in an attempt to improve on this the down-scaling effect.

3.5 Model tuning toward improving delay simulation

In an effort to improve on the APS mitigation results using WRF, we consulted model developers as well as meteorologists from the model user community (Dudhia and Ferretti, 2010). It was recommended to increase the model spin-up time (i.e., the time interval between the model initialization and the SAR acquisition epoch) to allow atmospheric processes such as turbulent mixing at fine scales to fully develop.

In addition, Foster et al. (2006) and Puyssegur et al. (2007) used more dense vertical levels in their model simulations, for instance Puyssegur et al. (2007) uses 42 vertical levels with 30 below sigma level 0.8 (approximately corresponding to 2 km above ground surface). Since the bulk of water vapor in the troposphere is concentrated within the ABL which has a typical depth of 2 km, these seems to be a reasonable approach. Therefore, we re-do the model simulations with the following adjustments: (i) a longer spin-up time, ranging from 26 to 30 hours; (ii) increased number of vertical levels with 35 out of 70 levels below sigma level 0.8. However, the applied adjustments did not lead to any considerable improvements, neither in terms of pixel-wise delay correction nor turbulence statistics. For demonstration we choose the cases where the turbulence strength is the most severely underestimated from each of the four regions and plot their variograms in Fig. 3.13 using both the old and new model results. Height-dependent delays are removed for the Hawaii and Mexico City cases. Although the case from the Netherlands shows a slight increase in turbulence strength after the model tuning, the turbulence strengths are still largely underestimated (by approximately one order of magnitude) at all spatial scales. The Mexico City case, however, shows a decrease of turbulence strength instead of an increase. In the other two cases the turbulence strength stays more or less the same. Furthermore, by comparing the variograms of the residues (green lines) to the variograms of the original interferograms (blue lines) for each case in Fig. 3.13 we find that even after the model tuning there is still no delay reduction at all spatial scales. Therefore, we conclude that longer spin-up time and denser vertical levels do not necessarily improve the quality of turbulent mixing predictions.

The finest resolution of the WRF simulations is 1 km while InSAR has a 20-m resolution (down-sampled by multilooking to 1 km, see section 3.3). Meteorological processes at scales smaller than 1 km can not be modelled explicitely by WRF. The effects of such phenomena are partially accounted for via parameterization. We hypothesize that the underestimation of turbulent mixing stems from un-modelled sub-scale processes. If this is the case than we would expect to observe a difference in the strength of turbulent mixing between simulations at different resolutions. To investigate this possibility, we compute the variograms of wet delays, shown in Fig. 3.14, based on WRF simulations at 1, 3, 9 and 27 km resolutions for the Netherlands case of 31 October 2004. We use a 28-hour spin-up time and one-way nesting in which communications between the coarser and finer domains are strictly one way from coarse to fine (Wang et al., 2009). The variograms clearly indicate that the turbulence strength simulated by WRF is independent of the chosen resolutions, i.e., at overlapping wavelengths (spatial scales) their magnitudes are identical. Therefore we conclude that the relatively low resolution of our simulations is not responsible for the significant underestimation of turbulent mixing. Moreover, this conclusion is also substantiated by the Kolmogorov turbulence theory which proposes that turbulence at fine scales (i.e., 3-D turbulence) is excited by larger-scale turbulences, i.e., the energy cascades downward from large-scale structures towards small-scale structures (Kolmogorov, 1941).

Although the above discussion does not reveal the causes of the underestimation of turbulence, it does provide us some hints. One potential cause could be a bias

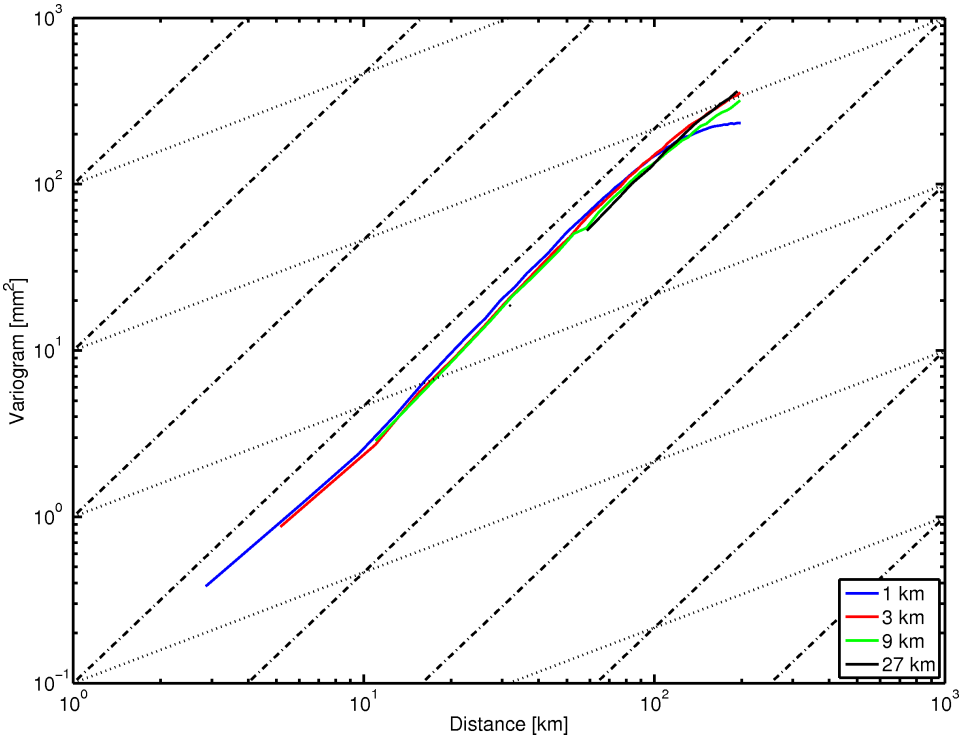

Fig. 3.14. Variograms of delay simulations with varying spatial resolutions (1, 3, 9 and 27 km). The simulations are carried out for the Netherlands on 31-Oct-2004 with a 28-hour spin-up time. At overlapping wavelengths (spatial scales) the magnitudes of the variograms with different spatial resolutions are virtually identical. Therefore, the turbulence strength simulated by WRF is independent of the model resolution.

in the initial conditions (the FNL data). If the turbulence power were in the first place underestimated in the initial conditions, following the power law behavior (see section 2.2.2) the turbulences at fine scales would be inevitably underestimated as well. The other possibility is related to the physical models available in WRF (a.o., boundary layer, surface and microphysics schemes, see section 3.2 and Tab. 3.1) for high spatial resolution forecasting. It is possible that these models are not sophisticated enough from the point of view of the application at hand.

3.6 Summary

We assess the feasibility of using WRF for mitigating the tropospheric delay in C-band interferometry, dominated by the space-time fluctuations of water vapor. We compare WRF simulation results to atmosphere-only interferograms from four climatic regions. The comparison is carried out both deterministically by means of pixel-wise corrections and stochastically using variograms. The pixel-wise correction

leads to considerable reductions ($\sim 50\%$) of the delay RMS error and strong delay correlations (up to 0.9) in cases when the delays in both the WRF model results and the interferograms are strongly correlated with the land topography (i.e., Hawaii, Mexico City). This delay reduction is achieved by removing the height-dependent delay. When there is no noticeable air stratification (i.e., over flat areas), the WRF simulations can hardly mitigate the delay in the interferograms and in many cases they even lead to a deterioration of the original interferograms, i.e., they amplify the atmospheric effect. This is the result of poor modeling of the delay lateral variations which are driven by turbulent mixing. Moreover, the height-dependent delays simulated by WRF in mountainous regions are not always reliable. Consequently, applying WRF for InSAR correction without caution in such areas may result in the non-existent height-correlated delay being interpreted as ground deformation.

In a stochastic approach, variograms are computed from the original atmosphere-only interferograms and the WRF simulation results following the removal of the height-dependent delay component. We find that in each case WRF underestimates the variability of turbulence by one order of magnitude at all spatial scales between 1 and 50 km. This underestimation prevents the use of WRF data as an indication of the significance of water vapor f fluctuations during SAR acquisitions. Such a-priori information could be used to aid internal adjustment based approaches such as interferogram stacking, persistent scatterers and the small baseline subset method.

Attempts have been made to increase the turbulence strength in the WRF simulations by increasing the model spin-up time and increasing the number of vertical model levels especially in the ABL where the bulk of water vapor is located. However, we find no evidence suggesting that a longer spin-up time and denser model vertical levels could substantially increase the strength of turbulence. In addition, we also find that the underestimation of turbulence is not caused by the limited spatial resolution of the model. The turbulence strengths predicted by WRF at different spatial resolutions are consistent in a stochastic sense, i.e., their variograms are identical at common wavelengths. Furthermore, by comparing the WRF predictions to cloud-free water vapor measurements acquired by MERIS over Southwest Australia we find that WRF agrees with MERIS reasonably well in terms of the mean water vapor content with a mean bias of $1.2\,\mathrm{kg/m^2}$. However, regarding the water vapor lateral variations there is little resemblance between WRF and MERIS and in each case WRF significantly underestimates the real variations.

Although our study is based on the WRF model only, this model is expected to outperform older generation models such as NH3D and MM5 (Bowman, 2009). Therefore, we come to the conclusion that delays simulated by numerical weather models do not provide a reliable, practical means for mitigating the tropospheric delay in SAR Interferometry. To become a globally applicable, operational tool for delay mitigation, the reliability and the degree of spatial detail of water vapor simulations need to be improved.

Chapter 4

Least-squares collocation (LSC) method for InSAR time series

This chapter provides a mathematical framework of parameter estimation and prediction for InSAR time series analysis based on the persistent scatterers SAR Interferometry (PSInSAR) technique. We begin this chapter by first reviewing the original algorithm for separating ground deformation and atmospheric phase screen (APS) proposed by Ferretti et al. (2000). The drawbacks of the algorithm are addressed. To overcome the drawbacks we propose a new method based on least-squares collocation (LSC) (Moritz, 1962; Krarup, 1969) to separate complex ground deformation and APS with the best precision. Features of the proposed method are stochastic modeling of possible complex ground deformation, precision assessment of the estimated deformation time series, spatio-temporal characterization of tropospheric delay, including estimation of the (time-varying) variance of tropospheric turbulence and its spatial variance-covariance function per SAR acquisition, and the scaling effect of delay caused by strong topography variation in mountainous regions. Last but not the least, we will show in this chapter that there is a strong connection between the original algorithm and the new method. The former is actually a special realization of the latter under certain circumstance.

4.1 The standard window-based filtering method

4.1.1 Method review

In the standard PSInSAR technique (Ferretti et al., 2000), the observation model for the unwrapped differential interferometric phase in interferogram k ($\Phi_{p,r}^{k,\mathrm{unw}}$) between two pre-selected persistent scatterer (PS) p and q can be written as (Colesanti et al., 2003):

$$\Phi_{p,q}^{k,\mathrm{unw}} = \phi_{p,q}^{k,\mathrm{topo}} + \phi_{p,q}^{k,\mathrm{defo}} + \phi_{p,q}^{k,\mathrm{aps}} + \phi_{p,q}^{k,\mathrm{noise}}, \tag{4.1.1}$$

where $\phi_{p,q}^{k,\mathrm{topo}}$ is the phase due to inaccuracy of the reference DEM, $\phi_{p,q}^{k,\mathrm{defo}}$ is the phase due to ground deformation with respect to the master acquisition, $\phi_{p,q}^{k,\mathrm{aps}}$ is the atmospheric phase screen (APS) and $\phi_{p,q}^{k,\mathrm{noise}}$ is decorrelation and thermal noise. The unwrapped phase $\Phi_{p,q}^{k,\mathrm{unw}}$ is not directly observable but needs to be estimated

(i.e., unwrapped) from its wrapped version $\phi_{p,q}^{k,\mathrm{wrap}}$. To make the phase unwrapping possible (i.e., to ensure the phase gradient between adjacent acquisitions within (-π, π], a functional model is assumed and used to model $\phi_{p,q}^{k,\mathrm{topo}}$ and $\phi_{p,q}^{k,\mathrm{defo}}$. Any deformation that is not modeled by the functional model is referred to as *unmodeled* deformation. Here we denote it as $s_{p,q}^{k,\mathrm{defo}}$. During the phase unwrapping, $\phi_{p,q}^{k,\mathrm{topo}}$ and $\phi_{p,q}^{k,\mathrm{defo}}$ are estimated and then subtracted from the unwrapped phase, see Colesanti et al. (2003); Kampes and Hanssen (2004); Kampes (2005).

The remaining phase components in the phase residue are the *unmodeled* ground deformation $s_{p,q}^{k,\mathrm{defo}}$, APS $\phi_{p,q}^{k,\mathrm{aps}}$ and phase noise $\phi_{p,q}^{k,\mathrm{noise}}$. In the standard PSInSAR it is assumed that $s_{p,q}^{k,\mathrm{defo}}$ might have some degree of correlation in time (depending on the source of subsidence), whereas $\phi_{p,q}^{k,\mathrm{aps}}$ and $\phi_{p,q}^{k,\mathrm{noise}}$ are not correlated in time. Such an assumption is often valid in practice when the ground deformation has a progressive and seasonal characteristic (Colesanti et al., 2003) and the temporal baselines between the consecutive SAR images in the time series are larger than 1-day. The latter is because beyond the time interval APS is not correlated any longer (see discussion in section 2.2.2). Based on such an assumption, the authors propose to separate $s_{p,q}^{k,\mathrm{defo}}$ from $\phi_{p,q}^{k,\mathrm{aps}}$ and $\phi_{p,q}^{k,\mathrm{noise}}$ by means of a temporal low-pass filtering. A wealth of low-pass filters exists, but commonly used low-pass filters in InSAR literatures are triangle (Ferretti et al., 2000) and Gaussian (Hooper et al., 2007) filters.

Mathematically, the temporal low-pass filtering is a discrete convolution operation:

$$\hat{s}_{p,q}^{k,\mathrm{defo}} = \sum_{i=0}^{N-1} w(k-i)\cdot \phi_{\mathrm{res}}^{i'} = w(k-i) \otimes \phi_{\mathrm{res}}^{i'} \quad \text{and}$$
$$\phi_{\mathrm{res}}^{i'} = \Phi_{p,q}^{i,\mathrm{unw}} - \hat{\phi}_{p,q}^{i,\mathrm{topo}} - \hat{\phi}_{p,q}^{i,\mathrm{defo}} - E\{\Phi_{p,q}^{i,\mathrm{unw}} - \hat{\phi}_{p,q}^{i,\mathrm{defo}} - \hat{\phi}_{p,q}^{i,\mathrm{topo}}\}, \quad (4.1.2)$$

where $\otimes$ and $E\{.\}$ denote a convolution and an expectation operator respectively. $\hat{s}_{p,q}^{k,\mathrm{defo}}$ is the estimated *unmodeled* deformation of interferogram k ($\in$[0,N-1]), N is the number of interferograms in the time series (also the number of slave images) and $\hat{\phi}_{p,q}^{i,\mathrm{defo}}$ is the estimated deterministic deformation (e.g., linear deformation). The expectation in Eq. (4.1.2) is an estimate of master APS. This is because APS and phase noise are assumed not correlated in time and the master APS appears as a constant in all interferograms. The master APS has to be subtracted before filtering otherwise it will pass the filtering and bias the deformation estimation. Furthermore, w are window coefficients which satisfy: $\sum w(i) = 1$, $w(i) \geq 0$ and $w(i) = w(-i)$. Here, we define the effective window length as the number of window coefficients that are larger than zero. The effective window length can be expressed in terms of the time interval between the first and last SAR acquisitions involved in the filtering (i.e., with non-zero window coefficients) to estimate $\hat{s}_{p,q}^{k,\mathrm{defo}}$. Ferretti et al. (2000) use one-year as the effective window length for all PS. From now on, we call the effective window length simply window length.

Moreover, the convolution in Eq. (4.1.2) is equivalent to a matrix multiplication:

$$\hat{\mathbf{s}}_{p,q}^{\mathrm{defo}} = W\boldsymbol{\Phi}_{p,q}^{'}, \quad (4.1.3)$$

where $\hat{\mathbf{s}}_{p,q}^{\mathrm{defo}}$ is an $N\times1$ vector which stores the time series of the estimated *unmodeled* deformation between PS p and q with respect to the master acquisition and $\mathbf{\Phi}_{p,q}^{'}$ is an $N\times1$ vector that contains the time series of $\phi_{\mathrm{res}}^{i'}$ in Eq. (4.1.2). W is an $N\times N$ toeplitz matrix which is constructed by the window coefficients in Eq. (4.1.2).

After subtracting the estimated *unmodeled* deformation from the phase residue, Ferretti et al. (2000) use a spatial low-pass window ($2\times2\,\mathrm{km}^2$) to separate APS $\phi_{p,q}^{k,\mathrm{aps}}$ and phase noise $\phi_{p,q}^{k,\mathrm{noise}}$ in space. It is noted later by Colesanti et al. (2003) that the spatial filtering can be better performed by Kriging (Journel and Huijbregts, 1978; Stein, 1999) that takes the spatial correlation of APS into account via its spatial variogram. Given the spatial correlation, APS at non-PS pixels can be obtained by interpolation such Kriging based interpolation.

4.1.2 Drawbacks of the window-based filtering method

Despite its simple form and easy implementation, the filtering method in section 4.1.1 does not necessarily give the optimal estimation of each phase component (i.e., deformation, DEM inaccuracy and APS). This is because of the following drawbacks of the algorithm:

- The algorithm only models ground deformation deterministically via a functional model but does not consider the complexity of deformation which might not be sufficiently modeled using the deterministic approach. Any inconsistency between the real deformation and the proposed functional model is not taken into account and therefore can lead to significant estimation error in the final deformation estimate.

To be able to carry out phase unwrapping, ground deformation at PS is modeled deterministically by a functional model (e.g., linear, quadratic or trigonometric polynomials). The *unmodeled* deformation is simply treated as a temporal correlated phase component and its stochastic characteristics (e.g., variance, correlation length, etc.) in time are not exploited at all.

In addition, no criteria are provided for optimally choosing a window and a window length for the low-pass temporal filtering. A proper window should reflect the shape (or pattern) of the temporal correlation in the *unmodeled* deformation. The window length should reflect the degree of correlation in the *unmodeled* deformation. Moreover, the optimal window length may vary from one PS to another. In other words, some PS targets might experience relatively slow and smooth deformation, whereas the other PS targets might undertake rapid and less smooth deformation. Such information are usually not known a-priori and therefore the optimal window length can hardly be obtained before analyzing the InSAR time series.

Last but not the least, the variance of the *unmodeled* deformation might also change from one PS to another and it is not known a-priori neither. The variance is an important statistical factor that allows us to assess the accuracy of the estimated ground deformation and APS.

- The algorithm ignores the difference in spatial variance of APS from one ac-

quisition to another. Moreover, it also ignores the difference in magnitude of APS disturbance from one spatial arc (i.e., line connecting two PS) to another in an interferogram.

The ignorance of the time-varying APS spatial variance can be seen from Eq. 4.1.3. It is equivalent to multiplying an identity matrix to $\mathbf{\Phi}'_{p,q}$ followed by W. Obviously, the identity matrix gives the same weight to all acquisitions. This can cause a leakage of APS to ground deformation for acquisitions taken under extreme weather such as thunderstorms.

For spatial arcs in an interferogram, the APS disturbance increases with the lengths of the arcs. This is because of the power-law behavior of APS discussed in section 2.2.2. Moreover, in mountainous regions, APS disturbance is further increased by atmosphere vertical stratification in which atmospheric delay is strongly correlated with land topography. Obviously, a good modeling of APS should take all these spatial characteristics into account.

Because of the ignorances, the low-pass temporal filtering may fail when there are acquisition gaps in the InSAR time series. In such a case, less elements from $\mathbf{\Phi}'_{p,q}$ are involved in the convolution in Eq. (4.1.2) and make the APS suppression not effective.

- No quality assessments for the estimated phase components.

Unlike conventional geodetic survey techniques such as leveling and GPS, there is not yet an InSAR standard such as technical specifications that can be adapted by industry for real-life operations. The standard PSInSAR algorithm for example does not distinguish deterministic and stochastic deformation and ignores the spatio-temporal variation of APS. Therefore, it is difficult to assess the qualities of its final estimates.

4.2 Least-squares collocation and variance covariance estimation

This section provides a review of least-squares collocation (LSC) and its application to a *trend-signal-noise* model which is generally applicable to many estimation and prediction problems in geosciences based on observations collected from field or satellite measurements. An analogue to the *trend-signal-noise* model in geostatistics is known as universal Kriging when the trend is unknown or simple Kriging when the trend is absent or set to zero, see Journel and Huijbregts (1978) and Wackernagel (1995). In this paper, the *trend-signal-noise* model serves as a generic mathematical frame for modeling the relation between the observed (or derived) interferometric phase and the possible phase contributors, e.g., ground deformation, APS, phase noise, etc. A successful application of LSC requires a good modeling of the stochastic variates in the *trend-signal-noise* model. The estimation of these stochastic variates needs to be performed separately. In the following we will combine variance-covariance estimation (VCE) to estimate stochastic properties needed for LSC. A desirable estimator should give an unbiased estimation of the stochastic

property, meanwhile the estimation should have a minimum estimation error (in the least-squares sense) among all the unbiased estimators.

4.2.1 Least-squares collocation

In the *trend-signal-noise* model (also known as least-squares collocation with parameters), the observable vector $\underline{y}$ is written as a sum of three terms as:

$$\underline{y} = t + \underline{s} + \underline{n}, \tag{4.2.1}$$

where t is a deterministic but unknown trend (in space or time), $\underline{s}$ is a zero-mean random signal vector, and $\underline{n}$ is a zero-mean noise vector. The underlines in Eq. (4.2.1) are used to distinguish stochastic variables from deterministic ones. The trend is usually further parameterized by means of an unknown deterministic parameter vector $\mathbf{x}$ as $t = Ax$, where A is the so-called design matrix (Teunissen et al., 2005). The signal and noise vector are assumed to be uncorrelated and their variance-covariance matrices (VCM) are denoted as Q_{ss} and Q_{nn} respectively. Thus, a complete version of the *trend-signal-noise* model can be written as (Teunissen et al., 2005):

$$\begin{aligned} &\underline{y} = Ax + \underline{s} + \underline{n} \quad \text{and} \\ &Q_{yy} = Q_{ss} + Q_{nn}, \end{aligned} \tag{4.2.2}$$

where Q_{yy} is the VCM of $\underline{y}$ and is obtained by applying the error propagation law (Teunissen et al., 2005) to Eq. (4.2.1).

From now on, we speak of estimation when an observable random vector such as $\underline{y}$ is used to estimate the value of an unknown deterministic parameter such as x. We speak of prediction in case that an observable random vector is used to predict the outcome or realization of a random variable such as $\underline{s}$. The best linear unbiased estimation (BLUE) of x is given as (Teunissen et al., 2005):

$$\hat{\underline{x}} = (A^T Q_{yy}^{-1} A)^{-1} A^T Q_{yy}^{-1} \underline{y}, \tag{4.2.3}$$

where T denotes a matrix transpose, and the hat above $\underline{\mathrm{x}}$ denotes an estimation of x. Here, the unbiasedness is a statistical criterion that requires $\hat{\underline{x}}$ on average to be equal to the true x, i.e., $E\{\hat{\underline{x}}\} = x$ ($E\{.\}$ denotes the expectation operator). The 'best' means among all unbiased estimates of x, the estimate $\hat{\underline{x}}$ in Eq. (4.2.3) has the minimum estimation uncertainty, i.e., $E\{\|\hat{\underline{x}} - x\|^2\} \leq E\{\|\hat{\underline{x}}' - x\|^2\}$, where $\hat{\underline{x}}'$ is an arbitrary unbiased estimate of x other than $\hat{\underline{x}}$. Given the BLUE of x, we can obtain the best linear unbiased prediction (BLUP) of $\underline{s}$ and $\underline{n}$ respectively as (Teunissen et al., 2005) :

$$\begin{aligned} &\hat{\underline{s}} = Q_{ss} Q_{yy}^{-1} (\underline{y} - A\hat{\underline{x}}) \quad \text{and} \\ &\hat{\underline{n}} = \underline{y} - A\hat{\underline{x}} - \hat{\underline{s}}. \end{aligned} \tag{4.2.4}$$

Again the unbiasedness of $\hat{\underline{s}}$ means $E\{\hat{\underline{s}}\} = \underline{s}$, and the 'best' implies that $E\{\|\hat{\underline{s}} - \underline{s}\|^2\} \leq E\{\|\hat{\underline{s}}' - \underline{s}\|^2\}$, where $\hat{\underline{s}}'$ is an arbitrary unbiased prediction of $\underline{s}$ other than $\hat{\underline{s}}$. The combination of BLUE in Eq. (4.2.3) and BLUP in Eq. (4.2.4) is called least-squares collocation with parameters (Moritz, 1962; Krarup, 1969).

A desirable feature of LSC is that it gives not only the best estimation and prediction of the parameters of interest but also an accuracy assessment of these parameters provided that Q_{ss} and Q_{nn} (so Q_{yy}) are known. The VCM of the BLUE of x is given as (Teunissen et al., 2005):

$$Q_{\hat{x}\hat{x}} = (A^T Q_{yy}^{-1} A)^{-1}. \tag{4.2.5}$$

Using error propagation law the accuracy of the estimated trend $\underline{\hat{t}} = A\underline{\hat{x}}$ can be assessed by:

$$Q_{\hat{t}\hat{t}} = A Q_{\hat{x}\hat{x}} A^T. \tag{4.2.6}$$

For the BLUP of $\underline{s}$, let us denote the prediction error as $\epsilon_s = \underline{s} - \underline{\hat{s}}$. Combing Eqs. (4.2.3) and (4.2.4) we have $\hat{\epsilon}_s = (s - Q_{ss}Q_{yy}^{-1}y) + Q_{ss}Q_{yy}^{-1}A\underline{\hat{x}}$. Since the first bracketed term is uncorrelated with $\underline{y}$ and $\underline{\hat{x}}$ is function of $\underline{y}$ (i.e., correlated with $\underline{y}$), therefore the two bracketed terms are uncorrelated. Applying the error propagation law to $\hat{\epsilon}_s$ we obtain:

$$\begin{aligned} Q_{\hat{\epsilon}_s\hat{\epsilon}_s} &= Q_{ss} - Q_{ss}Q_{yy}^{-1}Q_{ss} \\ &\quad + (Q_{ss}Q_{yy}^{-1}A)Q_{\hat{x}\hat{x}}(Q_{ss}Q_{yy}^{-1}A)^T, \end{aligned} \tag{4.2.7}$$

where the first term is the original uncertainty of $\underline{s}$ itself, and it is reduced by the second term given the observation $\underline{y}$. The reduced uncertainty is then increased by the third term which is due to the uncertainty of the estimate $\underline{\hat{x}}$ (i.e., unknown trend).

4.2.2 Variance-covariance estimation

To apply LSC to the *trend-signal-noise* model in Eq. (4.2.1) we need to know the VCM of the signal (Q_{ss}) and noise (Q_{nn}). However, they are rarely known a-priori in practice and they could have varying forms from one realization to another (i.e., non-stationary). For instance, interferograms with varying temporal baselines usually suffer from different degrees of phase decorrelation (Zebker and Villasenor, 1992). If Q_{nn} is the VCM of the phase decorrelation in this case, it will vary corresponding to the temporal baselines of the interferograms. A common way to model a stochastic variable in geostatistics is to compute its variogram from its observations (i.e., realizations) (Journel and Huijbregts, 1978; Wackernagel, 1995). To guarantee the variogram being negative definite, the computed variogram is usually fitted by a negative definite variogram model, e.g., Gaussian or spherical (Journel and Huijbregts, 1978). By determining the parameters, i.e., range and sill (Journel and Huijbregts, 1978), of the model via (un)weighted least-squares (Cressie, 1985), a positive definite and invertible VCM of the variable can be constructed, assuming the variable is second-order stationary (Wackernagel, 1995). Then, the constructed VCM can be used for LSC.

However, the above approach cannot be applied to the *trend-signal-noise* model if the trend embedded in the observable vector $\underline{y}$ is not negligible. A dominant and non-constant trend in $\underline{y}$ will bias the variogram estimation (Starks and Fang, 1982; Myers, 1989). Therefore, in order to achieve an unbiased estimation of the variogram the trend in $\underline{y}$ has to be removed beforehand. However, the trend is unknown

and has to be estimated from $\underline{y}$. From Eq. (4.2.3) we see that to compute the BLUE of the trend, we have to know the VCM of $\underline{y}$. Therefore, we are faced with a chicken-and-egg problem unfortunately. A trivial solution to this dilemma is to estimate the trend using unweighted least-squares, i.e., replacing Q_{yy} in Eq. (4.2.3) by an identity matrix. After the trend being estimated in this way, it is subtracted from $\underline{y}$, then a variogram is computed from the residue. Unfortunately, it has been pointed out by many authors that the computed variogram based on the residue is biased (Matheron, 1973; Armstrong, 1984; Kitanidis, 1993). In addition, an iterative least-squares method has been proposed by Neuman and Jacobson (1984) to approximate the real variogram iteratively starting with the residue obtained from the unweighted least-squares. However, it has been shown by Cressie (1987) that the final approximation of the variogram is still biased no matter the number of iterations.

Several methods (Kitanidis, 1983; Kitanidis and Lane, 1985; Stein, 1986; Kitanidis, 1987; Teunissen and Amiri-Simkooei, 2006) have been developed to model the stochastic variable without explicitly estimating the trend. In these methods, a linear transformation is applied to the observable vector $\underline{y}$ to filter out the trend as:

$$\begin{aligned} &\underline{z} = T\underline{y} = T(Ax) + T\underline{\varepsilon} \\ &\text{satisfy: } TA = 0 \text{ (null matrix)}, \end{aligned} \tag{4.2.8}$$

where $\underline{\varepsilon} = \underline{s} + \underline{n}$, T is a transformation matrix and has the form: $T = (I - A(A^TA)^{-1}A^T)$, where I is an identity matrix. The transformed version of Eq. (4.2.2) is therefore:

$$\begin{aligned} &\underline{z} = T\underline{\varepsilon} \text{ and} \\ &Q_{zz} = TQ_{yy}T^T = TQ_{\varepsilon\varepsilon}T^T. \end{aligned} \tag{4.2.9}$$

Note, the transformation matrix T does not have a full rank. If x is an n-element vector and there are m observations in $\underline{y}$, then T is an $m \times m$ matrix with a rank deficiency of n. Therefore, to make Q_{zz} invertible we have to drop n linear dependent rows from T. After row dropping we have:

$$\begin{aligned} &\underline{z} = \Lambda\underline{\varepsilon} \text{ and} \\ &Q_{zz} = \Lambda Q_{yy}\Lambda^T = \Lambda Q_{\varepsilon\varepsilon}\Lambda^T, \end{aligned} \tag{4.2.10}$$

where Λ is obtained by dropping n arbitrary rows of T.

Now our goal is to estimate Q_{yy} from the transformed vector $\underline{z}$. We may use a parametric approach to determine Q_{yy}. That is, based on some prior knowledge about $\underline{s}$ and $\underline{n}$ we assume Q_{ss} and Q_{nn} are realizations of some positive-definite variance-covariance models. Based on such assumption, we simply need to estimate the model parameters (usually only a few) to construct these matrices. We will elaborate on the variance-covariance model selection in section 4.3.3. One advantage of the parametric approach is that the estimated Q_{ss} and Q_{nn} are positive-definite and therefore invertible. The estimators that we look for to estimate the model parameters should be unbiased, meanwhile the estimation error should be the smallest among all the

unbiased estimators. The restricted maximum likelihood estimator (RMLE) proposed by Kitanidis (1983); Kitanidis and Lane (1985); Kitanidis (1987) is one of such estimators. Other estimators, such as minimum-variance unbiased quadratic estimator (MVUQE) and minimum-norm (least-squares) unbiased quadratic estimator (MNUQE), of the same kind can be found in Stein (1986); Kitanidis (1987); Teunissen and Amiri-Simkooei (2006). However, these estimators require the variance-covariance model to be a linear function of the model parameters, e.g., a linear combination of a set of unknown variance components (see Teunissen and Amiri-Simkooei (2006)). Under the assumption that the joint probability density function (PDF) of the transformed observable vector $\underline{z}$ in Eq. (4.2.8) has a Gaussian distribution: $P(\underline{z}|\theta) = (2\pi)^{-\frac{N}{2}}|Q_{zz}|^{-\frac{1}{2}}\exp(-\frac{1}{2}\underline{z}^T Q_{zz}^{-1}\underline{z})$, the objective function of RMLE to be minimized reads (Kitanidis and Lane, 1985):

$$\begin{aligned} L(\underline{z}|\theta) &= -\ln^{P(\underline{z}|\theta)} \\ &= \frac{N}{2}\ln^{2\pi} + \frac{1}{2}\ln^{|Q_{zz}|} + \frac{1}{2}\underline{z}^T Q_{zz}^{-1}\underline{z}, \end{aligned} \tag{4.2.11}$$

where θ is a vector which contains the unknown parameters of the variance-covariance models, N is the number of observations in $\underline{y}$ and $|Q_{zz}|$ denotes the determinant of Q_{zz}. The $\hat{\theta}$ that minimizes the negative log likelihood function in Eq. (4.2.11) is the best unbiased estimate of θ. The minimization of Eq. (4.2.11) usually has to be solved iteratively due to its nonlinearity. A commonly used iteration approach for the minimization is the Gauss-Newton method (Kitanidis and Lane, 1985) because of its computational efficiency. Note, an initial guess of Q_{yy} (i.e., an initial guess of θ) is required in order to start the iteration. The accuracy of $\hat{\theta}$ can be assessed via a so-called Fisher information matrix (Kitanidis, 1987):

$$(F_{\theta\theta})_{ij} = \frac{1}{2}\mathrm{tr}(Q_{zz}^{-1}Q_i Q_{yy}^{-1}Q_j), \tag{4.2.12}$$

where tr stands for the trace of a matrix, i and j are the ith and the jth element of θ respectively and Q_i denotes $\frac{\partial Q_{zz}}{\partial\theta_i}$. The inverse of $F_{\theta\theta}$ is the Crawer-Rao lower bound of the VCM ($V_{\theta\theta}$) of $\hat{\theta}$ (Kitanidis, 1983), i.e., $V_{\theta\theta} \geq (F_{\theta\theta})^{-1}$.

4.3 Least-squares collocation applied to Persistent Scatterers InSAR

In this section we apply the LSC framework to PSInSAR (Ferretti et al., 2000) to detect and estimate possible ground deformation signal in the presence of atmospheric phase screen (APS) as well as other signals due to, e.g., satellite orbit, phase decorrelation, land topography, etc. We use the restricted maximum likelihood estimator (RMLE) discussed in section 4.2.2 to estimate variance-covariance matrices (VCM) of the signals. Given the estimated VCMs, we can obtain the optimal estimation and prediction of the signals as well as their accuracies.

4.3.1 LSC applied to a time series per arc

Given N+1 SAR images, we form N interferograms with respect to the master image. Moreover, from the N+1 SAR images, we select M+1 pixels which have a low

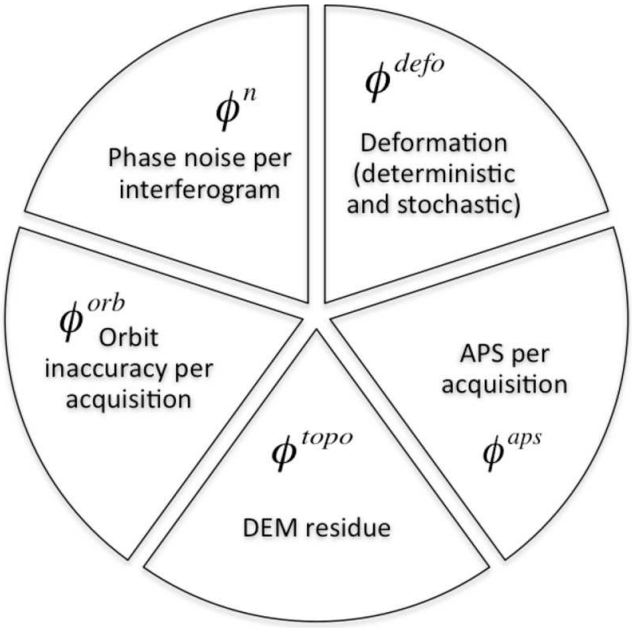

Fig. 4.1. Pie chart of the phase components in the observed interferometric phase.

amplitude dispersion index (e.g., $D_A \leq 0.25$) (Ferretti et al., 2000) as persistent scatter (PS) candidates (Kampes and Hanssen, 2004). After phase unwrapping (Kampes and Hanssen, 2004), we obtain the unwrapped phases per arc formed by a PS p with respect to the same reference PS r. Assuming the phase unwrapping is carried out successfully, we model the unwrapped phase from one of the interferograms for this arc as (see Fig. 4.1):

$$\begin{aligned} \underline{\phi}_{p,r}^{\mathrm{obs}} &= \underline{\phi}_{p,r}^{\mathrm{defo}} + \phi_{p,r}^{\mathrm{topo}} + \phi_{p,r}^{m,\mathrm{aps}} + \phi_{p,r}^{m,\mathrm{orb}} \\ &\quad -\underline{\phi}_{p,r}^{s,\mathrm{aps}} - \underline{\phi}_{p,r}^{s,\mathrm{orb}} + \underline{\phi}_{p,r}^{\mathrm{noise}}, \end{aligned} \tag{4.3.1}$$

where $\underline{\phi}_{p,r}^{\mathrm{obs}}$ is the unwrapped interferometric phase serving as an observable, $\underline{\phi}_{p,r}^{\mathrm{defo}}$ is the phase caused by ground deformation, $\phi_{p,r}^{\mathrm{topo}}$ is the phase due to unmodeled topographic contribution, $\phi_{p,r}^{m,\mathrm{aps}}$ and $\phi_{p,r}^{s,\mathrm{aps}}$ are the APS of the master and a slave respectively, $\phi_{p,r}^{m,\mathrm{orb}}$ and $\underline{\phi}_{p,r}^{s,\mathrm{orb}}$ are the results of orbit uncertainties of the master and a slave respectively, $\underline{\phi}_{p,r}^{\mathrm{noise}}$ accounts for a phase noise due to phase decorrelation and thermal noise. Here, we denote stochastic variables by underlines to distinguish them from deterministic variables. The deformation phase $\underline{\phi}_{p,r}^{\mathrm{defo}}$ is denoted as a stochastic variable because we model the total deformation as the sum of a deterministic term which can be modeled by a linear function (e.g., a linear, quadratic or periodic trend) and a stochastic term which has a zero-mean and is second-order stationary in time, i.e., $\underline{\phi}_{p,r}^{\mathrm{defo}} = \phi_{p,r}^{\mathrm{defo,\ det}} + \underline{\phi}_{p,r}^{\mathrm{defo,\ sto}}$. Moreover, $\phi_{p,r}^{m,\mathrm{aps}}$ and $\phi_{p,r}^{m,\mathrm{orb}}$ are also denoted as deterministic variables since they appear in every interferogram as a constant.

Given the modeling above (see Fig. 4.1), we can write the full phase time series of this arc by the *trend-signal-noise* model in a matrix form as:

$$\underline{\Phi}_{p,r}^{\text{obs}} = Ax_{p,r} + \underline{s}_{p,r} + \underline{n}_{p,r}, \tag{4.3.2}$$

where $\underline{\Phi}_{p,r}^{\text{obs}}$ is an $N\times1$ vector which contains the unwrapped interferometric phases. $Ax_{p,r}$ is the temporal trend component in which $x_{p,r}$ is an $n\times1$ vector that contains unknown deterministic parameters, including coefficients of the linear function used to model the deterministic part of the deformation $\phi_{p,r}^{\text{defo, det}}$, the unmodeled topographic contribution $\phi_{p,r}^{\text{topo}}$ and a component ξ which is the sum of $\phi_{p,r}^{\text{m, aps}}$, $\phi_{p,r}^{\text{m, orb}}$, i.e., $\xi = \phi_{p,r}^{\text{m, aps}} + \phi_{p,r}^{\text{m, orb}}$. The choice of the linear function to model $\phi_{p,r}^{\text{defo, det}}$ is arbitrary but usually depends on a priori assumption/knowledge about the deformation in the area of interest. Assumptions that can be explicit or implicit are often needed in parameter estimation because many inverse problems such as the one in Eq. (4.3.1) are inherently under-determined and ill-posed. Matrix A is a design matrix with N rows and n columns. For instance, if $\phi_{p,r}^{\text{det, defo}}$ can be modeled as a linear function of time (i.e., a constant velocity), then A is an $N\times3$ matrix which has the form:

$$A = -\frac{4\pi}{\lambda}\begin{bmatrix} \frac{B_{\perp}^{1}}{r_p^m \sin\theta_p^m} & B_{\text{T}}^{1} & 1 \\ \frac{B_{\perp}^{2}}{r_p^m \sin\theta_p^m} & B_{\text{T}}^{2} & 1 \\ \cdots & \cdots & \cdots \\ \frac{B_{\perp}^{N}}{r_p^m \sin\theta_p^m} & B_{\text{T}}^{N} & 1 \end{bmatrix}, \tag{4.3.3}$$

where $B_{\perp}$ and B_{T} are the perpendicular and temporal baselines of an interferogram, λ is the radar wavelength, r_p^m is the range from the master sensor to the PS p and θ_p^m is the local incidence angle. The first column of A relates $\phi_{p,r}^{\text{dem}}$ with the uncertainty in the DEM model used for removing the topographic phase contribution (Rodriguez and Martin, 1992). The second column serves as the base function for the linear deformation $\phi_{p,r}^{\text{defo, det}}$ and the third column relates the component ξ with the unwrapped phase. Finally, the factor $-\frac{4\pi}{\lambda}$ is a range to phase converter (Rosen et al., 2000).

The signal component $\underline{s}_{p,r}$ is an $N\times1$ vector which contains the stochastic part of the deformation, i.e., $\underline{s}_{p,r} = \underline{\phi}_{p,r}^{\text{defo, sto}}$. We assume that $\underline{\phi}_{p,r}^{\text{defo, sto}}$ is second-order stationary in time and has a normal distribution with a zero mean. Moreover, the noise component $\underline{n}_{p,r}$ is also an $N\times1$ vector which reads:

$$\underline{n}_{p,r} = -(\underline{\Phi}_{p,r}^{s,\text{aps}} + \underline{\Phi}_{p,r}^{s,\text{orb}} - \underline{\Phi}_{p,r}^{\text{noise}}). \tag{4.3.4}$$

Similar to $\underline{s}_{p,r}$, we also assume that $\underline{n}_{p,r}$ is second-order stationary in time and has a normal distribution with a zero mean. Furthermore, we assume $\underline{n}_{p,r}$ has no correlation in time. Applying the error propagation law to Eq. (4.3.2) we have:

$$\begin{aligned} Q_{\Phi\Phi}^{p,r} &= Q_{ss}^{p,r} + Q_{nn}^{p,r} \\ &= Q_{ss}^{p,r} + Q_{\text{aps}}^{p,r} + Q_{\text{orb}}^{p,r} + Q_{\text{noise}}^{p,r} \end{aligned} \tag{4.3.5}$$

where $Q^{p,r}_{\Phi\Phi}$, $Q^{p,r}_{ss}$, $Q^{p,r}_{\text{aps}}$, $Q^{p,r}_{\text{orb}}$ and $Q^{p,r}_{\text{noise}}$ are the temporal VCMs of $\underline{\Phi}^{\text{obs}}_{p,r}$, $\underline{s}_{p,r}$, $\underline{\Phi}^{s,\text{aps}}_{p,r}$, $\underline{\Phi}^{s,\text{orb}}_{p,r}$ and $\underline{\Phi}^{\text{noise}}_{p,r}$ respectively, assuming these phase components are mutually uncorrelated. In practice, $Q^{p,r}_{\Phi\Phi}$, $Q^{p,r}_{ss}$ and $Q^{p,r}_{nn}$ are not known a-priori and therefore have to be estimated. We will discuss their estimation in section 4.3.3.

According to Eq. (4.2.3), the best linear unbiased estimation (BLUE) of $x_{p,r}$ is:

$$\underline{\hat{x}}_{p,r} = (A^T(Q^{p,r}_{\Phi\Phi})^{-1}A)^{-1}A^T(Q^{p,r}_{\Phi\Phi})^{-1}\Phi^{\text{obs}}_{p,r}, \tag{4.3.6}$$

and its accuracy can be assessed by:

$$Q^{p,r}_{\hat{x}\hat{x}} = (A^T(Q^{p,r}_{\Phi\Phi})^{-1}A)^{-1}. \tag{4.3.7}$$

Moreover, the best linear unbiased prediction (BLUP) of $\underline{s}_{p,r}$ is (see Eq. (4.2.4)):

$$\underline{\hat{s}}_{p,r} = Q^{p,r}_{ss}(Q^{p,r}_{\Phi\Phi})^{-1}(\Phi^{\text{obs}}_{p,r} - A\underline{\hat{x}}_{p,r}), \tag{4.3.8}$$

and its prediction error $\underline{\epsilon}_s = \underline{\hat{s}}_{p,r} - \underline{s}_{p,r}$ can be evaluated by (see Eq. (4.2.7)):

$$\begin{aligned} Q^{p,r}_{\hat{\epsilon}_s\hat{\epsilon}_s} &= Q^{p,r}_{ss} - Q^{p,r}_{ss}(Q^{p,r}_{\Phi\Phi})^{-1}Q^{p,r}_{ss} + \\ &\quad (Q^{p,r}_{ss}(Q^{p,r}_{\Phi\Phi})^{-1}A)Q^{p,r}_{\hat{x}\hat{x}}(Q^{p,r}_{ss}(Q^{p,r}_{\Phi\Phi})^{-1}A)^T. \end{aligned} \tag{4.3.9}$$

Finally, the BLUP of $\underline{n}$ is:

$$\underline{\hat{n}}_{p,r} = -(\Phi^{\text{obs}}_{p,r} - A\underline{\hat{x}}_{p,r} - \underline{\hat{s}}_{p,r}), \tag{4.3.10}$$

and its prediction error $\underline{\epsilon}_n = \underline{\hat{n}}_{p,r} - \underline{n}_{p,r}$ can be evaluated in analogue to Eq. (4.3.9) as:

$$\begin{aligned} Q^{p,r}_{\hat{\epsilon}_n\hat{\epsilon}_n} &= Q^{p,r}_{nn} - Q^{p,r}_{nn}(Q^{p,r}_{\Phi\Phi})^{-1}Q^{p,r}_{nn} + \\ &\quad (Q^{p,r}_{nn}(Q^{p,r}_{\Phi\Phi})^{-1}A)Q^{p,r}_{\hat{x}\hat{x}}(Q^{p,r}_{nn}(Q^{p,r}_{\Phi\Phi})^{-1}A)^T. \end{aligned} \tag{4.3.11}$$

In this section we apply LSC to the time series of each arc in time domain. The time series consists of the unwrapped phases of each arc with respect to a global reference PS r. The outputs from LSC are the estimates of deterministic deformation, stochastic deformation, DEM phase residue and the sum of phases of APS, satellite orbit and noise for each arc with respect to the global reference PS. In next section we will use LSC to separate APS, satellite orbit and noise in spatial domain.

4.3.2 LSC applied to spatial arcs per SAR acquisition

Till now, we have obtained the best prediction of $\underline{\hat{n}}$ for the time series of each arc with respect to the same reference PS r. Next, we are going to separate, in space, the APS ($\underline{\phi}^{s,\text{aps}}$) and orbit error ($\underline{\phi}^{s,\text{orb}}$) per slave as well as the phase noise ($\underline{\phi}^{\text{noise}}$) per interferogram by utilizing their spatial characteristics. Taking one slave acquisition as an example, the $\underline{n}^k$ (k denotes the kth slave acquisition) in space can be written as:

$$\underline{n}^k = \begin{bmatrix} \underline{n}^k_{1,r} \\ \cdots \\ \underline{n}^k_{p,r} \\ \cdots \\ \underline{n}^k_{M,r} \end{bmatrix} = - \begin{bmatrix} \underline{\phi}^{k,\text{aps}}_{1,r} + \underline{\phi}^{k,\text{orb}}_{1,r} + \underline{\phi}^{k,\text{noise}}_{1,r} \\ \cdots \\ \underline{\phi}^{k,\text{aps}}_{p,r} + \underline{\phi}^{k,\text{orb}}_{p,r} + \underline{\phi}^{k,\text{noise}}_{p,r} \\ \cdots \\ \underline{\phi}^{k,\text{aps}}_{M,r} + \underline{\phi}^{k,\text{orb}}_{M,r} + \underline{\phi}^{k,\text{noise}}_{M,r} \end{bmatrix}. \tag{4.3.12}$$

For the APS component $\underline{\phi}^{k,\,\mathrm{aps}}$, we model it in space as a spatial trend plus a spatial variation and if applicable a height-dependent component usually known as the atmospheric vertical stratification. The spatial trend usually manifests itself as a long wavelength linear surface trend which has been observed from many ERS-1/2 tandem interferograms (Hanssen, 2001) and it might be the result of the large spatial extent of high and low pressure zones. The spatial variation component is mainly caused by the high spatial variation of water vapor in the lower troposphere, i.e., turbulent mixing. It is usually modeled as a zero mean stochastic process and its spatial characteristics can be revealed by its variogram (Hanssen, 2001; Liu et al., 2009; Knospe and Jonsson, 2010). The height dependent component is applicable when the variation of the land topography in the area of interest is significant (e.g., ≥ 1000 m) (Liu et al., 2009) and it can often be modeled as a linear function of height (Liu et al., 2009). The orbital phase term $\underline{\phi}^{k,\mathrm{orb}}$ usually presents in interferograms as surface phase ramps and can be sufficiently modeled as a linear surface trend over a typical spatial extent of 100 by 100 km (Hanssen, 2001). Since $\underline{\phi}^{k,\mathrm{aps}}$and $\underline{\phi}^{k,\mathrm{orb}}$ share the common spatial characteristic (i.e., a long wavelength trend) it is not possible to separate them in practice without any external data. Finally, we model the phase noise term $\underline{\phi}^{k,\mathrm{noise}}$ as white noise, i.e., uncorrelated in space, a normal distribution with zero mean.

Based on the spatial characteristics of the signals discussed above and in analogue to Eq. (4.3.2) in the time domain, we model $\underline{n}^k$ per slave in space by the *trend-signal-noise* model as:

$$\underline{n}^k = Ry^k + \underline{\nu}^k + \underline{\mu}^k, \tag{4.3.13}$$

where R is a spatial design matrix which has M rows (recall that there are in total $M+1$ PSs) and 4 columns, y^k is an 4×1 parameter vector which contains three coefficients for determining a linear surface trend caused by troposphere and orbit errors and one coefficient taking into account the vertical stratification as a linear function of height with respect to the reference PS r. Moreover, $\underline{\nu}^k$ is an $M\times 1$ vector which contains the phase component due to the turbulent mixing and $\underline{\mu}^k$ accounts for the noise component. Applying the error propagation law to Eq. (4.3.13) we obtain:

$$Q^k_{nn} = Q^k_{\nu\nu} + Q^k_{\mu\mu}, \tag{4.3.14}$$

where Q^k_{nn}, $Q^k_{\nu\nu}$ and $Q^k_{\mu\mu}$ are the spatial VCMs ($M \times M$) of $\underline{n}^k$, $\underline{\nu}^k$ and $\underline{\mu}^k$ for the kth slave acquisition respectively, assuming $\underline{\nu}^k$ and $\underline{\mu}^k$ are mutually uncorrelated. Again, these VCMs are not known a-priori in practice and we will discuss their estimation in section 4.3.3.

Since $\underline{n}^k$ is not directly observable but predicted from Eq. (4.3.10), its prediction error $\underline{\epsilon}^k_n = \underline{\hat{n}}^k - \underline{n}^k$ needs to be modeled as well. The actual observation equation in space reads:

$$\underline{\hat{n}}^k = Ry^k + \underline{\nu}^k + \underline{\mu}^k + \underline{\epsilon}^k_n, \tag{4.3.15}$$

and the corresponding stochastic model reads:

$$Q^k_{\hat{n}\hat{n}} = Q^k_{\nu\nu} + Q^k_{\mu\mu} + K^k_{\epsilon_n\epsilon_n}, \tag{4.3.16}$$

assuming $\hat{\underline{\epsilon}}_n$ is neither correlated with $\underline{\nu}$ nor $\underline{\mu}$. $K^k_{\epsilon_n\epsilon_n}$ is the spatial VCM of the prediction error $\underline{\epsilon}_n$ of $\underline{n}$ in Eq. (4.3.10) for all arcs in the kth interferogram. Here, we use $K^k_{\epsilon_n\epsilon_n}$ to distinguish it from $Q^{p,r}_{\hat{\epsilon}_n\hat{\epsilon}_n}$ in Eq. (4.3.11).

The BLUE of y^k is given as:

$$\hat{\underline{y}}^k = (R^T(Q^k_{\hat{n}\hat{n}})^{-1}R)^{-1}R^T(Q^k_{\hat{n}\hat{n}})^{-1}\hat{\underline{n}}^k, \tag{4.3.17}$$

and its accuracy can be evaluated by:

$$Q_{\hat{y}\hat{y}} = (R^T(Q^k_{\hat{n}\hat{n}})^{-1}R)^{-1}. \tag{4.3.18}$$

The BLUE of the spatial trend (due to troposphere and orbit errors) plus the vertical stratification can be obtained as: $R\hat{\underline{y}}^k$. To separate the turbulent mixing component from the phase noise $\underline{\phi}^{k,\text{noise}}$, we apply BLUP to the residual $\hat{\underline{\zeta}}^k$ $(= \hat{\underline{n}}^k - R\hat{\underline{y}}^k)$:

$$\hat{\underline{\nu}}^k = Q^k_{\nu\nu}(Q^k_{\hat{n}\hat{n}})^{-1}\hat{\underline{\zeta}}^k. \tag{4.3.19}$$

Combining Eqs. (4.3.17) and (4.3.19) , the APS at non-PS pixels can be spatially predicted/interpolated by:

$$\hat{\underline{\nu}}'^k = R'^T\hat{\underline{y}}^k + Q^k_{\nu'\nu}(Q^k_{\nu\nu})^{-1}\hat{\underline{\zeta}}^k, \tag{4.3.20}$$

where ν'^k is the APS at the non-PS pixels and R' is the spatial design matrix corresponding to the non-PS pixels and $Q^k_{\nu'\nu}$ is the spatial cross VCM between PSs and non-PS pixels.

By now, we have theoretically obtained the optimal estimation and prediction of ground deformation $\phi^{\text{defo,det}}$ and $\phi^{\text{defo,sto}}$, unmodeled topographic contribution ϕ^{topo} and APS together with orbit errors $\underline{\phi}^{\text{aps+orbit}}$ for each PS w.r.t. the same reference PS r per SAR image. In addition, we have also obtained the optimal prediction of APS at non-PS pixels.

4.3.3 Variance-covariance modeling and estimation

Our objective is to estimate the temporal VCMs in Eq. (4.3.5) for the time series of each arc and the spatial VCMs in Eq. (4.3.16) for each slave acquisition and interferogram from the unwrapped phases. All these VCMs are summarized in Tab. **??**. The modeling of the temporal and spatial VCMs is discussed in this section. Based on the modeling, we implement their estimations using RMLE which has been discussed in section 4.2.2.

Temporal variance-covariance estimation

The VCMs per arc to be estimated are: (i) $Q^{p,r}_{ss}$, which is the temporal VCM of the stochastic ground deformation $\underline{s}_{p,r}$ in Eq. (4.3.2), (ii) $Q^{p,r}_{\text{aps}}$, which is the temporal VCM of slave APS $\underline{\phi}^{s,\text{aps}}_{p,r}$ including the spatial trend, vertical stratification and turbulent mixing, (iii) $Q^{p,r}_{\text{orb}}$, which is the temporal VCM of orbital uncertainty $\underline{\phi}^{s,\text{orb}}_{p,r}$ and (iv) $Q^{p,r}_{\text{noise}}$, which is the temporal VCM of phase noise $\underline{\phi}^{\text{noise}}_{p,r}$, see Eq. (4.3.4).

Table 4.1. Variance-covariance matrices required by the least-squares collocation method. N and M are the number of interferograms and the number of first-order PS (excluding the reference PS) respectively. The used estimation methods are parametric based (presumed variance-covariance model with limited number of model parameters) and non-parametric based (each individual element is estimated).

VCM	Structure	Size	Estimation method
Temporal			
Deformation: $Q_{ss}^{p,r}$	full matrix	N by N	parametric
APS: $Q_{\text{aps}}^{p,r}$	diagonal	N by N	non-parametric
Orbit: $Q_{\text{orb}}^{p,r}$	diagonal	N by N	non-parametric
Noise: $Q_{\text{noise}}^{p,r}$	diagonal	N by N	non-parametric
Spatial			
Turbulence: $Q_{\nu\nu}^{k}$	full matrix	M by M	parametric (Matérn)
Noise: $Q_{\mu\mu}^{k}$	diagonal	M by M	non-parametric
Prediction error: $K_{\epsilon_n\epsilon_n}^{k}$	diagonal	M by M	nonparametric

Suppose the full time series is composed of N interferograms, $Q_{ss}^{p,r}$ will be an $N \times N$ matrix. Moreover, since ground deformation often takes place gradually in time, $Q_{ss}^{p,r}$ is therefore a full matrix and its off-diagonal elements account for the temporal covariance of the deformation. For the arc between p and r (the reference PS), the stochastic ground deformation between the master acquisition at t_0 and a slave acquisition at t_i can be written as:

$$\underline{s}_{p,r}^{t_0,t_i} = (\underline{s}_p^{t_0} - \underline{s}_r^{t_0}) - (\underline{s}_p^{t_i} - \underline{s}_r^{t_i}), \tag{4.3.21}$$

where $\underline{s}_p^t$ and $\underline{s}_r^t$ are the stochastic deformations on the PSs p and r respectively during the epoch t . The covariance between $\underline{s}_{p,r}^{t_0,t_i}$ and $\underline{s}_{p,r}^{t_0,t_j}$ (j denotes another slave acquisition) is:

$$\begin{aligned} E\{\underline{s}_{p,r}^{t_0,t_i}\,\underline{s}_{p,r}^{t_0,t_j}\} &= E\{(\underline{s}_p^{t_0} - \underline{s}_r^{t_0} - \underline{s}_p^{t_i} + \underline{s}_r^{t_i})(\underline{s}_p^{t_0} - \underline{s}_r^{t_0} - \underline{s}_p^{t_j} + \underline{s}_r^{t_j})\} \\ &= E\{\underline{s}_p^{t_i}\,\underline{s}_p^{t_j} - \underline{s}_p^{t_i}\,\underline{s}_r^{t_j} - \underline{s}_p^{t_i}\,\underline{s}_p^{t_0} + \underline{s}_p^{t_i}\,\underline{s}_r^{t_0} \\ &\quad - \underline{s}_r^{t_i}\,\underline{s}_p^{t_j} + \underline{s}_r^{t_i}\,\underline{s}_r^{t_j} + \underline{s}_r^{t_i}\,\underline{s}_p^{t_0} - \underline{s}_r^{t_i}\,\underline{s}_r^{t_0} \\ &\quad - \underline{s}_p^{t_0}\,\underline{s}_p^{t_j} + \underline{s}_p^{t_0}\,\underline{s}_r^{t_j} + \underline{s}_p^{t_0}\,\underline{s}_p^{t_0} - \underline{s}_p^{t_0}\,\underline{s}_r^{t_0} \\ &\quad + \underline{s}_r^{t_0}\,\underline{s}_p^{t_j} - \underline{s}_r^{t_0}\,\underline{s}_r^{t_j} - \underline{s}_r^{t_0}\,\underline{s}_p^{t_0} + \underline{s}_r^{t_0}\,\underline{s}_r^{t_0}\}. \end{aligned} \tag{4.3.22}$$

As we can see from Eq. (4.3.22), to fully model the covariance we also need to model the spatial and spatio-temporal covariances of the stochastic deformation, e.g., $E\{\underline{s}_p^{t_i}\,\underline{s}_r^{t_j}\}$, $E\{\underline{s}_p^{t_i}\,\underline{s}_r^{t_i}\}$. However, in reality, we do not know a-priori whether $\underline{s}_p$ and $\underline{s}_r$ are correlated in space or not. When they are correlated we do not know a-priori whether the correlation is stationary in space or not. For PSs that are close to the reference PS r it might be reasonable to assume they are correlated both in space and time. But for PSs that are far away from r such an assumption might become invalid and it will vary from one specific ground deformation to another. Fortunately, modeling of the spatial and sptio-temporal covariances can be circumvented by choosing a non-deforming PS as the reference PS. This is often possible in

practice using some prior information about the ground surface under investigation. In such a case, Eq. (4.3.22) can be simplified to:

$$\begin{aligned} E\{\underline{s}_{p,r}^{t_0,t_i}\,\underline{s}_{p,r}^{t_0,t_j}\} &= E\{\underline{s}_p^{t_i}\,\underline{s}_p^{t_j}\} - E\{\underline{s}_p^{t_i}\,\underline{s}_p^{t_0}\} - E\{\underline{s}_p^{t_j}\,\underline{s}_p^{t_0}\} + E\{\underline{s}_p^{t_0}\,\underline{s}_p^{t_0}\} \\ &= \sigma_{\underline{s}_p^{t_i,t_j}} - \sigma_{\underline{s}_p^{t_i,t_0}} - \sigma_{\underline{s}_p^{t_j,t_0}} + \sigma_{\underline{s}_p}^2 \end{aligned} \tag{4.3.23}$$

where $\sigma_{\underline{s}_p}^2$ is the variance of the stochastic deformation at p, and $\sigma_{\underline{s}_p^{t_i,t_j}}$, $\sigma_{\underline{s}_p^{t_i,t_0}}$ and $\sigma_{\underline{s}_p^{t_j,t_0}}$ are the covariances of the stochastic deformation between time epochs t_i and t_j, t_i and t_0 and t_j and t_0 respectively. Thus, we simplify the modeling of $Q_{ss}^{p,r}$ to the modeling of Q_{ss}^{p}.

One difficulty of modeling Q_{ss}^{p} is the number of unknown elements in Q_{ss}^{p}. It is a symmetric matrix and there are in total $N(N+1)/2$ independent unknown elements that need to be estimated. To reduce the number of unknowns for estimation, we may use a positive definite covariance model (e.g., Gaussian, spheric or exponential, etc.) which only has a few unknown parameters to approximate Q_{ss}^{p}. The choice of covariance models is usually subject to the prior knowledge or assumption about the deformation in the area of interest. By estimating the model parameters we can obtain the estimation of Q_{ss}^{p} without explicitly estimating the $N(N+1)/2$ elements.

The temporal VCM $Q_{\text{aps}}^{p,r}$ is an $N\times N$ diagonal matrix, which is the result of a generally accepted assumption that APSs are temporally uncorrelated when the time interval between SAR acquisitions is longer than 1-day (see e.g. Ferretti et al. (2000)Hanssen (2001)). We can write the APS component $\underline{\phi}_{p,r}^{s,\text{aps}}$ as:

$$\underline{\phi}_{p,r}^{s,\text{aps}} = \underline{\phi}_{p}^{s,\text{aps}} - \underline{\phi}_{r}^{s,\text{aps}}, \tag{4.3.24}$$

where $\underline{\phi}_{p}^{s,\text{aps}}$ and $\underline{\phi}_{r}^{s,\text{aps}}$ are the APSs at p and r respectively during a slave acquisition. Taking into account the spatial characteristics of APS as discussed in section 4.3.2 we can rewrite Eq. (4.3.24) as:

$$\underline{\phi}_{p,r}^{s,\text{aps}} = \underline{\phi}_{p,r}^{s,\text{trend}} + \underline{\phi}_{p,r}^{s,\text{vs}} + \underline{\phi}_{p,r}^{s,\text{tm}}, \tag{4.3.25}$$

where $\underline{\phi}_{p,r}^{s,\text{trend}}$ is the phase gradient due to atmospheric trend in space, $\underline{\phi}_{p,r}^{s,\text{vs}}$ is caused by atmospheric vertical stratification and $\underline{\phi}_{p,r}^{s,\text{tm}}$ is the phase difference due to spatial variation of water vapor, i.e., turbulent mixing. Applying the error propagation law to Eq. (4.3.25) and writing the result in matrices we have:

$$Q_{\text{aps}}^{p,r} = Q_{\text{trend}}^{p,r} + Q_{\text{vs}}^{p,r} + Q_{\text{tm}}^{p,r}, \tag{4.3.26}$$

assuming each component of APS is uncorrelated with each other. If we assume the trend and vertical stratification components are stationary in time, $Q_{\text{trend}}^{p,r}$ and $Q_{\text{vs}}^{p,r}$ can be reduced to $\sigma_{\text{trend}}^2 \cdot I$ and $\sigma_{\text{vs}}^2 \cdot I$, where I is an $N\times N$ identity matrix, σ_{trend}^2 and σ_{vs}^2 are the temporal variances of $\underline{\phi}_{p,r}^{\text{trend}}$ and $\underline{\phi}_{p,r}^{\text{vs}}$ respectively. σ_{trend}^2 is proportional to the spatial distance between p and r and σ_{vs}^2 is scaled by the height difference between p and r. If the full time series of $\underline{\phi}_{p,r}^{\text{trend}}$ and $\underline{\phi}_{p,r}^{\text{vs}}$ can be estimated

beforehand we can estimate σ^2_{trend} and σ^2_{vs} by computing the temporal dispersions of the estimated time series of $\underline{\phi}^{\text{trend}}_{p,r}$ and $\underline{\phi}^{\text{vs}}_{p,r}$ respectively.

The turbulent mixing component, however, cannot be assumed stationary in time. Tandem interferograms of ERS-1/2 have revealed that the variability of turbulent mixing varies from one acquisition to another depending on how turbulent the local atmosphere is during the acquisition (Hanssen, 2001). Therefore, the whole diagonal elements of $Q^{p,r}_{\text{tm}}$ have to be estimated. Applying the error propagation law to Eq. (4.3.24) for the turbulent mixing component we have:

$$\sigma^2_{\underline{\phi}^{\text{tm}}_{p,r}} = \sigma^2_{\underline{\phi}^{\text{tm}}_{p}} + \sigma^2_{\underline{\phi}^{\text{tm}}_{r}} - 2\sigma^{\text{tm}}_{p,r}, \tag{4.3.27}$$

where $\sigma^2_{\underline{\phi}^{\text{tm}}_{p}}$ and $\sigma^2_{\underline{\phi}^{\text{tm}}_{r}}$ are the variances of turbulent mixing at p and r respectively, $\sigma^{\text{tm}}_{p,r}$ is the spatial covariance of turbulent mixing between p and r. If we assume the turbulent mixing component per acquisition is spatially stationary and isotropic within a spatial extent of 100×100 km (i.e., a typical spatial extent of an interferogram), Eq. (4.3.27) can be simplified to:

$$\sigma^2_{\underline{\phi}^{\text{tm}}_{p,r}} = 2\sigma^2_{\underline{\phi}^{\text{tm}}} - 2\sigma^{\text{tm}}_{p,r}, \tag{4.3.28}$$

where $\sigma^2_{\underline{\phi}^{\text{tm}}}$ is the global variance of turbulent mixing during a slave acquisition and it varies from one acquisition to another. Moreover, the covariance $\sigma^{\text{tm}}_{p,r}$ will only depend on the spatial distance between p and r because of the assumed spatial isotropy. On average, the smaller the distance between p and r the smaller $\sigma^2_{\underline{\phi}^{\text{tm}}_{p,r}}$ will be, i.e., APS has less impact on short arcs. Note, to estimate $\sigma^2_{\underline{\phi}^{\text{tm}}_{p,r}}$ we need know the spatial covariance $\sigma^{\text{tm}}_{p,r}$ which can be estimated in space if APS at PSs during every slave acquisition is known.

Strictly speaking, the temporal decorrelation noise can often be correlated in time (De Zan and Rocca, 2005; Rocca, 2007). But since the selected PSs have a very low amplitude dispersion (i.e., $D_A \leq 0.25$) we may expect the decorrelation noises on the PSs are small.Thus, the temporal covariance of the decorrelation is small and can be neglected. As a result, $Q^{p,r}_{\text{noise}}$ can be modeled as an $N \times N$ diagonal matrix. Moreover, $\underline{\phi}^{\text{noise}}_{p,r}$ is not stationary in time and its temporal variance varies with perpendicular and temporal baselines (Gatelli et al., 1994)Zebker and Villasenor (1992). Therefore, each main diagonal element of $Q^{p,r}_{\text{noise}}$ has to be estimated individually. We use the approach described by Kampes (2005) based on the least-squares variance component estimation (Teunissen and Amiri-Simkooei, 2006). In this approach $\underline{\phi}^{\text{noise}}_{p,r}$ is assumed stationary in space. Therefore $Q^{p,r}_{\text{noise}}$ becomes identical for all arcs in space but varies from one interferogram to another. From now on, we replace $Q^{p,r}_{\text{noise}}$ by Q^{t}_{noise}. Finally, since the orbit error has the same spatial characteristic as the atmospheric trend, therefore it is not possible to estimate $Q^{p,r}_{\text{trend}}$ and $Q^{p,r}_{\text{orb}}$ separately. The estimation of $Q^{p,r}_{\text{trend}}$ is actually the sum of $\hat{Q}^{p,r}_{\text{trend}}$ and $\hat{Q}^{p,r}_{\text{orb}}$.

Spatial variance-covariance estimation

The spatial VCMs to be estimated are: (i) $Q^k_{\nu\nu}$, which is the spatial VCM of the turbulent mixing component ($\underline{\nu}$, see Eq. (4.3.15)) of APS for the kth (k $\in [1\ N]$) slave acquisition; (ii) $Q^k_{\mu\mu}$, which is the spatial VCM of the phase noise ($\underline{\mu}$, see Eq.(4.3.16)) for the kth interferogram and (iii) $K^k_{\epsilon_n\epsilon_n}$, which is the kth spatial VCM of the prediction error ϵ_n of $\underline{n}$ (see Eqs. (4.3.10) and (4.3.11)) for all arcs in space.

$Q^k_{\nu\nu}$ will be an $M\times M$ matrix if the number of selected PS is $M+1$ (i.e., M non-reference PS form M spatial arcs w.r.t. the reference PS). Moreover, $Q^k_{\nu\nu}$ is a full symmetric matrix since APS is spatially correlated (Tatarskii, 1971; Hanssen, 2001). As a result, there are $M(M+1)/2$ independent elements of $Q^k_{\nu\nu}$ need to be estimated in order to construct $Q_{\nu\nu}$. We assume APS is spatially stationary and isotropic, then the ith element on the main diagonal can be evaluated by:

$$\begin{aligned}\sigma^2_{\underline{\nu}^k_{i,r}} &= E\{\underline{\nu}^k_{i,r}\cdot\underline{\nu}^k_{i,r}\}\\ &= E\{(\underline{\nu}^k_i-\underline{\nu}^k_r)^2\}\\ &= 2\sigma^2_{\underline{\nu}^k}-2\sigma_{\underline{\nu}^k_{i,r}},\end{aligned}\tag{4.3.29}$$

where $\sigma^2_{\underline{\nu}^k}$ is the global variance of turbulent mixing during the kth slave acquisition and $\sigma_{\underline{\nu}^k_{i,r}}$ is the covariance of APS between the PS i and the reference PS r. Furthermore, the element at row i and column j of $Q_{\nu\nu}$ can be evaluated by:

$$\begin{aligned}\sigma_{\underline{\nu}^k_{i,j,r}} &= E\{\underline{\nu}^k_{i,r}\cdot\underline{\nu}^k_{j,r}\}\\ &= E\{(\underline{\nu}^k_i-\underline{\nu}^k_r)\cdot(\underline{\nu}^k_j-\underline{\nu}^k_r)\}\\ &= \sigma_{\underline{\nu}^k_{i,j}}-\sigma_{\underline{\nu}^k_{i,r}}-\sigma_{\underline{\nu}^k_{j,r}}+\sigma^2_{\underline{\nu}^k}.\end{aligned}\tag{4.3.30}$$

To reduce the number of unknowns we assume $Q^k_{\nu\nu}$ can be approximated by a covariance model from mátern-family (Handcock and Wallis, 1994; Stein, 1999, 2005; Grebenitcharsky and Hanssen, 2005). It has been shown by Tatarskii (1971) that models from Mátern-family are capable of describing the well known power-law of 2D ("2/3-law") and 3D ("2/3-law") turbulence proposed by Kolmogorov's elementary turbulence theory (Kolmogorov, 1941). The covariance model we choose has the form:

$$C(h)=\frac{\sigma^2_{\underline{\nu}^k}}{2^{(\tau-1)}\Gamma(\tau)}\left(\frac{2\sqrt{\tau}|h|}{R}\right)^{\tau}K_{\tau}\left(\frac{2\sqrt{\tau}|h|}{R}\right),\tag{4.3.31}$$

where τ is the model parameter which controls the spatial smoothness of $\underline{\nu}$, R is the spatial range of $\underline{\nu}$ beyond which the atmospheric turbulence becomes totally decorrelated, Γ is the Gamma function and K is the modified Bessel function of the second kind. By estimating the three model parameters, i.e., R, τ and $\sigma^2_{\underline{\nu}}$, we are able to estimate $Q^k_{\nu\nu}$ per slave.

$Q^k_{\mu\mu}$ has the same size as $Q_{\nu\nu}$ and is also a full symmetric matrix. The ith main

diagonal element of $Q^k_{\mu\mu}$ can be evaluated by:

$$\begin{aligned}\sigma^2_{\underline{\mu}^k_{i,r}} &= E\{\underline{\mu}^k_{i,r} \cdot \underline{\mu}^k_{i,r}\} \\ &= E\{(\underline{\mu}^k_i - \underline{\mu}^k_r)^2\} \\ &= 2\sigma^2_{\underline{\mu}^k},\end{aligned} \tag{4.3.32}$$

assuming μ is spatially stationary and uncorrelated. $\sigma^2_{\underline{\mu}^k}$ is the global spatial variance of $\underline{\mu}$ for the kth interferogram. Furthermore, its off-diagonal elements can be evaluated by:

$$\begin{aligned}\sigma_{\underline{\mu}^k_{i,j,r}} &= E\{\underline{\nu}^k_{i,r} \cdot \underline{\nu}^k_{j,r}\} \\ &= E\{(\underline{\mu}^k_i - \underline{\mu}^k_r) \cdot (\underline{\mu}^k_j - \underline{\mu}^k_r)\} \\ &= \sigma^2_{\underline{\mu}^k}.\end{aligned} \tag{4.3.33}$$

$\sigma^2_{\underline{\mu}^k}$ is equal to the kth element on the main diagonal of Q^t_{noise} which is the temporal VCM of the phase noise for all arcs, see section 4.3.3.

The prediction error ϵ_n of $\underline{n}$ in Eq. (4.3.10) is evaluated independently per arc (see Eq. (4.3.11) in section 4.3.1) and we may assume $\hat{\epsilon}_n$ is uncorrelated in space. Thus, the spatial VCM $K_{\epsilon_n\epsilon_n}$ of ϵ_n is an $M \times M$ diagonal matrix whose diagonal elements are different from one arc to another. The ith diagonal element of $K^k_{\epsilon_n\epsilon_n}$ can be obtained from the kth diagonal element of $Q^{i,j}_{\hat{\epsilon}_n\hat{\epsilon}_n}$ in Eq. (4.3.11).

Estimation implementation

We carry out the estimation of the temporal and spatial VCMs modeled in 4.3.3 and 4.3.3 respectively in a sequential and iterative way. The full procedure of our implementation is given in the end of this section. It starts with the unwrapped phase time series per arc. As we discussed in section 4.3.3, one way to estimate the temporal VCM $Q^{p,r}_{nn}$ is via estimating $Q^{p,r}_{\text{aps}}$, $Q^{p,r}_{\text{orb}}$ and $Q^{p,r}_{\text{noise}}$ (Q^t_{noise}) separately, see Eq. (4.3.5). However, this requires that $\underline{\phi}^{s,\text{aps}}_{p,r}$, $\underline{\phi}^{s,\text{orb}}_{p,r}$ and $\underline{\phi}^{s,\text{noise}}_{p,r}$ in Eq. (4.3.4) are known already. The other way we can estimate $Q^{p,r}_{nn}$ is to directly estimate its main diagonal elements. Note, as a rule of thumb, given the same number of observations, the estimation accuracy of the unknowns in a functional/stochastic model decreases with the increase of the number of unknowns. Thus we believe that the first approach of estimating $Q^{p,r}_{nn}$ is superior to the second. However, we have to start with the second approach at the first place. It will become clear later that once we have initial predicts of $\underline{\phi}^{s,\text{aps}}_{p,r}$, $\underline{\phi}^{s,\text{orb}}_{p,r}$ and $\underline{\phi}^{s,\text{noise}}_{p,r}$ we can switch to the first approach for a better accuracy. Now, the question becomes that are the main diagonal elements of $Q^{p,r}_{nn}$ estimable given the unwrapped phase time series as observations? Suppose the chosen positive definite covariance model to model $Q^{p,r}_{ss}$ has m parameters, there will be $N + m$ unknowns to be estimated, where N is the number of interferograms in the time series. The maximum number of estimable unknowns of a stochastic model (i.e., VCM) is $b(b+1)/2$ (Teunissen and Amiri-Simkooei, 2006), where $b = N - n$ and n is the number of unknowns in the corresponding functional model, for example the

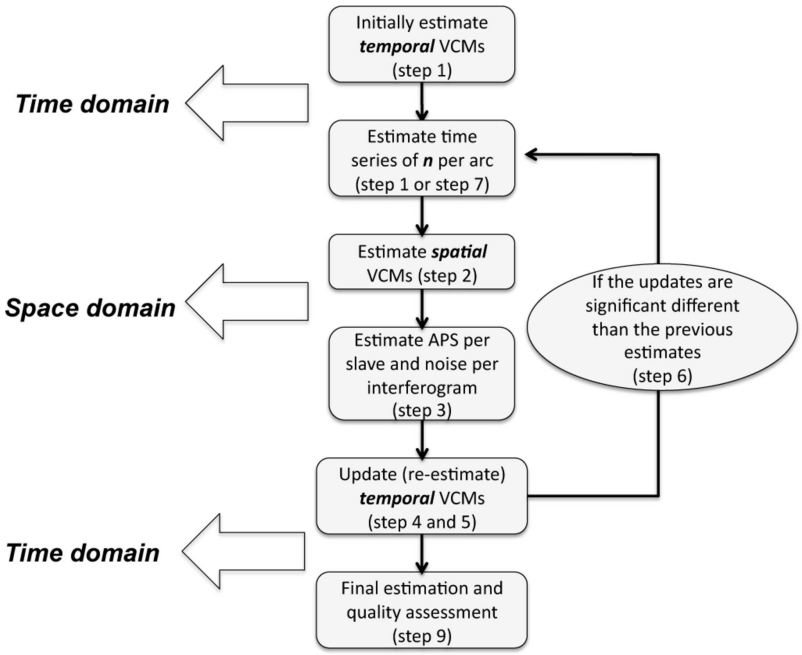

Fig. 4.2. Implementation diagram of the collocation method.

trend component (i.e., $Ax_{p,r}$) in Eq. (4.3.2). Since m and n are usually small (~ 3) and N is relatively large (> 15), thus $N+m$ is usually less than $b(b+1)/2$. Therefore, in practice we are able to estimate $Q_{ss}^{p,r}$ and $Q_{nn}^{p,r}$ given the number of observations. We use the maximum likelihood estimator (RMLE) given in section 4.2.2 for their estimations.

Next, in space, we use RMLE to estimate $Q_{\nu\nu}^{k}$ and $Q_{\mu\mu}^{k}$ based on the initial prediction of $\underline{n}^{k}$ (see Eq. (4.3.15)). Moreover, we compute $K_{\epsilon_n\epsilon_n}$ by Eq. (4.3.11). Given the initial estimation of $Q_{\nu\nu}^{k}$, $Q_{\mu\mu}^{k}$ and $K_{\epsilon_n\epsilon_n}$ we are able to initially predict APS, including spatial trend, turbulent mixing and vertical stratification components, per slave and phase noise per arc and per interferogram. Then, we use the initially predicted APS and phase noise to estimate the temporal VCMs (i.e., $Q_{\text{aps}}^{p,r}$, $Q_{\text{orb}}^{p,r}$ and $Q_{\text{noise}}^{p,r}$) from which $Q_{nn}^{p,r}$ can be updated. Finally, we re-estimate $Q_{ss}^{p,r}$ based on the updated estimation of $Q_{nn}^{p,r}$.

To achieve the best estimation and prediction accuracy we implement our algorithm sequentially and iteratively as follow (see Fig. 4.2 as well):

1. initially estimate $Q_{ss}^{p,r}$ (via a positive definite covariance model) and $Q_{nn}^{p,r}$ (by its main diagonal elements) and solve Eq. (4.3.10) for $\underline{n}$ for every arc (w.r.t. the same reference PS).

2. given the prediction $\hat{\underline{n}}$, estimate $Q_{\nu\nu}^{k}$ and $Q_{\mu\mu}^{k}$ and compute $K_{\epsilon_n\epsilon_n}$ by Eq. (4.3.11).

3. solve Eq. (4.3.17) for $\underline{\phi}^{\mathrm{s,aps}}$ (including $\underline{\phi}^{\mathrm{orb}}$) per slave and Eq. (4.3.19) for $\underline{\phi}^{\mathrm{noise}}$ per interferogram for all arcs.

4. update $Q_{nn}^{p,r}$ by estimating $Q_{\mathrm{aps}}^{p,r}$, $Q_{\mathrm{orb}}^{p,r}$ and $Q_{\mathrm{noise}}^{p,r}$ separately based on the results from step 3.

5. re-estimate $Q_{ss}^{p,r}$ given the updated $Q_{nn}^{p,r}$ from step 4.

6. compare the new estimated $Q_{ss}^{p,r}$ (via the model parameters) with the previous estimate, if they differ significantly go to step 7, otherwise go to step 9

7. solve Eq. (4.3.10) for a new $\underline{\hat{n}}$ based on the new estimates of $Q_{nn}^{p,r}$ and $Q_{ss}^{p,r}$ from step 4 and 5 respectively.

8. go to step 2.

9. solve Eqs. (4.3.6) and (4.3.8) for the ground deformation and solve Eqs. (4.3.7) and (4.3.9) for the accuracy of the ground deformation estimation.

The diagram of the implementation is sketched in Fig. 4.2.

4.4 Summary

We review the standard window-based filtering method (Ferretti et al., 2000) in section 4.1 and introduce the collocation method in sections 4.2 and 4.3. In the following we compare the two methods and show the theoretic advantages of the collocation method over the filtering method.

- The collocation method takes into account the stochastic characteristics of the *unmodeled* deformation. The characteristics of the *unmodeled* deformation is modeled by its temporal variance-covariance matrix (VCM) in Eq. 4.3.5.

The variance-covariance model in the collocation method is corresponding to the temporal low-pass window in the filtering method. However, by using a variance-covariance model we allow the choice of the variance-covariance model become falsifiable. The falsifiability may come from external data, e.g., GPS, leveling, etc., in the area under investigation or based on the geophysical properties of the deformation process.

Commonly used variance-covariance models (e.g., Gauss, spheric, hole effect, etc.) have two parameters. One is the signal variance and the other is the correlation length of the signal. These two parameters are estimated for each PS from its unwrapped phase time series. In contrast, the filtering method treat all PSs having the same variance and correlation length for the *unmodeled* deformation. In addition, the filtering method needs the user to specify a window length before the filtering can be performed. However the optimal window length is hardly known a-priori in practice. Last but not least, for the collocation method the estimated variance and correlation length are again falsifiable.

- Both spatial and temporal variation of APS are taken into account in the collocation method.

In the collocation method, different spatial characteristics, e.g., long-wavelength spatial trend, vertical stratification (in mountainous regions) and turbulent mixing, of APS are distinguished and modeled accordingly. They are estimated by BLUE and predicted by BLUP, see Eqs. (4.3.17) and (4.3.19).

The temporal variation of APS is taken into account and used for weighting observations (i.e., unwrapped phases of PSs), see Eq. (4.3.8). Comparing Eq. (4.2.4) and Eq. (4.1.3) we notice that the collocation method use the VCM of the observations for weighting. The VCM of the observations incorporates the temporal variation of APS via its temporal VCM, see Eq. (4.3.5). Acquisitions which experience large APS disturbance will be assigned a small weight and vice versa. Because of the weighting, the APS estimation from the collocation method should not be sensitive to the acquisition gaps in the time series.

- The filtering method is a special case of the collocation method.

This can be seen by comparing Eqs. (4.1.3) and (4.3.8). If the weight matrix W in Eq. (4.1.3) is constructed using the variance-covariance matrix of the deformation ($Q_{ss}^{p,r}$ in Eq. (4.3.8)) and the phase residue $\mathbf{\Phi}_{p,q}^{'}$ in Eq. (4.1.3) is firstly weighted by the inverse of $Q_{\Phi\Phi}^{p,r}$ in Eq. (4.3.8), the two methods will become equivalent. In other words, if the ground deformation has a variance-covariance function equivalent to a window function and APS in every acquisition has a similar degree of variation, then the two methods will give identical results.

- Unlike the filtering method, the precision of the result from the collocation method can be assessed in a systematic and falsifiable manner.

Given the VCM of each phase component, LSC provides a framework to allow users to compute the precision for each estimated or predicted phase component via Eqs. (4.2.6) and (4.2.7).

Last but not the least, we need to stress that the LSC method gives the best estimates of APS and deformation only when the presumed functional and stochastic model for deformation can well describe the signal. In next chapter we will show via simulations the sensitivity of the method to the mis-specification of the functional and stochastic model respectively.

Chapter 5

Evaluation of the least-squares collocation method using simulated InSAR time series

In this chapter the collocation method developed in chapter 4 is evaluated using simulated data. The simulated data provides the ground truth for validating the estimates of APS and ground deformation as well as the estimated precisions for the estimates. In case of real data ground truth is often unknown or unaccessible, particularly for APS which has relatively small magnitude with respect to total atmospheric delay and unprecedented spatial resolution. Although not all signals and noise sources that are present in real data can be simulated, the virtual evidence collected from properly designed simulations will help us to comprehend many complex and random processes in the real world.

Section 5.1 provides the stimulation strategies used for simulating ground deformation, APS, orbit error and phase noise. Section 5.2 reports and validates the result of the collocation method using the simulated data. The collocation method needs a-priori knowledge (i.e., suitable functional and stochastic models) of ground deformation, however such knowledge is usually unknown in practice. Thus, in section 5.3 we assess the sensitivity of the collocation method to different functional and stochastic models for ground deformation modeling. Finally, section 5.4 provides a summary of the evaluation results.

5.1 Simulation strategies

In this section we elaborate on the simulation strategies used for simulating ground deformation, APS, orbit errors and phase noise. Since the input data for the collocation method developed in chapter 4 is the time series of unwrapped phases for each PS and the method assumes that the phase unwrapping is carried out successfully. Thus, in our simulation we directly simulate unwrapped phases for each signal component of interest and do not take into account the possible phase unwrapping errors. In addition, we do not simulate the phase caused by DEM inaccuracy, which lead to a simplification of the functional model in Eq. (4.3.2), i.e., dropping out the deterministic parameter counting for the DEM inaccuracy. Such a simplification will not influence our method evaluation with regard to separating complex ground

deformation and APS.

In our simulation the time span of the InSAR time series is set to 3 years. The spatial size of our simulation is 256 by 256 pixels. From the full set of pixels we randomly select 300 pixels as PSs using an uniform distribution in space. The satellite repeat orbit is set to 12 days, which corresponds 91 acquisitions. We choose the 46th acquisition as the master of the time series.

5.1.1 Simulation of ground deformation

We divide the 300 randomly selected PSs into 3 categories. For the first category which consists of 75 PSs (randomly selected from the 300 PSs), we simulate a deterministic ground deformation for each of them using a linear model:

$$d^i(T) = v^i T, \tag{5.1.1}$$

where T is a 91×1 vector that contains the temporal baselines w.r.t. the master acquisition (the temporal baseline of the master is zero), and v^i is the deformation rate at PS i. For each of the PSs the deformation rate is simulated using uniform distribution within (2, 20) mm/year.

The second category consists of another 75 PSs which are randomly selected from the remaining 225 PSs. For each of them we simulate a ground deformation as:

$$\underline{d}^j(T) = v^j T + \underline{s}^j, \tag{5.1.2}$$

where $\underline{s}^j$ is an 91×1 vector that contains the stochastic part of the ground deformation on PS j. v^j is the simulated (using an uniform distribution) deformation rate on PS j and $v^j \in (2, 20)$ mm/year. To simulate $\underline{s}^j$ we assume that $\underline{s}^j$ is second-order stationary in time, i.e., a constant mean and variance. We use a 1D (one-dimension) hole-effect model that is often used to model a pseudo-periodic random process (Journel and Huijbregts, 1978; Kitanidis, 1997) to simulate its variance-covariance as a function of t:

$$r^j(t) = \begin{cases} \sigma_j^2(1 - \frac{t}{L_j})\exp(-\frac{t}{L_j}) & \text{for } \mathbf{t} \le L_j, \\ 0 & \text{for } \mathbf{t} > L_j, \end{cases} \tag{5.1.3}$$

where σ_j^2 denotes the variance of $\underline{s}^j$ and L_j is its correlation length in time (also called range in Geostatistics). We set the correlation length to 1-year which is often used assumption in practice for all the PSs and simulate σ_j^2 per PS using uniform distribution within in (9, 225) mm^2. Given the variance-covariance model in Eq. (5.1.3), $\underline{s}^j$ can be simulated by:

$$\underline{s}^j = \text{chol}(R)\underline{n}^j, \tag{5.1.4}$$

where *chol* stands for the Cholesky factorization, R is the variance-covariance matrix of $\underline{s}^j$ and it is a 91×91 Toeplitz matrix constructed from $r^j(t)$, and $\underline{n}^j$ is a 91×1 vector simulated by a standard normal distribution (i.e., zero mean and unit variance). To see $\underline{s}^j$ has the desired variance-covariance we apply the error-propagation law (Teunissen et al., 2005) to Eq. (5.1.4):

$$Q_{s^j} = \text{chol}(R) Q_{n^j} \text{chol}(R)^T = \text{chol}(R) I \text{chol}(R)^T = R, \tag{5.1.5}$$

where I is an 91×91 identity matrix and the superscript T denotes a matrix transpose.

Finally, the remaining 150 PSs in the third category are deformation free. Moreover, we choose the PS (from this category) which is closest to the spatial center of our simulations as the reference PS. For demonstration, the simulated deformation rates and variances are shown in Fig. 5.1 a and b respectively. In addition, Fig. 5.1 c shows the deformation time series of a PS (from the second category) which has the largest deformation variance, whereas Fig. 5.1 d plots the time series of a PS (also from the second category) which has the smallest variance. Note, in our simulation we do not attempt to simulate a spatial correlation of deformation between PSs. This is not necessary because the collocation method does not require the deformation to be spatially correlated (see section 4.3.1). In practice, however, deformation at neighboring PSs are often spatially correlated.

5.1.2 Simulation of atmospheric phase screen

As discussed in section 4.3.2 we model APS in space per acquisition as a surface trend delay (i.e., long-wavelength delay), a stochastic delay (i.e., turbulent mixing) and a height dependent delay (i.e., vertical stratification) if local land topography variation is significant (e.g., Δh>1000 m). In this simulation we only simulate the first two terms. The estimation of the height dependent delay will be evaluated using real data in Chapter 6.

To model the spatial surface trend delay we use the model:

$$z(x, y) = ax + by + c, \tag{5.1.6}$$

where $z(x, y)$ is the trend delay (unit: mm) at lateral position (x, y) and a, b, c are the trend coefficients. We simulate a, b and c independently using a standard normal distribution (i.e., zero mean and one-unit standard deviation). Based on the eight ERS-1/2 tandem interferograms from Groningen, the Netherlands analyzed by Hanssen (2001) we find that a more realistic trend can be obtained by down scaling the simulated coefficients by a factor of 16.

The stochastic delay can be modeled in a similar way as modeling the stochastic deformation in section 5.1.1. We assume the stochastic delay is second-order stationary and isotropic in space and choose the Mátern covariance model in Eq. (7.2.17) as its variance-covariance function. The most important parameter for simulating a realistic stochastic delay is its spatial variance. Note, because of the assumed stationarity and isotropy each APS simulation has a constant variance but the constant varies from one acquisition to another. To simulate a set of realistic spatial variances for all acquisitions we have considered the statistics of APS variance estimated from 26 tandem interferograms over the Netherlands by Hanssen (2001). Based on such statistics we simulate the variances (unit: mm^2) using a noncentral chi-square distribution which has the degree of freedom set to 5 and non-centrality set to 2. Figure 5.2 a shows the histogram of the simulated RMS. As we can see most APS in our simulation have an RMS between 3 and 8 mm. Moreover, Fig. 5.2 b plots the simulated (real) RMS (in blue) against the computed RMS (in red) from each APS

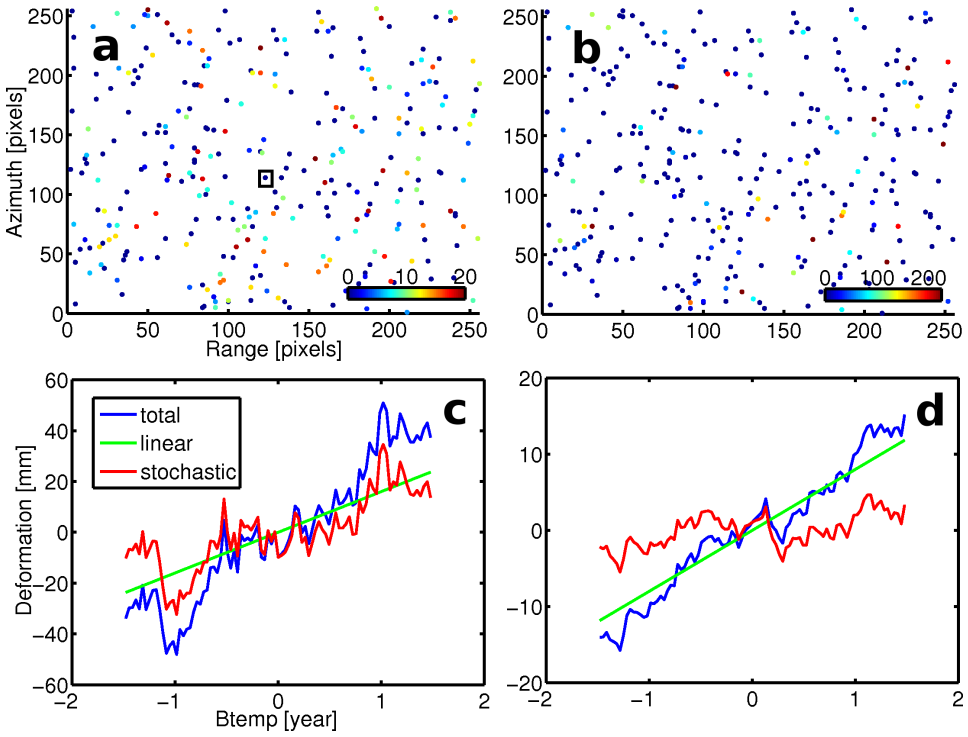

Fig. 5.1. Simulated deformation time series. **a)** Simulated linear velocities on the full set of PSs (300 PSs), color-bar unit: mm. The PS enclosed by the black square is chosen as the reference PS. **b)** Variances of the simulated stochastic deformation on the PSs, color-bar unit: mm^2. **c)** Simulated deformation time series of the PS that has the largest stochastic deformation variance (225 mm^2). **d)** Simulated deformation time series of the PS that has the smallest stochastic deformation variance (9 mm^2). Note, in our simulation we do not attempt to simulate spatial correlation of deformation between PSs. This is not necessary because the collocation method does not require the deformation to be spatially correlated (see section4.3.1).

simulation after removing a surface trend estimated by unweighted least-squares. The mean of the true RMS is 6.7 mm and the mean of the estimated RMS is 5.7 mm. Figure. 5.2 b is used to demonstrate that using unweighted least-squares to remove the trend in data will later on lead to a biased estimation of the variance of the stochastic signal embedded in the data, see discussion in section 4.2.

It has been revealed by Hanssen (2001) that the power spectrum of APS in space is scale variant and its slope decreases from approximately 5/3 below 1.5 km to 2/3 beyond 2km. In our simulations we set the parameter τ in Mátern model (see Eq. (7.2.17)), which controls the spatial smoothness of the stochastic delay to 4/3 for all the acquisitions. Note, the chosen spatial smoothness does not represent the real statistics of turbulence but is merely used for evaluating how good the least-squares

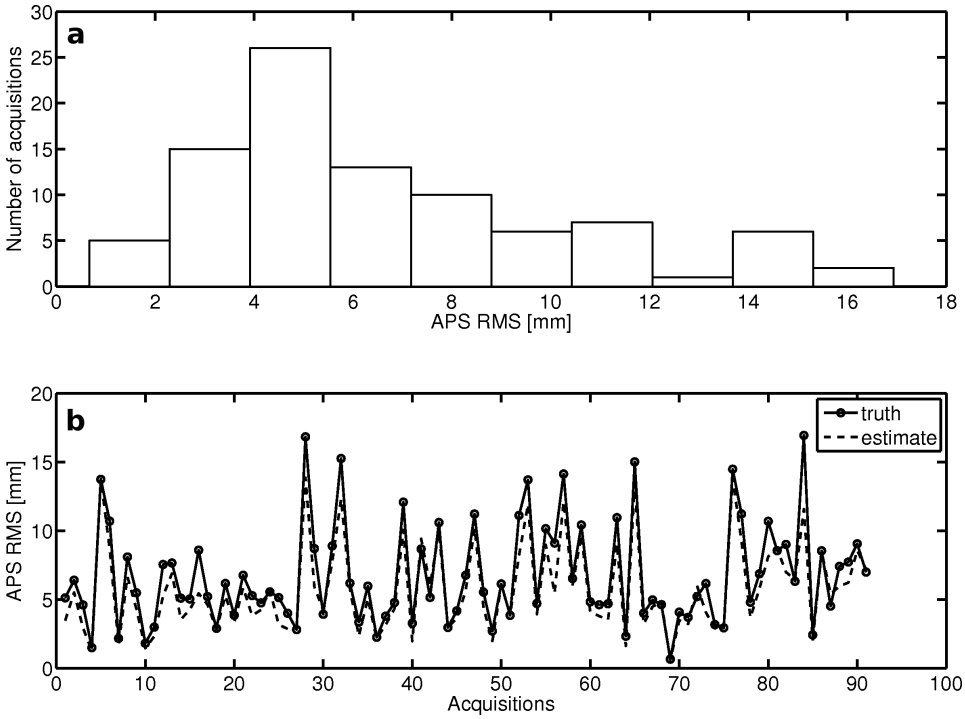

Fig. 5.2. RMS of simulated APS. **a**) Histogram of the RMS of simulated APS (in total 91 acquisitions). Most APS simulations have a RMS between 3 and 8 mm. **b**) True RMS of the simulated APS (blue) and computed RMS (red) after removing a surface trend using unweighted least-squares. The mean of the true RMS values is 6.7 mm and the mean of the estimated RMS values is 5.7 mm. The plot is used to demonstrate that using unweighted least-squares to remove the trend in data will later on lead to a biased estimation of the variance of the stochastic signal embedded in the data, see section 4.2.

collocation method can estimate this parameter. Moreover, the spatial correlation length (R in Eq. (7.2.17)) of APS is simulated for each acquisition using an uniform distribution within (30, 80) pixels.

We use the algorithm developed by Dietrich and Newsam (1993) for a 2D random simulation. Figure 5.3 shows the simulated 2D isotropic and homogeneous random fields based on the spheric model (Fig. 5.3 a), the Gaussian model (Fig. 5.3 b), the Mátern model with $\tau = 2/3$ (Fig. 5.3 c), the Mátern model with $\tau = 5/3$ (Fig. 5.3 d), the hole effect model (Fig. 5.3 e) and the exponential model (Fig. 5.3 e). The mathematic equations for these models are given in Appendix A. To make the simulated random fields in Fig. 5.3 comparable, each of the simulations uses unit variance and a spatial correlation length of 64 pixels. From the figure we observe that the simulation based on Gauss model has the smoothest spatial variation. In addition, the simulations based on spheric, hole effect, exponential and Mátern ($\tau = 5/3$) models

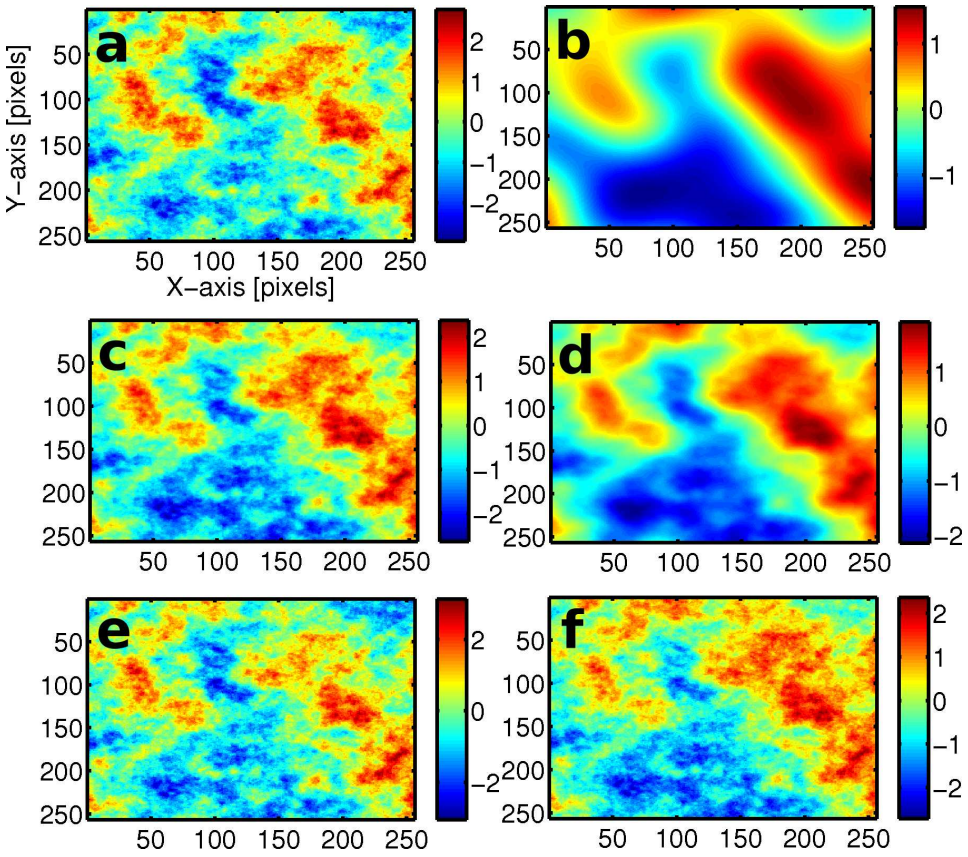

Fig. 5.3. Simulation of 2D isotropic and homogeneous random fields (unit: mm) using the algorithm developed by Dietrich and Newsam (1993). **a**) Spherical model. **b**) Gauss model. **c**) Mátern model with τ=2/3. **d**) Mátern model with τ=5/3. **e**) Hole effect model. **f**) Exponential model. All the simulations have a unit variance and a spatial correlation of 64 pixels.

have a similar degree of spatial smoothness. Last but not least, by increasing the parameter τ in the Mátern model we can obtain a smoother random field. Note, the variance-covariance model dependent smoothness is also applicable for 1D isotropic and homogenous random field.

The simulated master APS which has a spatial RMS of 6.8 mm is visualized in Fig. 5.4. Note, the spatial RMS here is the RMS of the turbulent mixing part of delay but not of the total delay. For slave APS simulations we show the one which has the largest spatial variance (16.9 mm) in Fig. 5.5 a and b and the one which has the smallest RMS (0.7 mm) in Fig. 5.5 c and d.

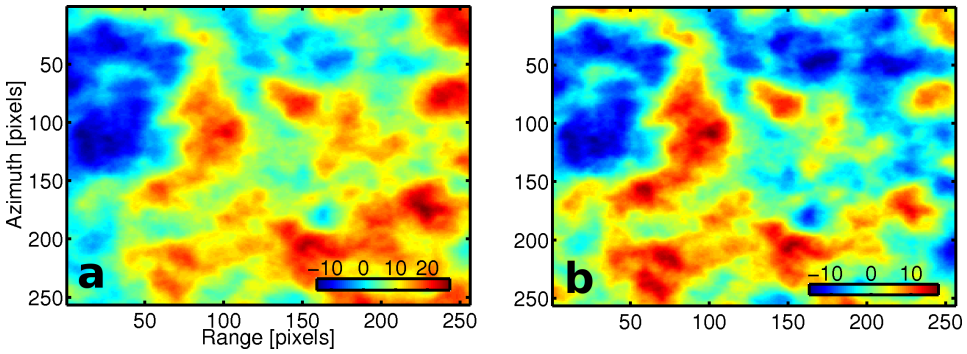

Fig. 5.4. Simulated master APS (unit: mm). **a**) Total APS. **b**) Turbulent mixing (RMS: 6.8 mm).

5.1.3 Simulation of satellite orbit error and phase noise

Since orbit error has the same spatial characteristics as the atmospheric trend, it has been included during APS simulation in section 5.1.2. In addition, we simulate phase noise for all PSs per acquisition independently using a normal distribution centered at zero. The variance of the simulated noise is within (1,2) mm^2.

5.1.4 Single-master interferograms formation

To form interferograms with a common master, we first compute the temporal phase difference between the master and each slave per PS. Afterwards, we compute the spatial phase difference between non-reference PSs and the pre-selected reference PS (see Fig. 5.1 a).

5.2 Result validation: a-prior knowledge of deformation is given

In this section we evaluate the developed collocation method by comparing its result against ground truth. We also compare the result with the result obtained from the standard low-pass filtering method discussed in section 4.1. To assess the best achievable accuracy from the collocation method we take the advantage of the a-priori knowledge about the deformation. That is, we assign the right model (i.e., linear function) and stochastic model (i.e., hole effect) of deformation to the collocation method. In practice, however, such a-priori knowledge is usually not available and the choice for the deformation models is often arbitrary. We will investigate the sensitivity of the collocation method to the choice of deformation models in section 5.3.

5.2.1 Validation of the stochastic models

For all experiments in our study we use a constrained minimization to minimize the objective function of RMLE in Eq. (4.2.11). In other words, we set the boundaries

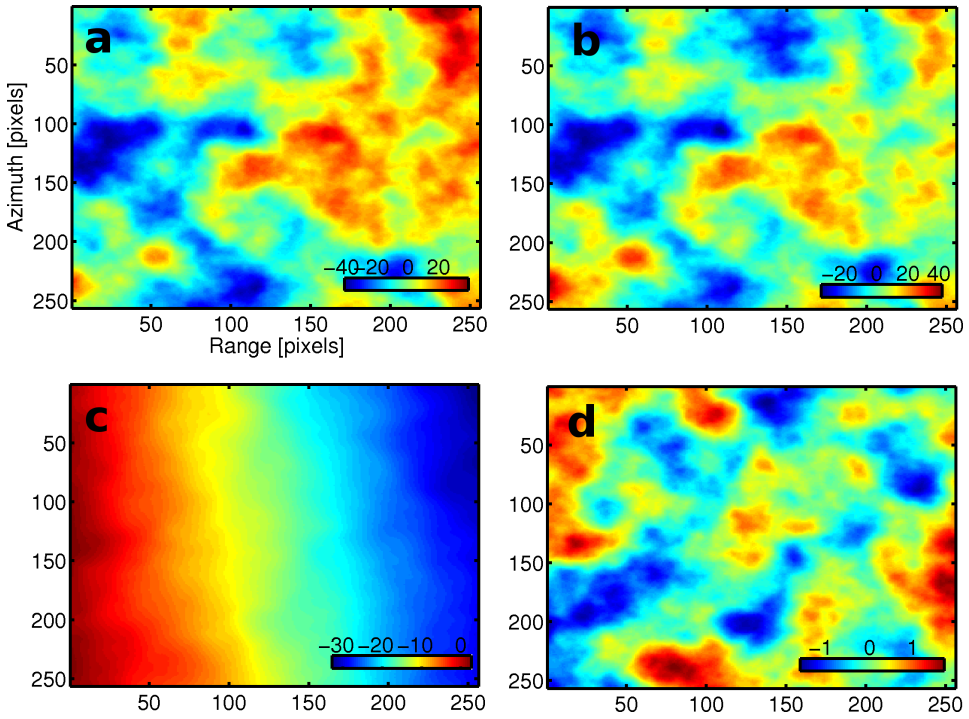

Fig. 5.5. Two simulated slave APS (unit: mm). The one that has the largest RMS (16.9 mm) is shown in Fig. 5.5 a (total delay) and b (turbulent mixing). The one that has the smallest RMS (0.7 mm) is shown in Fig. 5.5 c (total delay) and d (turbulent mixing).

for the parameters of a stochastic model. Then, the search for the parameters that minimize the objective function is constrained by the boundaries. In this experiment we set the boundaries of the correlation length of deformation to (0.5, 1.5) in year(s). In addition, the boundaries of the parameter τ in Mátern model is set to (2/3, 5/3) and the boundaries of the spatial correlation length of Mátern model is set to (20, 100) in pixels. Although the correlation length does not have a physical meaning, the main purpose is to test how accurately it can be estimated by the collocation method. Moreover, the boundaries of the temporal variance of the ground deformation and the spatial variance of APS per acquisition are both set to $(0, +\infty)\,\mathrm{mm}^2$. Table 5.1 lists the real (simulated) range of each parameter as well as its search boundaries.

Turbulent mixing

The estimated APS RMS (blue) against the simulated (true) APS RMS (green) per acquisition as well as their difference (i.e., estimation error) highlighted in red are plotted in Fig. 5.6 a. From the figure we observe that the estimated APS RMS agrees very well with the ground truth. The mean of the estimation error is -0.02 mm and

Table 5.1. Search intervals for the parameters of the stochastic models used in simulation of InSAR time series (see section 5.1). The real (simulated) range of each parameter is given for reference.

Parameter	Range	Search interval
APS RMS [mm]	(0.7,16.9)	(0,+∞)
Deformation RMS [mm]	(3,15)	(0,+∞)
APS correlation length [pixels]	(30,80)	(20,100)
Deformation correlation length [year]	1	(0.5,1.5)
APS spatial smoothness (τ)	4/3	(2/3,5/3)

the error RMS is 1.2 mm. The scatter plot of the estimated and real APS RMS is given in Fig. 5.6 c and the correlation between them is 0.95. Hence, we conclude that APS RMS per acquisition can be well estimated by RMLE. In addition, with regard to the spatial correlation length of APS, its estimation accuracy is less satisfactory, see Fig. 5.6 d. The correlation between the estimated and the real spatial correlation is only 0.59. Nevertheless, a clear linear relationship between them can be observed. In the end, Fig 5.6 b shows the comparison between the estimated and the real APS spatial smoothness (τ in Mátern model) per acquisition. The RMS error of its estimates is 0.33. The above results are summarized in Tab. 5.2.

Stochastic ground deformation

Figure 5.7 a,b show the true (simulated) and estimated (stochastic) deformation RMS per PS respectively. These PSs (75 in total) are from the second category of the simulated PSs which have stochastic ground deformation, see section 5.1.1. Moreover, the difference (i.e., estimation error) between the real and estimated RMS is shown in Figure 5.7 c. From the figure we do not see a dependency of the estimation error on the spatial distance between non-reference PSs and the reference PS.

Figure 5.8 a shows the estimation error of the deformation RMS in ascending order (sorted using the simulated deformation RMS). From the figure we do not observe a dependency of the estimation error on the magnitude of the real RMS. In addition, the histogram of the estimation error is plotted in Fig. 5.8 b and we observe that the histogram largely resembles a norm distribution centered at 1.2 mm with a standard deviation of 3.3 mm. Moreover, the scatter-plot between the estimated and the simulated RMS is given in Fig. 5.8 c. A clear linear relationship is observed and the correlation between them is 0.69.

Finally, the estimated deformation correlation length (in time) per PS is shown in Fig. 5.9. Unlike the other parameters, the correlation length cannot be estimated reliably, too small (i.e., close to the lower boundary) or too large (i.e., close to the upper boundary). The poor estimation is likely due to the presence of APS in the estimated deformation time series. It suggests that in real applications we should provide a range of possible correlation as small as possible to RMLE. The above results are summarized in Tab. 5.2.

We also evaluate the parameter estimation on the remaining 225 PSs (from the first

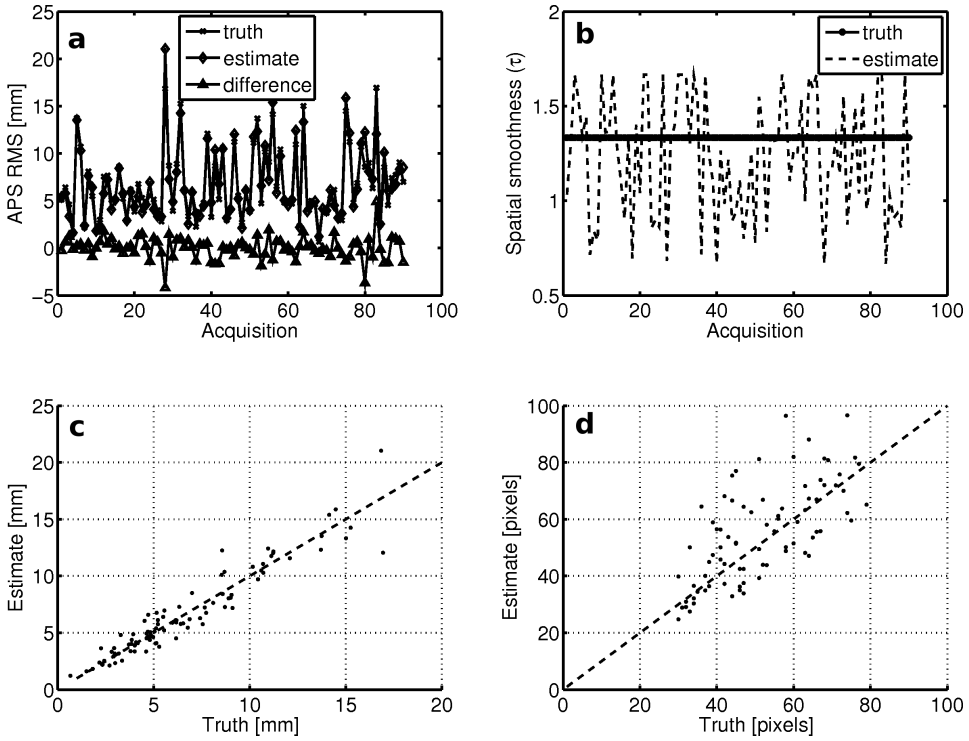

Fig. 5.6. Evaluation of the estimated parameters of APS variance-covariance function per acquisition. **a**) Estimated APS RMS (unit: mm) per acquisition (blue), simulated (true) APS RMS per acquisition (green) and their differences (red). The mean and RMS of their differences are -0.02 and 1.2 mm respectively. **b**) Estimated spatial smoothness (τ in Mátern model) per acquisition (blue) and real τ per acquisition (green). **c**) Scatter plot of the estimated and the real APS RMS. The correlation between them is 0.95 and the red line follows a unit slope for reference. **d**) Scatter plot of the estimated and the real APS spatial correlation length in pixels. The correlation between them is 0.59.

and third categories) which do not have a stochastic deformation. The evaluation tells us about the possible false alarm of stochastic deformation (i.e., non-zero deformation RMS) raised by the collocation method. In total, there are 91 from the 225 PSs showing false alarm and the histogram of the false alarm is plotted in Fig. 5.10. From the figure we observe that the false alarm ranges from 0 to 5 mm. The mean of the false alarm is 2.3 mm. In contrast, the mean of the simulated deformation RMS on the 75 PSs who do have stochastic deformation (from the second category) is 8.6 mm. Therefore, we conclude that the false alarm is relatively small and should be acceptable.

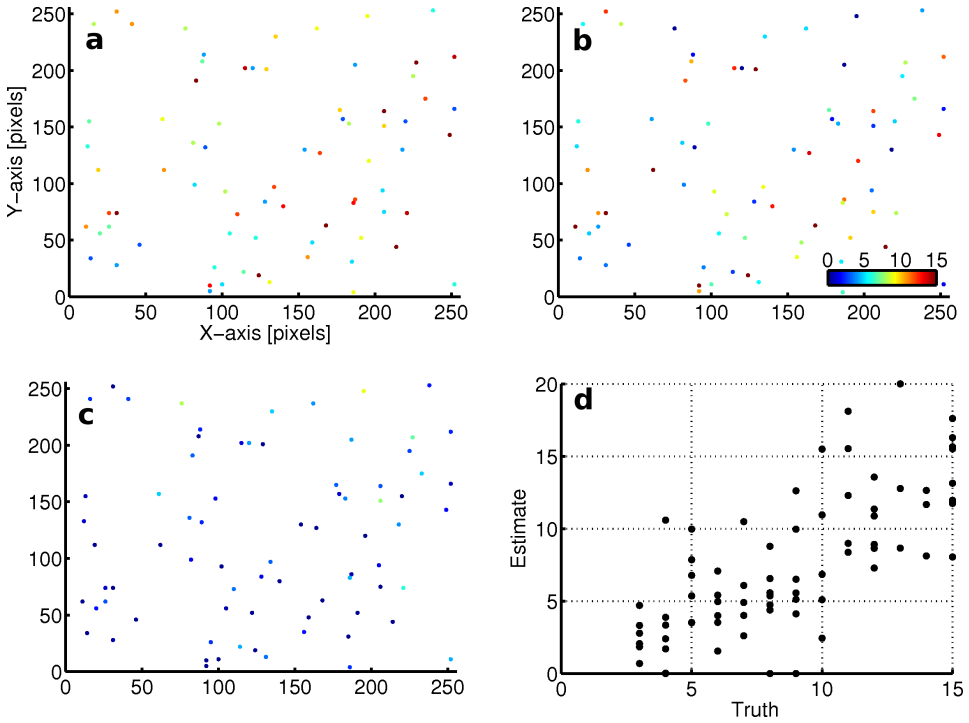

Fig. 5.7. Evaluation of the deformation RMS (unit: mm) estimation. **a**) Simulated (true) RMS for the PSs in the second category of simulated PSs (see section 5.1.1). **b**) Estimated RMS for these PSs. **c**) Their difference, i.e., estimation error. Note, the estimation error does not have a dependency on the spatial distance between non-reference PSs and the reference PS. **d**) Scatter plot of estimated and simulated deformation RMS.

5.2.2 Validation of the final result

Given the estimated variance-covariance matrices from the previous section we use least-squares collocation to separate APS and ground deformation in this section. The result is evaluated by comparison against ground truth (i.e., the original simulation). In addition, the result obtained from the standard low-pass filtering method using a one-year Gaussian window is also assessed in this section.

APS estimates

The most straightforward way of validation is to compare APS estimate per acquisition to the corresponding ground truth. We can also carry out the validation in terms of single-master interferograms, i.e., APS temporal difference between the common master and a slave. In this experiment, we can carry out both comparisons because the ground truth is perfectly known from our simulation. But we have to keep in mind that in practice such comparisons are usually not possible due to the lack of ground truth. In practice, the best ground truth available is short temporal baseline

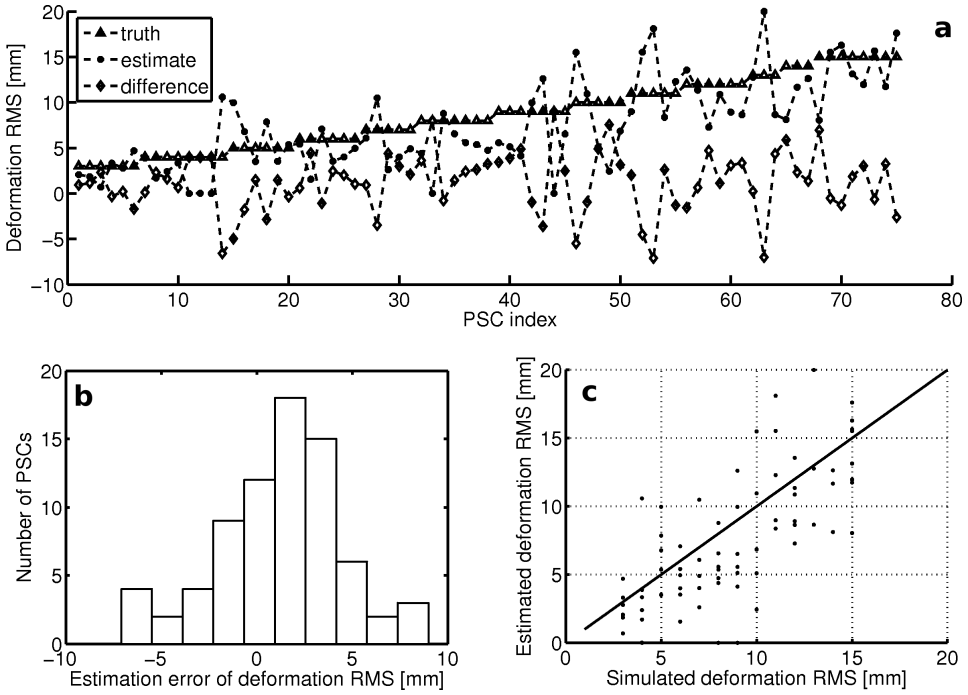

Fig. 5.8. Continued evaluation of the deformation RMS estimation following Fig. 5.7. **a**) Estimation error (in red) of the deformation RMS in ascending order (sorted based on the real deformation RMS in green). Note, the estimation error does not have a dependency on the magnitude of the real deformation RMS. **b**) Histogram of the estimation error. It is centered at 1.2 mm with a standard deviation of 3.3 mm. **c**) Scatter-plot between estimated and simulated RMS. Their correlation is 0.69. The red line follows a unit slope for reference.

(i.e., a few months) interferograms whose interferometric phases are dominated by APS, provided that the ground area does not undertake rapid deformation.

Figure 5.11 a b and c show the simulated master APS, estimated master APS by the collocation method by unweighted least-squares respectively. The unweighted least-squares is carried out by replacing the variance-covariance matrix in Eq. (4.3.6) by an identity matrix. The histogram of the estimation error is plotted in Fig. 5.12 a for the collocation method and in Fig. 5.12 b for unweighted least-squares. The estimation error made by the collocation method has a -0.3 mm mean and a standard deviation of 1.9 mm. In contrast, the estimation error made by unweighted least-squares has a -0.6 mm mean and a standard deviation of 4.4 mm. Therefore, the collocation method leads to a better estimation of master APS through modeling the variance-covariance functions of APS and ground deformation.

Regarding slave APS estimation, the overall comparison is shown in Fig. 5.13. The RMS of the estimation error made by the collocation method is shown in blue and

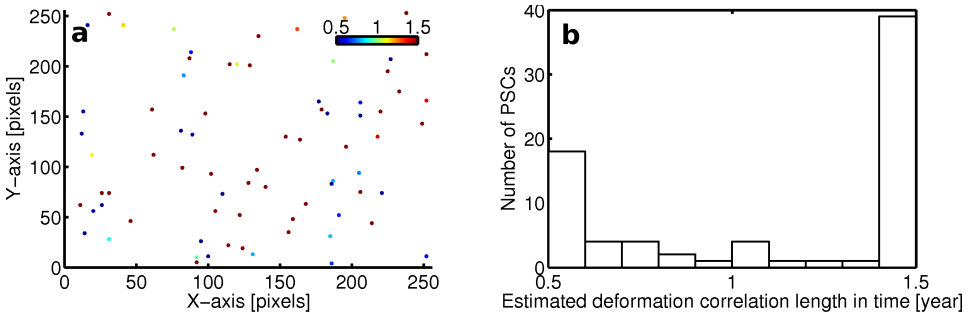

Fig. 5.9. Evaluation of the deformation correlation length (unit: year) estimation. The real correlation length (1 year) is identical for all PSs. **a)** Estimated correlation length for the PSs who have stochastic deformation (see section 5.1.1). **b)** Histogram of the estimated correlation length. The poor estimation of the correlation length is likely due to the presence of APS in the estimated deformation time series.

the mean of the RMS is 2.1 mm. In contrast, the RMS of the estimation error made by the filtering method is shown in red and the mean of the RMS is 3.4 mm. The mean of the real RMS of slave APS shown in green is 8.7 mm. Note, for the filtering method a Gaussian window with a window length of 1-year is used. Thus, we conclude that the collocation method results in a better APS estimation. The above results are summarized in Tab. 5.2.

Ground deformation estimates

The simulated (real) deformation rates are shown in Fig. 5.14 a and the estimated rates by the collocation method and the filtering are plotted in Fig. 5.14 b and c respectively. In the filtering method, the deformation rate is estimated by unweighted least-squares. In addition, the histograms of the estimation errors are displayed in Fig. 5.15 a for the collocation method and in Fig. 5.15 b for the filtering method. The mean and RMS of the estimation error made by the collocation method is 0.46 mm and 3.3 mm respectively. The mean and RMS of the estimation error made by the filtering method is 0.78 mm and 3.6 mm respectively. Therefore, in terms of the deformation rate estimation these two methods give very similar results. In other words, the deformation rate estimation is not sensitive to weighted least-squares.

It is of also interesting to see how good the total deformation is estimated. Figure 5.16 shows the total deformation estimation of four PSs who have both deterministic (linear) and stochastic (hole-effect) ground deformations (from the second PS category). The simulated ground deformation is shown in green, the estimate made by the filtering method is shown in red and the collocation result is shown in blue with estimated errorbars (± standard deviation) in mm. Note, each errorbar is estimated individually for each deformation estimate in the time series using Eqs. (4.3.7) and (4.3.9). In general, the errorbar tends to be larger at the beginning as well as in the end of the time series. This is because of a so-called edge-effect in which less input data is involved in estimation. Comparing the estimates with the

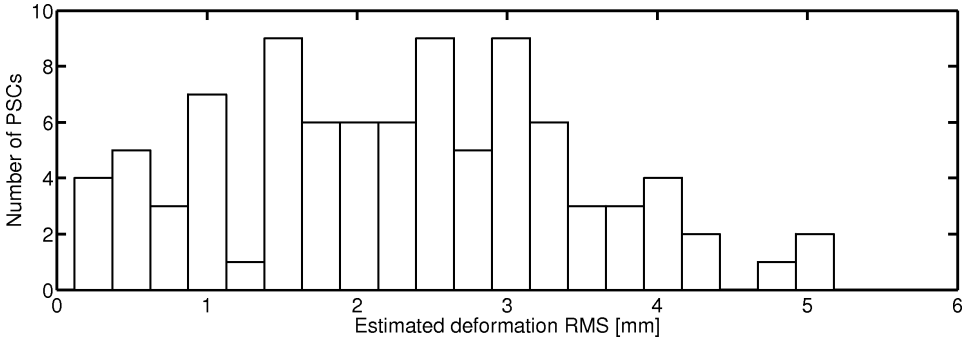

Fig. 5.10. Histogram of the estimated deformation RMS (unit: mm) on the PSs who do not have a stochastic deformation, i.e., deformation false alarm. In total, 91 from the 225 PSs (from the first and third categories) show false alarms which range from 0 to 5 mm. The mean of the false alarm is 2.3 mm. In contrast, the mean of the simulated deformation RMS on the PSs (from the first category) who have stochastic ground deformation is 8.6 mm.

real deformation, we can clearly see that the estimate obtained from the collocation method recoverers more small scale details of the real deformation and on average has a better fit to the ground truth. Moreover, the estimated errorbars provide a reasonable measure of the estimation error made by the collocation method.

Figure 5.17 plots the total deformation estimation of four PSs who have only deterministic deformation (from the first PS category). In addition, Fig. 5.18 displays the total deformation estimation of four PSs who are deformation free (from the third PS category). Clearly, we can see from both figures that the estimates of the filtering method always show an artificial seasonal deformation with a period (i.e., a time interval between a peak and a valley) of 0.5 year approximately. The artificial seasonal pattern is caused by the leakage of APS.

5.2.3 Sensitivity to the acquisition rate in time

In this section, our goal is to investigate the sensitivity of separating APS and ground deformation to input data (i.e., unwrapped phases of PSs) which has a lower temporal resolution (i.e., longer satellite repeat orbit). In the previous section we have shown the validation result based on simulated time series with a temporal resolution of 12-day. The validation shows that our collocation method can better separate APS and ground deformation than the standard window-based filtering method. This is because the collocation method uses weighted least-squares via the estimated variance-covariance matrices of the signals of interest (i.e., deformation and APS). In practice, one of the limitations that could influence the stochastic modeling (i.e., variance-covariance estimation) is the temporal resolution of the input data. Moreover, given the same variance-covariance functions, the collocation method is expected to give less accurate result as the temporal resolution decreases. This also applies to the filtering method in which less acquisitions will be involved

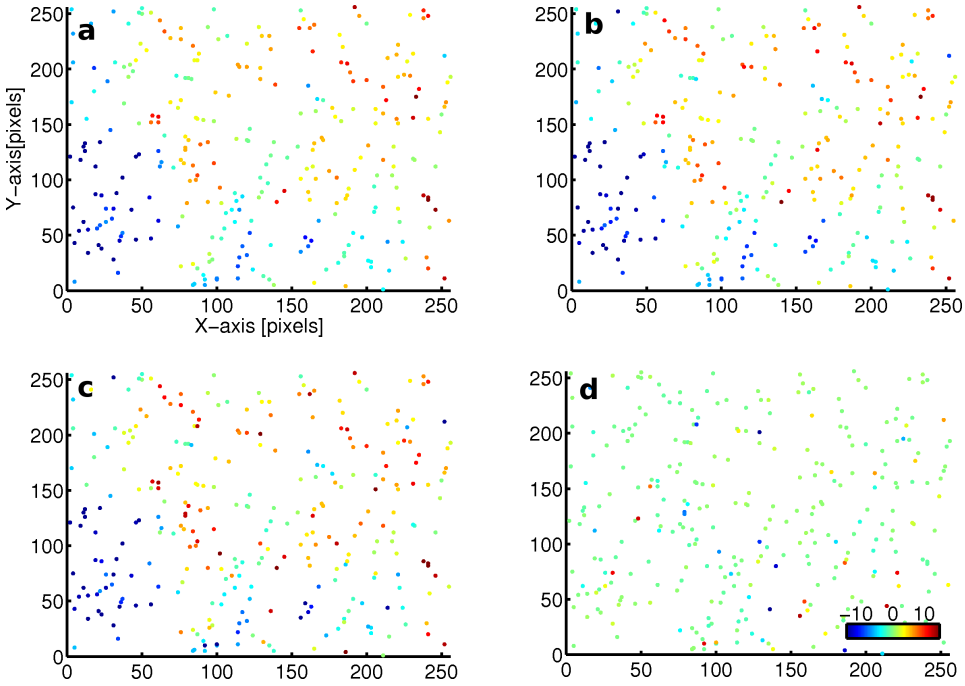

Fig. 5.11. Estimated master APS (unit: mm). **a**) Simulated master APS. **b**) Estimated master APS by the collocation method. **c**) Estimated master by unweighted least-squares (same as the filtering method). **d**) Difference between the two master APS estimates

in averaging out APS.

We decide to decrease the temporal resolution to 36-day which is approximately the repeat orbit of ESA's ERS1/2 and Envisat satellites (35-day) by selecting a subset of the original time series simulated in section 5.1 with a 36-day interval starting from the first acquisition of the simulation. We apply our collocation method to the subset of the time series in the same way as we did in section 5.2 and the result (after validation) is shown in Tab 5.3. Comparing to the result listed in Tab 5.2 we find that the accuracy of the stochastic parameters obtained from the subset time series is slightly worse. With regard to APS and ground deformation estimation, both filtering and collocation methods give less accurate results. This is what we expected. Therefore, we conclude that the decrease of the temporal resolution of input data will have a noticeable impact on the separation of ground deformation and APS but only a minor affect on the stochastic modeling.

Regarding slave APS estimation with the 36-day temporal resolution, Fig. 5.19 shows the comparison between the collocation method and the filtering method. Similar to Fig. 5.13 (12-day temporal resolution) the estimates obtained from the collocation method are always more accurate than the estimates made by the filtering method. Moreover, we find that the estimation error of slave APS has a considerable corre-

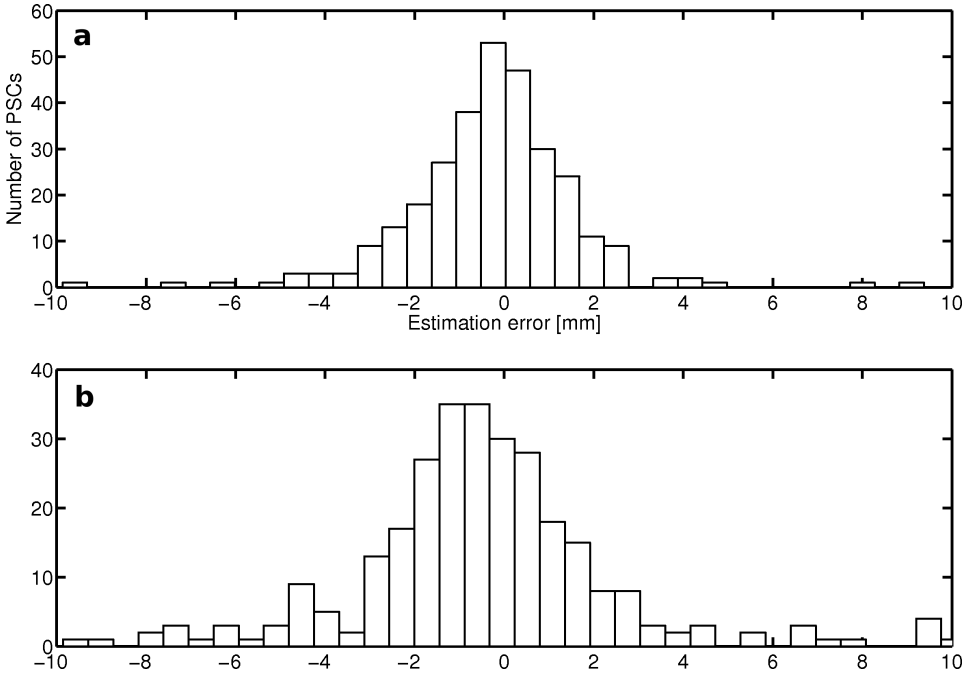

Fig. 5.12. Histogram of the estimation error of master APS. **a)** Estimation error made by the collocation method (mean: -0.3 mm, standard deviation:1.9 mm). **b)** Estimation error made by unweighted least-squares (mean: -0.6 mm, standard deviation: 4.4 mm).

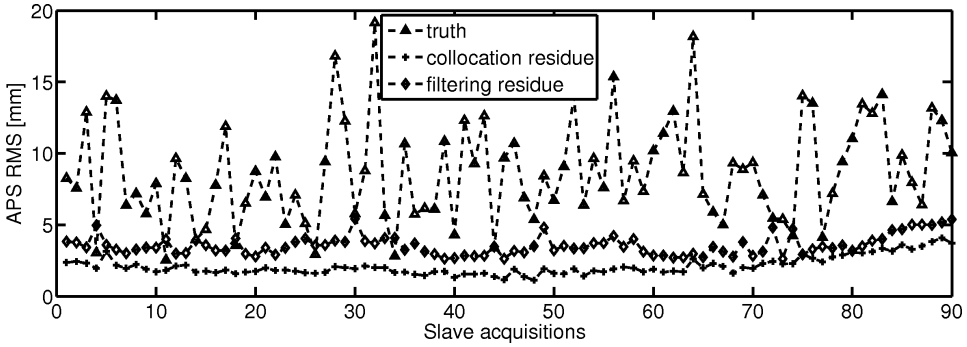

Fig. 5.13. Evaluation of slave APS estimation. The RMS (unit: mm) of the estimation error made by the collocation method is shown in blue and the mean of the RMS is 2.1 mm. In contrast, the RMS of the estimation error made by the filtering method is shown in red and the mean of the RMS is 3.4 mm. The mean of the RMS of the real RMS of slave APS shown in green is 8.7 mm. For the filtering method a Gaussian window with a window length of 1-year is used.

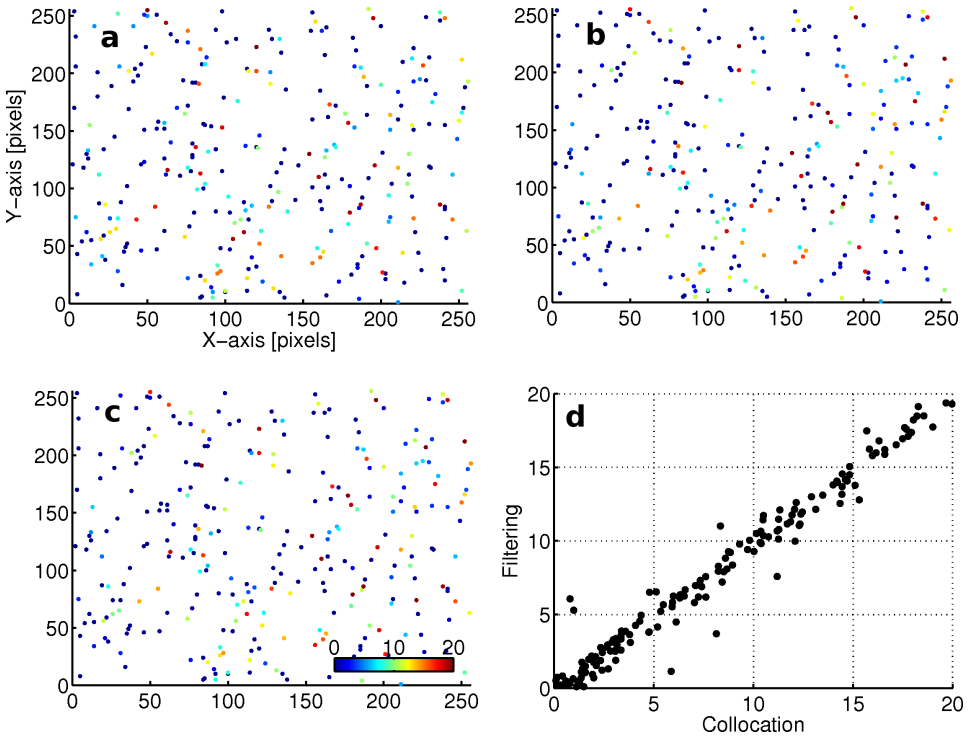

Fig. 5.14. Evaluation of the deformation rate (unit: mm/year) estimation. **a)** Simulated deformation rate. **b)** Estimated deformation rate by the collocation method. **c)** Estimated deformation rate by the filtering method (unweighted least-squares). **d)** Scatter plot of the two estimates. Their estimation errors are displayed in Fig. 5.15.

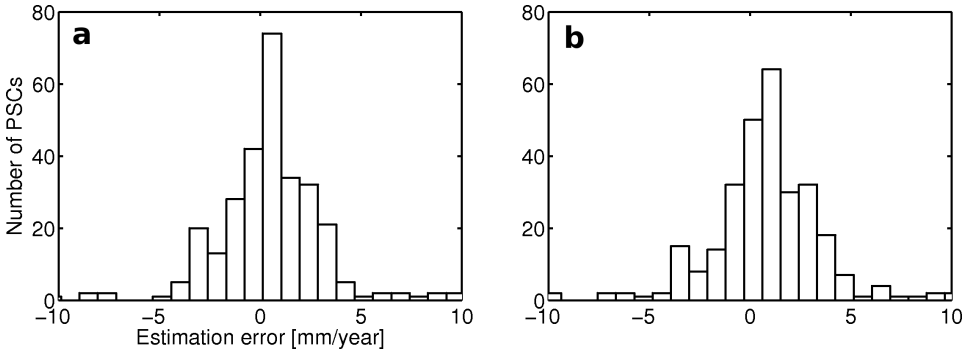

Fig. 5.15. Histogram of the estimation error of deformation rate. **a)** Estimation error made by the collocation method. **b)** Estimation error made by the filtering method.

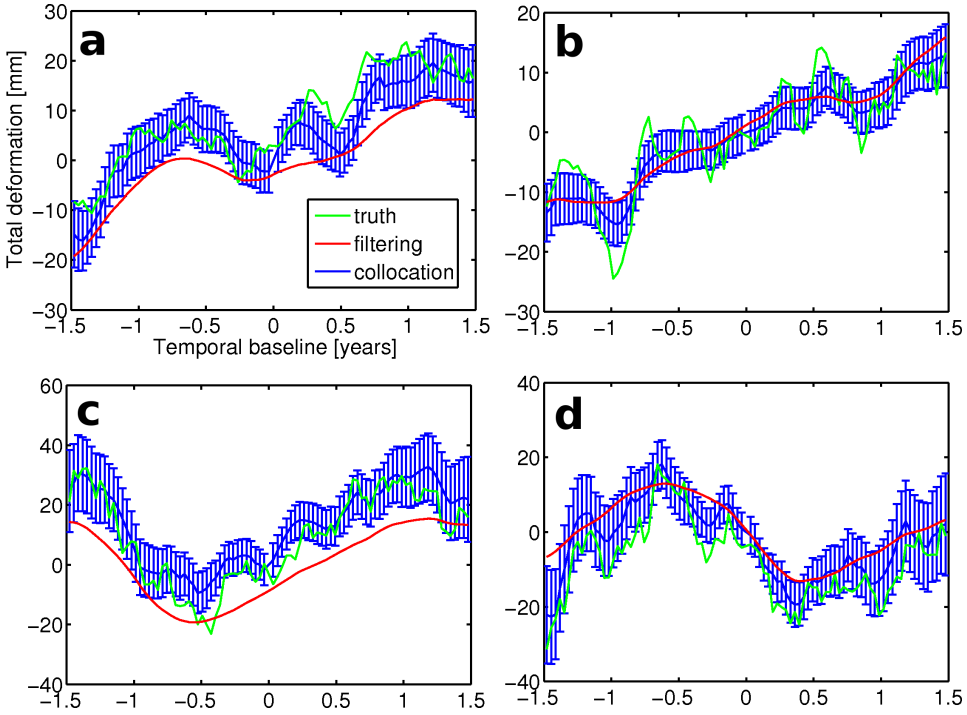

Fig. 5.16. Evaluation of the total deformation estimates for four PSs who have both deterministic and stochastic ground deformations (unit: mm). The simulated ground deformation is shown in green, the estimate from the filtering method (1-year Gaussian window) is shown in red and the estimate from the collocation method is shown in blue with an estimated errorbar for each estimate in the time series. **a**) PS No. 3 whose distance to the reference PS is 106 pixels. The RMS errors made by the collocation and filtering methods are 4.3 and 8.6 mm respectively. **b**) PS No. 7 whose distance to the reference PS is 72 pixels. The RMS errors made by the collocation and filtering methods are 3.8 and 4.8 mm respectively. **c**) PS No. 15 whose distance to the reference PS is 115 pixels. The RMS errors made by the collocation and filtering methods are 6.4 and 11.0 mm respectively. **d**) PS No. 26 whose distance to the reference PS is 61 pixels. The RMS errors made by the collocation and filtering methods are 6.2 and 9.7 mm respectively.

lation in time, especially among a sub-series of acquisitions in which one acquisition has a relatively large APS RMS. To show that, we plot the estimation errors of slave APS made by the collocation and the filtering method in Figs. 5.21 and 5.22 respectively for the 8, 9, 10 and $11th$ acquisitions. Among these acquisitions, the $10th$ slave APS shown in Fig. 5.20 has the largest RMS in the time series (see Fig. 5.19). Comparing Figs. 5.21 and 5.22 we find that the correlation is stronger among the estimation errors made by the filtering method. For instance, a clear positive estimation error from down-left to up-right can be seen in every subplot of Fig. 5.22.

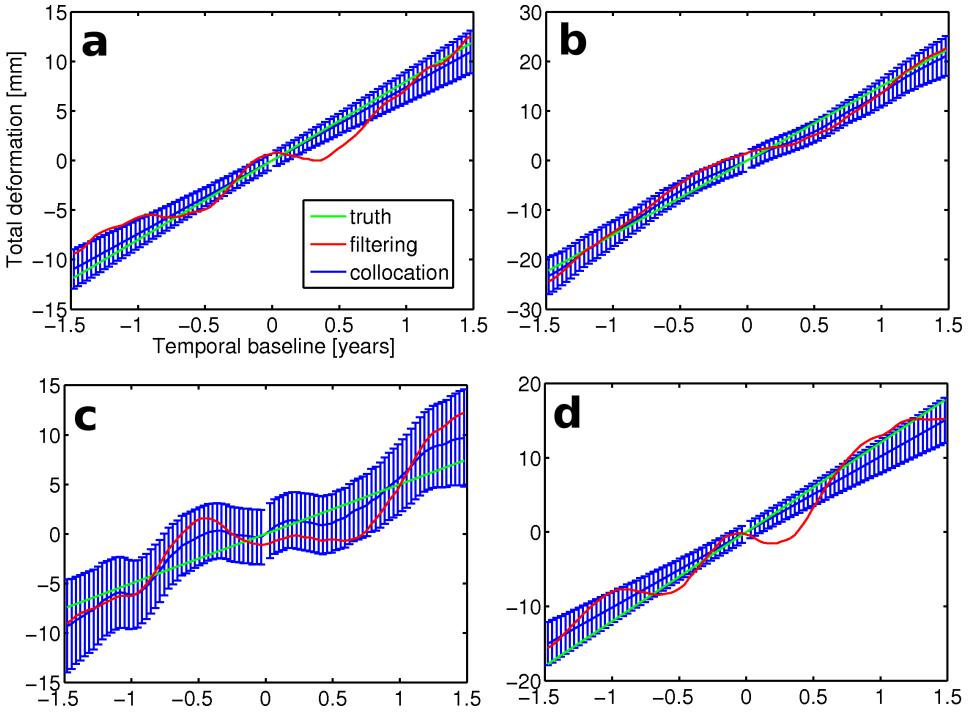

Fig. 5.17. Evaluation of the total deformation estimates for the PSs who have only deterministic deformation (unit: mm). The simulated ground deformation is shown in green, the estimate from the filtering method (1-year Gaussian window) is shown in red and the estimate from the collocation method is shown in blue with an estimated errorbar for each estimate in the time series. **a**) PS No. 81 whose distance to the reference PS is 47 pixels. The RMS errors made by the collocation and filtering methods are 0.5 and 1.6 mm respectively. **b**) PS No. 130 whose distance to the reference PS is 90 pixels. The RMS errors made by the collocation and filtering methods are 1.1 and 1.8 mm respectively. **c**) PS No. 131 whose distance to the reference PS is 143 pixels. The RMS errors made by the collocation and filtering methods are 1.4 and 2.5 mm respectively. **d**) PS No. 141 whose distance to the reference PS is 122 pixels. The RMS errors made by the collocation and filtering methods are 1.6 and 2.3 mm respectively.

By comparing the pattern of the estimation error to the $10th$ slave APS shown in Fig. 5.20 we can conclude that the strong correlation is caused by the leakage of the APS in the $10th$ slave acquisition. The estimation error made by the collocation method is smaller and less correlated in time, i.e., less leakage. This is what we can expect because the collocation method takes the temporal variability of APS into account and weight the observations accordingly, see discussion in section 4.4. Note, if we use the full time series (12-day temporal resolution) instead of the 36-day time series the correlation between the estimation errors will be much lower. This is because there are more observations are involved in averaging APS.

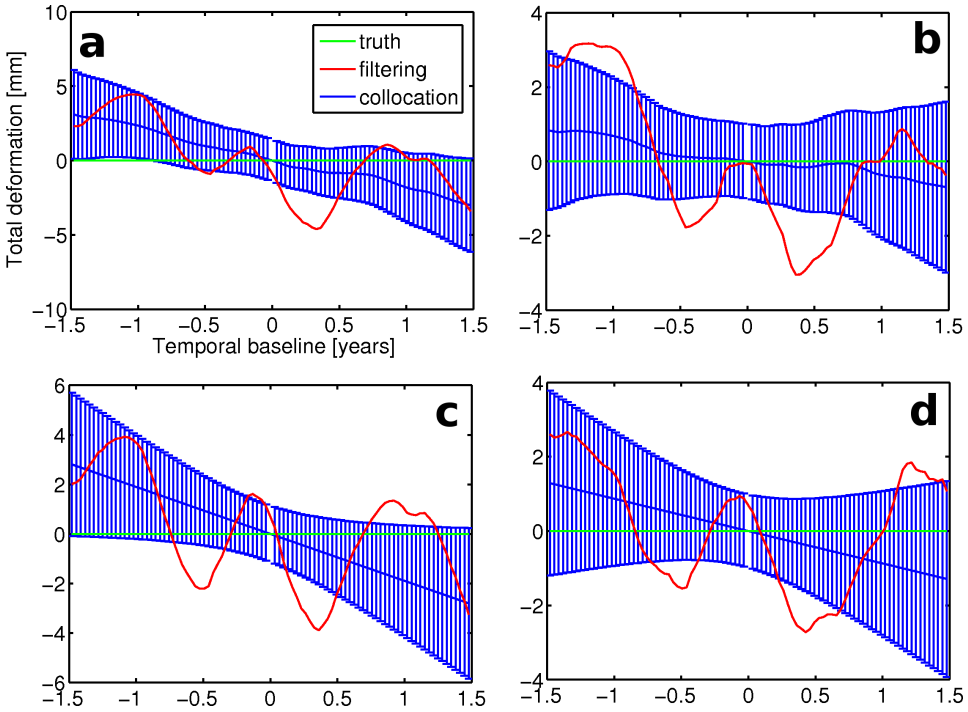

Fig. 5.18. Evaluation of the total deformation estimates for the PSs who are deformation free. The simulated ground deformation is shown in green, the estimate from the filtering method (1-year Gaussian window) is shown in red and the estimate from the collocation method is shown in blue with an estimated errorbar for each estimate in the time series. **a**) PS No. 159 whose distance to the reference PS is 114 pixels. The RMS errors made by the collocation and filtering methods are 1.8 and 2.5 mm respectively. **b**) PS No. 187 whose distance to the reference PS is 51 pixels. The RMS errors made by the collocation and filtering methods are 0.4 and 1.8 mm respectively. **c**) PS No. 200 whose distance to the reference PS is 115 pixels. The RMS errors made by the collocation and filtering methods are 1.6 and 2.2 mm respectively. **d**) PS No. 203 whose distance to the reference PS is 61 pixels. The RMS errors made by the collocation and filtering methods are 0.76 and 1.6 mm respectively.

5.3 Result validation: a-priori knowledge of deformation is unknown

In this section our goal is to investigate how good our collocation method will perform when a-priori knowledge of ground deformation is not known exactly. We have shown in section 5.2 that given the right assumptions (i.e., a-priori knowledge) about the ground deformation (i.e., deterministic and stochastic models) the collocation method always outperforms the standard filtering method. In the following investigation we will assess the sensitivity of the collocation method to the functional and stochastic model of deformation separately.

Table 5.2. An overview of the validation result when a-prior knowledge is available. The satellite repeat orbit is **12**-day. The column of *Correlation* is w.r.t. the ground truth (i.e., simulation). * is used to indicate that the value is an average over all slave APS. ** is used to indicate that the value is an average over the time series of all PSs. The value within the parentheses indicates the relative estimation error w.r.t. the original signal (simulation) in percentage. For the filtering method a Gaussian window with a 1-year length is used.

Variable	Mean error	RMS error	Correlation
Stochastic parameters			
Deformation RMS [mm]	-1.2	3.3	0.69
Deformation correlation length [year]	0.12	0.43	-
Deformation false alarm [mm]	2.3	2.6	-
APS RMS [mm]	0.0	1.2	0.95
APS correlation length [pixels]	10.1	28.8	0.59
APS smoothness (τ)	-0.1	0.33	-
Signals			
Deformation rate (collocation) [mm/year]	0.46	3.3	0.89
Deformation rate (filtering) [mm/year]	0.78	3.3	0.87
Master APS (collocation) [mm]	-0.28	1.9 (25%)	0.97
Master APS (filtering) [mm]	-0.6	4.5 (52%)	0.87
Slave APS (collocation) [mm]	-0.24*	2.1* (24%)	0.98*
Slave APS (filtering) [mm]	-0.5*	4.9* (40%)	0.84*
Total deformation (collocation) [mm]	-0.1**	3.1** (35%)	0.94**
Total deformation (filtering) [mm]	-0.1**	4.8** (55%)	0.84**

5.3.1 Sensitivity to the stochastic model

In this scenario we only change the stochastic model for modeling the stochastic ground deformation. We choose Gaussian and spheric models to evaluate the sensitivity. In section 5.1 we have demonstrated by simulations (see Fig. 5.3) that given identical model parameters Gaussian model leads to a very smooth random field whereas spheric model results in a rather rough random field. We summarize the validation results based on the original simulation (full time series with 12-day temporal resolution) in Tab. 5.4 where Gaussian model is used and in Tab. 5.5 where spheric model is used. In general, the results based on these two stochastic models are similar. More specifically, the result based on spheric model has more or less the same accuracy as the result obtained based on hole effect model (see Tab. 5.2) which is the model used for simulating the stochastic deformation. This might be explained by the similarity between the simulations generated from these models using the same model parameters (i.e., variance and correlation length), see Fig. 5.3. The Gaussian model based result is less accurate and this is most likely due to its smooth nature. Nevertheless, even a less appropriate stochastic model is used the collocation method still gives a more accurate result than the filtering method. We believe this is mainly because of the robustness of the stochastic modeling of APS (i.e., temporal and spatial variance-covariance estimations), Moreover, we find

Table 5.3. An overview of the validation result when a-prior knowledge is available. The satellite repeat orbit is **36**-day. The column of *Correlation* is w.r.t. the ground truth (i.e., simulation). * is used to indicate that the value is an average over all slave APS. ** is used to indicate that the value is an average over the time series of all PSs. The value within the parentheses indicates the relative estimation error w.r.t. the original signal (simulation) in percentage. For the filtering method a Gaussian window with a 1-year length is used.

Variable	Mean error	RMS error	Correlation
Stochastic parameters			
Deformation RMS [mm]	-1.3	4.0	0.68
Deformation correlation length [year]	0.08	0.71	-
Deformation false alarm [mm]	3.1	3.5	-
APS RMS [mm]	0.0	1.8	0.94
APS correlation length [pixels]	11.9	36.0	0.49
APS smoothness (τ)	-0.4	0.47	-
Signals			
Deformation rate (collocation) [mm/year]	0.43	3.7	0.87
Deformation rate (filtering) [mm/year]	1.4	3.7	0.85
Master APS (collocation) [mm]	0.4	2.5 (32%)	0.95
Master APS (filtering) [mm]	0.4	4.2 (52%)	0.90
Slave APS (collocation) [mm]	0.6*	2.9* (36%)	0.96*
Slave APS (filtering) [mm]	0.6*	5.4* (55%)	0.81*
Total deformation (collocation) [mm]	-0.37**	4.0** (44%)	0.90**
Total deformation (filtering) [mm]	-0.13**	5.6** (62%)	0.80**

that the collocation method is more sensitive to the temporal resolution of input data than the choice of the stochastic model for deformation. This can be seen by comparing the results in Tab. 5.4 and Tab. 5.5 with the result in Tab. 5.3.

5.3.2 Sensitivity to the functional model

In section 5.1 we simulate the deterministic deformation as a linear function of time (i.e., a constant deformation rate), see Eq. (5.1.1). To assess the sensitivity of our collocation method to the functional model we re-simulate the deterministic deformation using a quadratic model in time as:

$$d^i(T) = v_1^i T^2 + v_2^i T, \tag{5.3.1}$$

where v_1^i ($\in$ (1,10) mm) and v_2^i ($\in$ (2,20) mm) are the model parameters for the PS i. We apply the collocation method to the new simulation using the linear function in Eq. (5.1.1) for modeling the deterministic deformation. The validation result in listed in Tab. 5.6. From the table we find that the deformation correlation length is largely overestimated by approximately 5 months. In addition, the deformation RMS for the second category PSs who have stochastic deformation (see section 5.1) is also overestimated by 2.6 mm. Moreover, for PSs who do not have stochastic deformation (the first and third category PSs) the deformation false alarm (i.e., a

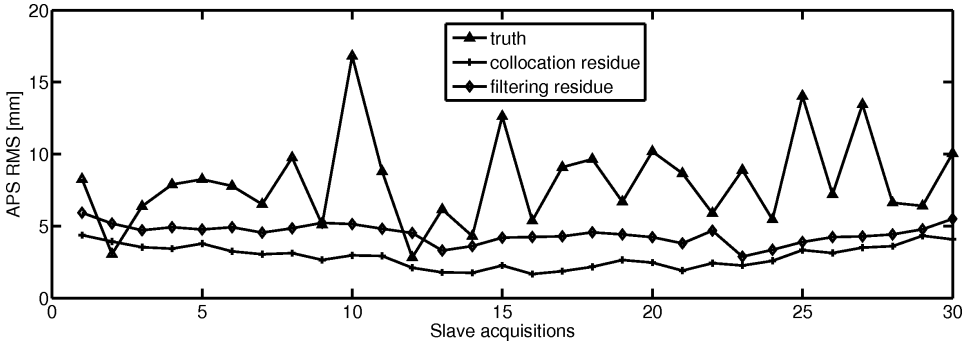

Fig. 5.19. Evaluation of the slave APS estimation for a time series with a 36-day temporal resolution. The RMS (unit: mm) of the estimation error made by the collocation method is shown in blue and the mean of the RMS is 2.9 mm. In contrast, the RMS of the estimation error made by the filtering method is shown in red and the mean of the RMS is 5.4 mm. The mean of the RMS of the simulated slave APS shown in green is 8.1 mm. For the filtering method a Gaussian window with a window length of 1-year is used.

non-zero deformation RMS) is doubled with respect to the corresponding value in Tab. 5.2. All these overestimation effects are caused by the inappropriate functional model (i.e., the linear model) used for modeling the deterministic deformation. More precisely, the difference (i.e., discrepancy) between the modeled linear deformation and the realistic quadratic deformation is identified by the collocation method as the stochastic deformation since this difference is strongly correlated in time just as the real (simulated) stochastic deformation. Moreover, regarding master APS estimation the filtering method results in a considerable bias but the collocation method does not. The bias is caused by the leakage of deformation. That is the difference between the modeled linear deformation and the realistic quadratic deformation is partly identified by the filtering method as the master APS which is a constant in time (i.e., perfectly correlated). Due to the leakage of deformation the accuracy of the total deformation estimation obtained by the filtering method is much worse than the accuracy achieved by the collocation method. In conclusion, the collocation method is more robust than the filtering method when the a-priori knowledge of the functional model for ground deformation is unknown. In such a case, the unmodeled deformation, i.e., difference between modeled deformation by the chosen functional model and real deformation, can be incorporated into the stochastic part of deformation by the collocation method and prevent it being leaked to master APS.

5.4 Summaries

In this chapter we have assessed the performance of the collocation method developed in chapter 4 using simulated InSAR time series. We find the collocation method is robust and always results in a better estimation of ground deformation and APS

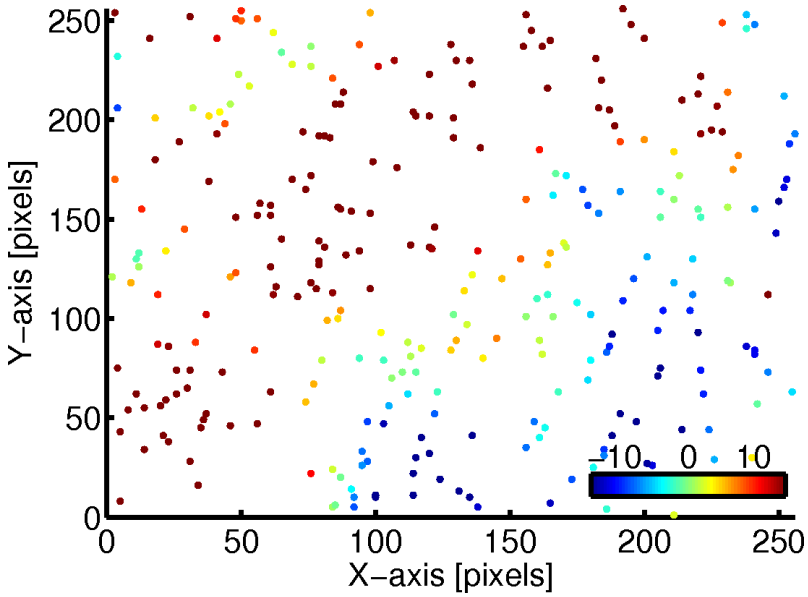

Fig. 5.20. Simulated (real) APS for the $10th$ slave acquisition. The simulated APS (unit: mm) has the largest delay RMS among all slave acquisitions, see Fig. 5.19.

compared to the standard window-based filtering method (see section 4.1). For ground deformation simulation, we divide the simulated PS (time series) into three categories. The first category consists of PSs whose deformation is simulated using a linear function of temporal baseline (see Eq. (5.1.1)), i.e., constant deformation rate. The deformation on the PSs from the second category is composed by a deterministic trend plus a stochastic variation. The deterministic trend is simulated using the linear function and the stochastic variation is simulated using a hole effect variance covariance model (see Eq. (5.1.3)). The PSs in the third category does not undertake any deformation. The APS per acquisition is simulated using Mátern variance-covariance model in Eq. (7.2.17). The variance of the simulated APS varies from one acquisition to another to account for the temporal variability of APS (see Fig. 5.2). Orbit errors are simulated as long-wavelength spatial trends and phase noise is simulated as white noise. Finally, the simulated signals are combined and double differenced (in time and in space) to form input data for the collocation method. The time span of the full time series is 3 years with a 12-day temporal resolution (i.e., repeat orbit).

The best result of the collocation method is achieved when a-priori knowledge of ground deformation (i.e., the functional and stochastic model used for simulating ground deformation) is given to the collocation method. In terms of the stochastic modeling of APS, the APS RMS estimation per acquisition is unbiased and the correlation between the estimate and ground truth is 0.95. The spatial correlation length of APS can also be estimated reasonably well but less satisfactorily with a

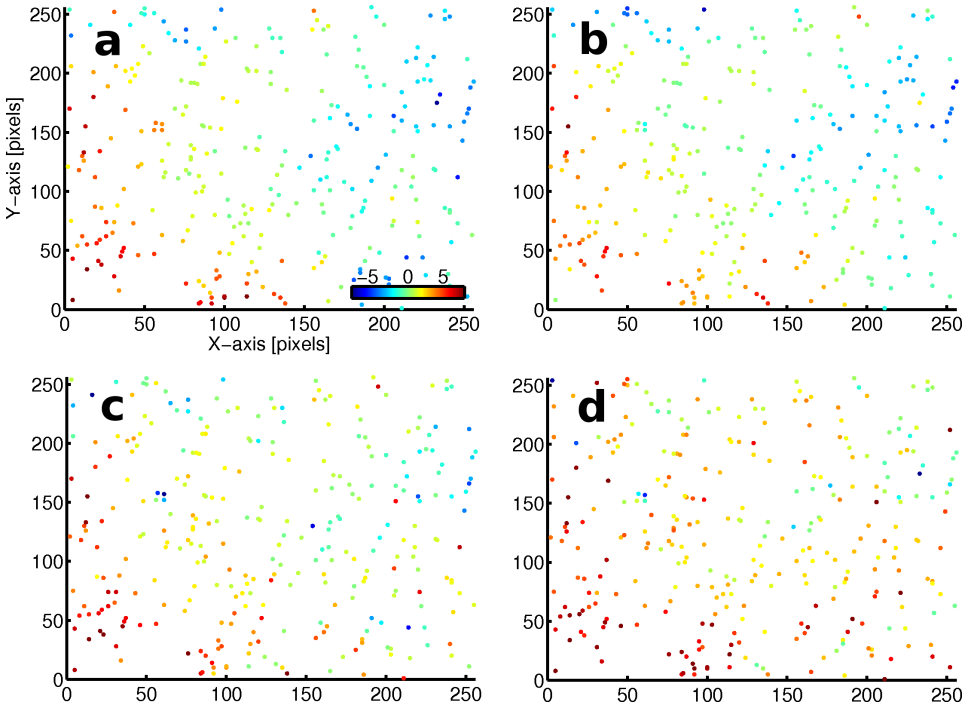

Fig. 5.21. Estimation error(unit: mm) of slave APS made by the collocation method. **a**) Estimation error for the $8th$ slave APS. **b**) Estimation error for the $9th$ slave APS. **c**) Estimation error for the $10th$ slave APS. **d**) Estimation error for the $11th$ slave APS. Note, the estimation errors, e.g., positive residues in the down-left of each subplot, have a noticeable correlation in time. This is caused by the leakage of APS in the $10th$ slave acquisition, see Fig. 5.20.

correlation of 0.59 with respect to the ground truth. In terms of the stochastic model of ground deformation, the estimate of ground deformation RMS (for the stochastic part) on the second category PSs is slightly biased by -1.2 mm and the correlation between the estimate and the ground truth is 0.69. It is more difficult to estimate the correlation length of deformation in time. Its estimate is either too small (i.e., close to the specified lower search boundary) or too large (i.e., close to the specified upper search boundary). Moreover, the collocation method may arise false alarm of ground deformation on PSs who do not have stochastic deformation by simulation. The probability of giving false alarm is high (91 out of 225 PSs) but the magnitude of the false alarm is relatively small, i.e., ranges from 0 to 5 mm with a mean of 2.3 mm. In terms of APS estimation, the collocation method can result in 75% delay reduction for master APS and 76% delay reduction on average for slave APS. In contrast, the delay reduction is 48% and 60% (on average) for master and slave APS respectively when the filtering method is used. In terms of ground deformation estimation, the estimate from the collocation method is strongly correlated with the

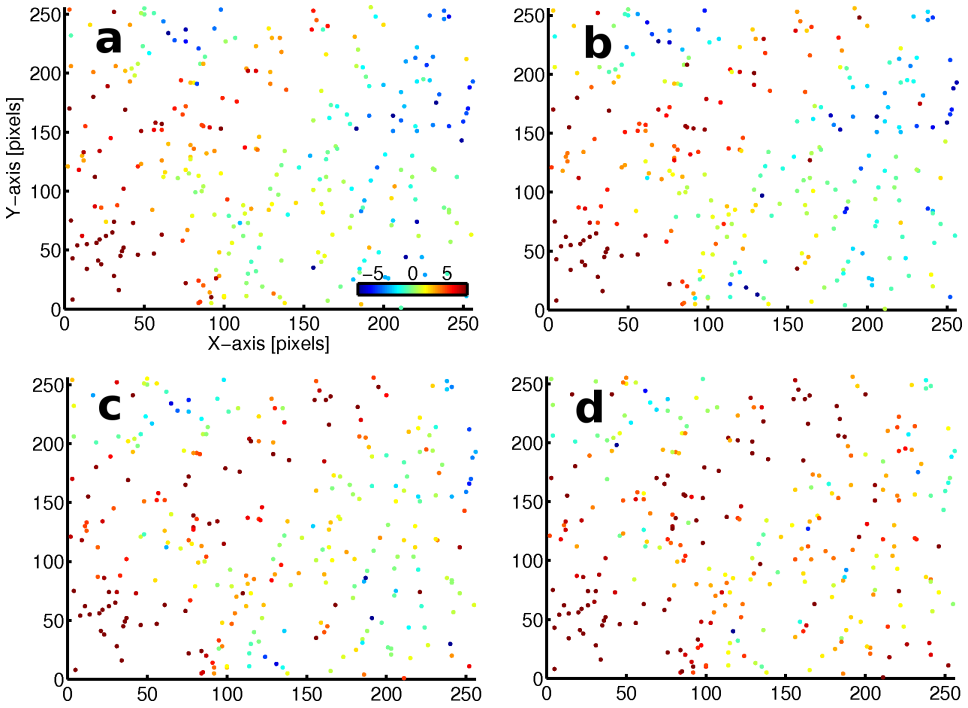

Fig. 5.22. Estimation error(unit: mm) of slave APS made by the filtering method. **a)** Estimation error for the $8th$ slave APS. **b)** Estimation error for the $9th$ slave APS. **c)** Estimation error for the $10th$ slave APS. **d)** Estimation error for the $11th$ slave APS. Note, comparing to the estimation errors shown in Fig. 5.21, the estimation errors made by the filtering method is larger and more correlated in time. This is because the filtering method does not take the temporal variability of APS into account and equally weight APS for all acquisitions, see discussion in section 4.4.

ground truth (0.94). In contrast the correlation between the estimate of filtering and the ground truth is 0.84. Moreover, the estimated ground deformation time series by the filtering method always present an artificial seasonal pattern with a period of approximately 0.5 year (see Figs. 5.17 and 5.18). The artificial pattern is caused by leakage of APS to deformation.

We have also evaluated the performance of the collocation method when a-priori knowledge of deformation is unknown. In one scenario, we assign an imperfect stochastic model (i.e., Gaussian or Spheric) to the collocation method. We find that the stochastic modeling of deformation and APS is almost unaffected and the final APS and deformation estimation become slightly less accurate when Gaussian model is used. We believe the degrade of estimation accuracy has something to do with the smooth nature of Gaussian model. Even when Gaussian model is used the collocation method still outperforms the filtering method in all aspects. In a second scenario, we re-simulate the deterministic ground deformation using a quadratic

Table 5.4. An overview of the validation result when a-prior knowledge of stochastic deformation (i.e., hole effect model) is unknown. **Gaussian** model is used to model the stochastic deformation. The satellite repeat orbit is **12**-day. The column of *Correlation* is w.r.t. the ground truth (i.e., simulation). * is used to indicate that the value is an average over all slave APS. ** is used to indicate that the value is an average over the time series of all PSs. The value within the parentheses indicates the relative estimation error w.r.t. the original signal (simulation) in percentage. For the filtering method a Gaussian window with a 1-year length is used.

Variable	Mean error	RMS error	Correlation
Stochastic parameters			
Deformation RMS [mm]	1.0	4.3	0.7
Deformation correlation length [year]	0.26	0.31	-
Deformation false alarm [mm]	3.2	3.6	-
APS RMS [mm]	0.1	1.3	0.95
APS correlation length [pixels]	8.7	24.6	0.62
APS smoothness (τ)	-0.1	0.36	-
Signals			
Deformation rate (collocation) [mm/year]	0.25	3.3	0.89
Deformation rate (filtering) [mm/year]	0.78	3.6	0.87
Master APS (collocation) [mm]	0.0	2.1 (28%)	0.96
Master APS (filtering) [mm]	-0.6	4.5 (52%)	0.87
Slave APS (collocation) [mm]	-0.20*	2.2* (26%)	0.97*
Slave APS (filtering) [mm]	-0.5*	4.9* (40%)	0.84*
Total deformation (collocation) [mm]	0.2 **	3.4** (39%)	0.92**
Total deformation (filtering) [mm]	-0.1**	4.8** (55%)	0.84**

model (see Eq. (5.3.1)) in time. We find that the master APS estimation obtained by the filtering method is very sensitive to the imperfection in the functional model and an estimation bias of 3.4 mm is observed. On the contrary, the result from the collocation method is not affected by the imperfection. This is because the temporally correlated unmodeled deterministic deformation (i.e., difference between the modeled deformation by the linear model and the real quadratic deformation) is incorporated into the stochastic deformation and modeled stochastically by the collocation method. In this sense, we conclude that the collocation method is more robust in practice when a-priori knowledge of deformation is unknown.

Finally, we find the most influencing factor for separating ground deformation and APS is the temporal resolution of the input data, i.e., satellite revisit frequency. Obviously, given the same a-priori knowledge about ground deformation, the dataset with lower temporal resolution leads to a less accurate result. It has been demonstrated by simulated time series with a 36-day temporal resolution spanning 3 years (see Tab. 5.3). Moreover, in terms of slave APS estimation we find its estimation error is noticeably correlated in time. The estimation error made by the filtering method can be large and strongly correlated (see Figs. 5.21 and 5.22). This usually happens in the neighborhood of an acquisition which has a relatively large APS

Table 5.5. An overview of the validation result when a-prior knowledge of stochastic deformation (i.e., hole effect model) is unknown. **Spheric** model is used to model the stochastic deformation. The satellite repeat orbit is **12**-day. The column of *Correlation* is w.r.t. the ground truth (i.e., simulation). * is used to indicate that the value is an average over all slave APS. ** is used to indicate that the value is an average over the time series of all PSs. The value within the parentheses indicates the relative estimation error w.r.t. the original signal (simulation) in percentage. For the filtering method a Gaussian window with a 1-year length is used.

Variable	Mean error	RMS error	Correlation
Stochastic parameters			
Deformation RMS [mm]	-0.9	3.2	0.72
Deformation correlation length [year]	0.17	0.35	-
Deformation false alarm [mm]	2.4	2.6	-
APS RMS [mm]	0.0	1.2	0.95
APS correlation length [pixels]	10.4	29.0	0.57
APS smoothness (τ)	-0.1	0.33	-
Signals			
Deformation rate (collocation) [mm/year]	0.45	3.3	0.88
Deformation rate (filtering) [mm/year]	0.78	3.6	0.87
Master APS (collocation) [mm]	-0.27	1.9 (25%)	0.97
Master APS (filtering) [mm]	-0.6	4.5 (52%)	0.87
Slave APS (collocation) [mm]	-0.24*	2.1* (24%)	0.98*
Slave APS (filtering) [mm]	-0.5*	4.9* (40%)	0.84*
Total deformation (collocation) [mm]	-0.1 **	3.1** (36%)	0.93**
Total deformation (filtering) [mm]	-0.1**	4.8** (55%)	0.84**

RMS, i.e., an acquisition taken during an extreme weather.

In next chapter we are going to assess the collocation and filtering methods using real interferograms over both flat and mountainous regions.

Table 5.6. An overview of the validation result when a-prior knowledge of the deterministic deformation (i.e., quadratic model, see Eq. (5.3.1)) is unknown. The **linear** model in Eq.(5.1.1) is used to model the deterministic deformation. The satellite repeat orbit is **12**-day. The values in the *Correlation* column is w.r.t. the ground truth (i.e., simulation). * is used to indicate that the value is an average over the time series of all slave APS. ** is used to indicate that the value is an average over all PSs. The value within the parentheses indicates the relative estimation error w.r.t. the original signal (simulation) in percentage. For the filtering method a Gaussian window with a 1-year length is used.

Variable	Mean error	RMS error	Correlation
Stochastic parameters			
Deformation RMS [mm]	2.6	3.1	0.68
Deformation correlation length [year]	0.4	0.28	-
Deformation false alarm [mm]	5.4	6.1	-
APS RMS [mm]	0.1	1.3	0.94
APS correlation length [pixels]	6.9	23.0	0.55
APS smoothness (τ)	-0.1	0.34	-
Signals			
Deformation rate (collocation) [mm/year]	-	-	-
Deformation rate (filtering) [mm/year]	-	-	-
Master APS (collocation) [mm]	0.1	2.0 (26%)	0.97
Master APS (filtering) [mm]	3.4	6.7 (57%)	0.78
Slave APS (collocation) [mm]	-0.16*	2.3* (27%)	0.97*
Slave APS (filtering) [mm]	-0.6*	5.0* (41%)	0.83*
Total deformation (collocation) [mm]	0.25 **	3.4** (31%)	0.95**
Total deformation (filtering) [mm]	4.2**	6.5** (59%)	0.80**

Chapter 6

Application of the least-squares collocation method to PSInSAR

In this chapter we assess the developed collocation method using real InSAR time series. To make the assessment generally acceptable we choose four areas, i.e., Dubai, Mexico City, the Netherlands and Hawaii, belonging to different climatic regions. Among them Hawaii has the most significant topography variation which often leads to a strong vertical stratification effect in atmospheric phase screen (APS). Water vapor variation in Dubai is significant, which is driven by the large air humidity. Moreover, significant acquisitions gaps are presented in the ASAR time series which is used for PS analysis. In Mexico city, large deformation rate (¿ 40 cm/year) is observed and non-linear deformation in some regions is expected. For assessing the APS estimates of the collocation method we compare the estimates with cloud-free MERIS measurements (if available), short temporal baseline interferograms and the APS estimates obtained from the standard filtering method (see section 4.1 and Ferretti et al. (2000)).

Since we do not have ground truth of deformation in these areas we attempt to evaluate the estimated ground deformation internally by comparing the results of the collocation and filtering methods. In principle, a better APS estimation will lead to a better separation of deformation and APS. Based on the evaluation of the APS estimates from the two methods we are able to identify the leakage from APS to deformation or the other way around in one of the methods or both. The chapter is organized as fellow. InSAR data pre-processing prior to the application of the collocation method is elaborated in section 6.1 . Each section between 6.2 to 6.5 is dedicated for one case study for one of the chosen areas. Summaries and conclusions are given in section 6.6.

6.1 Pre-processing

In this section we provide the details of data pre-processing including single-master interferogram formation, PS selection, PS network construction and phase unwrapping. All these steps are necessary to provide input data (i.e., unwrapped phase) for the least-squares collocation method elaborated in Chapter 4. The software

used for the pre-processing are: *Doris* (Delft Object-oriented Radar Interferometric Software) (Kampes and Usai, 1999), *DePSI* (Delft PSI) (Kampes, 2005; Ketelaar, 2008; Samiei-Esfahany, 2008) and *StaMPS* (Stanford Method for Persistent Scatterers) (Hooper, 2006).

6.1.1 Single master interferogram formation

Given $K+1$ SLC (Single Look Complex) images, K interferograms are formed with respect to a common SLC image called master (denoted as m). Usually, the master image is selected such that the dispersion of the perpendicular baselines is minimum, see Colesanti et al. (2003). In *DePSI*, the master image is selected by maximizing the expected stack coherence of the interferometric stack. The stack coherence is defined as (Kampes, 2005):

$$\gamma^m = \frac{1}{K}\sum_{k=0}^{K} g(B_\perp^{k,m}, B_\perp^{\max}) \times g(T^{k,m}, T_{\max}) \times g(f_{dc}^{k,m}, f_{\mathrm{dc}}^{\max}), \tag{6.1.1}$$

where

$$g(x,c) = \begin{cases} 1-|x|/c & \text{if} |x| < c, \\ 0 & \text{otherwise}, \end{cases} \tag{6.1.2}$$

and $B_\perp^{k,m}$ is the perpendicular baseline between images m and k at the center of the image, $T^{k,m}$ is the temporal baseline and $f_{\mathrm{dc}}^{k,m}$ is the Doppler baseline (the mean Doppler centroid frequency difference). In this study we use 1500 meters, 15 years and1380 Hz for $B_\perp^{\max}$, $T_{\max}$ and $f_{\mathrm{dc}}^{\max}$ respectively.

In the time domain an interferogram is formed by dot-multiplication of corresponding phases (pixel-wise) in master and slave after resampling the slave to the master geometry. The dot-multiplication is equivalent to a convolution in frequency domain, consequently, after the convolution the bandwidth of the interferogram is larger than the bandwidth of any of the SLCs. To avoid an aliasing effect caused by the increased bandwidth in combination with constant sampling frequency, all slave images are oversampled by a factor of two in both range and azimuth. Here, we need to stress that the oversampling does not improve the image spatial resolution because the image bandwidth is not increased by the oversampling. After oversampling, slave images are co-registered and resampled with respect to the master geometry. In rural areas and for interferograms having large temporal and perpendicular baselines, the co-registration step could be difficult due to significant signal decorrelation (Zebker and Villasenor, 1992; Gatelli et al., 1994). The difficulty can be relieved by distributing the co-registration windows around bright pixels (i.e., local amplitude maxima which are likely corresponding with terrain features that are stable in time) in master. Alternatively Hooper et al. (2007) develop an amplitude based algorithm which coregistrates image pairs having good correlation. Usually these image pairs have different masters with short temporal and perpendicular baselines. Moreover, for high resolution SAR images (e.g., TerraSAR-X) acquired over mountainous regions the co- registration becomes more difficult due to large topography variations. In such cases, a DEM assisted co-registration algorithm can

be applied, see Arikan et al. (2008); Nitti et al. (2011). After co- registration, slave images are resampled with respect to the master image geometry.

Next, interferograms are formed between the master and resampled slaves. We do not apply any spectral or phase filtering before generating the interferograms since these operations will shorten the measurable bandwidths of point targets. Afterwards, a so-called "flat earth" phase that is introduced by the WGS84 reference surface is computed and removed using ESA's precise satellite orbits (Scharroo and Visser, 1998). The precise orbit is also used during the co-registration step to approximately compute the offsets between master and slave geometries. Finally, the phase contribution due to local land topography is modeled and subtracted using SRTM (Shuttle Radar Topography Mission) DEM (Farr et al., 1999; Rao and Phalke, 2001; Rosen et al., 2001) which is available for the earth surface between $-57°$ and $60°$ with a 3 arc second lateral resolution. However, it has been pointed out by Colesanti et al. (2003) that it is not absolutely necessary to remove the topographic phase during the formation of interferograms. Alternatively, its removal can be carried out in the PS analysis. Nevertheless, in our data processing we perform the topography phase removal using SRTM and in our PS analysis we still model the topography contribution that actually accounts for the inaccuracy of SRTM. The processing chain for single master interferograms formation is sketched in Fig. 6.1.

6.1.2 Time series analysis using DePSI

Identification of PS candidates

Due to phase decorrelation not every pixel in an interferogram is useful for a time series analysis. Only pixels that contain point-like targets are useful and these targets often correspond to man-made objects. The selection of such pixels based on their phases is prevented by the wrapped nature of the interferometric phase. Instead, the selection is often carried out by analyzing the amplitude of each pixel. Ferretti et al. (2001) use a so-called *amplitude dispersion index* D_a as a criteria for selecting the useful pixels. D_a is defined as:

$$D_a = \frac{\sigma_a}{\bar{a}}, \tag{6.1.3}$$

where σ_a is the temporal standard deviation of the amplitude and $\bar{a}$ is the temporal mean of the amplitude for a certain pixel. Ferretti et al. (2001) show that for a constant signal and high signal to noise ratio (SNR), D_a is a good approximation of the phase standard deviation σ_ϕ, i.e., $D_a \approx \sigma_\phi$. Pixels which have a low D_a (e.g., $D_a < 0.4$) is identified as a potential Persistent Scatterer. In urban areas using $D_a = 0.4$ will typically result in a large number of pixels being identified as potential PS ($\gg$ 3 PSC/km^2). Such a high density of PS is usually not needed for APS estimation at a later stage but imposes a huge burden on numerical computations. Usually a PS density of 3 PS/km^2 is sufficient (Colesanti et al., 2003) for estimating APS. To keep a sufficient PS density, two groups of potential PSs are selected in *DePSI*. The first group consists of potential PSs which have an amplitude dispersion index less than a threshold of ~ 0.25. The potential PSs in the second group typically have a threshold larger than 0.25 but smaller than 0.4. Given a sufficient number of

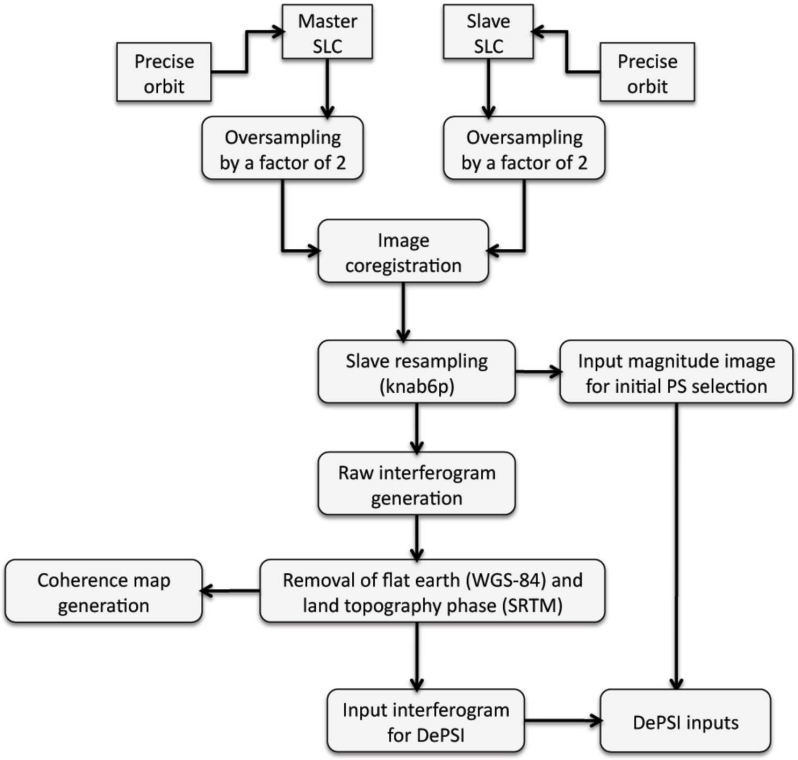

Fig. 6.1. Flow diagram for an interferogram generation using *Doris*.

SAR images (e.g., > 30), the amplitude dispersion based selection is very successful in identifying potential PSs in urban areas (Ferretti et al., 2001). However, in rural areas and when the number of available SAR images is small (e.g., < 20) the density of the PS selected by the method is often too small to allow for a reliable phase unwrapping (Hooper, 2006; Hooper et al., 2007). In such cases, the PS selection approach introduced by Hooper (2006) based on the pixel spatial coherence is preferred. Nevertheless, in our data processing we use the amplitude dispersion based method since the number of available images is more than sufficient and the areas of interest are mainly urban areas. Here we need to stress that prior to the computation of D_a all SLC images need to be calibrated in terms of their amplitudes. The reason for the calibration is to avoid amplitude variations due to sensor characteristics and viewing geometry. Different calibration methods can be found in Laur et al. (2002); Cassee (2004); Ketelaar (2008).

Network construction based on PS

Based on the selected PS which have a low amplitude dispersion index (e.g., < 0.25) a spatial network connecting all the PS can be formed for each interferogram. The formed network is referred to as the first-order network in *DePSI*. The arc (i.e., line

connecting two PS points) length of the network is restricted to a certain maximum to minimize the influences from atmosphere, orbit uncertainty, etc. A redundant network is preferred since it will provide redundant observations (i.e., phase difference between an arc) for error detection in the phase unwrapping step. Commonly used approaches for network construction include Delaunay triangulation and spider networks, see Kampes (2005); Ketelaar (2008).

Phase unwrapping

After forming the first-order networks, the phase unwrapping is carried out in time per arc. In *DePSI* the temporal unwrapping for each arc time series is regarded as an estimation problem whose observation equations can be for example written as:

$$E\{\begin{bmatrix}\underline{\phi}^1\\ \underline{\phi}^2\\ \vdots\\ \underline{\phi}^K\end{bmatrix}\} = \begin{bmatrix}-2\pi & & & \\ & -2\pi & & \\ & & \ddots & \\ & & & -2\pi\end{bmatrix}\begin{bmatrix}a^1\\ a^2\\ \vdots\\ a^K\end{bmatrix} + \begin{bmatrix}\beta_x^1 & B^T(1) & 1\\ \beta_x^2 & B^T(2) & 1\\ \cdots & \cdots & \cdots\\ \beta_x^K & B^T(K) & 1\end{bmatrix}\begin{bmatrix}\Delta h\\ v\\ \phi_{\text{aps}}^m\end{bmatrix}, \tag{6.1.4}$$

where the K by 1 vector on the left side of equation contains the time series of the wrapped phase of an arc, a^k is the unknown integer phase ambiguity for interferogram k, β_x^k is the height to phase convector (see Eq. (4.3.3)), B^T is an K by 1 vector that contains the temporal baseline of interferograms, Δh is the uncertainty of DEM (SRTM in our case), v is the unknown deformation rate (linear deformation model) and ϕ_{aps}^m is the unknown phase due to master APS.

Obviously Eq. (6.1.4) is undetermined (i.e., the number of unknowns is larger than the number of observations). Therefore, additional constraints have to be added in order to achieve a unique solution. As addressed by Hanssen et al. (2001); Bianchi (2003) the constrained observation equation can be written as:

$$E\{\begin{bmatrix}\underline{y}_1\\ \underline{y}_2\end{bmatrix}\} = \begin{bmatrix}A_1\\ A_2\end{bmatrix}a + \begin{bmatrix}B_1\\ B_2\end{bmatrix}b, \tag{6.1.5}$$

with

$$D\{\begin{bmatrix}\underline{y}_1\\ \underline{y}_2\end{bmatrix}\} = \begin{bmatrix}Q_{y_1} & \\ & Q_{y_2}\end{bmatrix}, \tag{6.1.6}$$

where $\underline{y}_1$, A_1 and B_1 are defined by Eq. (6.1.4), A_2 is a 3 by K zero matrix , B_2 is a 3 by 3 identity matrix and $\underline{y}_2$ is a 3 by 1 zero vector. Operator D{.} denotes the dispersion of the observations. There are various algorithms to solve Eq. (6.1.5), such as ambiguity function (Counselman and Gourevitch, 1981; Ferretti et al., 2001), integer bootstrapping (Teunissen, 2001; Kampes and Hanssen, 2004) and integer least-squares (Teunissen, 2001; Kampes and Hanssen, 2004). In our data processing the integer bootstrapping is used as the default algorithm. The advantages of which over the other algorithms are: 1. the stochastic properties of the observations are taken into account; 2. it is computationally efficient and the computation load does not increase with the increase of parameters added to Eq. (6.1.4).

After estimation of the unknown parameters in Eq. 6.1.4 per arc, a spatial phase unwrapping is carried out for all arcs per interferogram. The spatial phase differ-

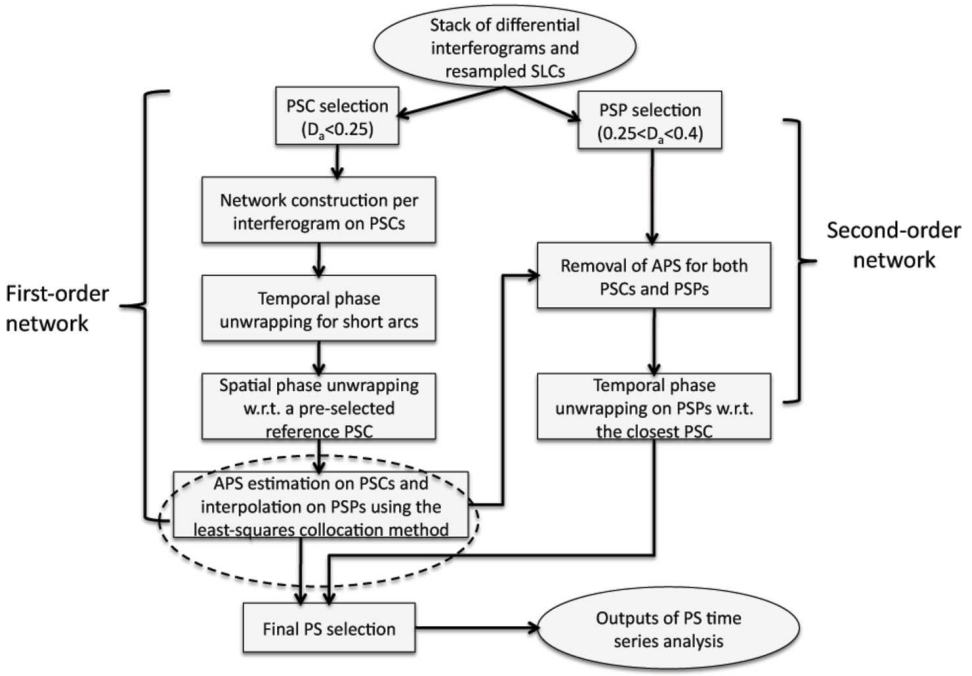

Fig. 6.2. Flow diagram for PSI analysis using *DePSI*. The contribution of the developed least-squares collocation method to *DePSI* is highlighted by the dashed ellipse. Note, in this diagram we use PSC (PS candidate) to refer to the PS which has a lower amplitude dispersion index and belongs to the first-order PS network. The PS which has a higher amplitude dispersion index and belongs to the second-order PS network is referred to as PSP (PS potential).

ence per arc is integrated to the phase difference with respect to a common PS, i.e., the fixed reference PS. Because the spatial network formed by the arcs is redundant, thus during the integration step possible temporal unwrapping errors (due to mis-identified PSC or imperfection of the deformation model) can be checked and rejected by following a DIA (Detection, Identification and Adaptation) procedure, see Baarda (1968); Teunissen (2000b). In this sense, the spatial phase unwrapping is actually equivalent to a free network adjustment in Geodesy such as leveling network adjustment. Note, the spatial unwrapping can be time-consuming when the success rate of the temporal unwrapping is low, which could be caused by the quality of the selected potential PS. This is another advantage to choose PS with very low amplitude dispersion ($D_a < 0.25$) during the PS identification step. Moreover, it has been pointed out by Ketelaar (2008) that the choice of the reference PS of the network is arbitrary because the relative accuracy of the phase difference between two arbitrary PS is independent of the choice. However, to apply the collocation method the reference PS has to be stable and does not suffer from any ground deformation, see Chapter 4 for the discussion.

APS estimation and interpolation

The APS estimation in *DePSI* starts with the phase residue (unwrapped) which reads:

$$\begin{aligned}\underline{\Phi}^{\mathrm{res}} &= \underline{\Phi}^{\mathrm{unwrap}} - \Phi^{\mathrm{defo}} - \Phi^{\mathrm{dem}} - \Phi^{m}_{\mathrm{aps}} \\ &= \underline{y} - B_1\underline{\hat{b}},\end{aligned} \tag{6.1.7}$$

where $\underline{\Phi}^{\mathrm{unwrap}}$ (also $\underline{y}$) is the unwrapped phase with respect to the reference PS, Φ^{defo} is the modeled (functional model) deformation phase, Φ^{dem} is the phase caused by DEM inaccuracy and Φ^{m}_{aps} is the master APS. B_1 and b are defined in Eq.(6.1.4) in case of a linear deformation model.

Before the collocation method being developed, the parameter vector b is estimated by a weighted least-squares:

$$\underline{\hat{b}} = (B_1^T W_y B_1)^{-1} B_1^T W_y^{-1} \underline{y}, \tag{6.1.8}$$

where the weight matrix W is the inverse of the variance-covariance matrix of the phase noise Q_{noise}. It is a diagonal matrix (i.e., the phase noise is uncorrelated in time) and is estimated before phase unwrapping from the first-order network formed by PS, see Kampes (2005). In the collocation method b is estimated using the best linear unbiased estimator (BLUE), which uses Q_y^{-1} as the weight matrix, see Chapter 4. The details for the APS estimation and interpolation using the standard filtering method and the collocation method are given in Chapter 4.

Phase unwrapping for the PS in the second-order network

As mentioned previously, a group of pixels which have D_a ranges between 0.25 and 0.4 are also identified as PS. The interpolated APS at these pixels are removed and the same temporal phase unwrapping discussed before is carried out. Afterwards, a spatial unwrapping (integration) is carried out with respect to its closest PS which has D_a less than 0.25. Finally, a selection of final PS is made based on a so-called temporal ensemble coherence (Ferretti et al., 2001) or a so-called a-posteriori variance factor (Kampes, 2005). For each PS, the topography height inaccuracy (height residue), ground deformation and APS are obtained with respect to the pre-selected reference PS. The diagram of the time series analysis using *DePSI* is given in Fig. 6.2.

6.2 Dubai

In chapter 4 we review the filtering method and introduce the collocation method. By comparing the two methods we find that there is a strong connection between the two, i.e., the filtering method is a special realization of the collocation method under certain circumstances (see discussion in section 4.4). One of the circumstances is when ground deformation is negligible. In such case, the variance-covariance matrix of the deformation is a null matrix. As a result, the two methods will give comparable results for deterministic variables such as deformation rate, DEM uncertainty and master APS which are constants in time (in the filtering method, the estimation

of the deterministic variables is done by weighted least-squares, see Eq. (6.1.8)). Nevertheless, the advantage of the collocation method is that it not only provides the estimates of the variables but also gives the expected precisions of the estimates. The filtering method however cannot provide a similar quality assessment.

On the other hand, with regards to slave APS estimation, the two methods will in general lead to different results. The difference will be relatively large for acquisitions taken under extreme weather (e.g., thunderstorm) and when there are acquisition gaps in the time series. This is because the filtering method does not take into account the varying magnitude of APS per acquisition and weight all acquisitions equally. As a result, the temporal averaging in the filtering method cannot sufficiently average out APS in the time series, see discussions in section 4.4. Therefore, the APS estimates from the filtering method will be biased, which results in part of the APS being identified as non-linear deformation. This is the case for Dubai city where the ground deformation is negligible and there are significant acquisition gaps in the ASAR time series and extreme weather in summer is not rare.

6.2.1 Test sites and data

Dubai city has several desirable aspects to select it as the first test site for evaluating the collocation method as presented in chapter 4. Firstly, it is a large and modern city with lots of man-made infrastructure, which provides a high quality pool of PS. Secondly, it has a humid atmosphere especially in summer (between June and September) due to sea water evaporation. The recorded maximum and minimum temperature is 41° C in August and 14.3° C in January respectively between 1984 and 2009 (Dubai Meteorological Office, 2011). The combination of high temperature and high humidity in summer can make atmospheric conditions extremely unstable. In addition, the annual precipitation over the city is less than 100 mm and most rainfall takes place in winter (Dubai Meteorological Office, 2011). Thirdly, because of the local climate cloud-free MERIS water vapor measurements over the city are often available from seasons other than winter. These measurements provide us the opportunity to cross validate the APS estimate per acquisition from the collocation method.

The test site is centered at 25°15′ northern latitude and 55°20′ eastern longitude with a spatial extent of 35 km in azimuth and 30 km in range, see Fig. 6.3. The available SAR acquisitions for the test site are from Envisat track 435 and frame 3105 in descending orbit. In total 31 ASAR (advanced SAR) images between 20-Mar-2003 and 9-Oct-2008 are available to this case study. The master image is selected as the image acquired on 3-May-2007. The baseline plot is given in Fig. 6.4. The minimum and maximum perpendicular baseline is 24 and 1041 m respectively and the largest temporal baseline is 4.1 years. Unfortunately, the ASAR acquisitions are not continuous in time, which causes significant acquisition gaps (maximum 1.5 years) in the full time series, see Fig. 6.4. Moreover, the difference in Doppler centroid between the ASAR images is under good control and does not cause any image rejection during the pre-processing step due to large shift in Doppler centroid.

Even though the urban area of Dubai is flat with a maximum terrain height difference

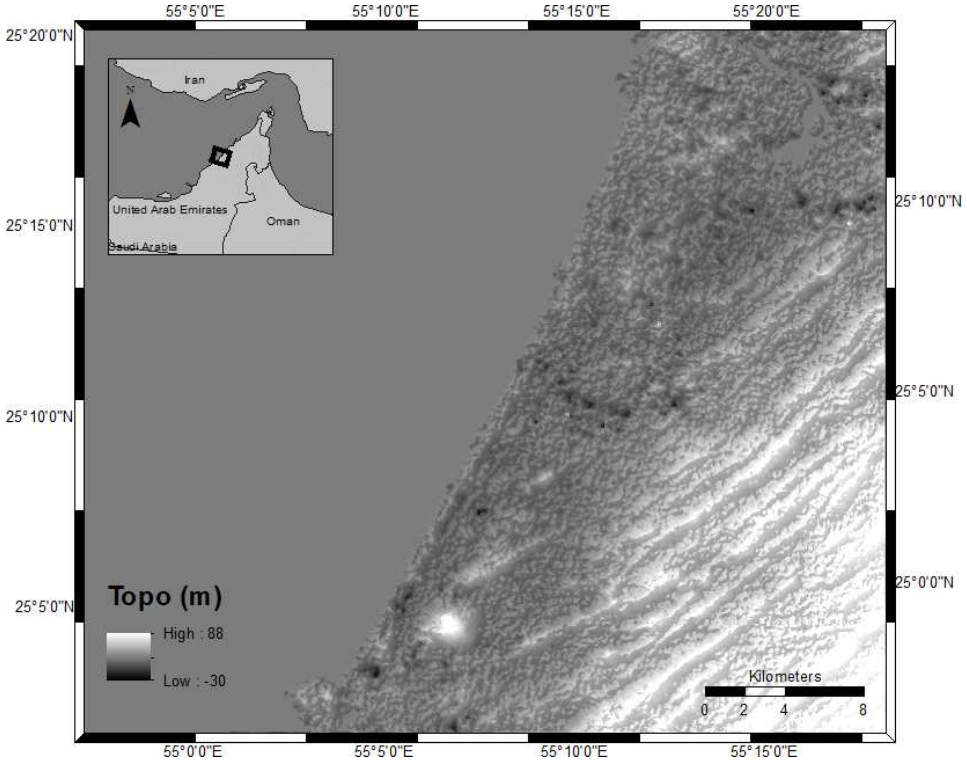

Fig. 6.3. Land topography of Dubai covered by ASAR acquisitions (track: 435, frame: 3105) with a spatial extent of 30 by 35 km.

less than 100 m (see Fig. 6.3), we remove the topography phase contribution using SRTM. For the initial selection of PS we set the threshold for amplitude dispersion index to 0.22 to keep a balance between the quality and the spatial density of PS. There are 1283 PS selected in total. For the spatial network (the first-order) formed by the PS the allowed maximum arc length is 3 km to suppress APS contribution to the double difference phase per arc. After spatial phase unwrapping (i.e., arc integration), the phase per PS is the phase difference between the PS and the pre-selected reference PS. By default *DePSI* chooses the PS which has the smallest a-posteriori variance factor (see Kampes (2005)) as the reference PS.

6.2.2 Time series analysis using LSC

The whole procedure for modeling different phase components is sketched in Fig. 4.2 in chapter 4. Firstly, we need to decide which functional and stochastic models that should be used to model ground deformation. Since we do not have any a-priori knowledge about the area regarding possible ground deformation, we therefore use a linear model with a constant deformation rate to model the deterministic deformation. For deformation that is not modeled by the linear model, we assume

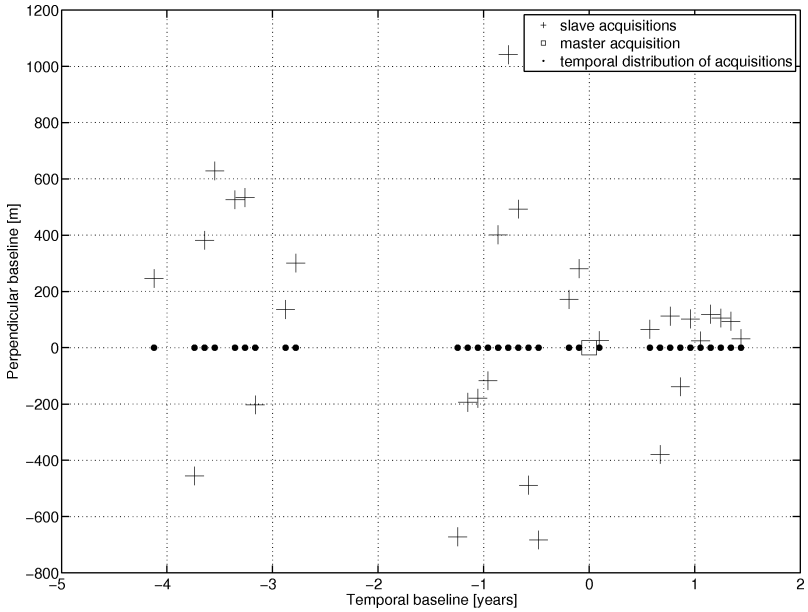

Fig. 6.4. Baseline plot for 31 ASAR acquisitions over Dubai from track 435 frame 3105. The master acquisition on 3-May-2007 is marked as a square. The maximum acquisition gap from the time series is 560 days.

that it is temporally stationary and model it stochastically via a variance-covariance model. As discussed in section 5.1.2 (see Fig. 5.3) the spherical and exponential models represent very similar stochastic processes and the Mátern model has one extra unknown parameter which reduces the redundancy in the model parameter estimation, therefore we decide to choose spherical and Gaussian models to model the stochastic deformation.

For APS, we model it per acquisition as a long wavelength surface trend plus a spatial variation due to water vapor. The former is modeled deterministically and the latter is modeled stochastically using the Mátern model, see the discussion in section 4.3.2. The height dependent delay, i.e., the vertical stratification, is not applicable for the test site which has a flat terrain. The orbit error per acquisition is modeled together with the atmospheric long wavelength surface trend. Moreover, the DEM inaccuracy of SRTM and the master APS are modeled as deterministic variables.

After selecting the functional and stochastic models for ground deformation, the estimation of the parameters of the stochastic models is carried out using the restricted maximum likelihood estimator (RMLE), see section 4.2.2. There are at least two difficulties in the parameter estimation. One is that it is difficult to validate the estimated parameters since the validation usually requires the entire distributions (i.e., probability density function) of the stochastic variables to be known. The other difficulty is due to the unknown phase quality of the selected PS. Some PS may turn

Table 6.1. Used constraints for minimizing the objective function of the restricted maximum likelihood estimator (RMLE) in Eq. (4.2.11). The constraints are the possible ranges (in physics or by assumptions) of the (variance-covariance) model parameters.

Parameter	Search boundary
APS RMS [mm]	(0,+∞)
Deformation RMS [mm]	(0,+∞)
APS correlation length [km]	(0,150)
Deformation correlation length [year]	(0.5,1.2)
APS spatial smoothness (τ)	(2/3,5/3)

out to be incoherent and carry large phase noise which can result in an unrealistic estimation of the model parameters. Therefore, we decide to use constraints in the estimation. The constraints are the feasible physical ranges of the model parameters. We list the constraint for each model parameter in Tab. 6.1. The upper boundaries of the APS RMS and stochastic deformation RMS are set to infinity because we do not know how turbulent the local atmosphere could be and whether or not the linear function (constant rate) for modeling the deformation is sufficient to capture most deformation signal (if there is). If the linear function is not sufficient, a large part of the deformation will be identified as the stochastic deformation that is strongly correlated in time. For the APS spatial correlation length the upper boundary is set to 150 km which is the maximum distance between two pixels in ASAR images. Because the water vapor variation in space is highly dynamic due to turbulent mixing we usually expect a correlation length much smaller than the upper boundary. With regard to the deformation correlation length in time we set the upper boundary to 1.2 years for two reasons. Firstly, the simulation in chapter 5 shows that the estimate of the deformation correlation length is not reliable and it always tends to be either too small (lower boundary) or too large (upper boundary). Secondly, an artificially large correlation length will result in leakage of deformation to APS, i.e., the ground deformation will be too smooth. We want to retrieve as much as possible the real ground deformation, therefore we are conservative in setting the upper boundary. On the other hand, a too small correlation length of deformation will cause APS to be identified as deformation and result in an oscillatory deformation time series. Finally, the parameter that controls the spatial smoothness of APS in the Mátern model is bounded between 2/3 and 5/3 which corresponds to a 2D and 3D turbulence respectively, see Hanssen (2001).

After the stochastic modeling, the collocation method is applied in the time domain to estimate master APS, DEM inaccuracy (e.g., skyscrapers not modeled by DEM), deterministic and stochastic deformation for each PS time series. Afterwards, the phase residue of each PS is collected per acquisition and is used to separate APS and phase noise using the collocation method in the space domain.

6.2.3 Result and evaluation

In this section we will first present the results of the stochastic modeling. In terms of ground deformation, the goal is to estimate the variance and temporal correlation of the stochastic deformation based on the chosen variance-covariance model. The estimation of variance and temporal correlation is made for each PS. With regards to APS, the goal is to estimate the parameters of the Mátern model per acquisition. Note, the model parameters of the stochastic models are regarded as deterministic variables. Next, based on the estimated model parameters, the variance-covariance functions of the deformation and APS can be established and the corresponding variance-covariance matrices can be constructed. Given the variance-covariance matrices, the deterministic variables (i.e., master APS, linear deformation rate, DEM uncertainty) can be estimated and the realizations of the stochastic variables (i.e., stochastic deformation, APS, phase noise) can be predicted using the collocation method.

Estimation of variance-covariance function of stochastic deformation

We use Gaussian and spherical variance-covariance models separately to model the possible stochastic deformation. The estimated standard deviation per PS of the stochastic deformation is shown in Fig. 6.5 a and b. The estimated correlation length (in years) per PS is displayed in Fig. 6.5 c and d. We observe from the figure that the Gaussian model detects stochastic deformation in some areas (see Fig. 6.5 b) and the most significant stochastic deformation is located in the bottom-left of Fig. 6.5 b. However, no stochastic deformation is detected in the same area (zero RMS) by spherical model. Since we do not have any ground truth for the ground deformation it is not possible to assess the results. However, from the simulations in chapter 5 we have learned that the collocation method could result in false alarms, i.e., non-zero RMS of deformation at stable PS. The false alarms are caused by the leakage of APS to deformation. By looking at Fig. 6.5 b and d, we observe that the PS which have non-zero deformation RMS also have relatively short temporal correlation ($\sim$ 0.5 year). Such coincidence is likely due to the leakage of APS to deformation on these PS. Therefore, we decide to use the spherical model to model the stochastic deformation in the rest of the analysis.

Estimation of the APS variance-coariance function

We plot the estimated parameters of the Mátern variance-covariance model for APS turbulent mixing per acquisition in Fig. 6.6. We observe that the histogram of the estimated turbulent mixing RMSs shown in Fig. 6.6 b does not resemble a Chi-square distribution but rather like an uniform distribution. The mean of the RMSs is 15.5 mm and the standard deviation is 9.1 mm. It implies that the APS disturbance in the area is on average 15.5 mm and during extreme weather the disturbance can be as large as 24.6 mm or more. Because of the relatively large mean we expect a strong APS disturbance on the PS. In contrast, the mean of the RMSs of turbulent mixing computed using 26 tandem interferogram over the Netherlands is only 6 mm, see Hanssen (2001). Moreover, the estimated spatial correlation length of APS per acquisition ranges from 35 km to 91 km and the mean is 52 km. The estimated

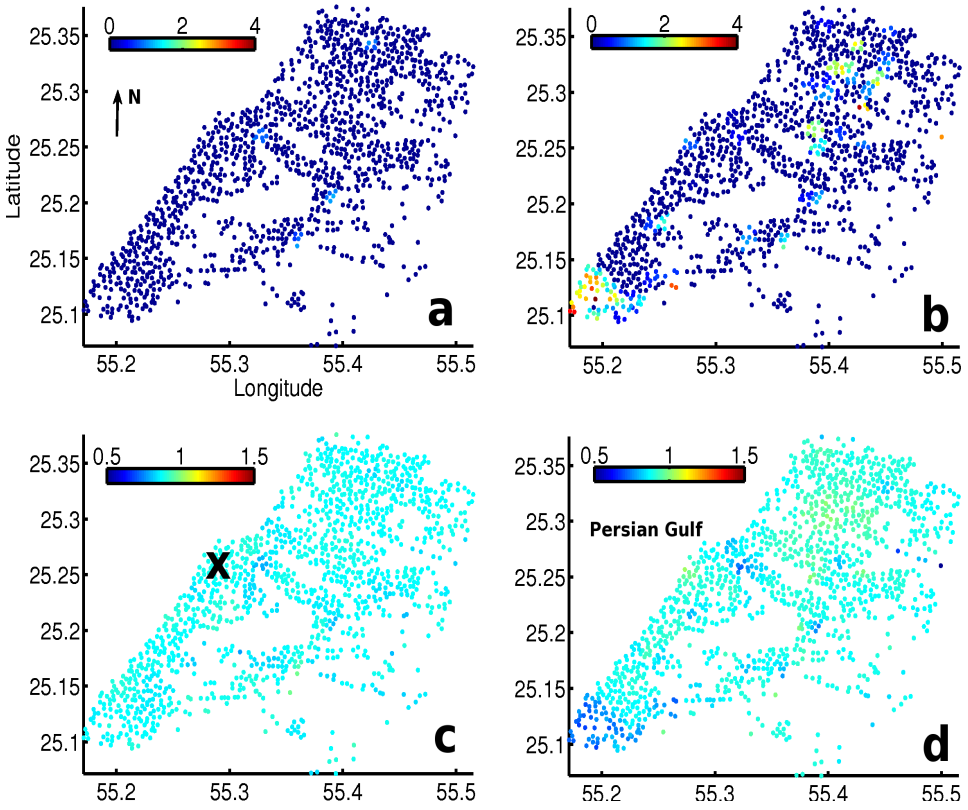

Fig. 6.5. Estimation of deformation variance and temporal correlation per PS over Dubai city. **a** and **b**) Estimated deformation standard deviation or RMS (unit: mm) using a spherical and Gaussian model respectively. The non-zero RMS in Fig. 6.5 b is likely a false alarm and caused by the leakage of APS to deformation. **c** and **d**) Estimated deformation correlation length (unit: years) using a spherical and Gaussian model respectively. In Fig. 6.5 d the location where the deformation correlation length is relatively short is exactly the location where the deformation RMS is sufficiently different from zero, see Fig. 6.5 b. The short correlation length could be an indication of APS leakage. The location of the reference PS is marked by the black cross in Fig. 6.5 c. Persian Gulf is located on the left side of the plots.

smoothness factor τ ranges from 0.67 to 1.4 with a mean of 0.84.

Estimation of the deterministic component of ground deformation

We have shown that the stochastic component of deformation over the city is negligible, which implies that the linear deformation model is sufficient for modeling the possible ground deformation. The estimated deformation rate and its precision (one standard deviation) obtained from the collocation method is shown in Fig. 6.7 a and b. We observe that the precision ranges from 1.2 to 2 mm/year in magnitude. More-

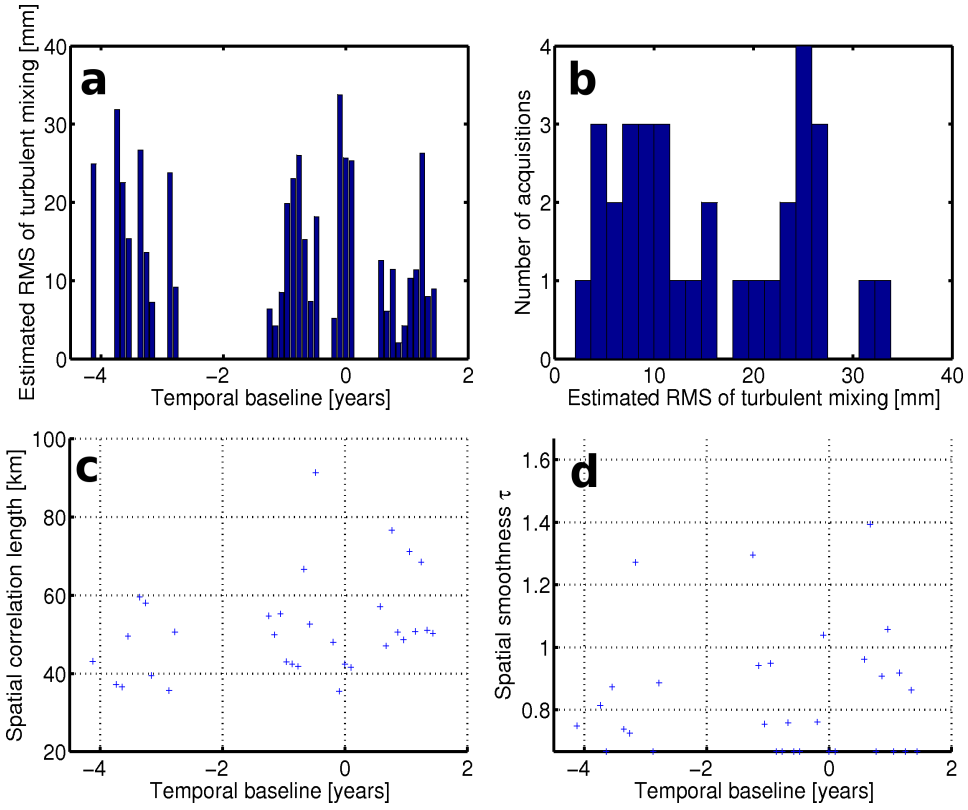

Fig. 6.6. Estimated parameters of the Mátern variance-covariance model for APS per acquisition over Dubai. **a**) Estimated RMS (unit: mm) of turbulent mixing per acquisition. **b**) Histogram of the estimated RMS of turbulent mixing. **c**) Estimated spatial correlation length (unit: km) of turbulent mixing per acquisition. **d**) Estimated spatial smoothness factor τ in the Mátern model per acquisition.

over, it decreases with the increase of the distance with respect to the preference PS which is highlighted as a black cross in Fig. 6.7 b. This is reasonable because APS disturbance in general increases with the increase of distance between PS. Moreover, we observe a spatial trend in Fig. 6.7 a. The trend suggests that the land close to the coast experiences uplift (with respect to the reference PS) and the land away from the coast suffers subsidence. However, there is no geophysical explanation for the spatial trend. A similar spatial trend has also been observed by Ketelaar (2008) from ASAR time series over Groningen, the Netherlands. Ketelaar (2008) has pointed out that such spatial trend is observable from ASAR time series but not from ERS1/2 and RadarSat-2 time series . Unfortunately, the cause of the trend is not clear so far. Since the trend is likely artificial, we therefore decide to remove the trend and present the de-trended (using a surface trend model) deformation rate map in Fig. 6.7 c. There are only a few PS in the figure showing considerable (> 5 mm) land

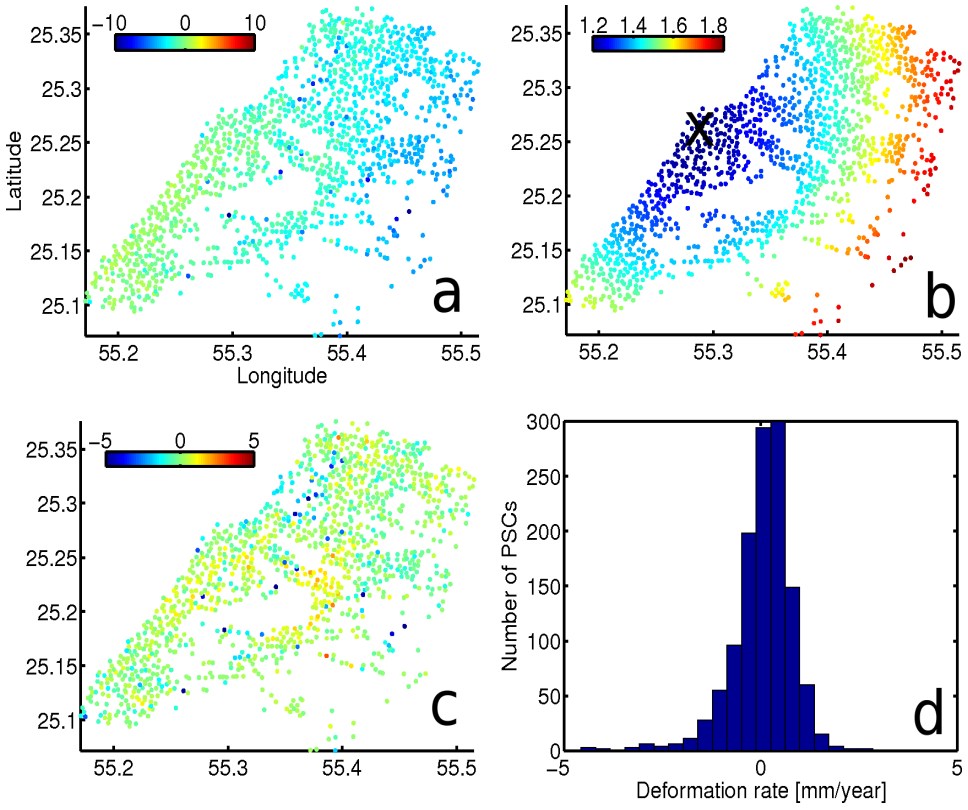

Fig. 6.7. Deterministic modeling of the ground deformation. **a**) Estimated deformation rate (unit: mm) per PS. Note, a spatial trend across the area of interest can be observed but the trend is not likely due to ground deformation. **b**) Estimated precision (one standard deviation, unit: mm/year) of the deformation rate in Fig. 6.7 a. The location of the reference PS is highlighted by the black cross. **c**) Deformation rate after removing a linear spatial trend from the original estimate in Fig. 6.7 a. **d**) Histogram of the deformation rate in Fig. 6.7 c. Therefore, we conclude that the urban area of the city is stable.

subsidence. By comparing the subsidence rate to the estimated deformation rate on the neighboring PS it seems that the estimated subsidence are most likely outliers (subsidence is usually spatially correlated). After de-trending, the histogram of the estimated deformation rates is plotted in Fig. 6.7 d from which we can see that the majority of PS have a deformation rate less than 2 mm/year. Considering the precision (1.2 to 2 mm/year) of the deformation rate estimate we conclude that the deformation over the city should be negligible. Next, we also use the weighted least-squares in Eq. (6.1.7) to estimate the deformation rate. This is the default approach to estimate deformation rate by *DePSI*. The weighting matrix is the inverse of the phase noise variance-covariance matrix, whereas the weighting matrix used

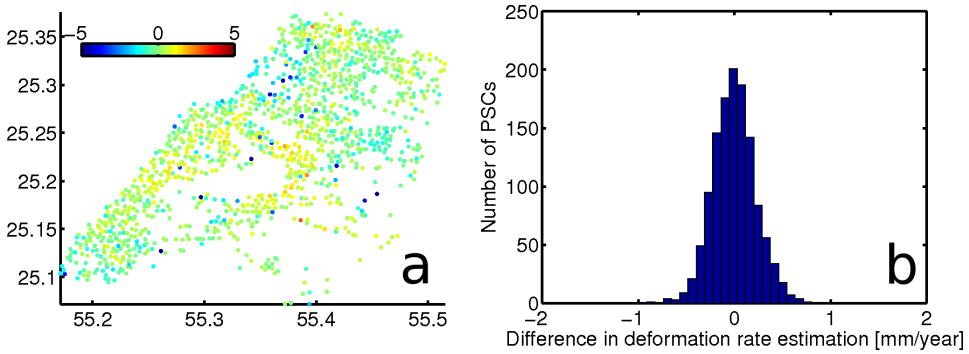

Fig. 6.8. Continued evaluation of the deformation rate estimation following Fig. 6.7. **a**) Estimated (also de-trended) deformation rate (unit: mm) on PS based on weighted least-squares. **b**) Histogram of the difference between the deformation rate estimates shown in Fig. 6.7 c and Fig. 6.8 a. In conclusion, in terms of deterministic deformation estimation, the weighted least-squares and collocation methods give very similar results.

by the collocation method is the inverse of the full variance-covariance matrix of the unwrapped phase time series, see Eq. (4.3.5). The de-trended deformation rate estimates using weighted least-squares are shown in Fig. 6.8 a and the histogram of the difference between the two estimates (i.e., one from the collocation method and one from weighted least-squares) is displayed in Fig. 6.8 b. The histogram resembles more or less a normal distribution. The mean of the difference is 0.0 mm/year and the standard deviation is 0.22 mm/year. Therefore, we conclude that the deformation rate estimation is not sensitive to the weighting matrices. This is the same conclusion we made in chapter 5 based on the simulated time series, see section 5.2.

DEM inaccuracy estimation

We present the DEM inaccuracy (Δh in Eq. (6.1.4) with respect to the reference PS) estimates obtained from the collocation method in Fig. 6.9 a. The precisions (one standard deviation) of the estimates are displayed in Fig. 6.9 b. Similar to the deformation, the precision decreases with the increasing of distance between a PS and the reference PS. The corresponding estimates using the weighted least-squares are shown in Fig. 6.9 c and the histogram of the difference between the two estimates are plotted in Fig. 6.9 d. The mean and standard deviation of the difference is 0.35 m and 0.39 m respectively. In conclusion, the DEM inaccuracy estimation is not that sensitive to the weighting matrices.

APS estimation

We present the master APS estimate obtained from the two methods in Fig. 6.10 a and b. The histogram of their difference (collocation minus filtering) is plotted in Fig. 6.10 d. The mean and standard deviation of the difference are 0.48 and 0.96 mm respectively. To validate the estimates we compare them with the MERIS water vapor measurement taken simultaneously as the master ASAR. The MERIS

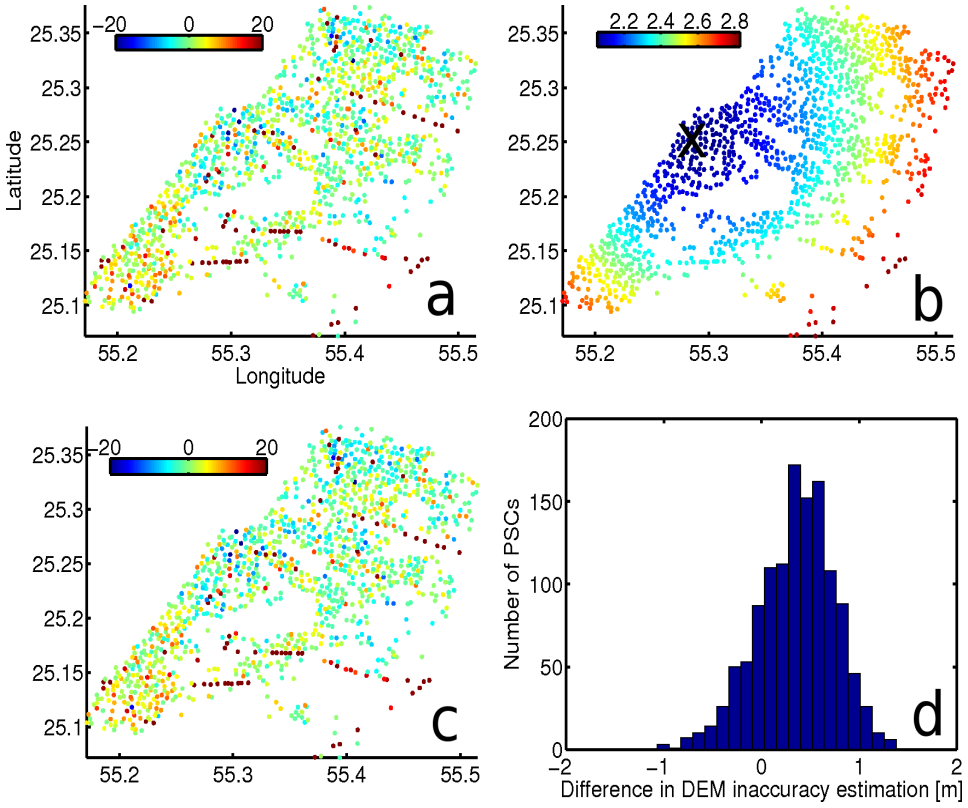

Fig. 6.9. Estimated DEM inaccuracy. **a**) Estimated DEM inaccuracy (unit: m) by the collocation method. **b**) Estimated precision (one standard deviation, unit: m) of the DEM inaccuracy estimation in Fig. 6.9 a. The location of the reference PS is highlighted by the black cross. **c**) Estimated DEM inaccuracy (unit: m) by weighted least-squares. **d**) histogram of the difference between the DEM inaccuracy estimates shown in Fig. 6.9 a and c. In conclusion, in terms of DEM uncertainty estimation, the weighted least-squares and collocation method give very similar results.

measurement is firstly converted to delay in mm from integrated water vapor (IWV) in g/m^2 using a constant factor Π=0.15, see Bevis et al. (1992, 1994). Then the converted zenith delay is mapped to the slant delay along the line-of-sight (LOS) of the radar. The slant delay obtained from MERIS is shown in Fig. 6.10 c. By comparing the master APS estimates with the MERIS delay we conclude that both methods give a good estimation of master APS. To assess which method gives a more accurate result we use the MERIS delay as a ground truth and compute the mean and standard deviation of the difference between the MERIS delay and one of the master APS estimates. For the collocation method the mean and standard deviation are 1.45 and 4.19 mm respectively. With regards to the weighted least-squares method, the mean and standard deviation are 1.93 and 4.11 mm respectively.

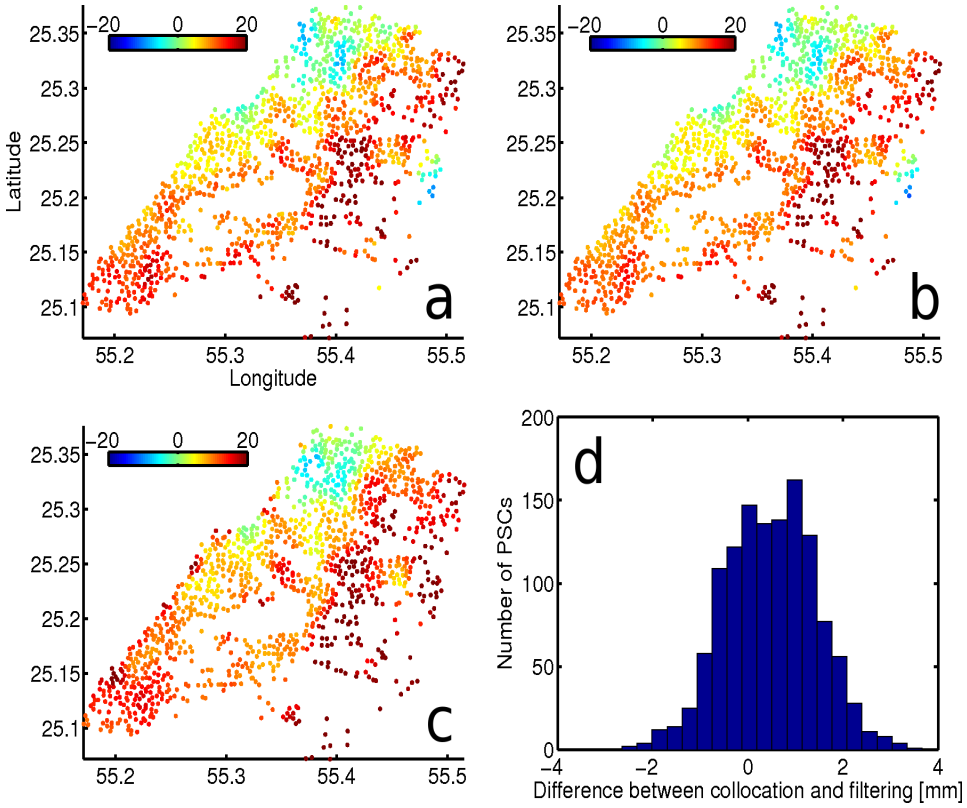

Fig. 6.10. Estimated master APS. **a**) Estimated master APS (unit: mm) by the collocation method. **b**) Estimated master APS (unit: mm) by weighted least-squares. **c**) Derived delay (unit: mm) from MERIS water vapor measurement taken simultaneously as the master ASAR. **d**) Histogram of the difference between the two estimates made by the collocation method and weighted least-squares respectively. In conclusion, the weight least-squares and collocation methods give comparable master APS estimates.

Thus, we conclude that the estimate by the weighted least-squares method is slightly more biased.

We are lacking ground truth data to validate the APS estimate for every slave and therefore decide to first compare the estimates made by the collocation method and the standard filtering method (using a 1-year Gaussian window) to see whether or not the estimates are different. If the difference is significant then it will be worthwhile to find out which method gives a better estimation. The overview of the comparison is displayed in Fig. 6.11 in terms of a-posteriori delay RMS computed from the estimated APS (including both spatial trend and turbulent mixing). From the figure we observe that the RMS of the slave APS estimates obtained from the collocation method is in general larger than the corresponding RMS obtained from the filtering method. In other words, the filtering method tends to give a smoother

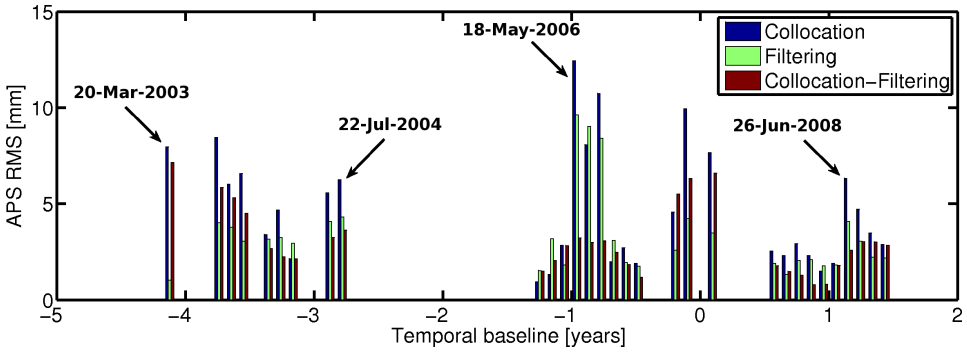

Fig. 6.11. Comparison between estimated APS per slave acquisition in terms of a-posteriori delay RMS (unit: mm). The RMSs of the estimates from the collocation and the filtering methods are shown in blue and green respectively. The filtering method uses a 1-year Gaussian window. The RMS of the difference between the APS estimates is shown in red. A large RMS of the difference indicates a significant difference between the estimates.

APS estimate per acquisition on average. The RMS of the APS estimate obtained from the collocation method ranges from 0.9 to 12.4 mm with a 4.7 mm mean. In contrast, the RMS of the APS estimate obtained with filtering method ranges from 1.0 to 9.6 mm with a 3.3 mm mean. The RMS of the difference between the estimates of the two methods ranges from 0.79 to 7.1 mm with a 3.1 mm mean. Therefore, the two methods give considerablely different estimates of slave APS.

To find out which method gives a better APS estimation we compare the estimates to MERIS water vapor measurements. In total 10 MERIS acquisitions are not severely affected by clouds (including the MERIS on master date). The mean correlation between the APS estimates from the collocation method and the corresponding MERIS measurements is 0.7, whereas the mean correlation for the APS estimates from the filtering method is 0.5. Note that the used MERIS measurements are not noise-free due to possible undetected clouds which can bias the retrieved water vapor (Bennartz and Fischer, 2001; ESA, 2006; Lindenbergh et al., 2007). For demonstrations we show comparisons between MERIS and the APS estimates for four slave acquisitions in Figs. 6.12 and 6.13. Two of the four acquisitions, i.e., acquisitions on 22-Mar-2003 and 22-Jul-2004, are at the edges of the acquisition gaps indicated in Figs. 6.4 b and 6.11. We expect a poor APS estimation from the filtering method for these two acquisitions because the method does not weight the time series based on the magnitude of the APS variation per acquisition and therefore requires a relatively large number of sequential images to smooth out (i.e., temporal averaging) APS. By comparing the APS estimates shown in Fig. 6.12 b, d with the MERIS derived delays shown in Fig. 6.12 e, f we indeed see that the APS estimations on these two dates are strongly biased. However, the estimates made by the collocation method shown in Fig. 6.12 a, b are not biased and agree well with the MERIS delays. Thanks to the proper weighting in the collocation method based

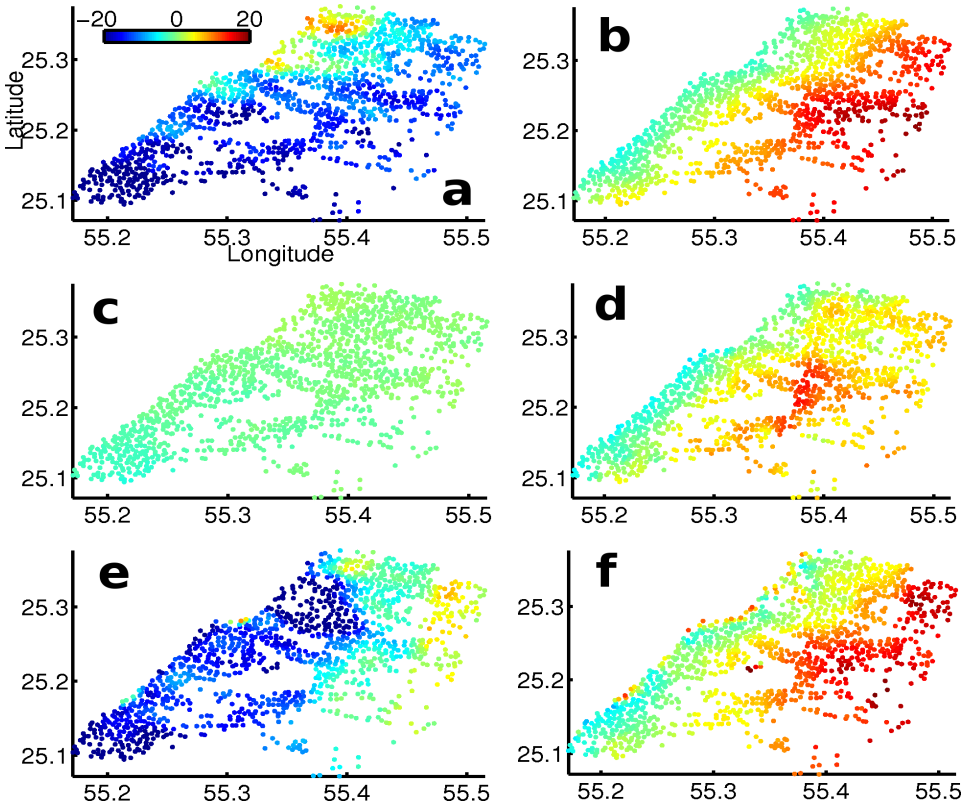

Fig. 6.12. Validation of slave APS estimates (unit: mm) using delays derived from MERIS cloud-free water vapor measurements. **a** and **b**) APS estimates for the acquisition on 22-Mar-2003 and 22-July-2004 respectively obtained from the collocation method. **c** and **d**) Obtained from the filtering method. **e** and **f**) Derived delay from MERIS. In conclusion, the APS estimates from the filtering method are largely biased. This is caused by the acquisition gaps in the time series, see Fig. 6.4 b.

on the estimated variance of APS per acquisition, the collocation method is not sensitive to the acquisition gaps and still results in a good estimation of true APS. The other two acquisitions, i.e., 18-May-2006 and 26-Jun-2008, are from the middle of two groups of sequential images and the groups are isolated by the acquisition gaps, see Figs. 6.4 b and Fig. 6.11. Although the APS estimates from the filtering method on these two dates suffer less from the acquisitions gaps, they are still problematic. This is because the two acquisitions have relatively large APS variations than their adjacent acquisitions, see 6.11. From Fig. 6.13 c, d we observe that the APS estimates from the filtering method are again significantly biased comparing to the estimates from the collocation method shown in Fig. 6.13 a, b. The latter agree reasonably well with the delays derived from MERIS shown in Fig. 6.13 e, f. Moreover, due to the relatively large variations of APS on these two acquisitions

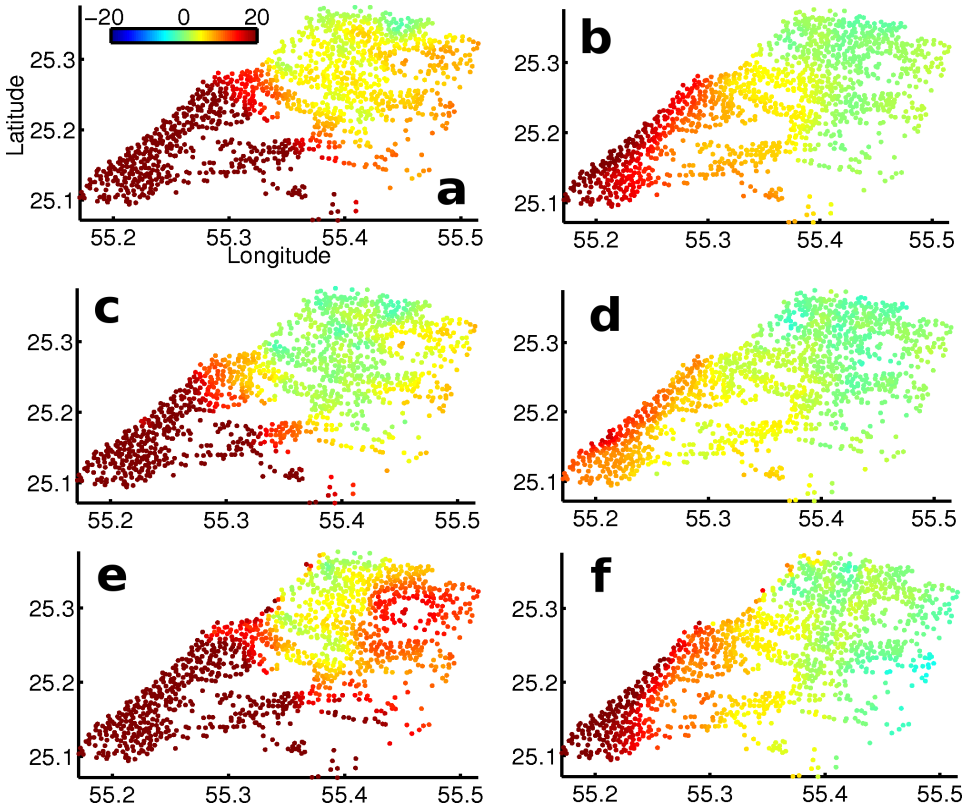

Fig. 6.13. Continued validation of APS estimates (unit: mm) using delays derived from MERIS cloud-free water vapor measurements. **a** and **b**) APS estimates for the acquisition on 18-May-2006 and 26-Jun-2008 respectively obtained from the collocation method. **c** and **d**) Obtained from the filtering method. **e** and **f**) Derived delay from MERIS. In conclusion, the APS estimates from the filtering method are biased. This is because the two acquisitions experience relatively large APS disturbance (i.e., large anomaly) comparing to the rest acquisitions, see Fig. 6.11.

the APS estimates from the filtering method for the adjacent acquisitions can be strongly biased as well. That is because the APS on these two acquisitions are not filtered out completely and leak to the deformation estimate in the adjacent acquisitions via temporal convolution (see Eq. 4.1.2). As a result, the APS estimates in these adjacent acquisitions are biased. This can be seen from Fig. 6.14 in which we plot the difference between the two methods for the APS estimates on 22-May-2008, 26-Jun-2008, 31-Jul-2008 and 4-Sept-2008. Clearly, the differences on 22-May-2008, 31-Jul-2008 and 4-Sept-2008 resemble the difference on 31-Jul-2008. In other words, the difference between slave APS estimates by the collocation and filtering methods per acquisition is strongly correlated in time. Such temporal correlation is due to the poor estimation of APS on 31-Jul-2008 by the filtering method, see Fig. 6.13.

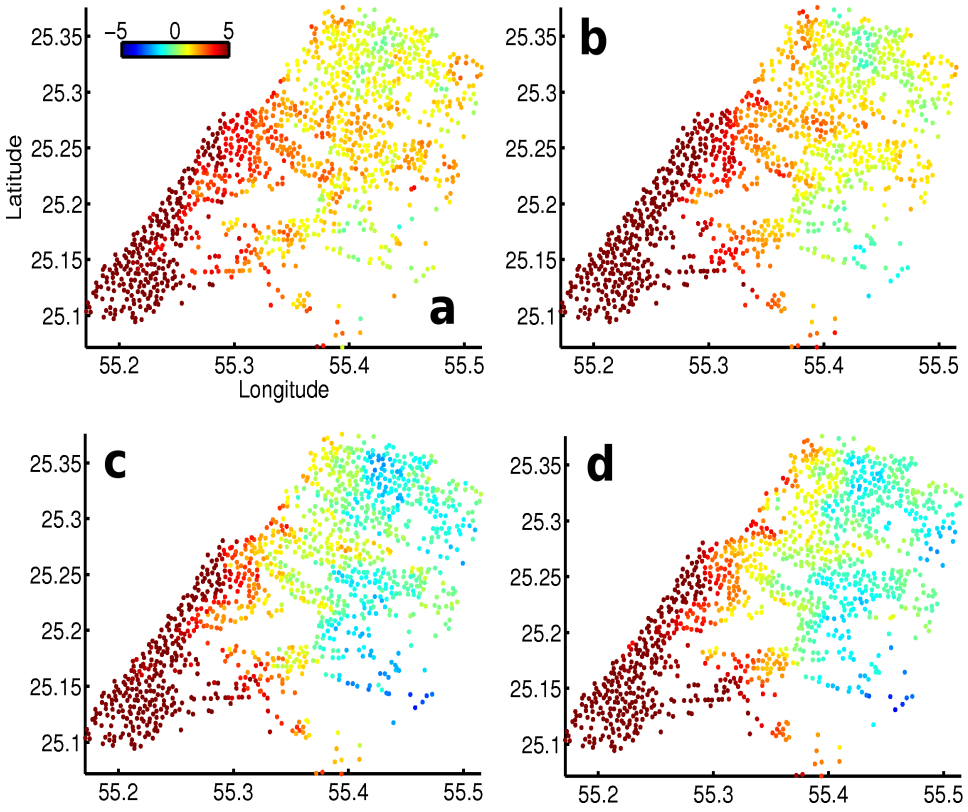

Fig. 6.14. Difference between APS estimates (unit: mm) made by the collocation and filtering methods. **a**) Difference on 22-May-2008. **b**) Difference on 26-Jun-2008. **c**) Difference on 31-Jul-2008. **d**) Difference on 4-Sept-2008. The differences are strongly correlated and it is caused by the biased estimation of APS obtained from the filtering method on 26-Jun-2008, see Fig. 6.13 b,d,f.

The poor estimation of APS by the filtering method seems to result in a significant leakage of APS into ground deformation. This can be clearly seen from Fig. 6.15 in which we plot total deformation time series of 6 PS. The distances between these PS and the reference PS shown in Fig. 6.7 range from 2.6 to 17.4 km. The APS leakage causes all the deformation time series to present an artificial seasonal deformation pattern. The same sort of artificial seasonal deformation pattern has been observed in Figs. 5.17 and Fig. 5.18 based on the simulated data in chapter 5. Moreover, the leakage of APS is significant at the acquisitions that are close to the acquisition gaps, e.g., the first acquisition (22-Mar-2003) in the time series.

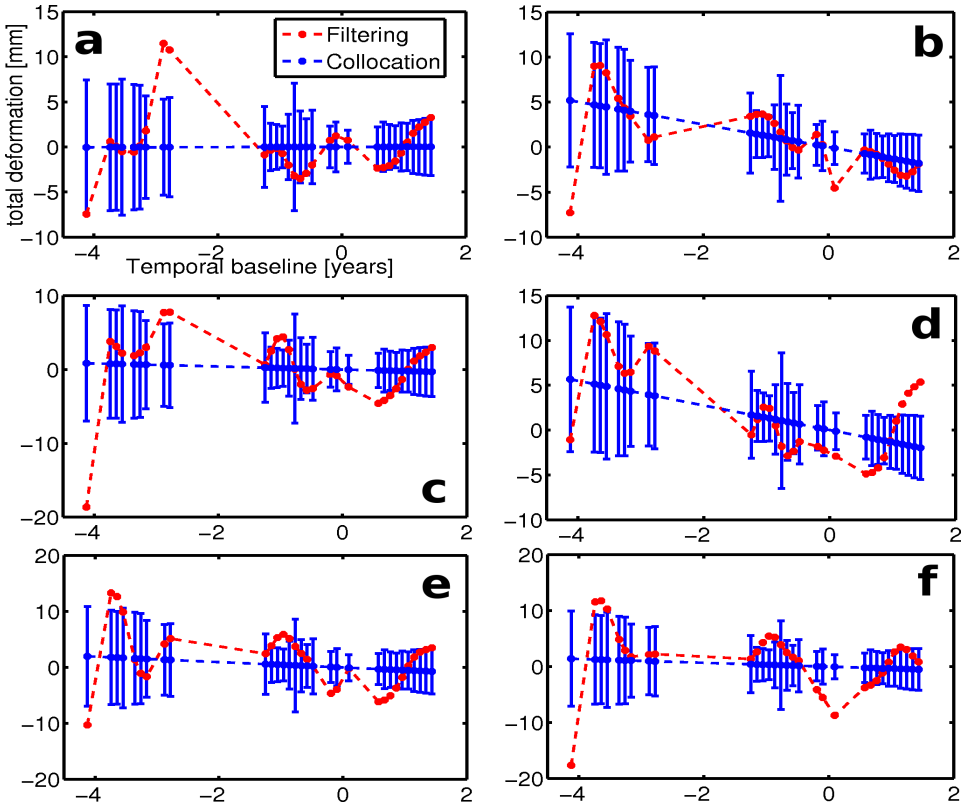

Fig. 6.15. Estimated total deformation time series (unit: mm) on 6 PS. **a**) A PS which is 4.2 km away from the reference PS. **b**) A PS which is 2.6 km away from the preference PS. **c**) A PS which is 8.3 km away from the preference PS. **d**) A PS which is 9.5 km away from the preference PS. **e**) A PS which is 17.4 km away from the preference PS. **f**) A PS which is 14.1 km away from the preference PS. The precision (one standard) deviation of the estimated deformation by the collocation method is given as the error bars. The precision of the estimate by the filtering method is however not defined by the method. In conclusion, the large temporal variations in the estimated deformation time series obtained from the filtering method is unrealistic and caused by the leakage of APS to deformation. The variations are typically found near the acquisition gaps and during acquisitions having relatively large APS disturbance.

6.2.4 Summary

We have applied the collocation method to the urban area of Dubai. We model the possible ground deformation using a linear functional model and a spherical variance-covariance model. We find that the ground deformation rates on most PS are within $\pm$ 2 mm/year. We also evaluate the precisions (one standard deviation) of the estimated deformation rates and they range from 1 to 2 mm/year. Moreover, we find that the estimated variances of possible stochastic deformation at the PS

are negligible. Therefore, we conclude that the urban area of Dubai is stable.

Regarding the estimation of the deterministic variables (i.e., deformation rate, master APS, DEM inaccuracy) the weighted least-squares and collocation methods give more or less identical results. This is because the variance-covariance matrix of the deformation is a null matrix and the deterministic variables are constants in time. Given the sufficiently long time series (i.e., 31 images between 2003 and 2008), the estimates of the deterministic variables are no longer sensitive to the varying magnitude of APS disturbance per acquisition.

However, with regards to the stochastic deformation (deformation that is not modeled by the functional model) estimation the filtering method typically results in a deformation time series having a considerable oscillation, see Fig. 6.15. By comparing the APS estimates from the filtering method with a number of cloud-free MERIS water vapor measurements we find that most of the APS estimates are biased (smoother than ground truth), especially for the acquisitions that are close to the acquisition gaps and that have relatively large APS RMS (i.e., acquisitions during extreme weather). Therefore, we suggest that the significant oscillations in the deformation time series obtained from the filtering method are artificial and caused by the leakage of APS to ground deformation. Our suggestion is supported by the fact that the filtering method does not take into account the varying magnitude of APS disturbance per acquisition and weight all acquisitions equally. Given a fixed filtering length in the time domain (i.e., one-year) the method may not be able to sufficiently average out APS, especially for acquisitions taken during extreme weather and when there are large acquisition gaps in the time series. As a result, some of the slave APS estimates can get biased and are partly identified as non-linear deformation, i,e., the oscillations in the time series.

6.3 Mexico City

From the Dubai case we have shown that the collocation and filtering methods give similar estimates for the deterministic variables, i.e., deformation rate, DEM uncertainty and master APS. This is because the local area is stable and insensitive to the selection of the functional model for deformation modeling. However, when the ground deformation is complex (e.g., non-constant rate) we expect different results from the two methods. As we see from the simulation result in section 5.3.2, in case of a complex deformation the filtering method (i.e., weighted least-squares) becomes sensitive to the functional model chosen for modeling the deformation. If the chosen functional model is not a good approximation of the actual deformation, the master APS estimate will be biased. This is because the un-modeled (by the functional model) deformation is strongly correlated in time and the master APS is a constant in time, i.e., perfectly correlated in time. Therefore, it is difficult to separate them without explicitly model them separately. The collocation method is however not sensitive to the functional model selection. This is because the method models the deformation both deterministically (via a functional model) and stochastically (via a stochastic model). In other words, any deformation that is not modeled by the functional model is taken into account by the stochastic model. This prevents the

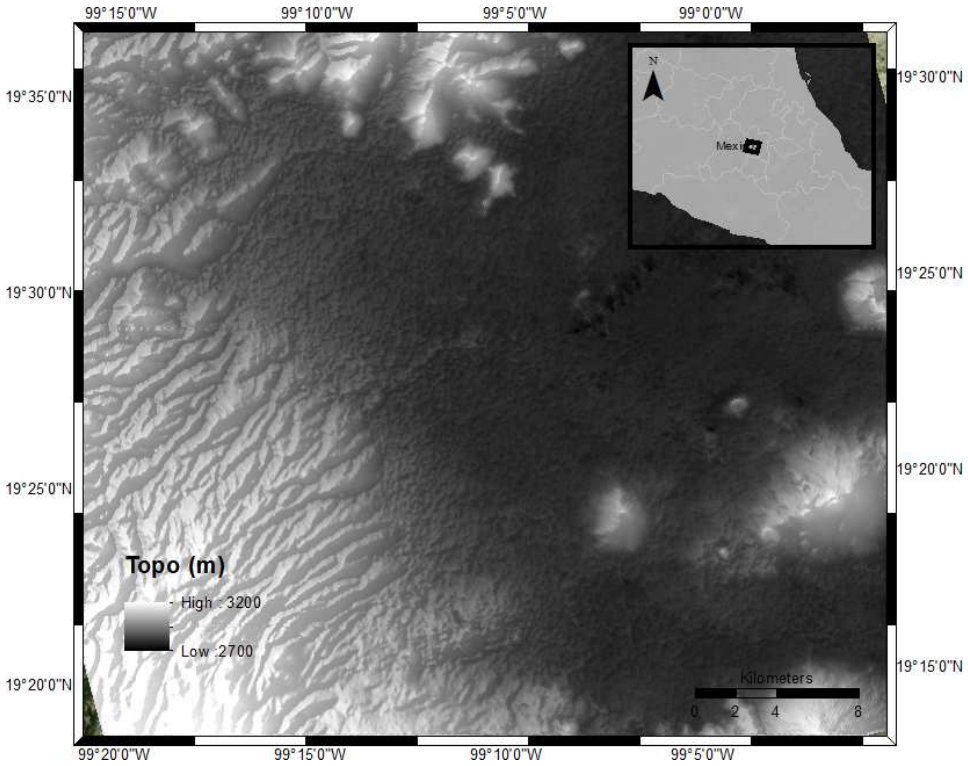

Fig. 6.16. Land topography of Mexico City covered by ASAR acquisitions (track: 255, frame: 3213) with a spatial extent of 40 by 40 km

deformation from being partly identified as the master APS. We will demonstrate the above discussion in this case study. Additionally, we will show that in case of acquisition gaps the collocation method gives better estimation of slave APS than the filtering method. For the filtering method, a better APS estimation can be achieved by increasing the filtering length (one-year by default) in time. But this could cause an over-smoothing of the deformation time series.

6.3.1 Test site and data

We choose Mexico City as another test site to evaluate the performance of the collocation method in the presence of rapid and complex ground subsidence. Many authors, e.g., Strozzi et al. (2003); Lopez-Quiroz et al. (2009) and Osmanoglu et al. (2011) have investigated the subsidence in Mexico City using InSAR. The largest subsidence rate that has been observed is 40 cm/year (Strozzi et al., 2003). The large subsidence rate is due to intensive ground water extraction and highly compressible clays on which the city is built. The city has a subtropic highland climate due to its tropical location and high elevation. The temperature of the region varies from $\sim$6°C in winter to $\sim$26° in summer (Servicio Meteorologico Nacional, 2011). The

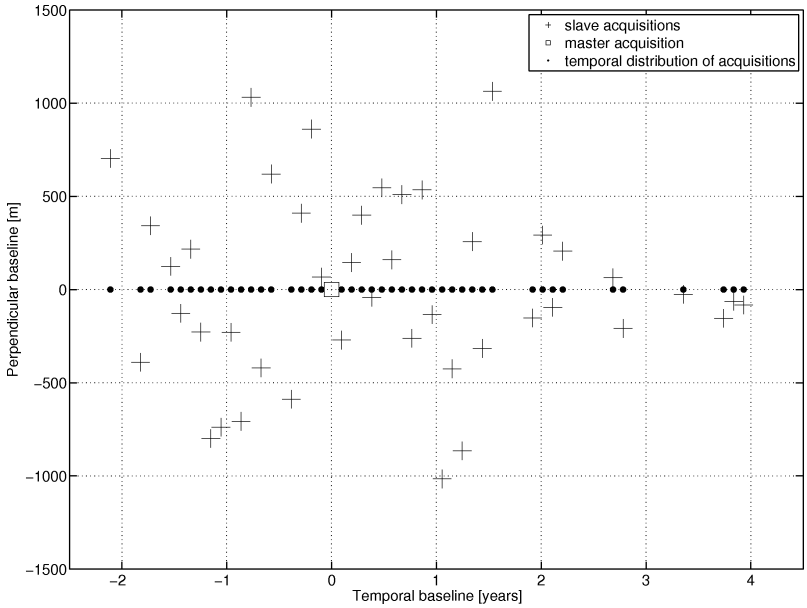

Fig. 6.17. Baseline plot for 45 ASAR acquisitions over Mexico City from track 255 frame 3213. The master acquisition on 31-Dec-2004 is marked as a square. The maximum acquisition gap from the time series is 210 days.

annual rainfall is about 816 mm and most of the rainfall takes place between June and September (Servicio Meteorologico Nacional, 2011).

The test site is centered at 19°25′ northern latitude and 99°2′ western longitude with a spatial extent of 40 km in both azimuth and range, see Fig. 6.16. The available ASAR acquisitions for the city are from track 255 and frame 3213 in descending orbit. In total 45 ASAR images between 22-Nov-2002 and 5-Dec-2008 are used for this case study. The master image is selected as the acquisition acquired on 31-Dec-2004. The baseline plot is given in Fig. 6.17. The minimum and maximum perpendicular baseline is 26 and 1064 m respectively and the largest temporal baseline is 3.9 years. Similar to the Dubai dataset, the ASAR acquisitions over the region are not regular in time, which causes considerable acquisition gaps (maximum 210 days) in the time series, see Fig. 6.17.

The topographic variation within the area of interest is only a few hundred meters, see Fig. 6.16. We remove its phase contribution using 3 arc second SRTM. For the initial selection of PS we set the threshold for amplitude dispersion index to 0.22. For the first-order network which is constructed by the PS, the allowed maximum arc length is 5 km to suppress APS. The pre-selected reference PS is highlighted as a black cross in Fig. 6.19.

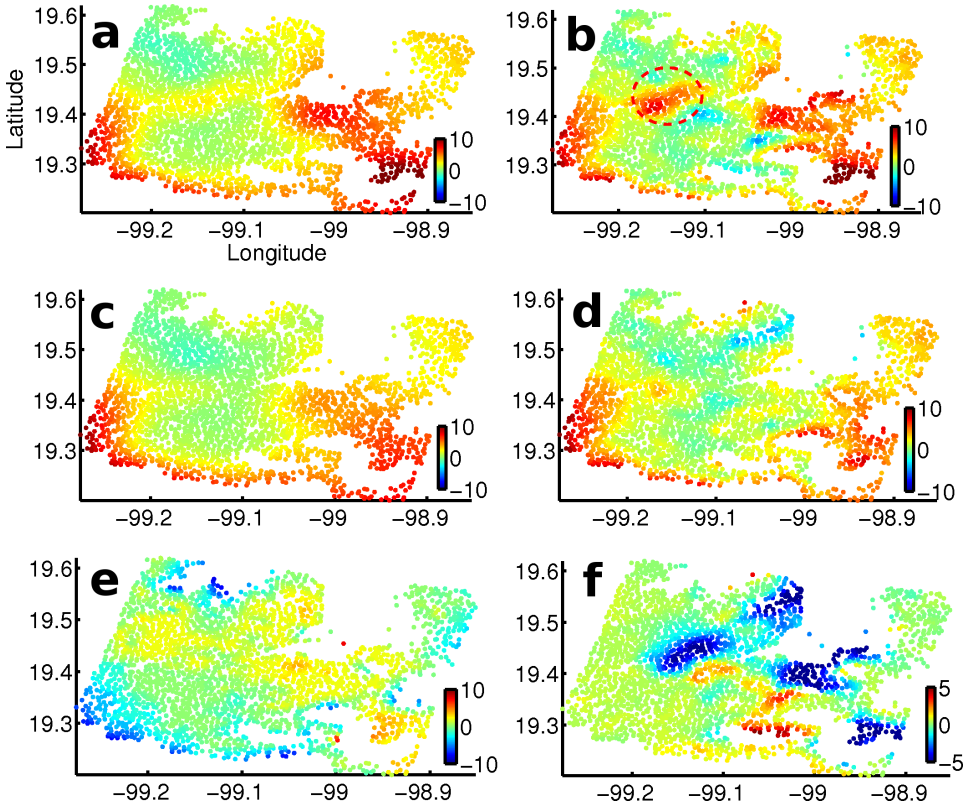

Fig. 6.18. Master APS estimation. **a** and **b**) Estimates (unit: mm) by collocation and WLS respectively based on a linear deformation model. **c** and **d**) Estimates (unit: mm) by collocation and WLS respectively based on a quadratic deformation model. **e**) Delay (unit: mm) derived from the MERIS acquisition acquired simultaneously as the master image. **f**) Difference (unit: mm) between the master APS estimates shown in Figs. 6.18 b and d. The large residue shown in Fig. 6.18 f indicates the WLS method is sensitive to the functional model selection for deformation modeling.

6.3.2 Sensitivity to the functional model for ground deformation

Osmanoglu et al. (2011) use a linear model for the ground subsidence in the urban area of the city using PSInSAR. They validate the modeled subsidence against the subsidence derived from local sparse GPS networks and find good agreement at the locations of the GPS stations. Hence, we decide to use the linear model as the first attempt to model the deterministic ground subsidence. In addition, we choose a hole effect variance-covariance model that is capable of describing some type of pseudo-perioditcity to model possible stochastic deformation. This is because strong seasonal deformation has been observed by the GPS network and the deformation is likely caused by aquifer recharge through precipitation, see the discussions in Osmanoglu et al. (2011).

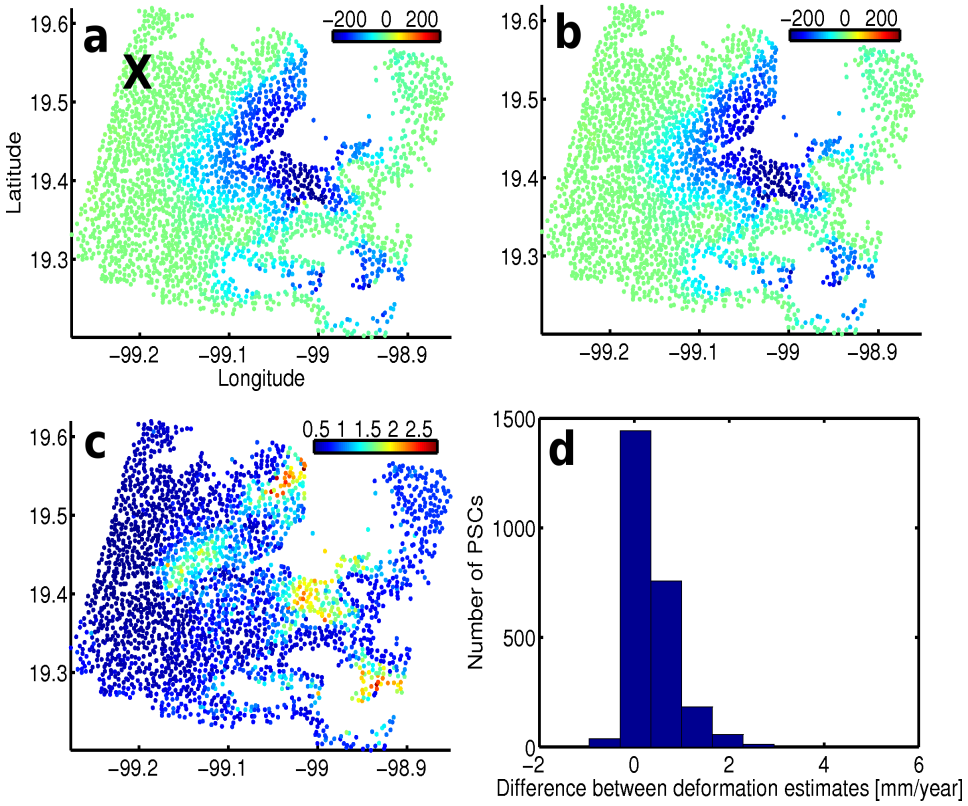

Fig. 6.19. Subsidence rate estimation based on a linear deformation model. **a** and **b**) Estimates (unit: mm/year) by collocation and WLS respectively. The reference PS is marked by a black cross. **c**) Estimated precision (one standard deviation, unit: mm/year) of the subsidence rate estimate in Fig. 6.19 a. **d**) Difference (unit: mm/years) between the estimates in Figs. 6.19 a and b. In conclusion, the deformation rate estimates from the two methods are similar.

The master APS estimates from the collocation and weighted least-squares (WLS) are displayed in Figs. 6.18 a, b respectively. The most significant disagreement between the two estimates is a band of positive delay highlighted by the dashed red circle in Fig. 6.18 b. Fortunately, the MERIS acquisition taken simultaneously as the master acquisition is not severely affected by clouds and can be used for validation, see Fig. 6.18 e. Clearly, the MERIS measurement suggests that the positive delay is probably artificial and the APS estimate from the collocation method shown in Fig. 6.18 a is more reliable. We will discuss the possible cause of the artificial delay later in this section.

Regarding the deformation rate, its estimates are plotted in Figs. 6.19 a, b using collocation and WLS respectively. The histogram of the difference between the two estimates is displayed in Fig. 6.19 d. The mean of the difference is 0.4 mm/year

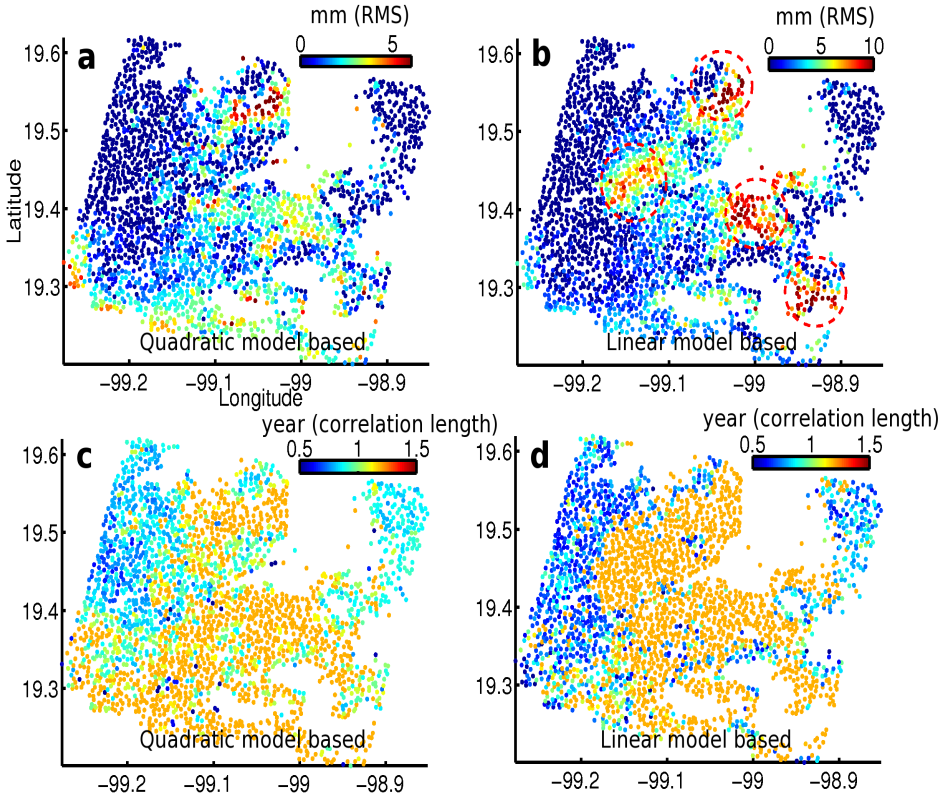

Fig. 6.20. Stochastic deformation estimation. **a** and **b**) Estimated RMS (unit: mm) of the stochastic deformation based on a quadratic and linear deformation model respectively. The regions with relatively large deformation RMS are highlighted by red circles. These regions are corresponding to the locations in Fig. 6.19 c where the precisions of the estimated subsidence rates are lower than the surroundings. **c** and **d**) Estimated temporal correlation length (unit: years) of the stochastic deformation shown in Fig. 6.20 a and b respectively. This figure demonstrates that the un-modeled deformation by the linear model will be modeled stochastically by the collocation method.

and the difference at most PS is less than 1 mm/year. Therefore, in terms of the deformation rate estimation the two methods provide the same result. In addition, the collocation method also gives the precision of the estimated deformation rate, see Fig. 6.19 c. As expected, the precision degrades with increasing distance from the reference PS. Here we need to stress that the indicated precision is relative and depends on the reference PS selection (Ketelaar, 2008). Therefore a low precision does not suggest a less coherent PS. In addition, at some locations the precision of the estimated deformation is unexpectedly worse than the surroundings. This can be explained by the estimated stochastic deformation shown in Fig. 6.20 b. The estimated RMS suggests that at these locations the linear model does not fit the

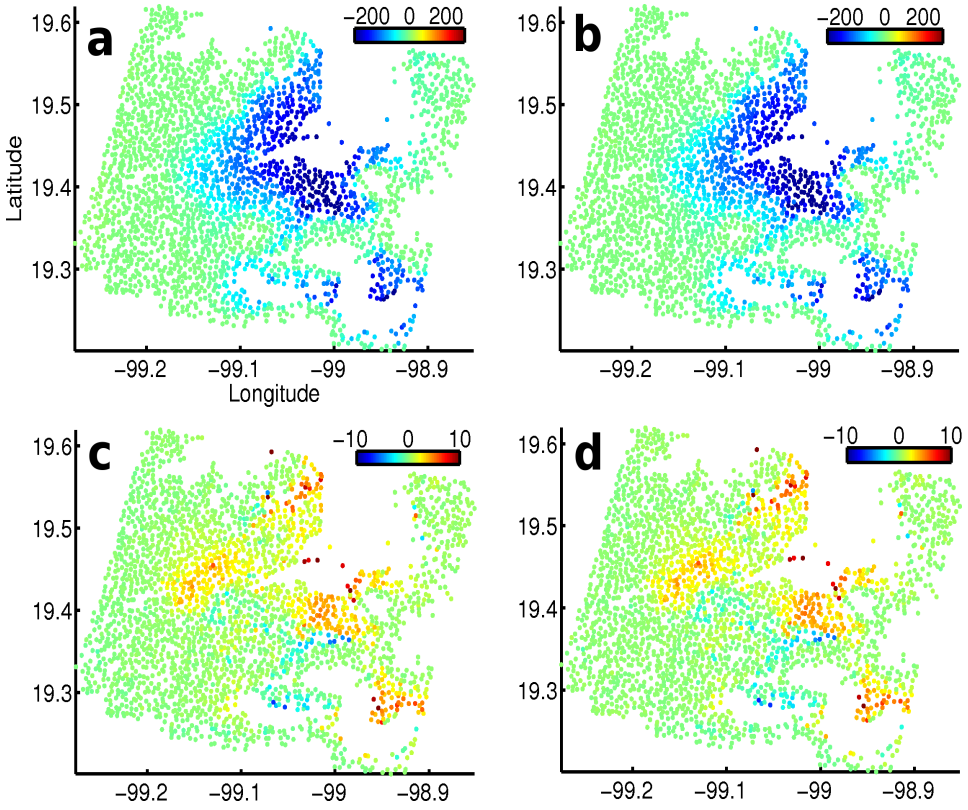

Fig. 6.21. Estimation of ground subsidence using a quadratic functional model. **a** and **b**) Estimated linear subsidence rate (unit: mm/year) by collocation and WLS respectively. **c** and **d**) Estimated quadratic subsidence rate (unit: mm/year^2) by collocation and WLS respectively. In conclusion, the deformation rate estimates from the two methods are similar, see also Fig. 6.22.

true subsidence very well and the discrepancy between the linear model and the true subsidence is therefore modeled as the stochastic deformation by the collocation method.

We have learned from the simulation in section 5.3.2 that when an inappropriate functional model is chosen for the deterministic component of ground deformation the discrepancy between the functional model and the real deformation will be large and become strongly correlated in time. This can be seen from Figs. 6.20 b and d. The figure tells us that the linear deformation model is probably not sufficient to model the deformation over the entire region. Therefore, we decide to use a quadratic model. Based on this functional model, we redo the stochastic modeling of the deformation using the same variance-covariance model (i.e., hole-effect model). The estimated variance and temporal correlation length are shown in Fig. 6.20 a and Fig. 6.20 c respectively.

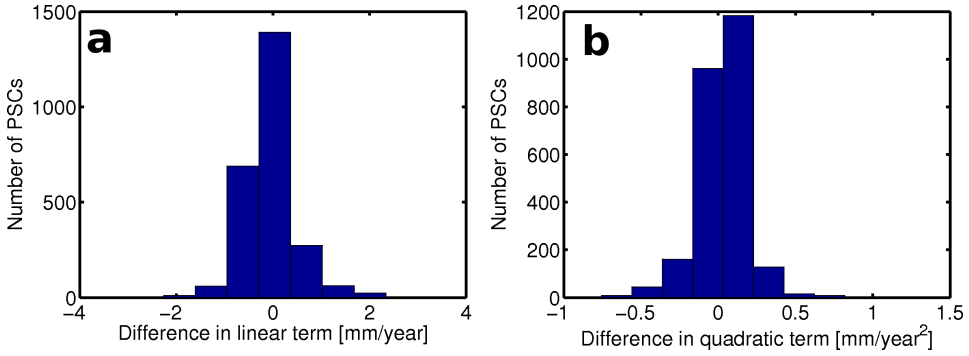

Fig. 6.22. a) Histogram of the difference (unit: mm) between the linear subsidence rate estimates shown in 6.21 a and c. a) Histogram of the difference (unit: mm/year^2) between the quadratic subsidence rate estimates shown in 6.21 b and d.

By comparing the estimated correlation lengths of the stochastic deformations shown in Fig. 6.20 c (based on the quadratic functional model) and Fig. 6.20 d (based on the linear functional model) we see that the strong correlation disappears when the quadratic model is used to model the deterministic deformation. This is because the stochastic deformation is now modeled by the quadratic term of the quadratic model. When the linear functional model is used to model the deterministic deformation, the locations where we observe a large correlation length in Fig. 6.20 d are exactly the locations where the stochastic deformations are significant, see red circles in Fig. 6.20 b. Therefore, we conclude that the deterministic deformation over the region can be better modeled by a quadratic model. As a rule of thumb, a stochastic modeling is preferred only when the ground deformation cannot be modeled well by a functional model. In practice, a suitable functional model for deformation in the area of interest is usually not known a-priori. A function model is however always preferred as long as it can model the deformation well. This is because estimation always has a better precision than prediction (i.e., more observation redundancy). Based on the discussion above we re-model the deterministic deformation by a quadratic model. The estimated model parameters (i.e., coefficients for the linear and quadratic terms) are shown in Fig. 6.21 a, c using the collocation method and in Fig. 6.21 b, d based on WLS. As we can see, at the discussed locations we do find the quadratic term of the subsidence larger than zero. The positive sign of the quadratic term indicates that the ground subsidence at these locations is decelerated with respect to their surroundings. Finally, the difference between the estimated model parameters by the two methods is visualized by histograms in Fig. 6.22 a, b. Again, we find that the model parameter estimates are almost identical.

In the end, we revisit the master APS estimate obtained from WLS shown in Fig. 6.18 b. We have concluded that the band of positive delay, indicated with the red dashed circle, is artificial and it must be the result of a leakage from another source. Among all possible sources (e.g., ground subsidence, DEM inaccuracy,

etc.) the ground subsidence has the largest likelihood. This is because the master APS is considered as a deterministic constant in WLS (see Eq. 6.1.8). Moreover, the stochastic subsidence, which is not modeled by the linear functional model, is relatively large and strongly correlated in time. Last but not the least, in the filtering method the master APS is estimated prior to temporal filtering that gives the estimate of the stochastic deformation. Therefore, the stochastic deformation is partly mis-identified as the master APS by WLS.

On the other hand, the collocation method takes into account the imperfection of the functional model used for the ground deformation modeling and uses a stochastic model to retrieve the un-modeled deformation as a stochastic deformation. Therefore, it prevents the stochastic deformation from being partly identified as master APS. After replacing the linear functional model by a quadratic functional model the new master APS estimate obtained from WLS is shown in Fig. 6.18 d. As we can see the artificial delay almost disappeared. The difference between the old and new master APS estimates is shown in Fig. 6.18 f. Clearly, the locations where the difference is significant are exactly the locations where the quadratic subsidence has been detected, see Fig. 6.22 c, d.

6.3.3 Slave APS estimation

The estimation of the slave APS is challenging since the region experiences rapid and complex ground subsidence (see Figs. 6.21 and 6.20) and there are large acquisition gaps (up to 210 days) in the time series, see Fig. 6.17. We expect the filtering method with 1-year window length to fail for the slave acquisitions close to the acquisition gaps. This is because there will be only a few acquisitions in the time series involved in the temporal filtering. The collocation method, however, should be much less sensitive to the gaps since it uses the estimated variance of APS per acquisition to weigh the time series before estimating stochastic ground subsidence. We compare the APS estimates by collocation and filtering methods in terms of a-posteriori delay RMS in Fig. 6.23. We can see that the difference between the two estimates tends to be significant for the acquisitions near the temporal acquisition gaps, see the enclosed acquisitions by the dashed rectangle in Fig. 6.23. This is very similar to the Dubai case discussed in section 6.2.

Unfortunately, we do not have cloud-free MERIS acquisitions over the region to validate the slave APS estimates. Fig. 6.24 gives an example of a cloud contaminated MERIS delay map on 5-May-2006. We have removed cloud pixels by using cloud flags provided by ESA,(ESA, 2006). Unfortunately, the cloud detection algorithm used by ESA (Fischer and Bennartz, 1997; Albert et al., 2001) can fail when the clouds are semitransparent cirrus (Puyssegur et al., 2007) for example. The negative delay in Fig. 6.24 b is subject to undetected clouds. As a result, it is not possible to evaluate the slave APS estimates individually. The only alternative left for validation is to compute the temporal difference between two APS estimates and then compare the temporal difference to the repeat-pass interferogram formed by the corresponding slave images. Note, to keep the repeat-pass interferogram remaining coherent its baselines need to be small. For urban areas a small temporal baseline is not always necessary to suppress decorrelation, but it will suppress ground deforma-

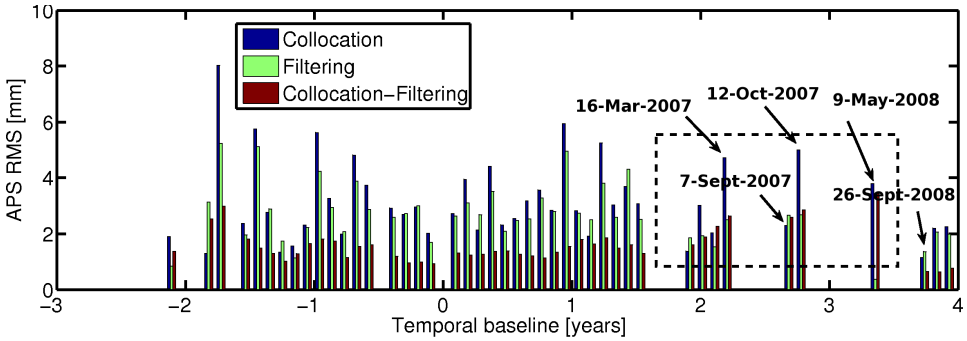

Fig. 6.23. Comparison between estimated APS per slave acquisition in terms of a-posteriori delay RMS (unit: mm). The RMSs of the estimates from the collocation and filtering methods are shown in blue and green respectively. The filtering method uses a 1-year Gaussian window. The RMS of the difference between the estimates is shown in red. The RMS of the difference tends to be large for the acquisitions close to the acquisition gaps (see the acquisitions enclosed by the dashed rectangular in the figure).

tion and leave APS as the dominant signal in the interferogram. Unfortunately, for the Mexico City case, even interferograms with 35-day temporal baselines cannot be considered as atmosphere-only interferograms because of the large subsidence rate in the region. Therefore, the repeat-pass interferogram based validation can only be carried out outside the subsiding zone of the region. Although we cannot validate the APS estimates within the subsiding zone, we can still deduce the influence of the acquisition gaps on the results of the collocation and filtering methods. This is because the separation of APS and stochastic subsidence is carried out in time per PS and the spatial distribution of APS can be often assumed isotropic. Therefore, an insufficient smoothing of APS due to the acquisition gaps will result in comparable APS leakage for arcs (with respect to the reference PS) with comparable lengths in space.

We show three comparisons in Figs. 6.25, 6.26 and 6.27 between the temporal differences of the slave APS estimates and the corresponding repeat-pass interferograms. The clearly visible APS signals are highlighted by the black dashed circles in each of the figures. The highlighted areas are outside of the subsiding region, see Fig. 6.22. We can clearly observe from all the figures that in the highlighted areas the collocation method gives a very good approximation of the true APS, whereas the APS estimates in the same areas made by the filtering method using a 1-year Gaussian window are largely biased. The biases are the result of leakage of APS to deformation and the leakage is caused by insufficient smoothing of APS due to the acquisition gaps in the time series. The bias given by the filtering method can be reduced by increasing the temporal window length to three years, see Figs. 6.25 d, 6.26 d and 6.27 d. Indeed, by increasing the window length a sufficient smoothing of APS can be achieved. Therefore, we conclude that for the filtering method a better estimation of slave APS can be achieved by increasing the temporal window length when

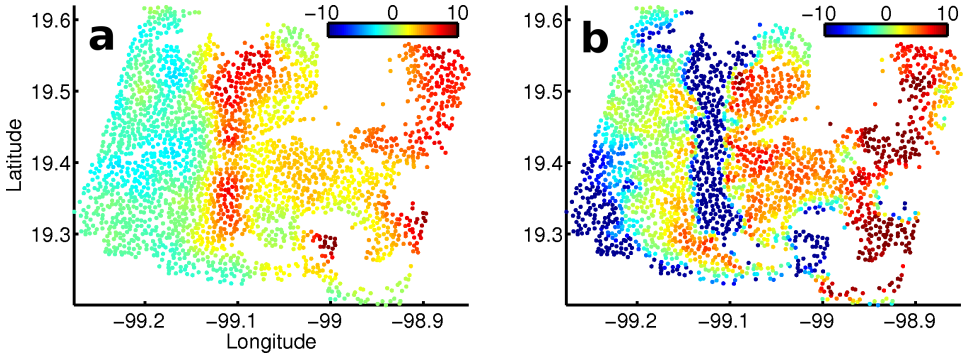

Fig. 6.24. An example of MERIS water vapor measurement by undetected clouds. **a**) Estimated APS (unit: mm) for acquisition on 5-May-2006 by the collocation method. **b**) Derived APS (unit: mm) from the MERIS measurement on the same date (simultaneously taken as the ASAR acquisition). The negative band of delay in the plot is likely caused by undetected clouds.

there are significant acquisition gaps in the time series. However, the increase of the temporal window length does not necessarily lead to a good separation of APS and ground deformation. When the stochastic deformation is not negligible a large temporal window will over smooth it and result in a leakage from deformation to APS. This can be seen from Fig. 6.28, in which we plot the estimated stochastic deformation time series of 2 PS coming from the area suffering from significant stochastic deformation (RMS $>$ 6 mm), see Fig. 6.20 a. From Fig. 6.28 we observe that given an one year window length, the filtering results deviate away from the collocation results around the acquisition gaps. We have shown that the deviation is caused by the leakage of APS to deformation. Moreover, the deviation is remedied by increasing the window length to three years. However, the increase of the window length compromises the temporal resolution of the deformation time series and result in over-smoothing the stochastic deformation. In contrast, the filtering length in the collocation method equals to the correlation length of the stochastic deformation and it is estimated from the time series other than a required input from a user.

6.3.4 Summary

In this case study we have shown that the urban area of Mexico city experienced rapid subsidence ($>$ 200 mm/year) between 2002 and 2008. The subsidence is complex in the sense that at some locations the subsidence rate is not constant. The complex subsidence leads to difficulties in subsidence modeling. At first, a linear model is used to model the subsidence since a-priori knowledge about the subsidence is unknown. Later, we find that the linear model is not appropriate and results in part of the subsidence that is not model by the linear model being identified as the master APS when weighted least-squares (WLS) is used. The collocation method is however robust against the functional model imperfection because it models the un-modeled subsidence stochastically. By replacing the linear model by a quadratic

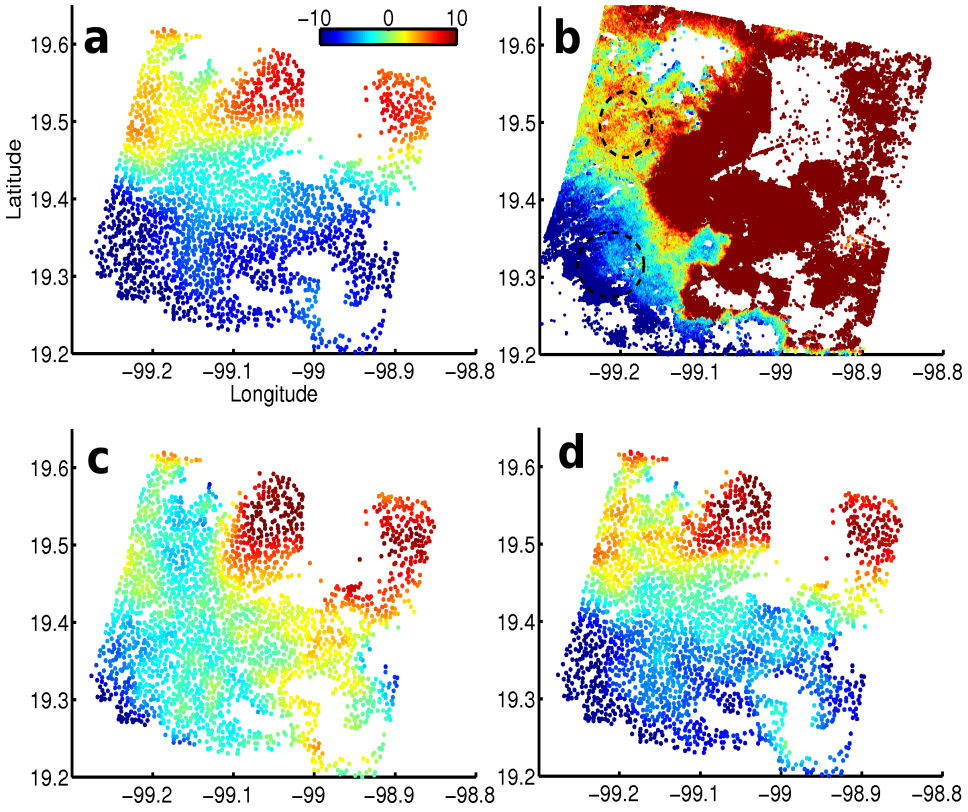

Fig. 6.25. Validation of slave APS estimates using a repeat-pass interferogram. **a**) Temporal difference of APS estimates made by the collocation method on 16-Mar-2007 (master) and 7-Sept-2007 (slave). **b**) Repeat-pass interferograms formed by SLCs on the same dates, including the dominant subsidence signal in the northeast. The clearly visible APS patterns are highlighted by the dashed black circles. The highlighted areas are outside of the subsiding zone. **c** and **d**) Temporal difference of APS estimates made by the filtering method on the same dates using a 1-year and three-year Gaussian window respectively.

model we identify the locations where the subsidence rate is not linear. The locations coincide with the locations where the collocation method detects stochastic deformation (via variance-covariance function). This implies that the collocation method should be used when the ground deformation is expected complex and in the mean time there is no reliable a-priori knowledge about the deformation available. If the filtering method is used in such cases, it may result in leakage of deformation to master APS.

With regards to slave APS estimation, the collocation method seems to give more realistic estimates comparing to the standard filtering method, see Figs. 6.25, 6.26 and 6.27. This is likely due to significant acquisition gaps in the time series. Given a

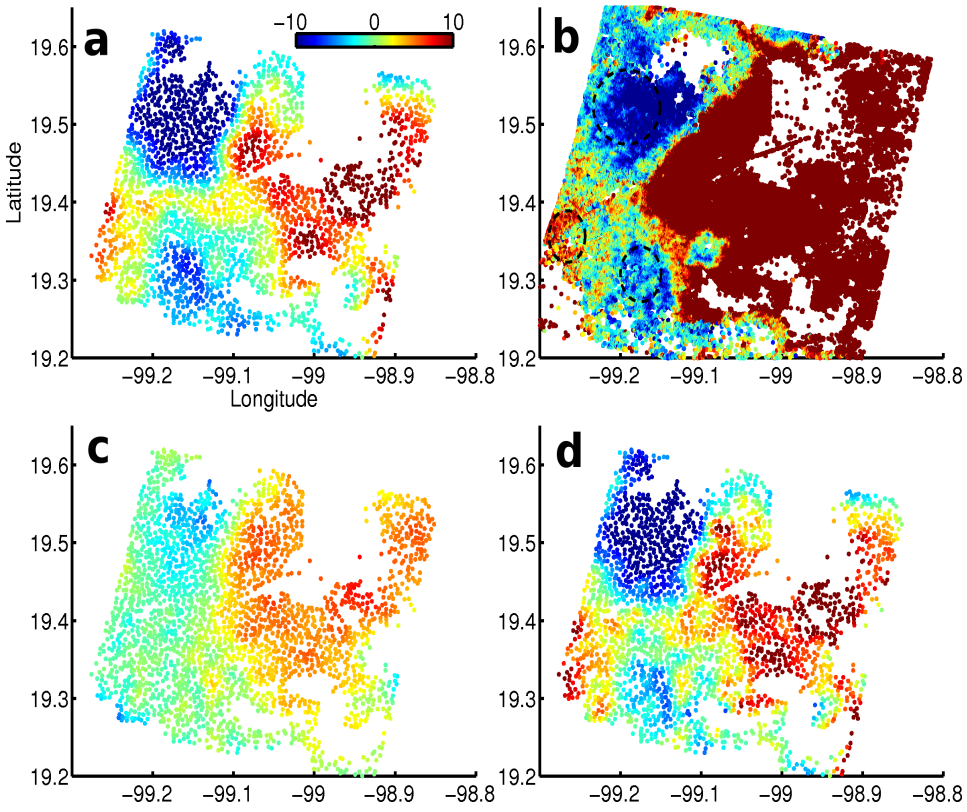

Fig. 6.26. Same as Fig 6.25 but for dates 12-Oct-2007 (master) and 9-May-2008 (slave).

1-year filtering length the filtering method tends to give a biased estimation of APS (smoother than real). The bias can be reduced by increasing the window length to, e.g., $\sim$ 3 years. However, a large window length may result in an underestimation (i.e., over-smoothing) of ground subsidence. The best window length should be the length of the temporal correlation of the ground subsidence. The collocation method tries to estimate the length from the time series itself rather than using a user's guess.

6.4 Groningen, the Netherlands

When ground deformation can be well modeled by a functional model and there are no significant acquisition gaps in time series, the difference of the results from the collocation and filtering methods will be much less noticeable with respect to the previous case studies, especially for the estimates of the deterministic variables (i.e., deformation rate, DEM uncertainty and master APS). However, there still can be a considerable difference between the slave APS estimates from the two methods for

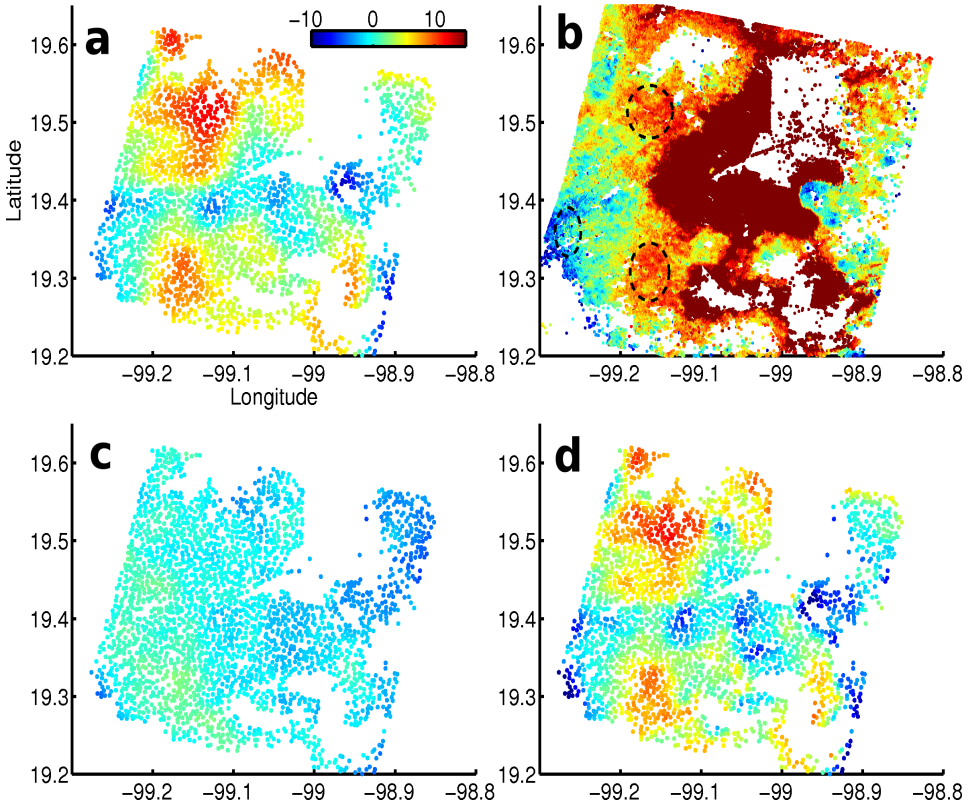

Fig. 6.27. Same as Fig 6.25 but for dates 9-May-2008 (master) and 26-Sept-2008 (slave).

acquisitions taken during extreme weather (e.g., thunderstorm). This is again caused by the equal weighting of slave APS in the filtering method and it may not sufficiently average out APS with large variations due to the extreme weather. Here, we will demonstrate this situation using continuous ASAR time series over Groningen where land subsidence is caused by ground gas extraction and the subsidence is steady in time.

One of the difficulties for comparing the slave APS estimates from the collocation and filtering methods is the lack of ground truth. Although a short baseline interferogram can provide a good mapping of APS (spatio-temporal APS), it may not always be useful for the comparison. This is because the errors (in the time series) made by the filtering method from separating the slave APS and the the unmodelled ground deformation can be temporally correlated. It implies that when a temporal difference is taken between two adjacent slave APS estimates, the errors in the two APS estimates will be largely canceled because of the correlation and result in a comparable spatio-temporal APS as the small baseline interferogram. We will show this effect in section 6.4.4.

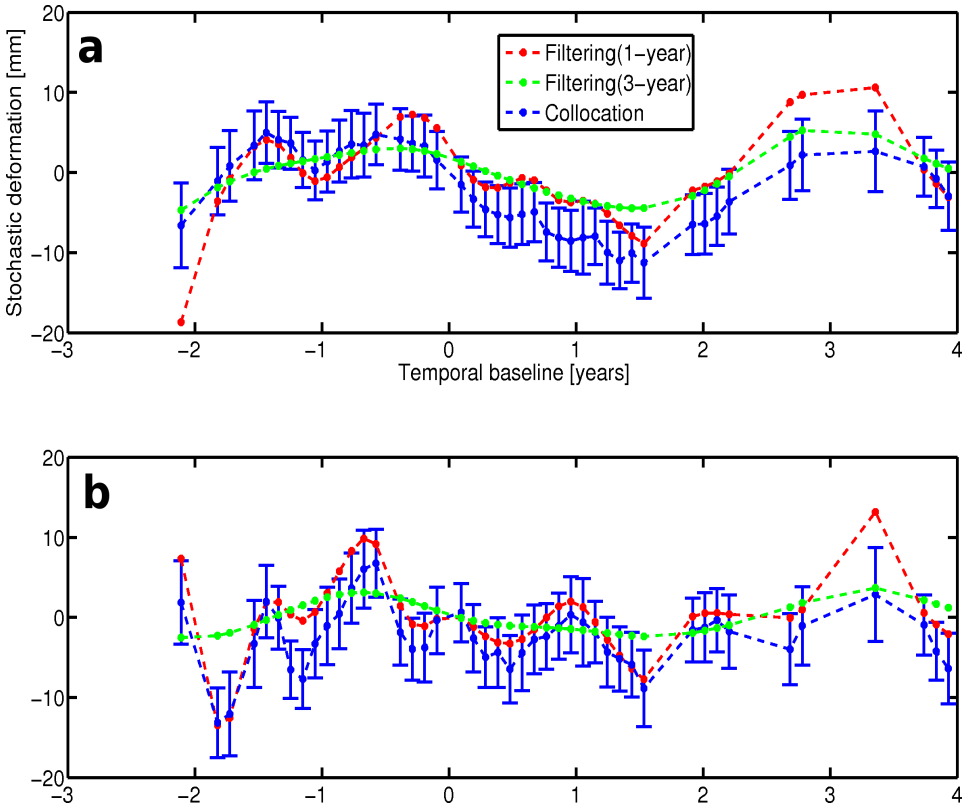

Fig. 6.28. a) Estimated stochastic deformation time series of a PS which has a deformation RMS of 6.2 mm and it is 22 km away from the reference PS shown in Fig. 6.19. b) Estimated stochastic deformation time series of a PS which has a deformation RMS of 6.5 mm and it is 20 km from the reference PSC. The filtering results are based on a Gaussian window with varying window lengths which are subject to users to define. A large window length corresponds to a smoother deformation time series and vice visa. In the collocation method the best window length, i.e., the correlation length of the subsidence, is estimated from the time series.

Last but not the least, in section 6.4.5 we will create artificial acquisition gaps in the time series and compare the slave APS estimates with the corresponding estimates obtained from the full time series. The comparison will tell us about the sensitivity of the collocation and filtering methods to the acquisition gaps.

6.4.1 Test site and data

The Netherlands has a moderate maritime climate with cool summers and mild winters. The warmest month in a year is August and ice days usually occur from December until February. Precipitation throughout the year is relatively equally shared per month. Summer and autumn months tend to have more precipitations

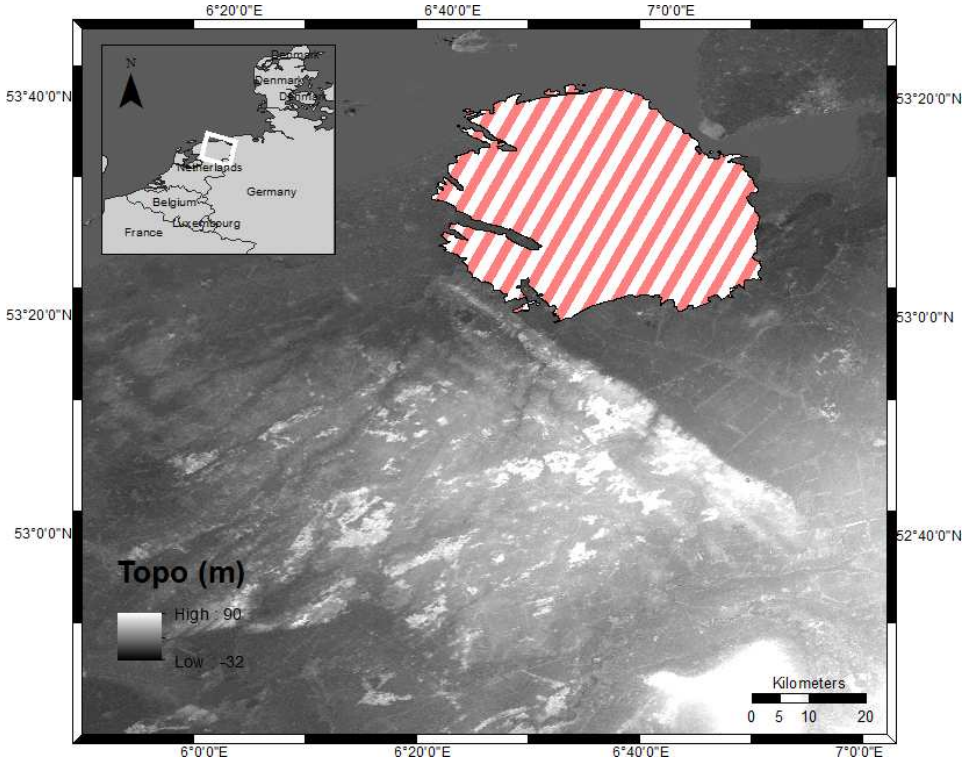

Fig. 6.29. Land topography of Groningen covered by ASAR acquisitions (track: 380, frame: 2533) with a spatial extent of 90 by 90 km. The Groningen gas field is highlighted.

and thunderstorms than the other months (see KNMI (2011)). Groningen is the most northeastern province of the Netherlands and it has the largest gas field (i.e., Groningen gas field) in western Europe. The gas field is currently operated by Nederlandse Aardolie Maatschappij B.V. (NAM) since 1963 and the annual gas production from the field is approximately 30 billion cubic meters. The horizontal extent of the gas field is of $\sim 900\,\mathrm{km}^2$ (see Fig. 6.29) and it is suited at a depth of 2750-2900 m (Ketelaar, 2008). The land subsidence around the gas field has been dedicatedly investigated by Ketelaar (2008) using PSInSAR. The discovered subsidence rate by Ketelaar (2008) in the gas field is less than 1 cm per year and the subsidence is steady in time and can be well approximated by a linear deformation model. Moreover, the land surface in the province is mainly used by agriculture.

The main focus of this case study is to assess the collocation and the filtering methods on APS estimation. Intuitively, a better APS estimation should lead to a better separation of deformation and APS. In this case study we choose Envisat ASAR images from track 380 and frame 2533 (centered at 53°6′ northern latitude and 6°36′ eastern longitude) in descending orbit. In total 68 ASAR images between 21-Dec-2003 and 3-Jan-2010 are available for this time series analysis. The ASAR image

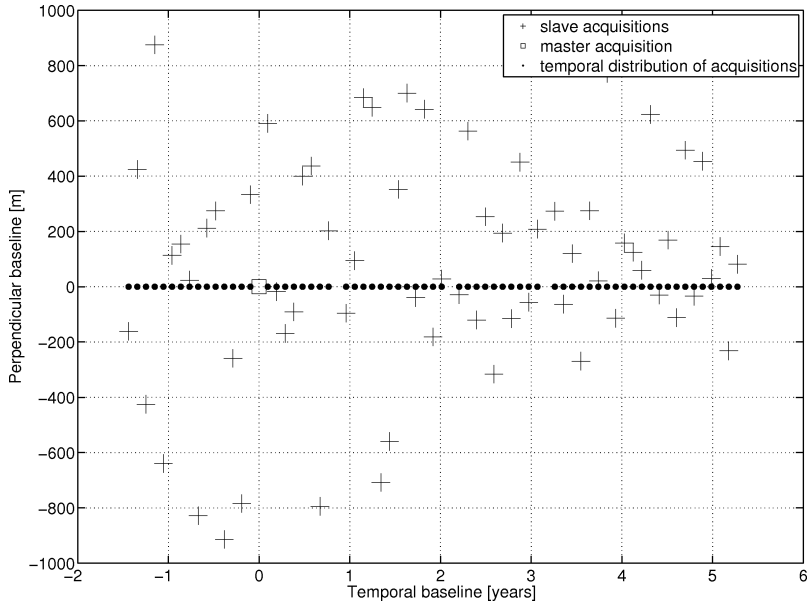

Fig. 6.30. Baseline plot for 68 ASAR acquisitions over Groningen from track 380 frame 2533. The master acquisition on 29-May-2005 is marked as a square. The maximum acquisition gap from the time series is 70 days.

acquired on 29-May-2005 is selected as the master of the time series. The baseline plot of the time series in displayed in Fig. 6.30. The perpendicular baselines range from 18 to 914 m and the longest temporal baseline is 5.3 years. Fortunately, there is no significant acquisition gap in the time series of Groningen, see Fig. 6.30.

For the initial selection of PS we set the thresholds for amplitude dispersion index to 0.22. The first-order PS network consists of 2576 PS with a maximum arc length of 10 km. The relatively large arc length is needed to prevent isolated subnetworks due to the lack of man made targets in the agriculture fields. The disadvantage is that many long arcs of the network will experience relatively large APS disturbance and result in arc rejections during spatial unwrapping. The pre-selected reference PS is located in the center of the region, see Fig. 6.32 a.

6.4.2 Ground deformation estimation

From a previous study by Ketelaar (2008) we already have a good knowledge about the subsidence in the Groningen gas field. The subsidence is steady in time and can be well modeled using a linear deformation model. Regarding possible seasonal deformation over the province due to e.g., soil compaction we model it using a hole effect stochastic model per PS. The estimated stochastic deformation is shown in Fig. 6.31. As we can see from the figure, the stochastic deformation is overall negligible, which implies that the linear deformation model can well describe the subsidence in the gas field. The estimated subsidence rate by the collocation method

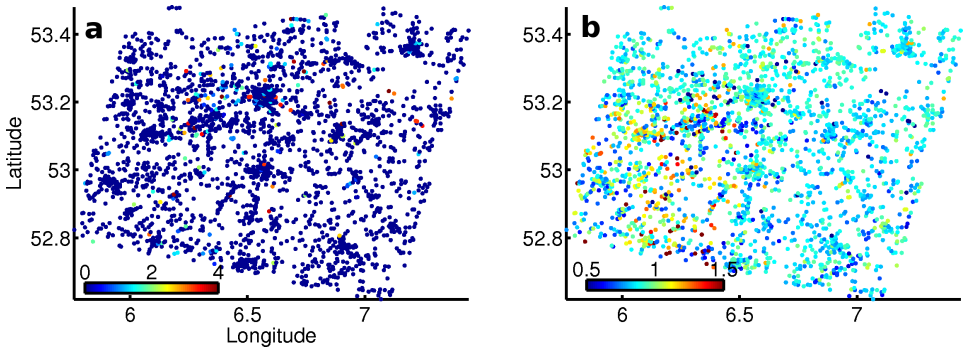

Fig. 6.31. Stochastic subsidence modeling (on PS) over Groningen using a hole effect variance-covariance model. **a**) Estimated RMS (unit: mm). **b**) Estimated temporal correlation length (unit: years). Although the estimated correlation length is not zero everywhere, the estimated RMS suggest that the non-linear deformation is negligible (less than 2 mm). Therefore, the local subsidence over the area of interest can be well modeled by a linear functional model.

is shown in Fig. 6.32 a. Similar to the Dubai dataset (see Fig. 6.7) we find that there is a spatial trend embedded in the estimated subsidence rate. The same spatial trend is also reported in Ketelaar (2008). The subsidence rate after de-trending is plotted in Fig. 6.32 b. For comparison we plot the subsidence rate estimated using WLS in Fig. 6.32 c. Finally, the difference between the two subsidence rate estimates are shown in Fig. 6.32 d. Similar to the precious case studies, the difference is again quite small. Therefore, we conclude that the subsidence in the gas field can be well modeled by both methods based on a simple linear functional model.

6.4.3 Master APS and DEM inaccuracy estimation

Since the subsidence in the area of interest is linear and steady and there are no significant acquisition gaps in the time series, the collocation and filtering methods therefore give comparable estimates for the DEM inaccuracy and master APS. Their estimates are presented in Appendix B.

6.4.4 Slave APS estimation

Clouds appear almost everyday in the Netherlands, which results in MERIS images from the same orbit track as the ASAR images being strongly contaminated and cannot be used to assess the slave APS estimates. Alternatively, considering the low subsidence rate over the region it is possible to assess the estimates by comparing them to atmosphere-only interferograms which have short temporal baselines (e.g., 35-day). Because the land surface of the region is mainly used for agriculture, many 35-day interferograms over the region are therefore too noisy (i.e., temporal decorrelation) to provide realistic APS for validation. Fortunately, there are a few 35-day interferograms with short perpendicular baselines (e.g., < 300 m) remaining

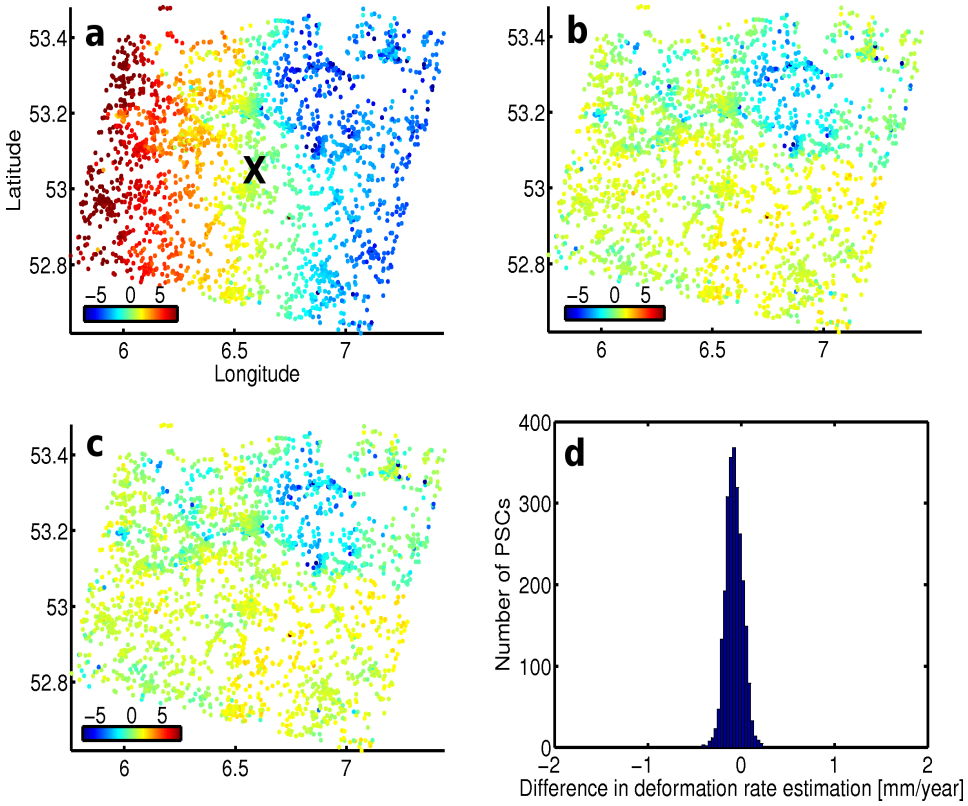

Fig. 6.32. Subsidence rate estimation over Groningen using a linear deformation model. **a**) Estimated deformation rate (unit: mm/year) using the collocation method. The reference PS of the first-order network is marked as a black cross. **b**) The deformation rate after removing the spatial trend in Fig. 6.32 a. **c**) Estimated deformation rate using WLS (de-trended as well). **d**) Histogram of the difference between the deformation rates shown in Fig. 6.32 b and c. In conclusion, the two methods give similar subsidence rate estimates.

coherent. Most of these interferograms are formed by images acquired during winters when the ground surface is relatively barren.

To enable a direct comparison with the slave APS estimates we first interpolate APS at the PS locations from the atmosphere-only interferograms and then spatially differentiate the interpolated APS with respect to the reference PS. The interpolation is carried out after phase unwrapping. We plot two atmosphere-only interferograms as examples in Fig. 6.33 e, f for the pair on 31-Oct-2004 and 5-Dec-2004 and the pair on 7-Aug-2005 and 11-Sept-2005 respectively. The corresponding collocation and filtering results are shown in Fig. 6.33 a, c for the first pair and in Fig. 6.33 b, d for the second. Clearly, both collocation and filtering results match well with the ground truth (i.e., the atmospheric-only interferograms). For the first pair we

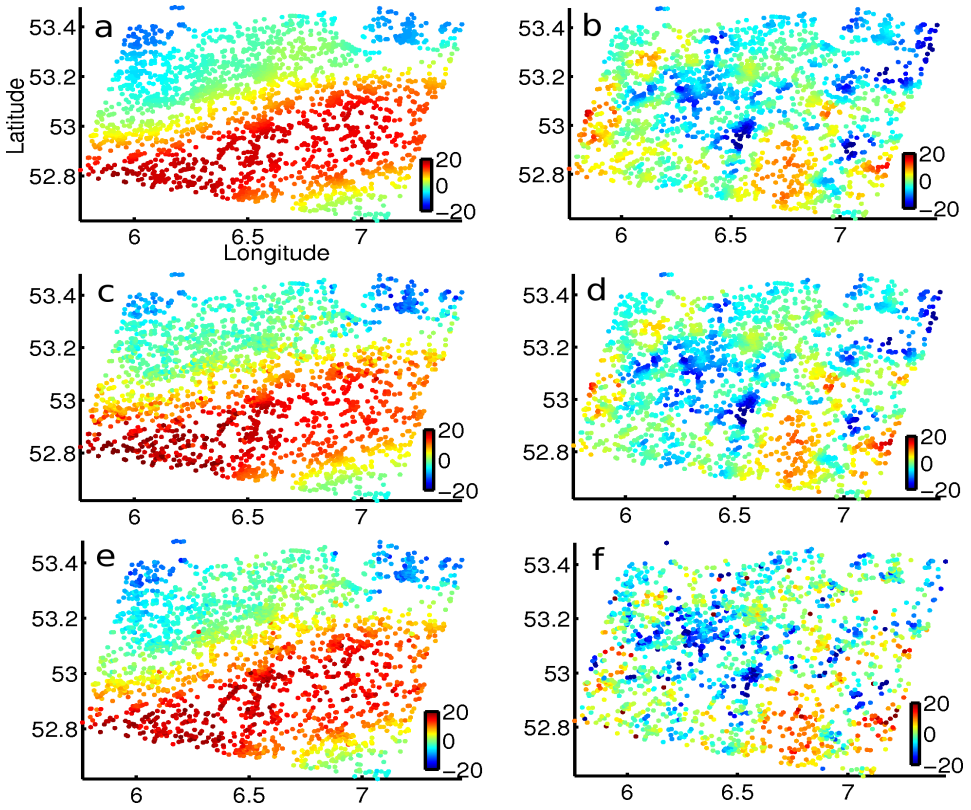

Fig. 6.33. Validation of slave APS estimates using atmospheric-only interferograms. **a**) Temporal difference (unit: mm) between slave estimates from the collocation method on 31-Oct-2004 and 5-Dec-2004. **b**) Temporal difference (unit: mm) between slave estimates from the collocation method on 7-Aug-2005 and 11-Sept-2005. **c**) Same as Fig. 6.33 a but the estimates are from the filtering method. **d**) Same as Fig. 6.33 b but the estimates are from the filtering method. **e**) Atmospheric-only interferogram (unit: mm) between 31-Oct-2004 and 5-Dec-2004. **f**) Atmospheric-only interferogram between 7-Aug-2005 and 11-Sept-2005.

plot the differences between the estimates and the ground truth in Fig. 6.34 a, b. The histograms of the differences are given in Fig. 6.34 c, d. The mean and RMS of the difference between the collocation result and the ground truth are 0.04 and 1.6 mm respectively. For the filtering result the mean and RMS are 0.1 and 2.5 mm respectively. Thus, for this pair the collocation result is slightly better. In the same way, we plot the differences for the second pair in Fig. 6.35 a, b. The corresponding histograms are displayed in Fig. 6.35 c, d. For the collocation method the mean and RMS of the difference is 0.18 and 5.7 mm respectively. With regard to the filtering method the mean and RMS are -0.01 and 5.4 mm respectively. Hence, in this case the filtering method is slightly better.

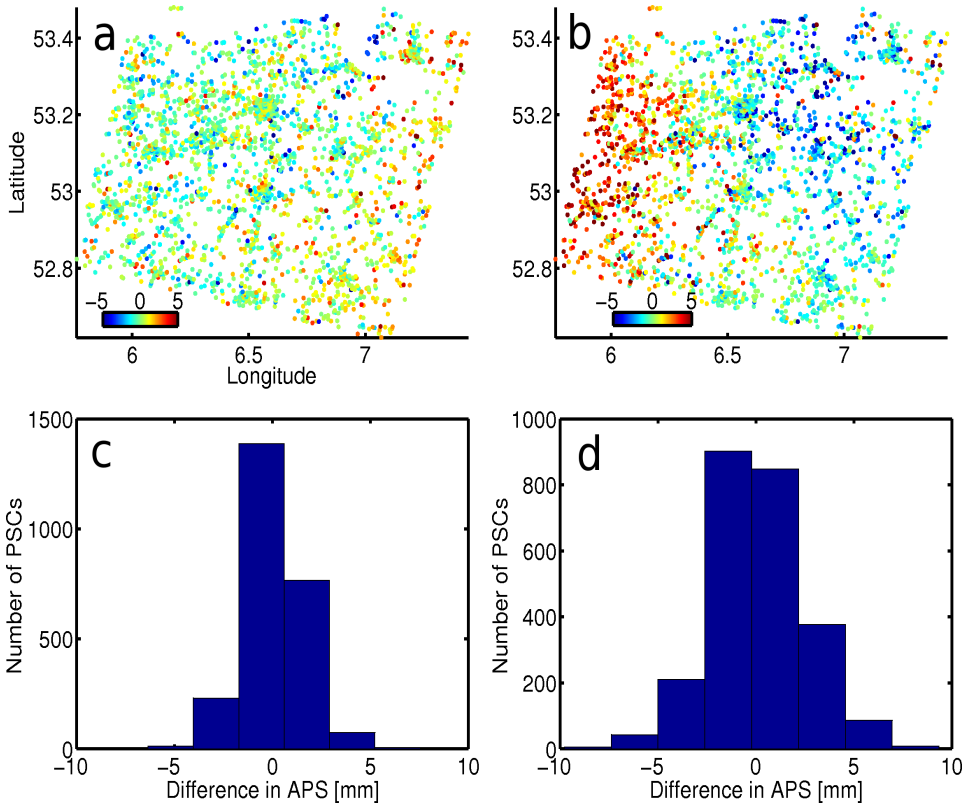

Fig. 6.34. **a**) Difference between the APS estimates shown in Fig. 6.33 a and the ground truth in Fig. 6.33 e. **b**) Difference between the APS estimates shown in Fig. 6.33 c and the ground truth in Fig. 6.33 e. **c**) Histogram of the difference shown in Fig. 6.34 a. **d**) Histogram of the difference shown in Fig. 6.34 b. In conclusion, the collocation method gives a slightly better APS estimates for the slave acquisitions.

We should however not misinterpret the comparisons to reach the conclusion that the slave APS estimates obtained from the two methods are comparable at all times. We have demonstrated in Chapter 5 (see Figs. 5.21 and 5.22) and section 6.2 (see Fig. 6.14) that the errors in slave APS estimates are strongly correlated in time. This is because the error is mis-identified as un-modeled deformation which is correlated in time. In other words, if we take the temporal difference between adjacent slave APS estimates the error will be largely canceled. To demonstrate that we use the slave APS estimates to compute the temporal difference of the estimates in a cascade way as:

$$\Delta\phi_{\mathrm{APS}}^{i,i-1} = \phi_{\mathrm{APS}}^{i} - \phi_{\mathrm{APS}}^{i-1}, \tag{6.4.1}$$

where i ranges from 2 to N, and N is the total number of SLCs in the time series. In this manner we obtain two sets of $\Delta\phi_{\mathrm{APS}}^{i,i-1}$. The first set is obtained based on estimates from the collocation method and the second set is from the filtering

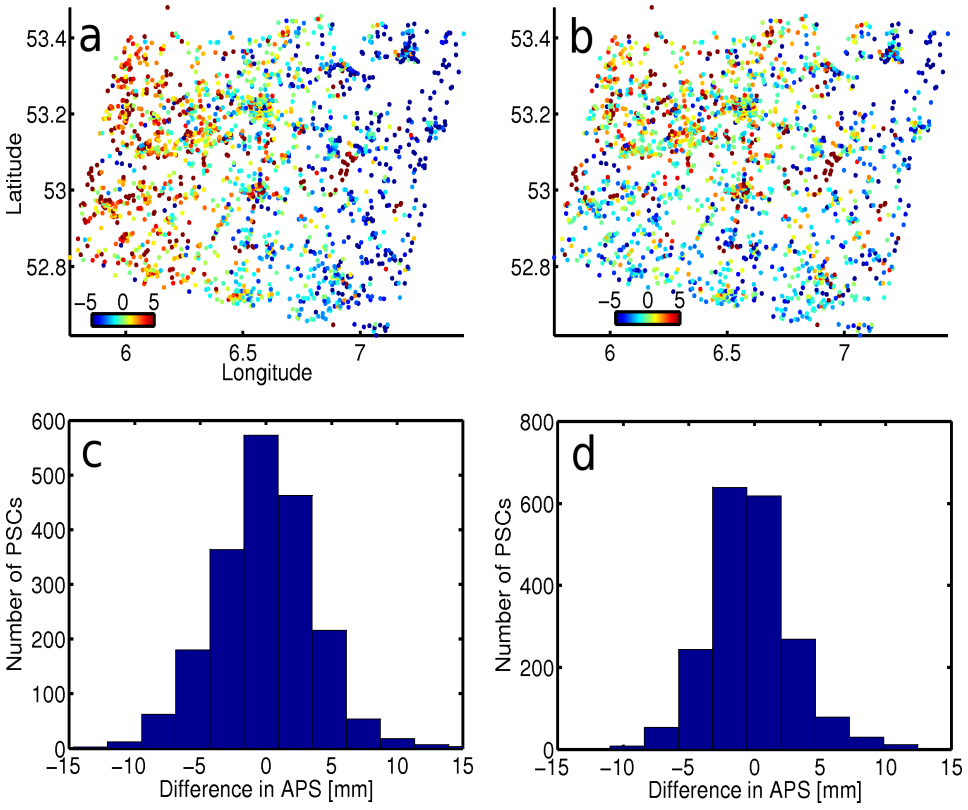

Fig. 6.35. **a**) Difference between the APS estimates shown in Fig. 6.33 b and the ground truth in Fig. 6.33 f. **b**) Difference between the APS estimates shown in Fig. 6.33 d and the ground truth in Fig. 6.33 f. **c**) Histogram of the difference shown in Fig. 6.35 a. **d**) Histogram of the difference shown in Fig. 6.35 b. In conclusion, the filtering method gives a slightly better APS estimates for the slave acquisitions.

estimates (using a 1-year Gaussian window). For every $\Delta\phi_{\mathrm{APS}}^{i,i-1}$ in each set we compute its RMS. The RMSs of the first and second sets are visualized in Fig. 6.36 b in blue and green respectively. To evaluate the difference of $\Delta\phi_{\mathrm{APS}}^{i,i-1}$ between the two sets we show the RMSs of their differences in red in Fig. 6.36 b. The mean of the RMSs shown in blue, green and red are 7.4, 7.3 and 1.7 mm respectively. Therefore, on average the two sets of $\Delta\phi_{\mathrm{APS}}^{i,i-1}$ agree reasonably well, which is consistent with what we have shown in Fig. 6.33 in which we compare the temporal differences of the APS estimates to the corresponding atmospheric-only interferograms having a 35-day temporal baseline.

However, if we look at Fig. 6.36 a in which we plot the same sort of RMSs but based on the APS estimate per slave we observe that the RMSs of the differences (shown in red) between the collocation and filtering results are on average considerably larger than the RMSs of the differences shown in Fig. 6.36 b. The mean of all RMSs in

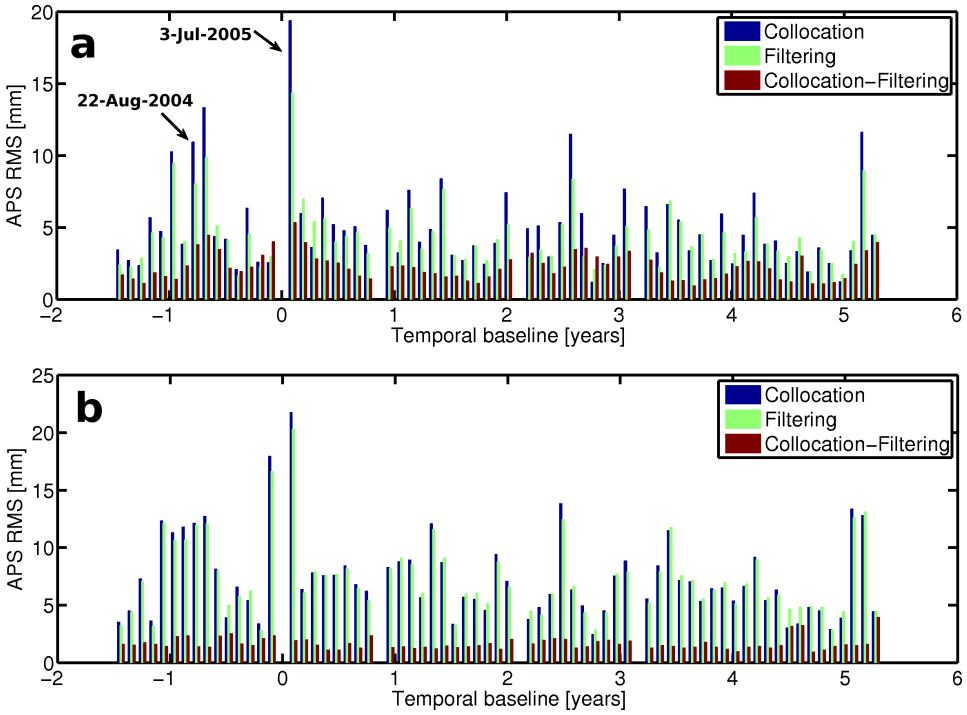

Fig. 6.36. a) RMSs of slave APS estimates. Blue: based on the collocation estimates. Green: based on the filtering estimates. Red: RMS of the differences between the two estimates. b) RMSs of the cascade APS computed using Eq. (6.4.1). Therefore, the collocation and filtering methods give different APS estimates for each individual slave acquisition, but the difference is largely canceled by taking the temporal difference between two adjacent APS estimates.

Fig. 6.36 a shown in blue, green and red are 5.1, 4.5 and 2.3 mm respectively. Thus, the slave estimates made by the two methods are more inconsistent by about 50%. Here we need stress that for the separation of APS and ground deformation the APS estimate per slave is important, given the same master APS estimate by the collocation and filtering methods.

In addition, from Fig. 6.36 a we also notice that the RMS of the difference becomes relatively large around acquisitions which have relatively large APS RMS. In other words, the slave APS estimates from the two methods are more different around slave acquisitions that were taken during extreme weather with a more turbulent troposphere than usual. In such cases we expect that the collocation method gives a more realistic estimation of APS and the large difference between the two methods should be mainly caused by the estimation error of the filtering method. In Chapter 4 we revealed that the filtering method treats the spatial variation of APS per acquisition equally during the temporal low-pass filtering. Given the limited window length (typically 1-year) it is difficult for the filtering method to completely average

out the APS at these acquisitions. Moreover, the APS estimates from the filtering method at the adjacent acquisitions are more prone to get biased by the strong APS at these acquisitions. This can be seen from Figs. 6.37 and 6.38 where we plot the corresponding APS estimates for a subset of continuous slave acquisitions. The acquisitions on 26-Sept-2004 and 3-Jul-2005 have the largest APS variations in their own neighborhoods, see Fig. 6.36. In addition, the acquisition on 22-Aug-2004 also has a large APS variation. From Fig. 6.37 we can see that the differences between the APS estimates on 22-Aug-2004, 26-Sept-2004 and 31-Oct-2004 are strongly correlated and the differences largely resemble the APS on 22-Aug-2004 and 26-Sept-2004. In Fig. 6.38 we see the same pattern that the differences between the APS estimates on 24-Apr-2005, 3-Jul-2005 and 7-Aug-2005 are highly correlated and they resemble the APS on 3-Jul-2005. We believe the equal weighting of APS in the filtering method causes the bias. Although we do not have a direct evidence to prove our hypothesis, the simulation in Chapter 5 (see Figs. 5.21 and 5.22) obviously supports the hypothesis. Therefore, we suggest that the collocation method should give a better estimation of the slave APS and it should be the result of the effectively weighting of the time series using the estimated APS variance per acquisition (see discussion in section 4.4).

6.4.5 Slave APS estimation in the presence of acquisition gaps

The goal of this section is to demonstrate that the collocation method is much less sensitive to acquisition gaps than the filtering method. From previous case studies we found that the slave APS estimates from the filtering method are considerably poor for the acquisitions close to the gaps (> 70 days). Fortunately in this case study no significant gaps exist in the whole time series. On the other hand, the time series of Groningen provides us an opportunity to investigate the effect of the gaps on slave APS estimation. The investigation can be done by taking out some of the slave acquisitions from the original time series to create artificial gaps. Consider two sets of slave APS estimates, one is obtained using the full time series and the other from the time series with gaps. The first set of APS estimates should be more accurate than the second since there are more acquisitions involved in the temporal filtering. Equivalently, with the same level of APS reduction, the required number of acquisitions for filtering out APS will be smaller (comparing to an equal weighting of all APS in the time series) if the APS per slave acquisition is properly weighted. In other words, the collocation method should be more effective than the filtering method in reducing APS when there are gaps in the time series.

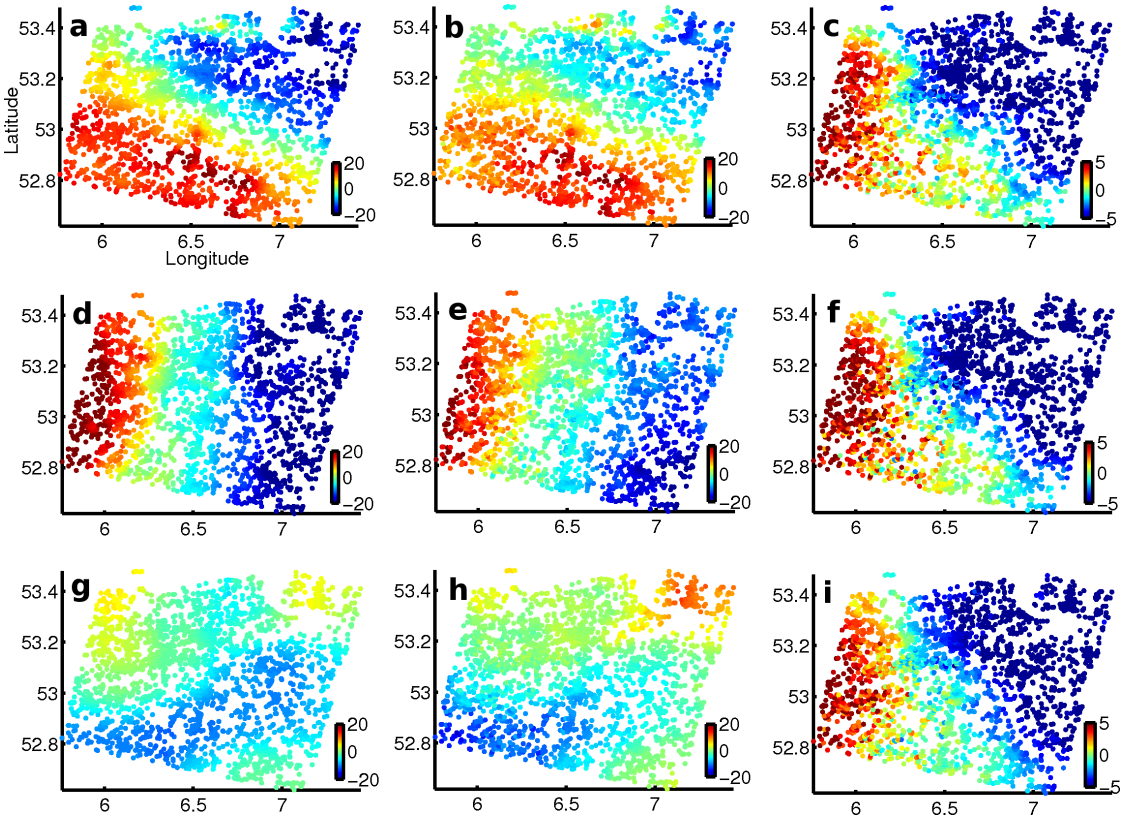

Fig. 6.37. $\mathbf{a}$, $\mathbf{d}$, $\mathbf{g}$) APS estimates by the collocation method on 22-Aug-2004, 26-Sept-2004 and 31-Oct-2004 respectively. $\mathbf{b}$, $\mathbf{e}$, $\mathbf{h}$) APS estimates by the filtering method using a 1-year Gaussian window. $\mathbf{c}$, $\mathbf{f}$, $\mathbf{i}$) Difference between the corresponding APS estimates of the two methods. As we can see the differences between the two estimates are temporally correlated and resemble the spatial pattern of the APS (on 26-Sept-2004) that has the largest spatial variation in its neighborhood.

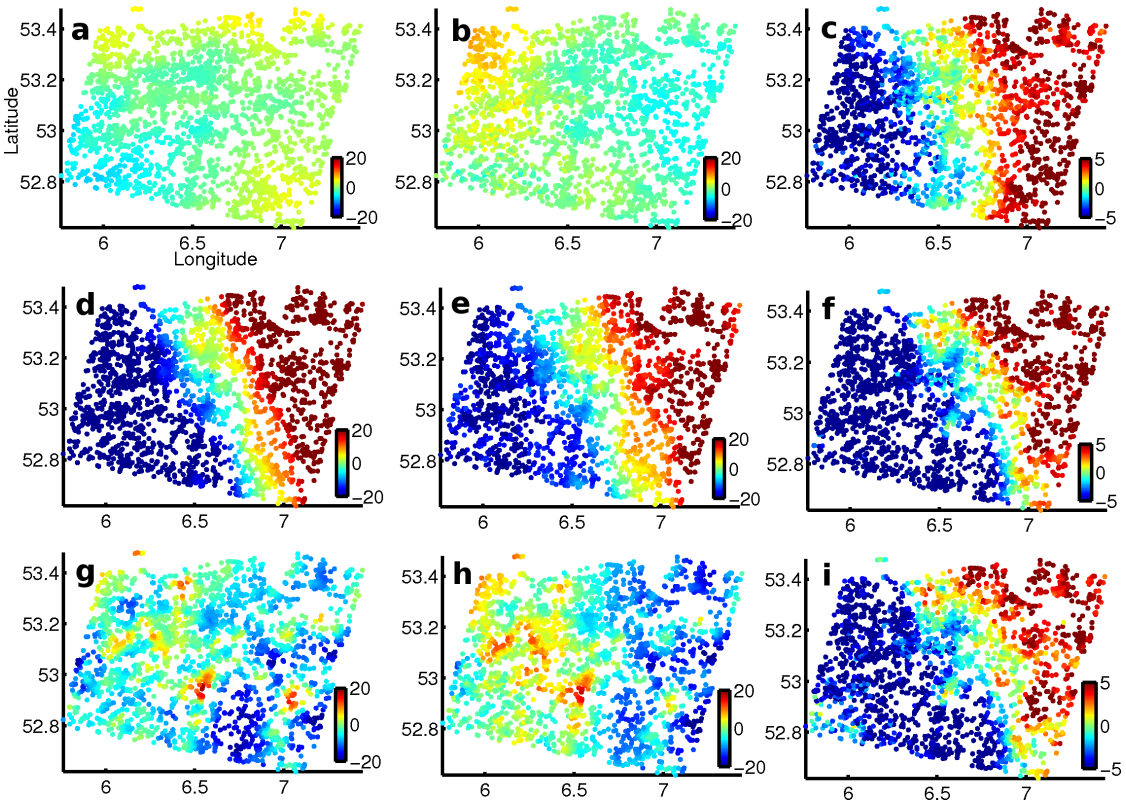

Fig. 6.38. $\mathbf{a}$, $\mathbf{d}$, $\mathbf{g}$) APS estimates by the collocation method on 24-Apr-2005, 3-Jul-2005 and 7-Aug-2005 respectively. $\mathbf{b}$, $\mathbf{e}$, $\mathbf{h}$) APS estimates by the filtering method using a 1-year Gaussian window. $\mathbf{c}$, $\mathbf{f}$, $\mathbf{i}$) Difference between the corresponding APS estimates of the two methods. As we can see the differences between the two estimates are temporally correlated and resemble the spatial pattern of the APS (on 3-Jul-2005) that has the largest spatial variation in its neighborhood.

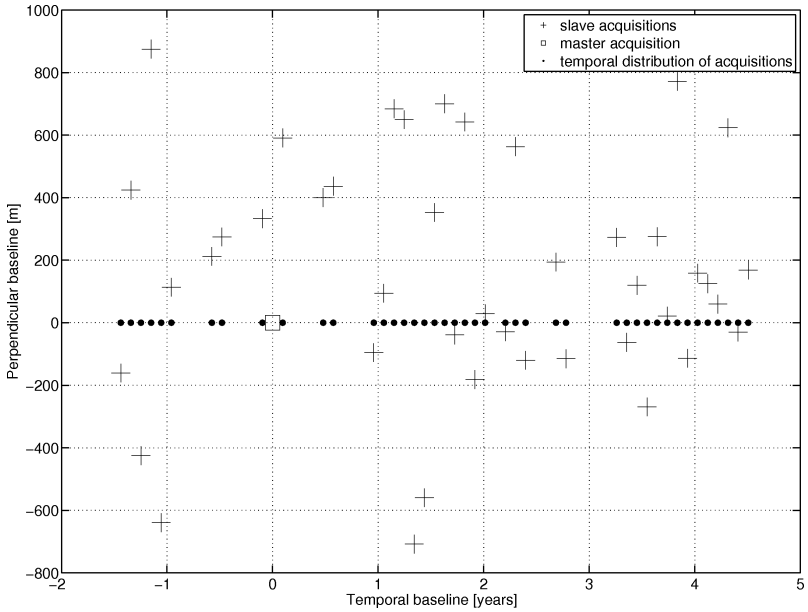

Fig. 6.39. a) Baseline plot of the new time series after taking out 24 slave acquisitions from the original time series, see Fig. 6.30 for comparison.

In line with the discussion above we randomly select 24 out of 67 slave acquisitions and take them out from the original time series. The baseline plot of the new time series is given in Fig. 6.39. The created acquisition gaps ranges from 105 to 175 days. We apply both methods to the new time series and compare the result from each method to the result obtained from the same method but based on the original full time series. We plot the comparison in terms of the mean and RMS of the residue (difference between the results from the same method) per acquisition in Fig. 6.40. It can be seen that the results from the collocation method are obviously much more consistent, i.e., less sensitive to the acquisition gaps than the filtering method. The RMSs of the collocation residues shown in Fig. 6.40 a are limited between 0.4 and 1.6 mm. In contrast, the RMSs of the filtering residues ranges from 1.0 to 9.3 mm. Moreover, the collocation residues shown in Fig. 6.40b in general have a smaller mean than the filtering residues, i.e., they are less biased with respect to the APS estimates obtained based on the full time series. Therefore, we have demonstrated that the filtering method is indeed sensitive to acquisition gaps, which results in a rather poor estimation of slave APS. In contrast, the collocation method is much less affected by the gaps and gives consistent estimates of slave APS.

6.4.6 Summary

In this case study we have investigated the land subsidence in the Groningen gas field using the collocation method. The results confirm the conclusion made by Ketelaar (2008) that the subsidence is steady in time and can be well modeled by

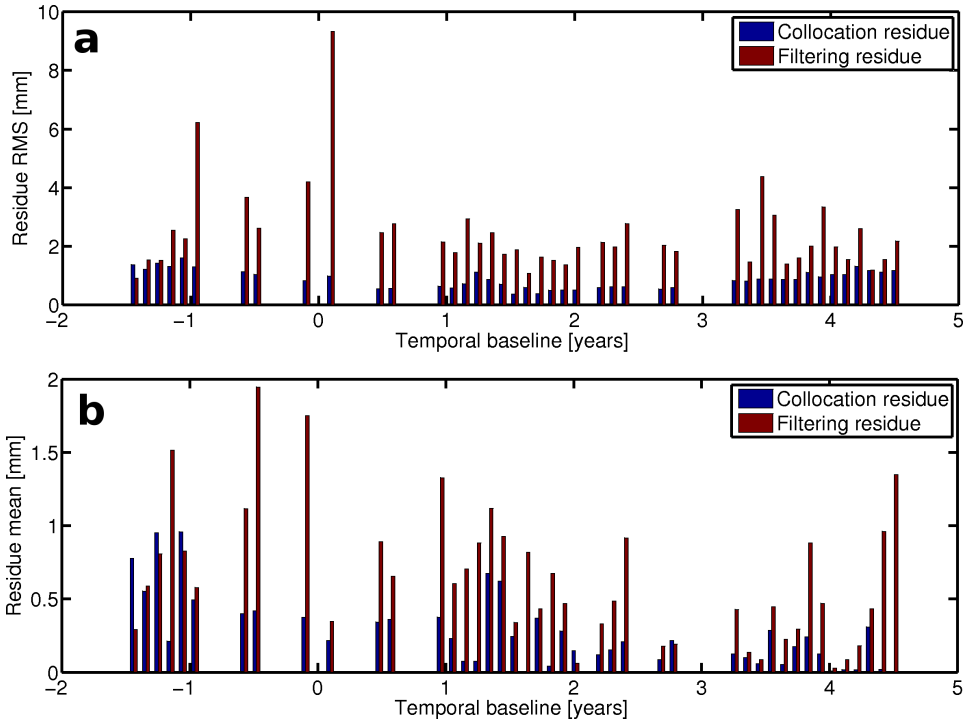

Fig. 6.40. a) Each blue bar represents the RMS (unit: mm) of the difference between slave APS estimates by the collocation method for the same acquisition. The difference is due to the created artificial gaps in the original full time series, see Fig. 6.39. Each red bar presents the RMS of the difference between slave APS estimates by the filtering method for the same acquisition. b) Each blue bar represents the mean (unit: mm) of the difference between slave APS estimates by the collocation method for the same acquisition. Each red bar presents the mean of the difference between slave APS estimates by the filtering method for the same acquisition. As we can see the collocation method gives more or less same estimates of slave APS with and without acquisition gaps. However, the estimates from the filtering method vary significantly if there are significant acquisition gaps in the time series.

a linear functional model. Because of the simple subsidence mechanism and the absence of large acquisition gaps the estimates of the deterministic variables from the collocation and filtering methods are comparable.

In terms of slave APS estimation we find that the results from the collocation and filtering methods exhibit considerable discrepancies for the acquisitions that have relatively large APS variation, i.e., acquisitions taken during turbulent weather. It seems that the discrepancies are mainly the result of the uncompensated APS originated from the filtering method in which every slave APS is weighted equally. Moreover, we find the discrepancies are highly correlated in time and resemble the spatial pattern of the APS that has the largest variation (taken during turbulent

weather) in its neighborhood. Because of the strong correlation it is difficult to validate the APS estimates using atmosphere-only interferograms which have small temporal baselines, i.e., interferograms formed by adjacent acquisitions.

Finally, we have also investigated the sensitivity of the two methods to the acquisition gaps by taking out a number of slave acquisitions from the original time series. We find that the filtering method is much more sensitive to the gaps and its estimates based on the full time series and on the time series with gaps are very different. The results from the collocation method is however not sensitive to the acquisition gaps.

6.5 Island of Hawaii

So far our investigations only focused on flat terrains where APS mainly manifests itself as a lateral variation. For volcano studies it is equivalently important to remove the dependency of APS on local terrain topography (known as vertical stratification) as it can be as large as the lateral variation or even larger, see chapter 3. Therefore, in this case study we will assess the feasibility for the collocation method to estimate both the vertical stratification and the lateral variation. In the collocation method the vertical stratification is modeled in the space domain deterministically using an analytic function of local terrain heights, whereas the lateral variation is modeled stochastically. In contrast, the filtering method does not distinguish the two effects and models them together simply as a temporally uncorrelated noise component.

6.5.1 Test site and data

The big island of Hawaii has a moist and heterogeneous tropical atmosphere. Because of its geographic location it only has two seasons: summer between May and October and winter for the rest of the year. In general, most of the precipitation in a year occurs during the winter season and drier conditions usually take place in summer. The temperature variation on the island is fairly small from 26 to 32 C° between winter and summer. Due to the dominant trade winds over the island clouds are often formed at low altitudes (< 2400 m) where air is more moist than the upper atmosphere (Morgan, 1996). From the MERIS dataset available to us over the island between 2003 and 2008 we can rarely find any cloud free MERIS image, which makes the validation of the APS estimates using MERIS not possible. Moreover, the island has a strong topography variation varying from sea level to approximately 4200 m, see Fig. 6.41. This leads to a strong tropospheric vertical stratification in many of the interferograms used for this case study. Therefore, for the time series analysis of this region we need to take into account the vertical stratification effect which could be ignored in the previous case studies. On the other hand, this provides an opportunity to test the collocation method for the capability of modeling tropospheric vertical stratification in the presence of ground deformation.

The ASAR image stack we use for the time series analysis is from track 200 and frame 3213 in descending orbit. In total there are 39 ASAR images which were acquired between 27-Jan-2003 and 5-Jan-2009. The ASAR image acquired on 7-Mar-2005 is selected as the master of the time series. To limit the computational load we select

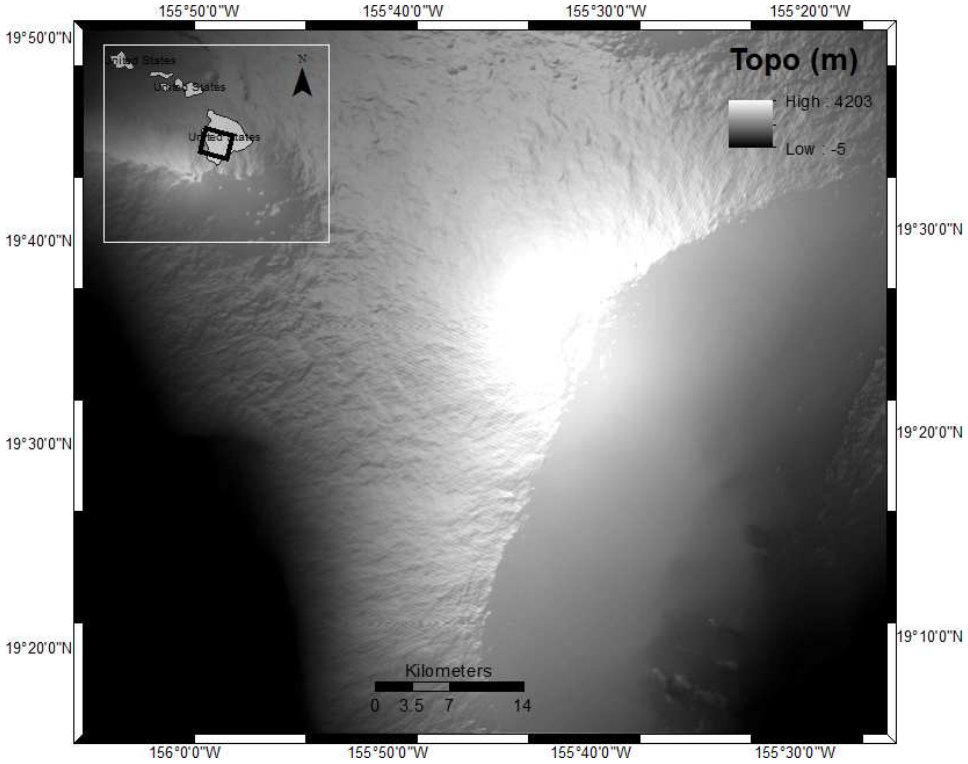

Fig. 6.41. Land topography of island of Hawaii covered by ASAR acquisitions (track: 200, frame: 3213) with a spatial extent of 60 by 60 km.

a 60 by 60 km crop covering the *Mauna Loa* volcano (centered at 19° 28' northern latitude and 155° 35' western longitude), see Fig. 6.41. The baseline plot of the time series is displayed in Fig. 6.42. The perpendicular baselines range from 12 to 1110 m and the longest temporal baseline is 3.8 years. In addition, acquisition gaps up to 175 days are found in time series, see Fig. 6.42.

6.5.2 Ground deformation estimation

Stochastic deformation

The surface deformation around *Mauna Loa* is associated with volcanic inflations, see Amelung et al. (2007). In this study we use a linear model (i.e., constant velocity) to model the deterministic part of the deformation. Given the linear model we attempt to model the stochastic deformation using different variance-covariance models, i.e., Gaussian, spherical and hole effect. The modeled stochastic deformations based on these models are displayed in Fig. 6.43. As we can see from the figure, the modeled stochastic deformations are in general similar to each other. All the models indicate that there is a significant (up to 15 mm/year) deformation component which is not

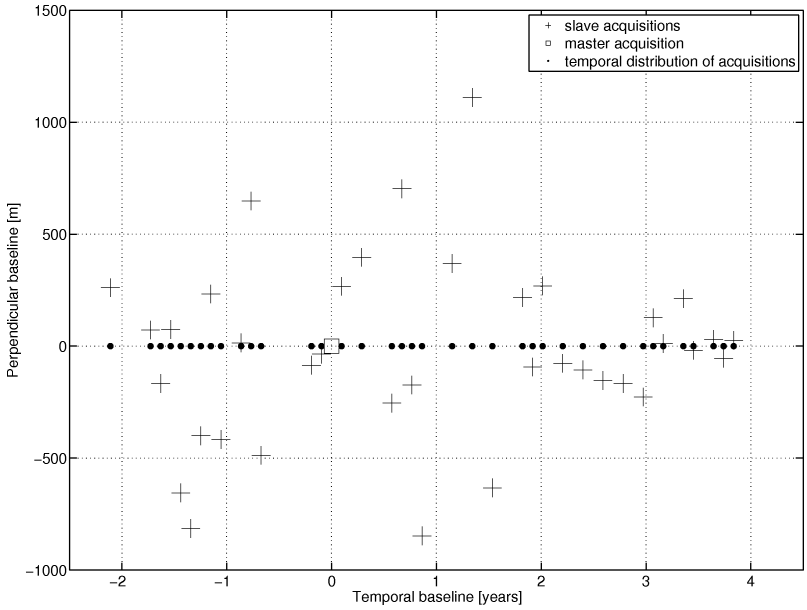

Fig. 6.42. Baseline plot for 39 ASAR acquisitions over the big island of Hawaii from track 200 frame 3213. The master acquisition on 7-Mar-2005 is marked as a square. The maximum acquisition gap from the time series is 175 days

captured by the functional model around the summit. In addition, there is also a noticeable stochastic deformation along the southwest side of the volcano. However, for this area different models give different estimates of the deformation correlation length. Both Gaussian and hole effect models give a relatively short correlation length (~ 0.5 year), but the spherical model suggests a longer correlation ($\sim$ 1 year) in the south. As we have learned from the simulation in chapter 5 the estimate of the correlation length is not always reliable and it can be either too short or too long. This is the reason why we need to fix the possible range of the correlation length between 0.5 and 1.2 years in the collocation method, see Tab. 6.1 On the other hand, the deformation over the area (i.e., along the southwest) however does not have a considerable RMS (i.e., smaller than 5 mm on average) and therefore the induced error by the correlation length should not be significant. Since we do not have the ground truth of the deformation over the area, we decide to used the result based on the hole effect model which is able to model random signals having periodic behaviors.

Deterministic deformation modeled by a functional model

Based on the hole effect variance-covariance model the estimated deterministic deformation using a linear model is shown in Fig. 6.44 a. From the figure we observe both uplift and subsidence, which is consistent with the result obtained by Pepe et al. (2010) using the small baseline subset (SBAS) approach. The subsidence is

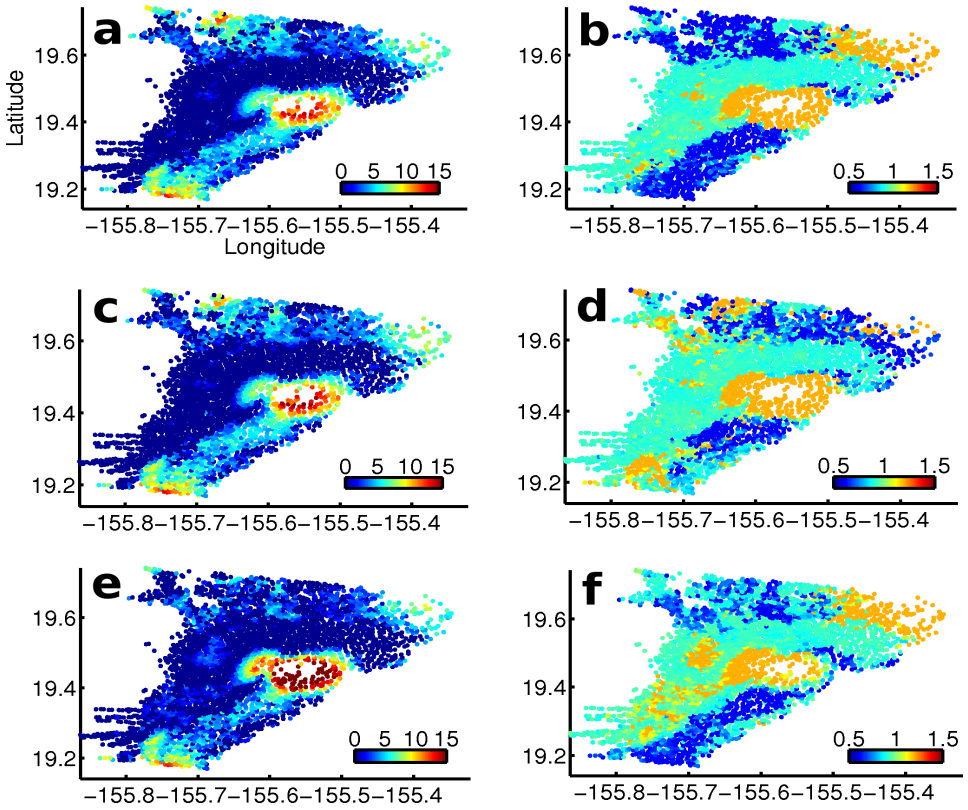

Fig. 6.43. Estimated stochastic surface deformation (over PS) at Mauna Loa volcano, Hawaii. **a** and **b**) RMS (unit: ,mm) and correlation length (unit: years) of the estimated stochastic deformation using a hole effect variance-covariance model. **c** and **d**) RMS and correlation length based on a spherical model. **e** and **f**) RMS and correlation length based on a Gaussian model. As we can see, all stochastic models indicate that the deformation around the submit is not linear and therefore modeled as a stochastic deformation.

observed in the west and south with respect to the summit. The uplift, which is more profound than the subsidence, takes place around the summit where we also observe strong stochastic deformation, see Fig. 6.43. In addition, Fig. 6.44 b shows the deformation rate estimated by WLS (see Eq. 6.1.8). Moreover, the histogram of the difference between the two estimates is given in Fig. 6.44 c. As we can see the absolute difference between the two estimates is less 1 mm. So far we have seen from all the cases that the estimated deformation rates by the two methods are always similar.

Finally, Fig. 6.45 shows full time series of ground deformation of 6 PS which are randomly selected from the subset of PS who have (stochastic) deformation RMS larger than 5 mm. The locations of the selected PS are highlighted in Fig. 6.44 a. One common feature of these time series is that the filtering method based on a Gaussian

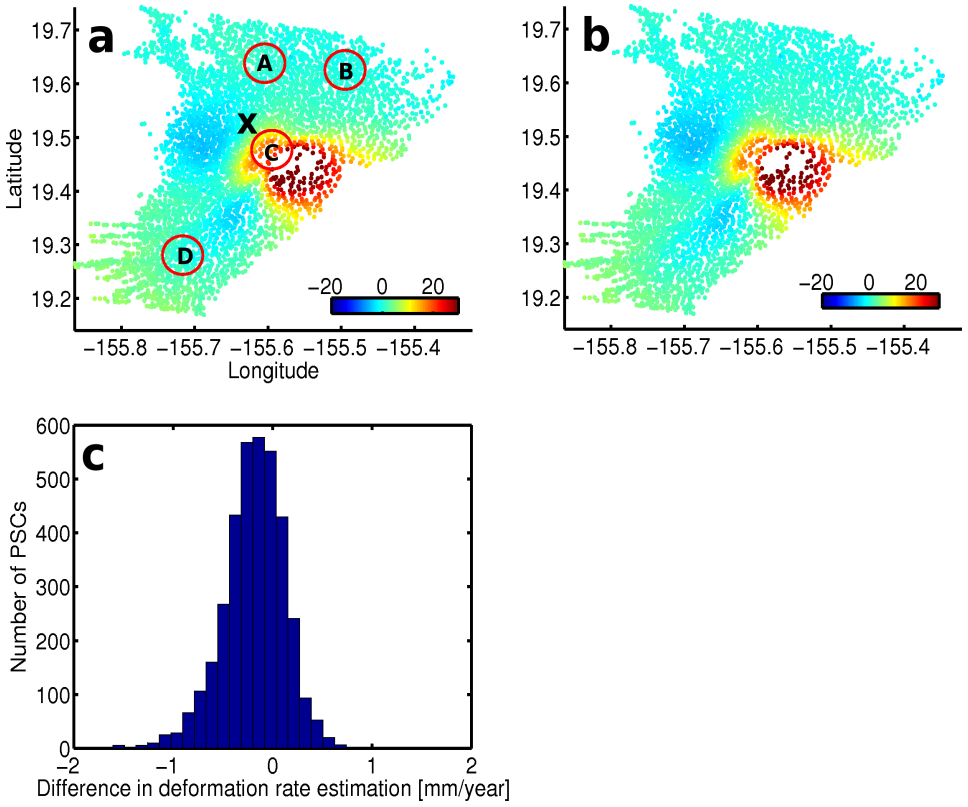

Fig. 6.44. Deformation rate estimation (over PS) over *Mauna Loa* using a linear deformation model. **a**) Estimated deformation rate (unit: mm/year) using the collocation method. The reference PS of the first-order network is marked as a black cross. The red circles highlight the locations of the PS shown in Fig. 6.45. **b**) Estimated deformation rate using WLS, see Eq. 6.1.8. **c**) Histogram of the difference between the deformation rates shown in Fig. 6.44 a and b.

window of one year constantly gives a more oscillating estimation of deformation, especially at locations (in the time domain) where there are significant acquisition gaps. From the precious studies we have learned that the relatively large oscillations are due to leakage of APS, which is caused by the equal weighting of APS variation together with the limited number of images involved in the filtering. The collocation method is however much less sensitive to the acquisition gaps because it weights APS according to its variation per acquisition and therefore does not need as many images as the filtering method to be available within the period of filtering.

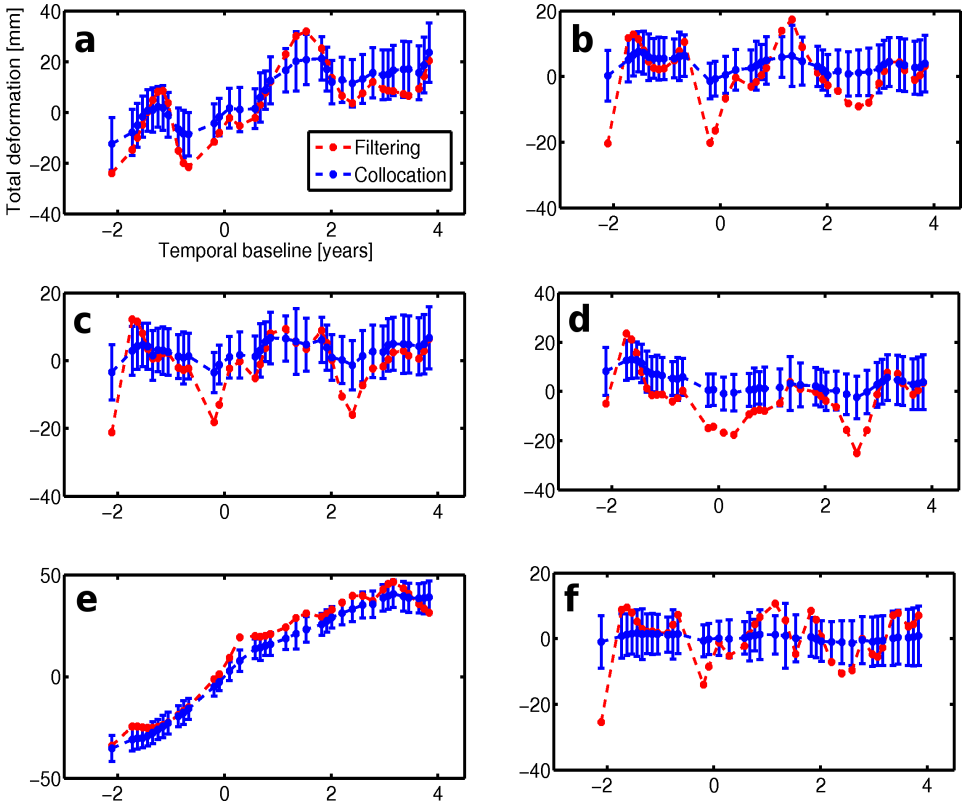

Fig. 6.45. Time series of total deformation estimation. **a**) Estimated deformation time series on a PS from region D in Fig. 6.44 a. The dot-dashed blue line is the result of the collocation method and the dot-dashed red line is the result of the filtering method using a 1-year Gaussian window. **b**, **c**, **d**) PS from region B in Fig. 6.44 a. **e**) PS from region C in Fig. 6.44 a. **f**) PS from region A in Fig. 6.44 a. The oscillations in the filtering results are likely artificial and caused by the acquisition gaps in the time series.

6.5.3 APS estimation

We do not show the estimates of master APS and DEM inaccuracy since the two methods (i.e., collocation and filtering) do not give noticeable difference, just like the precious case studies. Instead, in this section we will focus on the feasibility of estimating the tropospheric vertical stratification effect using the collocation method. Moreover, we will also investigate the slave APS estimates from the two methods (i.e., filtering and collocation). Since there are no cloud-free MERIS images available, the only way we can validate the estimates is to compare them with repeat-pass interferograms that have short baselines. Fortunately, the island on average remains fairly coherent in the interferograms having a 70-day baseline or shorter.

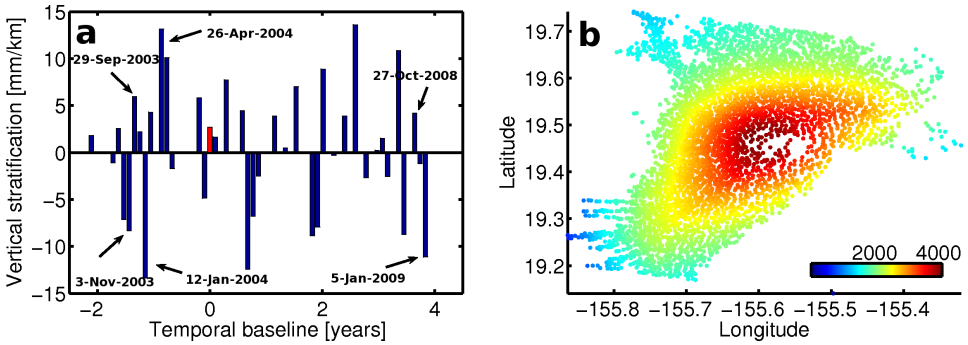

Fig. 6.46. Estimated vertical stratification coefficient (unit: mm/km) per acquisition by the collocation method. **a)** Estimated k per acquisition using a linear model, see Eq. 6.5.1. The $\hat{k}$ for master is highlighted in red. **b)** Topography heights in meters of PS (from SRTM).

Estimation of tropospheric vertical stratification

The topography heights of the PS are displayed in Fig. 6.46 b. To model the vertical stratification effect of delay between two PS p and q we choose a linear model (Elosegui et al., 1998; Delacourt et al., 1998; Onn and Zebker, 2006):

$$D^{\mathrm{vs}}_{p,q} = k\Delta H = k(H_p - H_q), \tag{6.5.1}$$

where k is a vertical stratification coefficient. If the units of delay and height are millimeter (mm) and meter (m) respectively then the unit of k is mm/m. For each ASAR acquisition we estimate a constant k over the full image. The estimate of k per acquisition is shown in Fig. 6.46 a. Obviously, the estimated k does not have a physical meaning since the delay should always increase as the microwave signal traveling further down to the sea level, i.e., a negative k. Therefore, we should always interpret the estimates of k in terms of their difference between acquisitions. To demonstrate this fact we plot the temporal difference of the estimates for some acquisitions in Fig. 6.47 against the k estimated from the corresponding repeat-pass interferograms using least-squares. The signal in these interferograms should mainly represent APS because of the short temporal baseline. From the figure we can see a very similar delay pattern against the topography height between the two estimates, although the collocation method constantly suggests a larger k. From the figure an overestimation of 5 mm/km on average of k is observed.

Slave APS estimation

We show the posteriori RMS of slave APS estimates obtained from the collocation and filtering methods (using a 1-year Gaussian window) in Fig. 6.48. As we can see the RMSs of the residues (difference) between the two APS estimates are considerably large (4.5 mm on average) comparing to the Groningen case, see Fig. 6.36. The average RMS of the APS estimates of the collocation and filtering methods are 8.5 mm and 6.4 mm respectively. It implies that the latter underestimates the slave

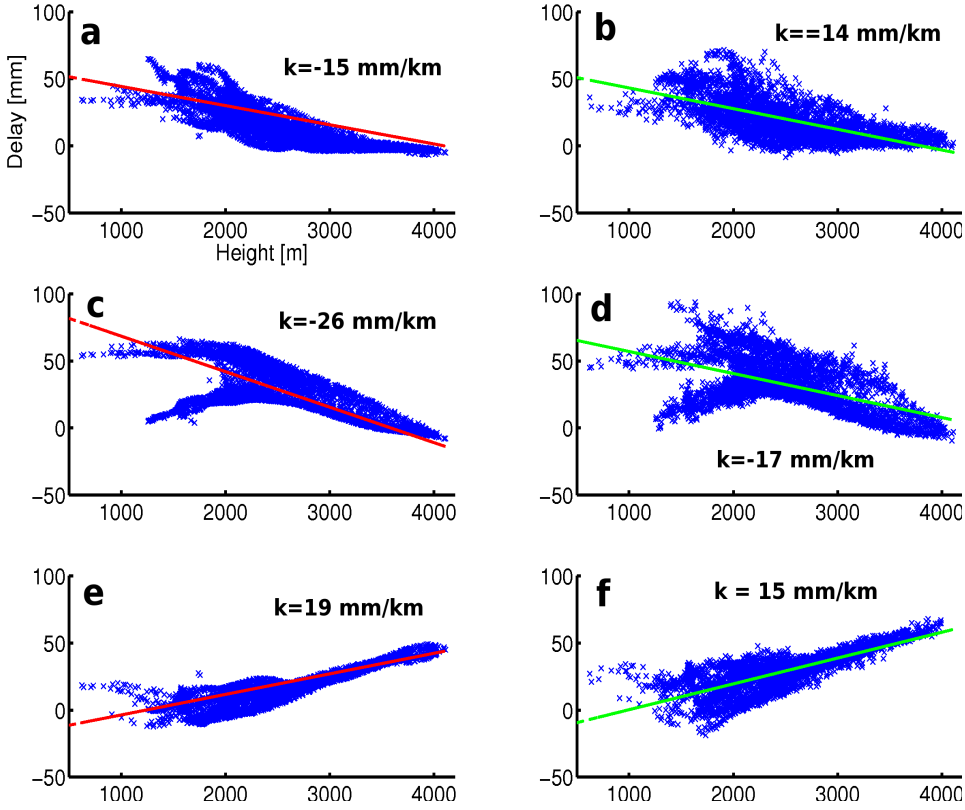

Fig. 6.47. Validation of the estimated vertical stratification coefficients by the collocation method using short-baseline repeat-pass interferograms. **a**) Temporal APS difference between the APS estimates (by the collocation method) on 29-Sep-2003 and 3-Nov-2003. The slope of the red line is the difference between the estimates of the vertical stratification coefficients for the two dates, see Fig. 6.46 a. **b**) Unwrapped phases of the interferogram on 29-Sep-2003 and 3-Nov-2003. The slope of the green line is the estimate of the vertical stratification coefficient for the interferogram using least-squares. **c**) Same as Fig. 6.47 a but on 12-Jan-2004 and 26-Apr-2004. **d**) Same as Fig. 6.47 b but on 12-Jan-2004 and 26-Apr-2004. **e**) Same as Fig. 6.47 a but on 27-Oct-2008 and 5-Jan-2009. **f**) Same as Fig. 6.47 b but on 27-Oct-2008 and 5-Jan-2009. In conclusion, the estimated vertical stratifications matche the ground truth.

APS on average. This is not a surprise because the island has a tropic climate (i.e., a turbulent troposphere) and there are large acquisition gaps ($\geq$ 70 days) in the time series. Given one year filtering length the filtering method is not able to average out the slave APS and therefore results in a leakage from APS to deformation, see Fig. 6.45. To validate the APS estimates we compare them with the corresponding short baseline repeat-pass interferograms in which APS is the dominant signal. Some examples are shown from Fig. 6.49 to Fig. 6.54. In all the examples, the APS

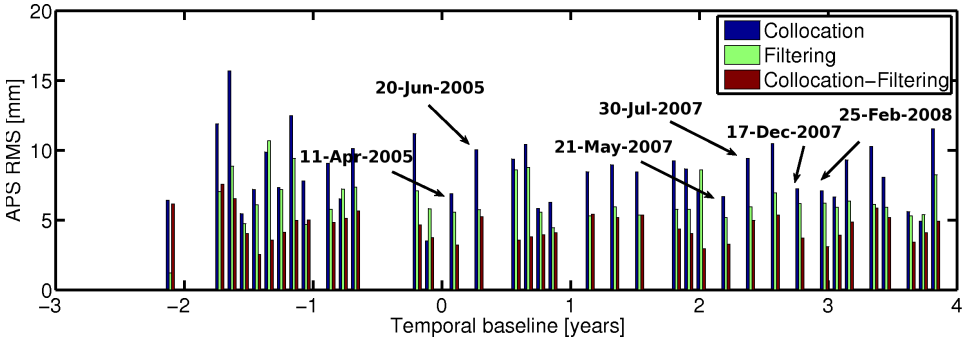

Fig. 6.48. Posteriori RMS (unit: mm) of APS estimate per slave acquisition. Blue: Estimates of the collocation method. Green: Estimates of the filtering method using a 1-year Gaussian window. Red: RMS of the difference between the two estimates. Large residues are seen for acquisitions close to acquisition gaps.

estimates from the collocation method are more accurate.

6.5.4 Summary

In this case study we have demonstrated that the collocation method is able to estimate both the vertical stratification and the lateral variation of APS. To model the vertical stratification we assume a constant vertical stratification coefficient per acquisition. A validation of the estimated coefficients using three short baseline repeat-pass interferograms (corresponding to 6 coefficients) suggests that the collocation method overestimates the effect on average by 5 mm/km. Moreover, we have also demonstrated that the collocation method gives a more reliable slave APS estimate than the filtering method when there are acquisitions gaps ($\geq$ 70 days) in the time series. On average the filtering method using a 1-year Gaussian window underestimates the slave APS by 2.1 mm and the error leaks into the deformation time series.

Regarding the ground deformation based on a linear deformation model we find both uplift and subsidence around the volcano. The velocity estimates by the collocation method and WLS differs less than 1 mm. Moreover, the collocation method suggests that the uplift around the summit is non-linear with a deformation RMS up to 15 mm.

6.6 Summary

In this chapter we applied the collocation method to InSAR time series from four different climatic regions (Dubai, Mexico city, Groningen and Hawaii). Among these regions the island of Hawaii has a strong land topography variation, which often leads to a strong vertical stratification effect in APS. The a-posteriori RMSs of the APS estimates for these regions indicate that the local troposphere is in general more turbulent in coastal regions (i.e., Hawaii, the Netherlands) and regions that have a

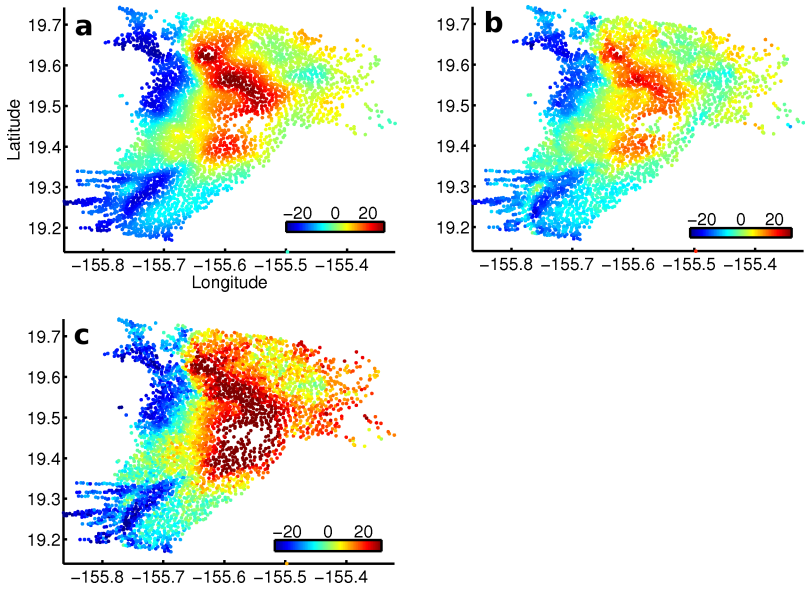

Fig. 6.49. Comparison of slave APS estimates (unit: mm) over PS for dates 11-Apr-2005 and 20-Jun-2005. **a** and **b**) Temporal differences of the two slave APS estimates by the collocation and filtering method resepctively. A 1-year Gaussian window is used by the filtering method. **c**) The corresponding repeat-pass interferogram. Note the strong signal in the submit is likely caused by atmospheric delay but it may also be caused by deformation which is highly nonlinear, see Fig. 6.44 and Fig. 6.43.

warm climate (i.e., Hawaii, Dubai).

Among these regions, Hawaii, Mexico City and Groningen experience ground deformations over the period of the InSAR time series. However, the observed ground deformations are caused by different mechanisms. The deformation in Hawaii is caused by volcanic inflations and the subsidences in the other two regions are related with human being activities, i.e., underground water/gas extraction. In terms of the deformation magnitude Mexico City experiences the largest subsidence (>100 mm/year) rate followed by *Mauna Loa* (~ 30 mm/year) volcano at Hawaii. The deformation over the gas field of Groningen is slow (~ 1 cm/year) and steady and can be well modeled by a linear deformation model. No deformation has been found in Dubai.

For deterministic variables (deformation rate, DEM inaccuracy and master APS), the collocation and filtering methods give similar estimates when there is no ground deformation or the deformation can be well modeled by the chosen functional model, see the Dubai case in section 6.2 and the Groningen case in section 6.4. The selection of the functional model in practice is often arbitrary due to the lack of a-priori knowledge of the deformation. When local ground deformation is complex and cannot be well modeled by the chosen functional model, part of the deformation will

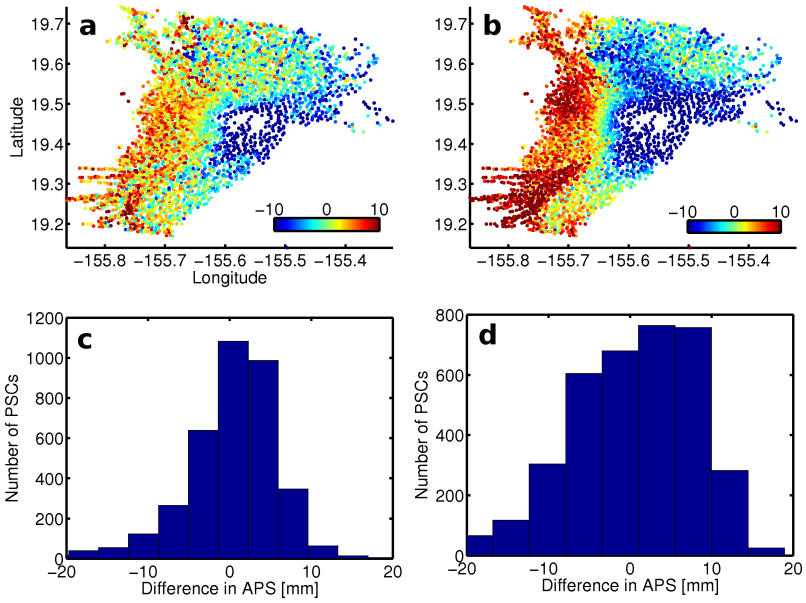

Fig. 6.50. Validation of the slave APS estimates shown in Fig. 6.49. **a**) Difference (unit: mm) between the APS shown in Fig. 6.49 a and c. **b**) Difference between the APS shown in Fig. 6.49 b and c. **c**) Histogram of the difference shown in Fig. 6.50 a. **d**) Histogram of the difference shown in Fig. 6.50 b. Obviously, the estimates from the collocation method match better with the ground truth.

likely be identified as master APS or the other way around if the filtering method is used, see the Mexico city case in section 6.3. The collocation method however always attempts to model (via stochastic modeling) the un-modeled deformation by the chosen functional model, which prevents the mis-identification.

Regarding slave APS estimation, the collocation method always gives better estimates than the filtering method, especially when there are significant acquisition gaps in the time series and for acquisitions taken during extreme weather (e.g., thunderstorm). When there are no significant acquisition gaps and given a shorter satellite repeat orbit (i.e., higher sampling rate in time) the filtering method will give similar slave APS estimates as the collocation method.

In terms of the quality of the deterministic and stochastic estimates, the collocation method can provide the precision assessments of the estimates. If the assumptions (such as functional and stochastic models used for deformation modeling) made for time series analysis are realistic, then the precision assessments should be reliable and realistic. In such cases, the collocation method not only gives the optimal estimate of each variable but also provides a reliable quality indication which will enhance the role of InSAR as a stand-alone technique for surface deformation monitoring.

In conclusion, we recommend to use the collocation method for InSAR time series analysis, especially when 1. there are acquisition gaps in the time series, 2. there

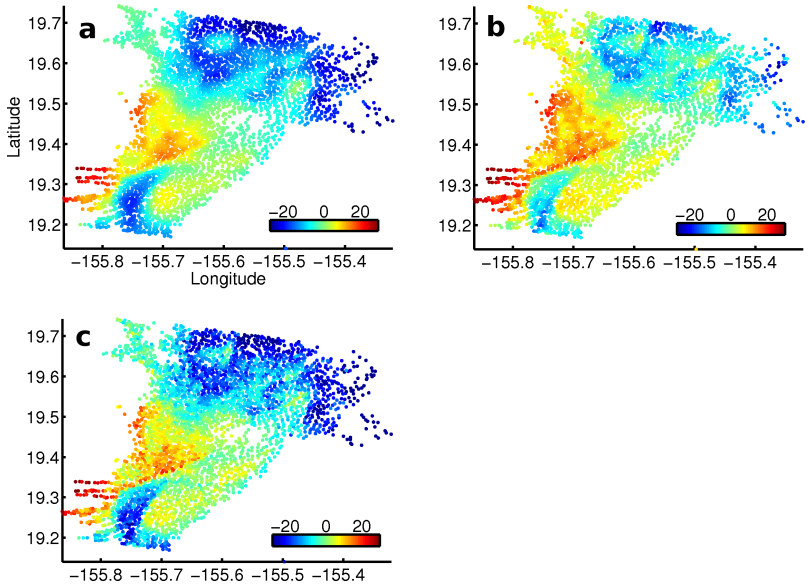

Fig. 6.51. Same as Fig. 6.49 but for dates 21-May-2007 and 30-Jul-2007.

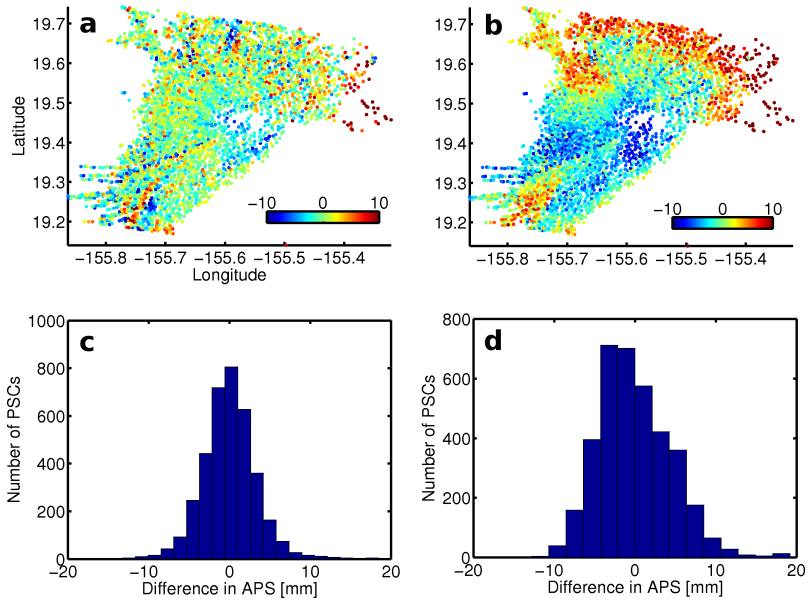

Fig. 6.52. Same as Fig. 6.50 but for dates 21-May-2007 and 30-Jul-2007. The collocation method gives better estimates.

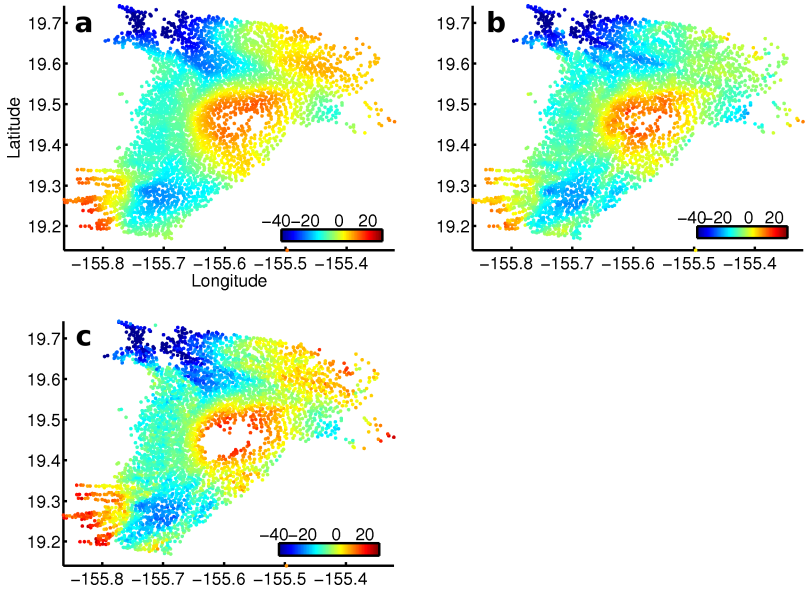

Fig. 6.53. Same as Fig. 6.49 but for dates 17-Dec-2007 and 25-Feb-2008.

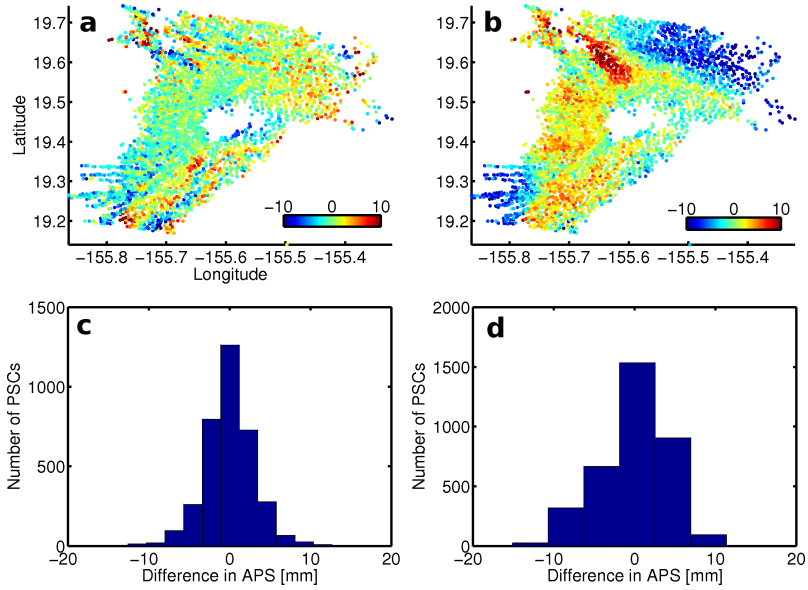

Fig. 6.54. Same as Fig. 6.50 but for dates 17-Dec-2007 and 25-Feb-2008. The collocation method gives better estimates.

are acquisitions in the time series taken during extreme weather and 3. a complex ground deformation is expected and no a-priori knowledge of the deformation is available.

Chapter 7

Optimal water vapor mapping: a network approach

Currently, space-borne InSAR is mainly used for ground deformation monitoring and land topography modeling. The observed spatio-temporal variation of atmospheric delay, which is mainly caused by water vapor in the lower part of the troposphere, is commonly regarded as a measurement noise. In this chapter, we consider the atmospheric delay observed by InSAR as a signal for atmospheric studies and propose a method to retrieve its spatial variation at the epochs of SAR acquisitions from a set of repeat-pass interferograms. The method is applicable to cases in which land deformation in the area of interest is negligible during the SAR acquisitions or the deformation signal is known and can be subtracted from the interferometric phases. Comparing to the least-squares collocation method discussed in previous chapters, this method can retrieve water vapor spatial variation with 1-km resolution or better covering a large ground surface rather than at PS points only, thanks to the good phase coherence provided by short baseline interferograms.

The method is introduced in section 7.2 and it uses a temporal network formed by small-baseline interferograms to estimate the water vapor distribution at each SAR acquisition by means of constrained least-squares adjustment. In section 7.3 we apply the approach to 40 interferograms formed by 22 ASAR images acquired by Envisat in descending orbit over a scene in south-west Australia. The estimated water vapor spatial variations during the 22 SAR acquisitions are evaluated in terms of estimation bias, power spectral density and temporal correlation. In addition, we cross validate some of the APS estimates for those dates on which cloud free MERIS integrated water vapor (IWV) measurements are available. Finally, the conclusions are given in section 7.4.

7.1 Motivation

Over the last two decades, great achievements of space-borne SAR Interferometry for Earth observation have been widely witnessed. Most of its applications can be found in the fields of ground deformation monitoring and land topography modeling. In these applications the atmospheric phase screen (APS) is commonly re-

garded as a phase noise with high spatio-temporal variations caused by water vapor in the lower part ($\leq$ 2 km) of the troposphere. On the other hand, it has been demonstrated that InSAR can provide high spatial resolution measurement of APS spatio-temporal variations (Hanssen et al., 1999; Hanssen, 2001), provided that the ground deformation is negligible and an external DEM model is available to compensate the topographic phase contribution. However, compared to the spatio-temporal variations of interferometric APS, its spatial variations at the epochs of SAR acquisitions are apparently more valuable for atmospheric studies related to climate (Rind et al., 1991), mesoscale meteorology and numerical forecasting (Emanuel et al., 1995; Crook, 1996). Therefore, for InSAR to be used as a tool for the atmospheric studies we need to be able to retrieve the APS spatial variation at the time of each individual SAR acquisition. Based on this motivation we develop an approach to estimate APS spatial variations at the epochs of SAR acquisitions from a set of small-baseline interferograms. Our approach is applicable to cases in which land deformation in the area of interest is negligible or the deformation signal is known and can be subtracted from the interferometric phases.

7.2 Methodology

The methodology consists of three steps. The first step is to form redundant temporal network of interferograms using coherent interferograms. These interferograms usually have relatively small baselines. The redundant network allows for a free network adjustment using least-squares by imposing an artificial constraint. After the network adjustment, in the second step a statistical testing is carried out to remove obvious outliers in the observations. In the last step, a spatial filtering and interpolation is performed to further reduce noise in the estimates and interpolate APS at locations where outliers are detected.

7.2.1 Spatio-temporal network formation and APS estimation

Given N+1 SAR acquisitions we can form $N(N+1)/2$ different interferograms, although only N of these interferograms are independent. For repeat-pass interferometry, baseline constrains (e.g. B_{perp}<500 m, B_t<180 days depending on the sensors and areas of interest) are necessary in order to suppress decorrelation noise (Zebker and Villasenor, 1992; Gatelli et al., 1994). Under the baseline constrains, the number of interferograms that can be formed is reduced substantially and their baseline plot would look similar to the temporal network sketched in Fig.7.1. For an arbitrary pixel p in the aligned interferograms (i.e. co-registrated with respect to a common image) in the network, its unwrapped interferometric phases can be written as:

$$\phi_p^{ij} = \phi_{\text{aps}}^{ij} + \phi_{\text{orb}}^{ij} + \phi_{\text{defo}}^{ij} + \phi_{\text{topo}}^{ij} + \phi_{\text{noise}}^{ij}, \tag{7.2.1}$$

where ϕ_{aps}^{ij} is the temporal difference of two APS spatial variations during acquisitions i and j (with respect to a common reference point in space), ϕ_{orb}^{ij} represents the phase caused by the error in satellite orbit, ϕ_{defo}^{ij} counts for the land deformation between the acquisitions and ϕ_{topo}^{ij} denotes the phase contribution from land

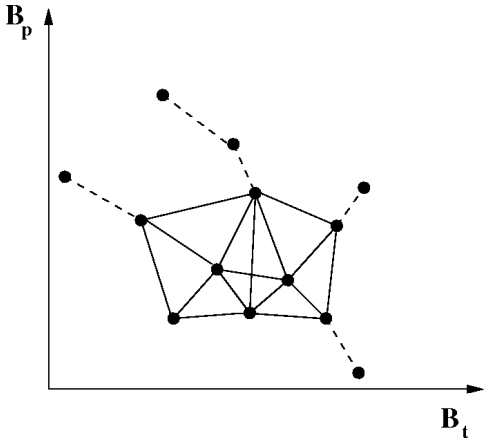

Fig. 7.1. Baseline-Network plot of SAR acquisitions. Horizontal-axis: temporal baseline. Vertical-axis: perpendicular baseline.Each node represents an acquisition and each edge connecting two nodes represents an interferogram formed by the two acquisitions. Dashed edges are the ones which cannot be included in the closed loop of the network due to baseline constrains.

topography and ϕ^{ij}_{noise} is the noise term including decorrelation noise, coregistration/resampling noise and processing noise. The deformation term can be removed from Eq. (7.2.1) for ground surfaces that do not suffer from ground deformation. The topography contribution can be compensated by using a global DEM (e.g. SRTM) and the orbit error can usually be modeled as a surface trend (Hanssen, 2001) and estimated separately from the unwrapped phase. Therefore we can rewrite Eq. (7.2.1) as :

$$\phi^{ij}_p = \phi^i_{\text{aps}} - \phi^j_{\text{aps}} + \phi_{\text{noise}}, \tag{7.2.2}$$

which can be written in a matrix form:

$$\underline{y}_p = Ax + \underline{e}, \tag{7.2.3}$$

where $\underline{y}$ is a $m\times1$ observation vector which contains the unwrapped interferometric phases at the pixel p and m is equal to the number of interferograms in the network, x is a $n\times1$ (deterministic) parameter vector which contains the unknown APS at the epochs of SAR acquisitions and n is the number of the SAR acquisitions from which the m interferograms are formed (note for the networks such as shown in Fig. 7.1, m is larger than n, i.e., redundant networks), A is a m by n matrix which represents the network configuration and $\underline{e}$ is the observation (random) noise vector. One simple realization of Eq. (7.2.2), for example, can be: given a network formed by three acquisitions namely a, b and c, $\underline{y} = (\phi^p_{ab}, \phi^p_{bc}, \phi^p_{ac})^T$, A = [1,-1, 0; 0, 1,-1; 1, 0,-1] and $x = (\phi^p_a, \phi^p_b, \phi^p_c)^T$, where T stands for a matrix transpose.

Since the m interferograms are formed from the n acquisitions, so there are only n-1 independent interferograms and the other m-n+1 interferograms can be obtained via the linear combinations of the n-1 independent interferograms. As a result, the

matrix A in Eq. (7.2.3) is rank deficient and it has only n-1 linear independent columns. Thus, Eq. (7.2.3) is inherently ill-posed and it has an infinite number of solutions, even tough the number of observations in Eq.(7.2.3) is larger than or equal to the unknowns. To overcome the rank deficiency we need to add one or more constraints to Eq. (7.2.3). One of the choices could be adding one or more external water vapor measurements, e.g., from GPS or MERIS in case of ASAR, acquired coincidently with the SAR acquisitions. However, these auxiliary measurements are not always available due to e.g., clouds or the spatial density of the GPS network. Alternatively, we can make use of the temporal mean of APS as a constraint/pseudo-observation. Because of the weak correlation between spatial variations of water vapor at different acquisitions, the temporal mean will decay toward zero as the number of acquisitions increases. For example, assuming the standard deviation of APS disturbance per acquisition is 5 mm on average, then by taking the average of 25 SAR acquisitions the standard deviation of the average will drop to 1 mm and the decay rate is $1/\sqrt{n}$, where n is the number of acquisitions involved in the temporal average. In line with the constrain, Eq. (7.2.3) can be modified to:

$$\underline{y}' = \begin{pmatrix} \underline{y} \\ \underline{y}_0 = 0 \end{pmatrix} = \begin{pmatrix} A \\ B \end{pmatrix} x + \begin{pmatrix} \underline{n} \\ 0 \end{pmatrix}, \tag{7.2.4}$$

where B is a $1 \times n$ vector with all its entries equal to $1/n$;

The weighted least squares (WLS) solution of $\mathbf{x}$ in Eq.(7.2.4) is given as (Teunissen et al., 2005):

$$\underline{\hat{x}} = (A^T Q_{y'}^{-1} A)^{-1} A^T Q_{y'}^{-1} \underline{y}', \tag{7.2.5}$$

and the variance-covariance matrix (VCM) $Q_{y'}$ of the observation vector $\underline{y}'$ reads:

$$\begin{aligned} Q_{y'} &= \begin{pmatrix} Q_y & 0 \\ \mathbf{0} & Q_{y_0} \end{pmatrix} \\ &= \begin{pmatrix} Q_e & 0 \\ 0 & \sum_{i=1}^{n} \sigma_{x_i}^2 / n^2 \end{pmatrix}, \end{aligned} \tag{7.2.6}$$

where Q_e is the VCM of the observation noise and it is a diagonal matrix because we assume that the phase noise in the interferograms is uncorrelated, $\sigma_{x_i}^2$ is the spatial variance of APS during the ith acquisition. To evaluate Q_e we use:

$$\begin{aligned} \sigma_\phi^2 &= E\{(\phi - \phi_0)^2\} = \int_{-\infty}^{\infty} (\phi - \phi_0)^2 pdf(\phi) d\phi \\ &= \int_{\phi_0 - \pi}^{\phi_0 + \pi} (\phi - \phi_0)^2 pdf(\phi) d\phi \\ &= \int_{-\pi}^{\pi} \phi^2 pdf(\phi + \phi_0) d\phi, \end{aligned} \tag{7.2.7}$$

where ϕ_0 is the expectation of ϕ (E is the expectation operator). In our case, ϕ_0 corresponds to the mean phase delay in the resolution cell. Since the variation of

the atmosphere phase delay at short distance (e.g. < 1 km) is limited, hence σ_ϕ^2 is a good approximation of the variance of the phase noise. For distributed scatters with Gaussian or Rayleigh scattering, the phase pdf in Eq. (7.2.7) has the form (Tough et al., 1995):

$$pdf(\phi,\gamma,L,\phi_0) = \frac{(1-|\gamma|^2)^2}{2\pi}\Bigg\{\frac{\Gamma(2L-1)}{[\Gamma(L)]^2 2^{2(L-1)}} \times \left[\frac{(2L-1)\beta}{(1-\beta^2)^{L+\frac{1}{2}}}\left(\frac{\pi}{2}+\arcsin\beta\right)+\frac{1}{(1-\beta^2)L}\right] + \frac{1}{2(L-1)} \times \sum_{r=0}^{L-2}\frac{\Gamma(L-1/2)}{\Gamma(L-\frac{1}{2}-r)}\Gamma(L-1-r)\Gamma(L-1)\frac{1+(2r+1)\beta^2}{(1-\beta^2)^{r+2}}\Bigg\}, \quad (7.2.8)$$

where $\beta = |\gamma|\cos(\phi-\phi_0)$; L is the multilook factor; γ is the complex coherence. Note, Eqs. (7.2.7) and (7.2.8) show that we do not need to know ϕ_0 in order to evaluate σ_ϕ^2. The magnitude of the complex coherence $|\gamma|$ can be estimated by (Seymour and Cumming, 1996):

$$|\hat{\gamma}| = \frac{|\sum_{n=1}^{N} y_1 y_2^*|}{\sqrt{\sum_{n=1}^{N}|y_1|^2 \sum_{n=1}^{N}|y_2|^2}}, \quad (7.2.9)$$

where y_1 and y_2 are the complex signals of master and slave respectively and $*$ denotes the complex conjugate. In practice, the estimate $|\hat{\gamma}|$ is biased towards higher values, i.e.$|\hat{\gamma}| > |\gamma_{true}|$, for low coherence and small estimation windows (Tough et al., 1995). In addition, for single-look data ($L = 1$) σ_ϕ^2 can be expressed in a closed form as (Bamler and Hartl, 1998):

$$\sigma_{\phi,L=1}^2 = \frac{\pi^2}{3} - \pi\arcsin(|\gamma|) + \arcsin^2(|\gamma|) - \frac{1}{2}\sum_{k=1}^{\infty}\frac{|\gamma|^{2k}}{k^2}. \quad (7.2.10)$$

Numerical evaluations of the phase pdf in Eq. (7.2.7) with varying $|\gamma|$ and L are shown in Fig. 7.2 a, b, c. The phase variance integrated numerically using Eqs. (7.2.7) and (7.2.8) as a function of $|\gamma|$ and L is plotted in Fig. 7.2 d. Note, for large L (i.e. L>80) the phase variance σ_ϕ^2 turns to depending on the coherence magnitude $|\gamma|$ only. To realize $Q_{y'}$ in Eq. (7.2.6) we need to know $\sigma_{x_i}^2$ as well. To estimate it we however need to know the atmospheric signal magnitude x which is not known a-priori and needs to be estimated from the data. Therefore, we need to compute $\hat{x}$ iteratively and in each iteration we compute $\sigma_{x_i}^2$ based on the estimate of x_i from the previous iteration. The initial approximation of $\sigma_{x_i}^2$ can be an approximation of the average of local atmosphere variance. After several iterations the update of $\sigma_{x_i}^2$ becomes trivial and therefore the WLS estimate of x can be obtained.

Finally, we need to stress that although APS at all acquisitions within the network in Fig. 7.1 can be estimated uniquely using Eq. (7.2.5), their estimates have different accuracies depending on their locations in the network. Assuming the same noise level for all interferograms in the network, the accuracy of the estimates at the

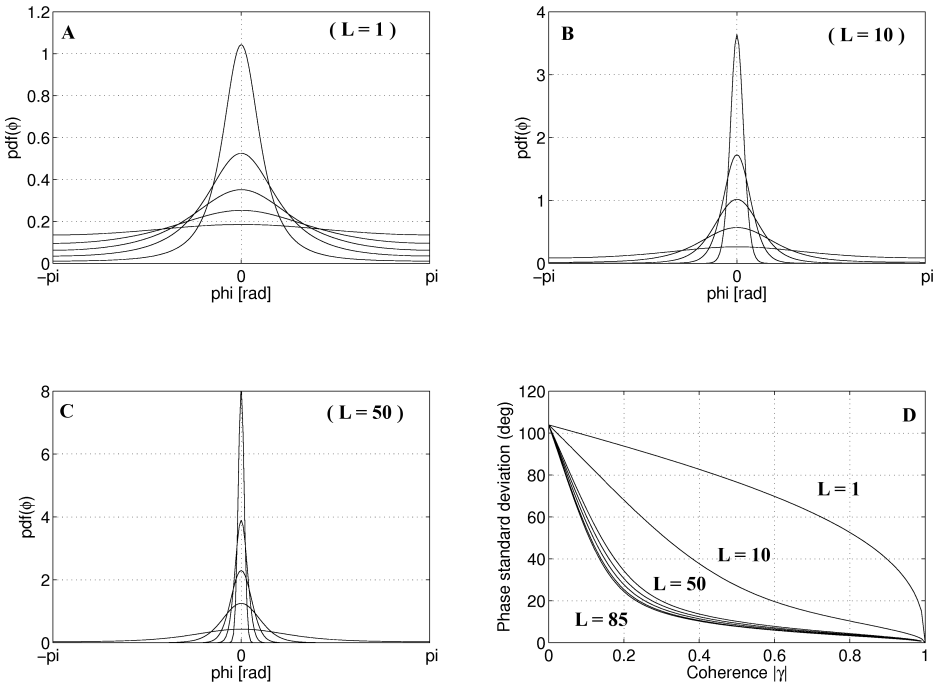

Fig. 7.2. Probability density function and standard deviation of the interferometric phase as a function of coherence and multilook level. **A**) Single look for coherence levels $|\gamma|$=0.1, 0.3, 0.5, 0.7, and 0.9 (smallest curves correspond with highest coherence). **B**) Multilook level 10. **C**) Multilook level 50. **D**) Phase standard deviation with varying multilook level (L=1,20,50,60,70,80 and 85) and coherence. For large L, σ_ϕ^2 turns to depending on $|\gamma|$ only.

network arcs (the dashed lines in Fig.7.1) which are not in the closed loop of the network (the solid lines in Fig.7.1) are lower than the accuracy of the estimates at the arcs within the loop. This is because there is no observation redundancy at the open arcs and therefore the noise in their observations cannot be adjusted. Moreover, for the same reason it is not possible to validate the estimates and remove possible outlier at these open arcs. Statistical testing and outliers detection are discussed in the following.

7.2.2 Statistical testing and outlier detection

The estimate of x obtained from WLS may have low precision due to outliers in the observations (i.e. unwrapped interferometric phases). Many contributors can cause outliers in the interferograms, e.g., phase unwrapping error, mis-coregistration between master and slave, DEM error that becomes larger as the perpendicular baseline increases, etc. Moreover, poor estimates of x can also be caused by errors in the stochastic model, i.e. the VCM $Q_{y'}$ of the observations in Eq. (7.2.6). The error is

likely to occur when the pixels used to estimate the coherence in Eq. (7.2.9) have low signal-to-noise ratio (SNR). In such case, the estimated phase noise variances from Eq. (7.2.7) for these pixels are underestimated, i.e., the quality of the data is overestimated ($\hat{\sigma}_{\phi}^2 < \sigma_{\phi,\text{true}}^2$). Therefore, the need for testing the validity of the estimate is obvious. We propose a testing procedure which is commonly used to detect outliers during the geodetic network adjustment. The procedure can be generally described by three steps: *detection*, *identification* and *adaptation* (DIA) (Teunissen, 2000b). Firstly, in the *detection* step a null-hypothesis, which assumes the model described by Eq. (7.2.4) is well supported by the data (i.e. observations), is tested against general model mis-specifications. This step is the *overall model test* (OMT) since it checks the overall validity of the model without the need to specify any particular alternative hypothesis. The appropriate test-statistic for this step reads:

$$T_{q=m-n}^{omt} = \underline{\hat{e}}^T Q_{y'}^{-1} \underline{\hat{e}}, \tag{7.2.11}$$

where $\underline{\hat{e}}$ is the WLS residue which is equal to $\underline{y}$ - $A\hat{x}$, m, n are the number of observations and unknown parameters respectively, m-n is the observation redundancy (degree of freedom). The null hypothesis is rejected when $T_{q=m-n}^{omt} > \chi_{\alpha}^2(m\text{-}n,\, 0)$, where $\chi_{\alpha}^2(m\text{-}n,\, 0)$ is a central Chi-square distribution with m-n degrees of freedom and α is called the level of significance which represents the likelihood of a type-I error of the test. The type-I error is caused by mis-specifying reliable observations as outliers which are therefore rejected by the test. On the other hand, there is a type-II error (the likelihood is denoted as β) which is the result of accepting the outliers in the observations. Given the type-II error β the power of the test is $\gamma =$ 1-β. These two types of errors are always co-existing in all hypothesis-based tests. Moreover, a decrease of α will result in an increase of β and vice versa. Therefore, there is no hypothesis test that can minimize α and β simultaneously. To get out of the dilemma, in practice, it is common to fix one type of error and then try to minimize the other type. The test (among all tests) which gives the minimum β for a fixed α is called a most powerful test since it maximizes the power of the test. In our case, we cannot afford rejecting correct observations since they are not re-measurable. Therefore a small α, e.g. 0.001 should be chosen. Assume maximally 10% of the interferometric phases within the closed loop of the network in Fig. 7.1 are outliers, α=0.001 implies that 1% of the identified outliers actually were correct observations. Obviously, the value of α should be increased as the noise level of the observations increases. Next, if the null hypothesis in the first step is rejected then it implies that there most likely exists one or more significant model mis-specifications due to outliers. The task of the second step, i.e. identification, is therefore to detect the outliers in the observations. For simplicity, we assume there is only one outlier in the observations and the test-statistic for detecting the outlier reads:

$$w_i = \frac{c_{y_i}^T Q_{y'}^{-1} \hat{e}}{\sqrt{c_{y_i}^T Q_{y'}^{-1} Q_{\hat{e}} Q_{y'}^{-1} c_{y_i}}}, \tag{7.2.12}$$

where $Q_{\hat{e}}$=Q_y-$A(A^T Q_y^{-1} A)^{-1} A^T$ is the VCM of the least squares residue $\underline{\hat{e}}$; c_{y_i} is an unit vector having the 1 as its ith entry. It can be shown that the w test in

Eq. (7.2.12) is a most powerful test (Teunissen, 2000b). In case that Q_y is a diagonal matrix then the test-statistic reduces to:

$$w_i = \frac{\hat{e}_i}{\sigma_{\hat{e}_i}}. \tag{7.2.13}$$

The jth observation is suspected to be an outlier when $|w_j| > |w_i|$ for all $i \neq j$ and $|w_j| > N_\alpha(0,1)$, where $N_\alpha(0,1)$ denotes the standard normal distribution. In the last step, the detected outlier, i.e. the observation y_j, is rejected and the parameters of interest are re-estimated using Eq. (7.2.5). The testing procedure iterates until there is no outlier that can be identified with the given α. Note, as mentioned in the end of section 7.2.1, the outlier detection is not possible for acquisitions which are not included in the closed loop of the network. Therefore, we need to either discard the APS estimates for these acquisitions or just accept them without reliability assessment.

7.2.3 Spatial filtering and interpolation

After testing, we obtain the pixel-wise APS estimates at all acquisitions. However, there can be pixels which do not have APS estimates at some acquisitions. This is because for these pixels Eq. (7.2.4) is ill-posed due to the rejection of outliers at these pixels after testing. On the other hand, there are pixels having APS estimates but the estimates are contaminated by noise. The noise in these estimates is propagated from the outliers which are not detected by testing due to the inherent type-II error. This error is often not negligible since during testing the type-I error α is fixed to a small value to prevent rejecting correct observations. Therefore, the goal of spatial filtering and interpolation described in this section is to refine the estimated APS and to interpolate APS at locations where no APS estimates are available. The filtering and interpolation are implemented by ordinary kriging which gives the unbiased estimation of the signal of interest, meanwhile its filtering/interpolation error is minimized in a least squares sense. To refine/interpolate APS at location $\mathbf{h}_0$ from its surrounding APS estimates (tested), the kriging equation reads (Wackernagel, 1995):

$$X(\mathbf{h}_0) = \sum_{i=1}^{N} \lambda_i X(\mathbf{h}_i),\ \mathbf{h} \in R^2 \tag{7.2.14}$$

where λ_i is the kriging weight for the sample X($\mathbf{h}_i$) at location $\mathbf{h}_i$. The kriging weights can be computed by solving the system of equations:

$$\begin{pmatrix} \gamma(\Delta\mathbf{h}_{12}) & \cdot\cdot & \gamma(\Delta\mathbf{h}_{1N}) & 1 \\ \gamma(\Delta\mathbf{h}_{21}) & \cdot\cdot & \gamma(\Delta\mathbf{h}_{2N}) & 1 \\ \vdots & \vdots & \vdots & \vdots \\ \gamma(\Delta\mathbf{h}_{1N}) & \cdot\cdot & \gamma(\Delta\mathbf{h}_{NN}) & 1 \\ 1 & \cdot\cdot & 1 & 0 \end{pmatrix} \begin{pmatrix} \lambda_1 \\ \lambda_2 \\ \vdots \\ \lambda_N \\ \mu \end{pmatrix} = \begin{pmatrix} \gamma(\Delta\mathbf{h}_{10}) \\ \gamma(\Delta\mathbf{h}_{20}) \\ \vdots \\ \gamma(\Delta\mathbf{h}_{N0}) \\ 1 \end{pmatrix}, \tag{7.2.15}$$

where $\gamma(\Delta\mathbf{h}_{ij})$ is called semi-variogram; μ is a Lagrange multiplier. To uniquely determine the kriging weights λ, the left hand side N+1 by N+1 matrix in Eq. (7.2.15)

needs to be positive-definite and therefore invertible. To satisfy the positive-definite requirement we first compute the raw semi-variogram by:

$$\gamma(\Delta\mathbf{h}_{ij}) = \frac{[X(\mathbf{h}_i) - X(\mathbf{h}_j)]^2}{2}, \tag{7.2.16}$$

and then we fit the raw variogram to a Matérn family model which can describe the well-known '2/3' law of the Kolmogorov turbulence theory (Tatarski, 1961). Assuming that the estimated APS is wide-sense stationary (otherwise we de-trend it), the model for the variogram can be obtained from:

$$\gamma(\Delta\mathbf{h}) = C(0) - C(\Delta\mathbf{h}), \tag{7.2.17}$$

where $C(\Delta\mathbf{h})$ is the covariance function of the Matérn class. The function reads (Stein, 2005):

$$C(\Delta\mathbf{h}) = \frac{c}{2^{\nu-1}\Gamma(\nu)}(\alpha|\Delta\mathbf{h}|)^{\nu}K_{\nu}(\alpha|\Delta\mathbf{h}|), \tag{7.2.18}$$

where c denotes the variance (power) of the turbulence; α represents the correlation length of the turbulence, ν defines the smoothness of the turbulence, Γ is the Gamma-function and K is the modified Bessel-function of the second kind.

We have so far introduced the methodology in detail. Forming a redundant temporal network is the key for the successful application of the methodology. Therefore, we prefer a testing area that allows for a good phase coherence for interferograms with relatively large temporal baselines, e.g., 6 months. In the meantime, the area shall be stable and have no or negligible ground deformation. In next section, we will demonstrate the methodology based on an area from southwest Australia.

7.3 Retrieving APS spatial variation: a case study

In this section we apply the developed methodology in the previous section to an area in southwest Australia.

7.3.1 Area of interest and data pre-processing

The area is centered at 30.36°S and 117°E from southwest Australia, see Fig. 7.3. It is barely vegetated due to the regional semi-arid climate. As a result, the phase coherence can remain high enough for a relatively long period ($\sim$ 6 months) as shown in Fig. 7.4.

The time span of the ASAR acquisitions used in this study is between May 2005 and April 2008. To apply the algorithm the surface deformation in the area should be either negligible or removed from the unwrapped interferograms beforehand. Since we find no evidence of ground deformation over the area based on a PSInSAR time series analysis, therefore we assume the ground deformation over the area is negligible. Starting with SLC (single-looking-complex) images, 40 interferograms with on average 85 days temporal and 205 m perpendicular baselines are formed from 22 SLCs, see the baseline plot in Fig. 7.5. The area has a smooth topography with an

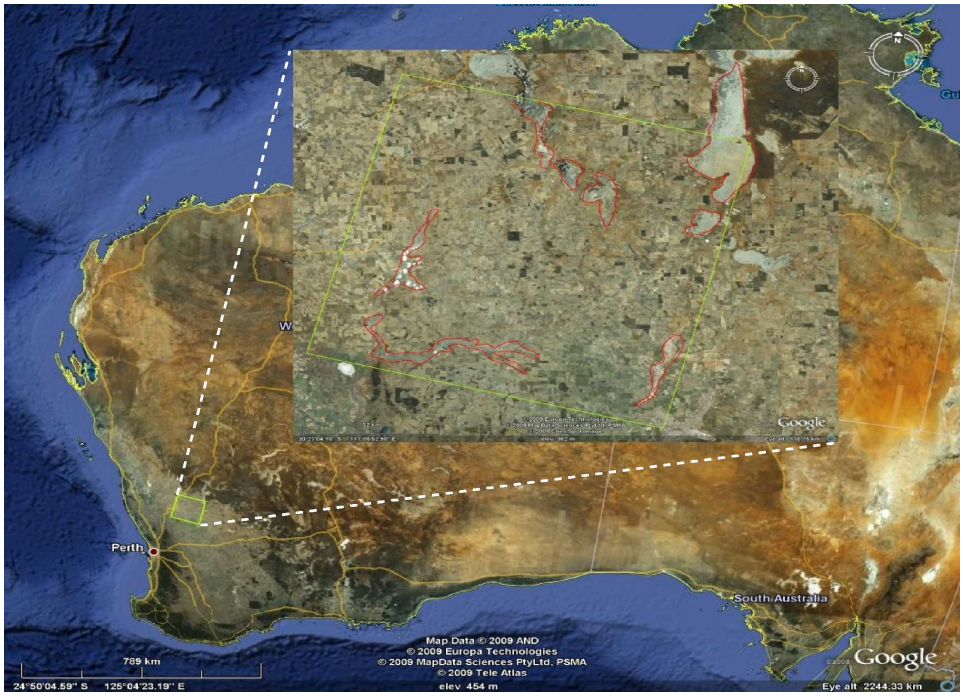

Fig. 7.3. The area (green square) chosen for the case study is located in southwest Australia with scene centered at 30.36°S and 117°E. The red polygons outline the dried salt lakes. The local time of the acquisitions is 9:40 am.

average height of 250 m and the maximum height difference is about 200 m. Therefore the vertical stratification effect of APS is negligible in this area. The topographic phases in the interferograms are modeled and subtracted using 3-arc-second SRTM data. To reduce phase noise due to geometric decorrelation range filtering is applied to all interferograms to cut off non-overlapping spectra of master and slave. After phase unwrapping, a coherence-based spatial average (i.e.multilook) is applied to the unwrapped phases to reduce random phase noise. The operation can be written as:

$$\bar{\phi} = \frac{1}{\sum_{i=1}^{m}\sum_{j=1}^{n} w_{i,j}} \sum_{i=1}^{m}\sum_{j=1}^{n} w_{i,j}\phi(i,j), \tag{7.3.1}$$

where

$$w_{i,j} = \begin{cases} 1 & \text{if } |\gamma|(i,j) > |\gamma|_{min} \\ 0 & \text{otherwise} \end{cases} \tag{7.3.2}$$

and $|\gamma|_{min}$ is a pre-defined coherence threshold (e.g. 0.35). Since APS is spatially smooth thus in this case a large window size (e.g. 250 by 50 in azimuth and range respectively) for averaging is admissible without invoking signal aliasing. In this study we spatially average the unwrapped interferograms to 1 km in both azimuth and range. After the spatial average a surface trend is estimated from each in-

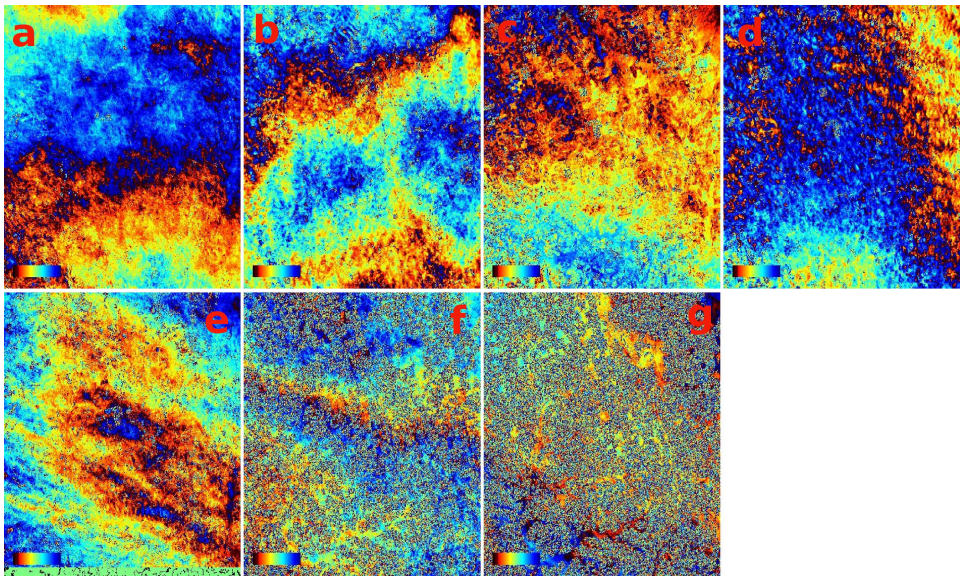

Fig. 7.4. Wrapped interferometric phases from the area of interest (100 by 100 km) with different temporal baselines; **a**) 35-day. **b**) 70-day. **c**) 105-day. **d**):140-day. **e**) 175-day. **f**) 210-day. **g**) 350-day. The coherent parts in Fig. 7.4 g are corresponding to the dried lakes highlighted in Fig. 7.3.

terferogram and the modeled trend is then subtracted from the interferogram to mitigate other phase contributions, i.e., orbit error, hydrostatic and ionospheric delays (Hanssen, 2001). The de-trended phase has a zero mean and is wide-sense stationary. In the end, the phase delay is converted to the range delay in zenith by multiplying with $-\frac{\lambda}{4\pi}\cos\theta$, where θ is the local mean incidence angle (23° for Envisat) and λ is the radar wave length, the minus sign is due to a phase increase corresponding to a range decrease.

7.3.2 Validation

We validate our APS estimates from four different aspects: estimation bias, stochastic characteristics, temporal auto-correlation and cross validation using MERIS. The first three do not need external and independent measurements of the troposphere so we regard them as internal validations. In line with the definition, the cross validation using MERIS can be therefore regarded as an external validation in which MERIS water vapor measurements acquired under cloud free condition are compared to the corresponding APS estimates.

Estimation bias

The APS estimates are biased due to the added constraint (see Eq. (7.2.4)) that is the temporal mean of all APS estimates should be equal to zero. It can be shown that the bias is a constant for all APS estimates and it is equal to the temporal mean

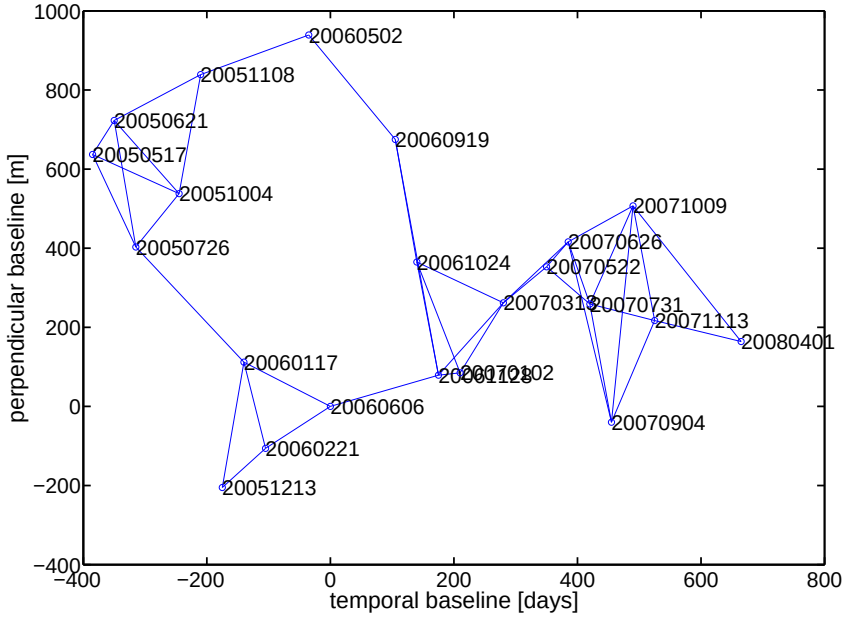

Fig. 7.5. Baseline plot of the ASAR acquisitions used in the case study. Each node represents an ASAR acquisition and each arc connecting two nodes represents the interferogram formed by the two acquisitions fulfilling the baseline criteria (less than 400 meters perpendicular baseline and short than 6 months temporal baseline). The track and frame numbers of the acquisitions are 203 and 4221 respectively.

which has a zero expectation. Given the estimated APS it is possible to evaluate the RMS of the bias (in terms of delay). Using the variance propagation law we find:

$$\hat{\sigma}_{\text{bias}}^{\text{APS}} = \sqrt{\frac{\sum_{i=1}^{22} \hat{\sigma}_i^2}{N^2}} = \sqrt{\frac{\sum_{i=1}^{22} \hat{\sigma}_i^2}{22^2}} = 0.8\text{mm}. \tag{7.3.3}$$

where N is the number of acquisitions involved in the temporal average and $\hat{\sigma}_i^2$ is the estimate of the a-posteriori variance of APS in acquisition i. In contrast, the mean RMS of the APS estimates is 3.6 mm which is about 5 times larger than the bias RMS. The histogram of the RMS for all APS estimates (in total 22) is shown in Fig. 7.6 b. As we can see that 17 out of 22 APS estimates do not have an RMS larger than 4 mm. The low delay RMS is likely related to the semi-arid climate in the region. The rightmost bar in the histogram is corresponding to an acquisition (on 08-Nov-06) probably taken during very turbulent weather. For comparison, the histogram of the APS derived from 11 MERIS IWV measurements on the same dates with clear sky is shown in Fig. 7.6 c. It can be seen from Figs. 7.6 b, c that the derived APS estimates from InSAR and MERIS show a similar magnitude of spatial

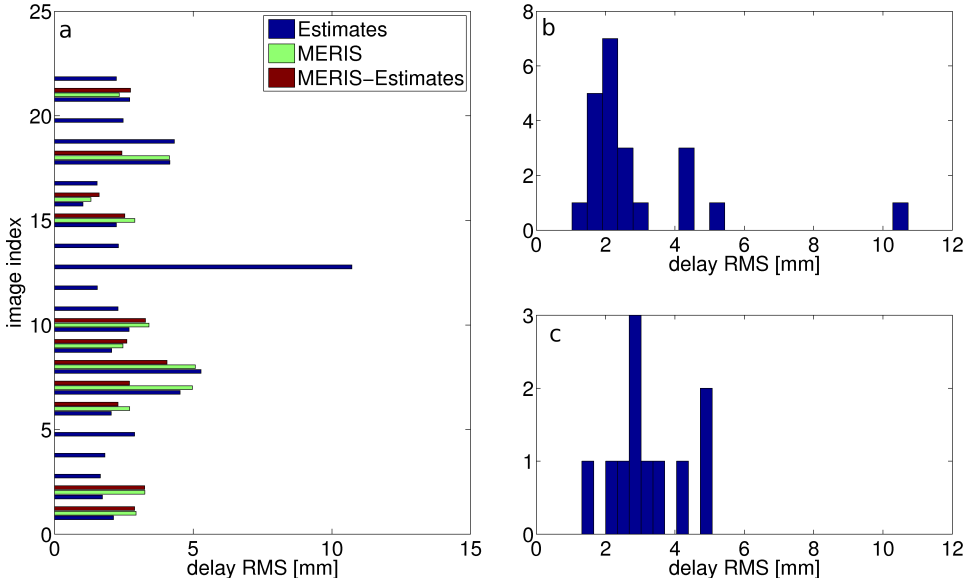

Fig. 7.6. Comparison between the APS (in terms of delay) derived from InSAR and MERIS IWV measurements (in total 11) of the same dates under clear-sky conditions. **a**) Blue-bar: delay RMS for 22 APS estimates derived from InSAR. Green-bar: delay RMS derived from 11 MERIS IWV measurements of the same dates under clear sky. Red-bar: differences (pixel-wise) between the derived APS from InSAR and MERIS. The relatively large RMS of the residue (pixel-wise difference) is caused by the errors in the MERIS measurements, see Fig. 7.9. **b**) Histogram of the APS estimates (in total 22), the rightmost bar is corresponding to an acquisition (on 08-Nov-06) likely taken during a very turbulent weather, see Fig.7.11 d . The MERIS measurement of that acquisition is completely obscured by clouds. **c**) Histogram of the APS derived from the 11 MERIS acquisitions. Although the derived APS from InSAR and MERIS show similar magnitude of spatial variations, their pixel-wise differences for some acquisitions indicate some considerable inconsistencies between the two.

variations.

Stochastic behavior

The raw variograms and power spectral densities (PSD) of the APS estimates are shown in Figs.7.7 a, b respectively. The PSDs are computed using the periodogram approach. The average of the raw variograms is plotted as the bold red line in Fig. 7.7 a. At short distances (i.e., a few kilometers) the slope (approximately 5/3) of the averaged variogram is steeper than the slope (dominated at 2/3) at larger distances and the slope turns to flat at the distances beyond about 40 km. The flattening effect is the result of the surface trend removal. Note, the uppermost raw variogram which corresponds to the APS spatial variation on date 08-Nov-06 is excluded from the averaging. It has a dominant anisotropic spatial pattern and

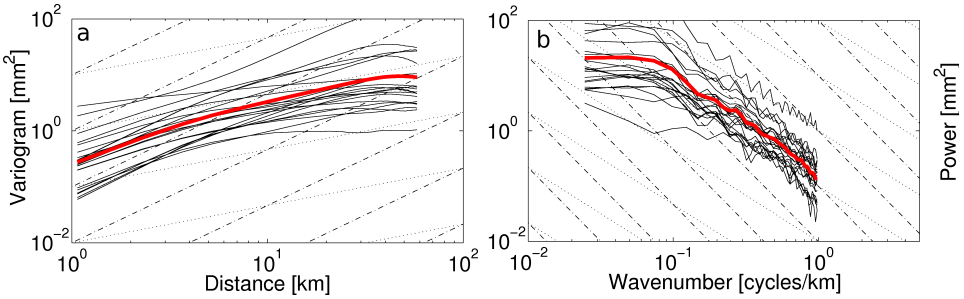

Fig. 7.7. Stochastic analysis of all 22 APS estimates for the 22 ASAR acquisitions used in the case study. Since the interferograms used for APS estimation were significantly subsampled, only wavelengths above 1 km are shown. Furthermore, wavelengths above 50 km are truncated since the signal power does not increase anymore beyond that wavelength due to the removal of average APS (spatial trend). **a**) Computed raw variograms (solid black) and their average (bold red) using a log-log scale, the background dot lines follow a 2/3 and a 5/3 slope for reference. **b**) Computed one-dimensional power spectra (solid black) using periodogram and their average(bold red), the background dot lines follow a -5/3 and -8/3 slope for reference. Note, although the area has a semi-arid climate the APS variation can still vary 2 orders of magnitude from one acquisition to another.

therefore bias the average based on only 22 acquisitions. The MERIS cloud masks for this date indicate the sky of the area was completely covered by clouds. There may be some significant precipitation during the acquisition but we do not have any meteorological data for validation. The averaged PSD is shown as the bold red line in Fig. 7.7 b. Its slope is also scale-variant, at large wavenumbers (> 0.4 cycle/km) the absolute slope (approximately -8/3) is higher than the absolute slope at smaller wavenumbers and the dominant slope is of -5/3. The computed variogram and PSD are therefore consistent with the theoretic power-law of the atmospheric turbulence (Tatarski, 1961; Hanssen, 2001).

Temporal correlation

It can be shown (e.g., Hanssen (2001)) that the sum or difference of two APSs from different acquisitions has the same power-law behavior as described in section 7.3.2. Therefore the stochastic analysis cannot discover any mixture of APS from different acquisitions. A mixture of APS can result in a considerable correlation between the APS estimates. Hence, we compute the pixel-wise cross-correlation between each two APS estimates to detect any possible mixture, see Fig. 7.8. Despite a few APS estimates show some considerable cross-correlation, the mean of the overall cross-correlation is as low as 0.1. Therefore, the mixture of APS from different acquisitions should be very limited. Thus, the estimated APS per acquisition should be reliable.

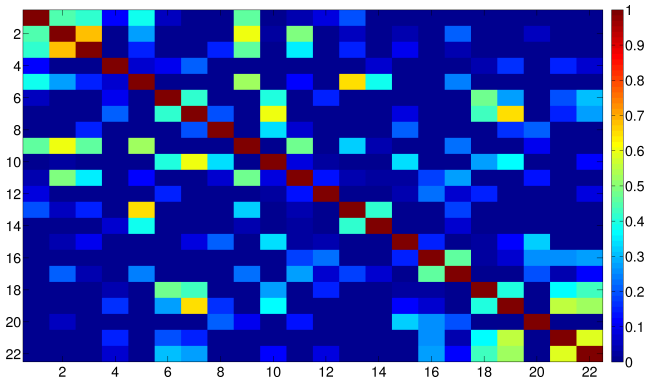

Fig. 7.8. Correlations between the APS estimates for 22 ASAR acquisitions. The elements in the main diagonal are the auto-correlation of the APS estimates. The elements in the off diagonal represent the cross-correlation between the APS estimates for different dates. As we can see, most of the off diagonal elements are close to zero, therefore the estimated APS per acquisition is not temporally correlated.

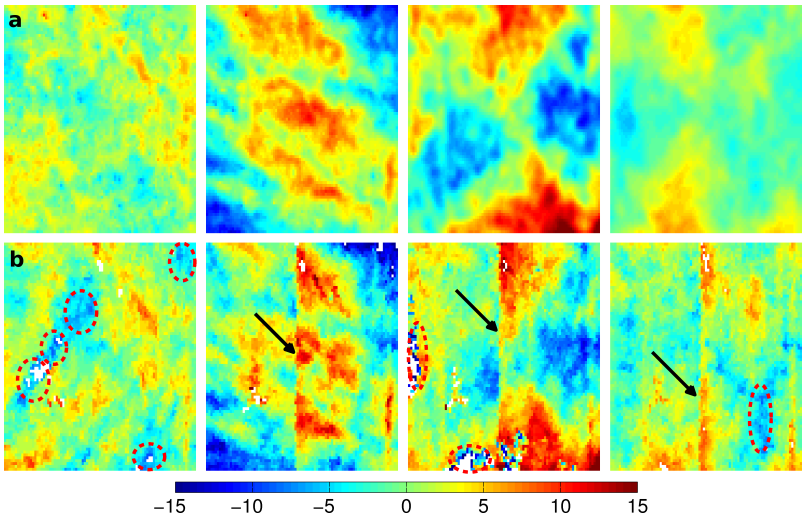

Fig. 7.9. Comparison between MERIS and APS estimates. **a**) Estimated APS spatial variations (from left to right) on 26-Jul-05, 19-Sept-06, 24-Oct-06 and 26-Jun-07 respectively. **b**) Corresponding spatial delay variations converted from the MERIS IWV measurements acquired under cloud free condition. The dashed red ellipses in Fig. 7.9 b indicate the locations where the APS signal is underestimated. The underestimation might be due to undetected thin clouds in MERIS. The black arrows in Fig. 7.9 b indicate the camera interface problems of MERIS.

Cross validation with MERIS

Figure 7.9 shows some representative comparisons between the estimated APS and the delay spatial variations derived from the MERIS cloud free IWV measurements. Although large spatial correspondence between them can be clearly seen from the figure, the quantitative comparison, see Fig. 7.6 a, between the two indicates some substantial inconsistencies between them. We believe the inconsistencies are due to the cloud masking errors of MERIS (see the red ellipses in Fig. 7.9) as well as the camera-interface effect (indicated by the black arrows in Fig. 7.9) of the on-board cameras (in total 5) which scan the ground surface under a push broom mechanism ESA (2006).

In the end, the retrieved 22 APSs in the network shown in Fig. 7.5 are presented in Fig. 7.10 to Fig. 7.12.

From this case study we have demonstrated the capability of the developed algorithm for optimal water vapor mapping. Thanks to the good phase coherence over the area of interest, the algorithm allows us to estimate APS spatial distributions during 22 ASAR acquisitions. The conclusions and recommendations will be given in next section.

7.4 Conclusions and recommendations

In this chapter we presented a method to retrieve the spatial variation of APS at each single acquisition from a stack of SLC images. The interferograms formed from these images result in a temporal network of interferograms under the baseline constraints. APS estimates at each acquisition of the network are obtained by using weighted least-squares with a constraint on the temporal average of APS in order to obtain an unique least-squares solution. Since the network provides redundant observations of APS spatial-temporal variations, the obtained APS estimates per acquisition can be tested using statistical hypothesis testing for validity. After the statistical testing, a kriging based interpolation and filtering is applied to the estimates and the final estimates of APS are obtained with a 1 km spatial resolution.

The APS estimates can be biased if the used constraint on the temporal average of APS becomes unrealistic in reality. As a rule of thumb, the larger the number of images in the network the less the bias is. After obtaining the final APS estimates we evaluate the bias in the estimates and the estimation of the bias for this case study is 0.8 mm which is relatively small comparing to the average RMS of the 22 APS estimates (3.6 mm). In addition, we have examined the stochastic characteristics of the APS estimates via their variograms and power spectra densities and they agree well with the theoretical power-law of the turbulence theory. Moreover, by computing the cross-correlation between the 22 APS estimates we find the correlation is on average 0.1 and it means the estimates are temporally uncorrelated, which agrees with the generally accepted assumption which says two APS fields become completely uncorrelated when their time interval is in the order of hours. We also compare the APS estimates to 11 MERIS water vapor measurements which are not severely contaminated by clouds. The match between the estimates and the MERIS

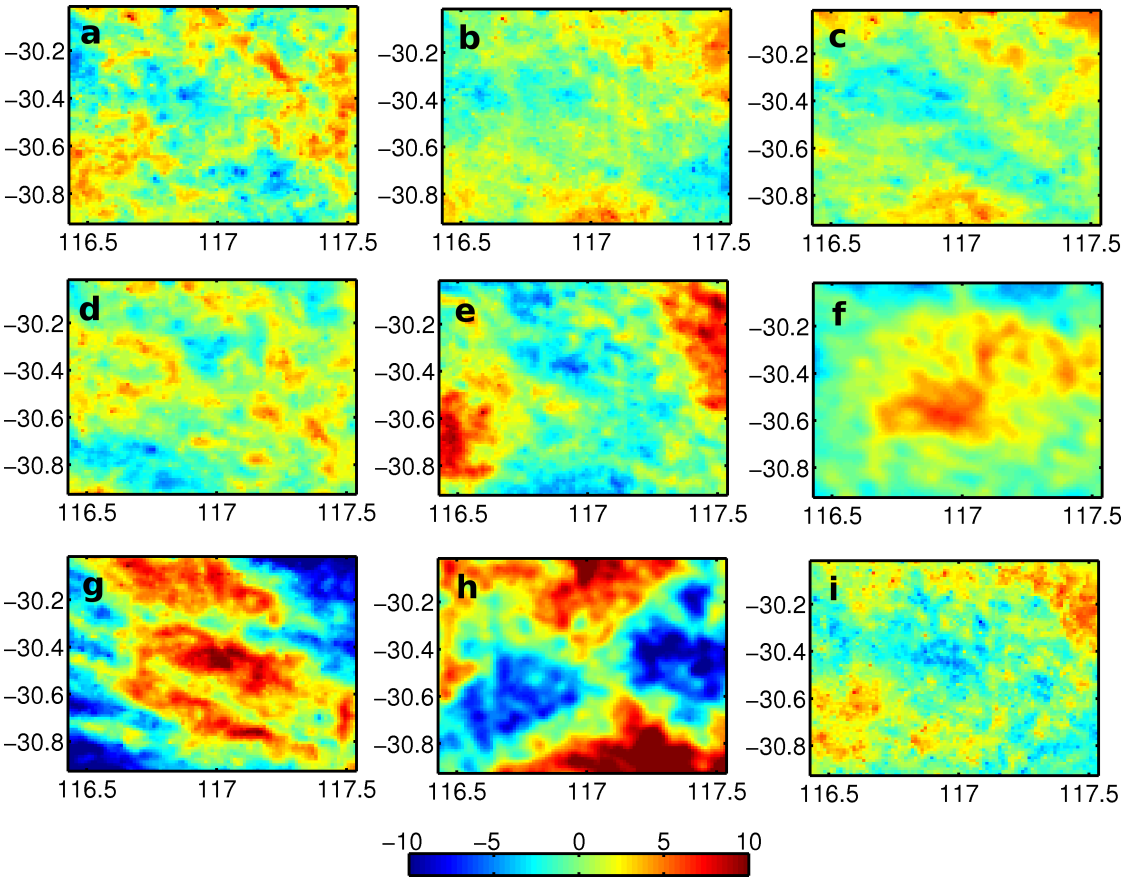

Fig. 7.10. Retrieved APS per single SAR acquisition (part 1). **a**) 17-May-2005 **b**) 21-Jun-2005 **c**) 26-Jul-2005 **d**) 4-Oct-2005 **e**) 8-Nov-2005 **f**) 13-Dec-2005 **g**) 17-Jan-2006 **h**) 21-Feb-2006 **i**) 2-May-2006. The unit of the colorbar is mm.

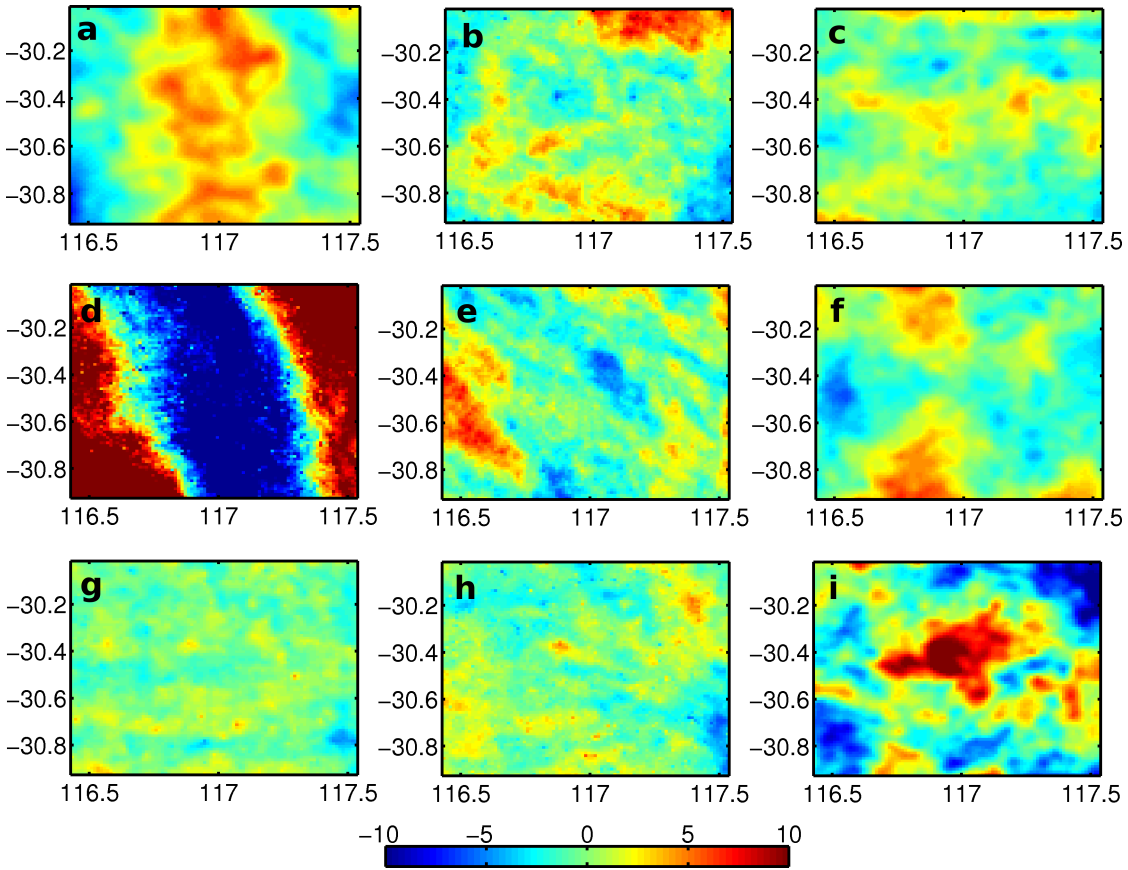

Fig. 7.11. Retrieved APS per single SAR acquisition (part 2). **a**) 6-Jun-2006 **b**) 19-Sep-2006 **c**) 24-Oc-2006 **d**) 28-Nov-2006 **e**) 2-Jan-2006 **f**) 13-Mar-2007 **g**) 22-May-2007 **h**) 26-Jun-2007 **i**) 31-Jul-2007. The unit of the colorbar is mm.

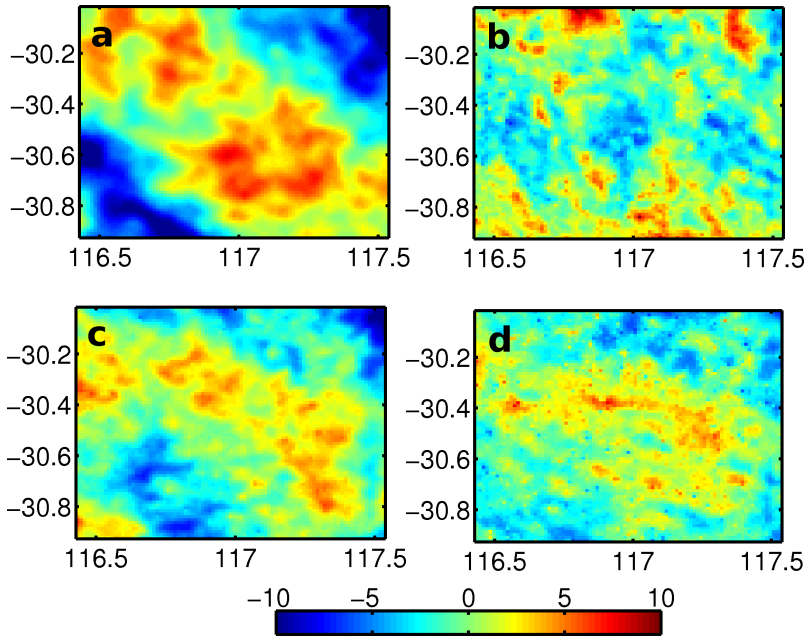

Fig. 7.12. Retrieved APS per single SAR acquisition (part 3). **a**) 4-Sep-2007 **b**) 9-Oct-2007 **c**) 13-Nov-2007 **d**) 1-Apr-2008. The unit of the colorbar is mm.

measurements is very well, especially considering the undetected clouds in some of the MERIS images and a common camera-interface effect of MERIS.

The advantage of the APS retrieving method is that it uses only small baseline interferograms and APS spatial variation at every pixel of 1 km resolution can be obtained over the whole imaging area. The network adjustment and kriging interpolation and filtering further reduce the noise in the estimated APS per acquisition. The limitations are that 1. the method assumes the ground deformation is negligible or already known a-priori; 2. the phase coherence in the area need to be good for a relatively long period in order to have a redundant temporal network of interferograms. However, the new generation of earth observation satellites such Sentinel-1A/B will provide full coverage of global land mass with a fast revisit orbit, e.g., 6-day when both satellites are in orbit. Moreover, most land surfaces do not suffer rapid deformation and our knowledge about deformation regions will keep improving. Therefore, we believe the method opens a door for further exploring the possibility of integrating InSAR observations for meteorology studies at fine spatial scales.

Chapter 8

Conclusions and Recommendations

This study has two themes: 1. mitigating atmospheric phase screen (APS) for InSAR based surface deformation monitoring and 2. mapping water vapor spatial distributions for meteorological purposes. For the first objective we developed two correction methods. The first correction method is based on numerical wether models (NWM) from which delay maps during SAR acquisitions are simulated and removed from original interferograms. The second correction method utilizes least-squares collocation (LSC) and variance-covariance estimation (VCE) to estimate APS and surface deformation from InSAR time series. For the second objective which is water vapor mapping, we developed a method to retrieve high resolution ($\sim 1\,\mathrm{km}$) water vapor spatial distributions at single SAR acquisitions from interferograms. The retrieved spatial distribution may be assimilated in advanced weather models to improve short-term and fine-scale weather forecast.

Section 8.1 provides the conclusions of this study. The contributions of the study are summarized in section 8.2. Finally, recommendations for future research are given in section 8.3.

8.1 Conclusions

In this section conclusions are given for the two APS correction methods as well as the method for water vapor mapping respectively.

8.1.1 APS mitigation using numerical weather models

In the first correction method, we use the state-of-the-art weather research and forecast (WRF) model to simulate APS at 1 km resolution during SAR acquisitions and use the simulated APS to correct original interferograms formed by ASAR (Envisat) images. These interferograms have small temporal ($< 70\,\mathrm{days}$) and perpendicular ($< 350\,\mathrm{m}$) baselines, meaning that the observed phases are mainly driven by tropospheric delay. Therefore, the feasibility of correcting delay using WRF can be assessed by the phase residue after removing the simulated APS from the atmosphere-only interferograms.

To prevent a regional bias in our analysis we chose four different climatic regions

which are Hawaii, Mexico City, Groningen (the Netherlands) and Southwest Australia. The first two regions have strong topography variations, whereas the other two have flat terrains. From our analysis we find that APS mitigation is only achievable in the mountainous regions in which WRF can simulate height (topography) dependent delay. We have analyzed 8 and 6 atmosphere-only interferograms from Hawaii and Mexico City respectively. WRF simulations suggest that five of these interferograms experience height dependent delay. However, in reality, only four of the five interferograms experience height dependent delay (80% success rate). In these four cases the height dependent delay can be largely removed by the WRF simulations. For the case in which height dependent delay is absent the WRF correction however deteriorates the original interferogram. This is because the predicted but artificial height dependent delay is added to the original interferogram after correction. For the other nine interferograms, WRF simulations show no height dependent delay and no APS reduction is observed.

For the flat regions, we have analyzed 9 and 6 interferograms from Groningen and Southwest Australia respectively. The observed APS in these interferograms are mainly caused by spatio-temporal variation of water vapor in the lower troposphere. From our analysis we find that WRF simulations hardly lead to APS mitigation and very often deteriorate the original interferograms. This is because WRF is not able to simulate the realistic water vapor spatial distributions at fine scales ($< 50\,\mathrm{km}$). This also explains why the nine interferograms from the mountainous regions cannot have APS reduction.

The spatio-temporal variation of water vapor is caused by the so-called turbulent mixing process which has a random characteristic and can hardly be modeled deterministically. This leads us to examine the possibility of using WRF to simulate stochastic properties of delay instead of its realizations (i.e., delay maps during satellite acquisitions). To do that, we compute spatial variograms of APS from the original interferograms and the WRF simulations respectively. The result shows that WRF systematically underestimates the spatial variability of water vapor at all scales from 1 to 50 km. Increasing the model spin-up time and the number of vertical model levels within the atmospheric boundary layer (ABL) did not improve the variability.

Although our study is based on the WRF model only, this model is expected to outperform older generation models such as MM5 (mesoscale model). Therefore, based on our analysis, we conclude that contemporary weather models are useful for correcting the height dependent delay in interferograms over mountainous regions. However, their corrections should not be considered reliable at all times. For correcting delay caused by turbulent mixing, the value of these models is very limited and we recommend not to use them for APS correction.

Based on the above discussion, we believe that the best APS estimate, nowadays, is likely from InSAR data themselves by using advanced signal estimation techniques as we will conclude in the following section.

8.1.2 Separate APS and ground deformation from InSAR time series using LSC

Due to the poor performance of weather models for correcting APS driven by the spatio-temporal variation of water vapor, we decide to estimate APS from InSAR data themselves. The main challenge in this approach is to discriminate the various sources of phase variation, e.g., deformation, topography and atmosphere.

The correction method based on LSC and VCE uses only InSAR data (InSAR time series) as input. It is developed for PSInSAR analysis and utilizes least-squares collocation (LSC) and variance-covariance estimation (VCE) to optimally separate APS and ground deformation. Comparing to the filtering method in conventional PSInSAR, the LSC method not only gives the best estimates of APS and deformation but also provides the quality assessment (i.e., precision) of the estimates.

In conventional PSInSAR, the separation of APS and deformation is implemented as a window-based temporal low-pass filter. The optimal window type and length are usually unknown a-priori and subject to specify. In addition, because the window type is pre-determined and does not have the flexibility to cope with the time-changing variability of APS per acquisition. Therefore, this method does not lead to an optimal separation of APS and deformation, especially when there are large acquisition gaps in the time series and for acquisitions taken under bad weather such as thunderstorms. Moreover, the quality of the separation cannot be systematically assessed by the method, which makes the uncertainty of the deformation estimate hard to be quantified.

In the LSC method, the time-changing variability of APS is taken into account by modeling APS stochastically in both space and time. In space, APS is modeled as a correlated random signal by a variance-covariance function from the Mátern-family. In time, it is modeled as an uncorrelated signal with varying variance per acquisition (i.e., a diagonal variance-covariance matrix). The spatial and temporal variance-covariance matrices are estimated from InSAR time series and no external information of APS is needed. In such a way, APS can be filtered out from input time series more effectively comparing to the window-based filter in conventional PSInSAR.

The nonlinearity of ground deformation is taken into account by modeling the deformation stochastically. The LSC method models the total deformation using a functional model (e.g., a linear or quadratic function of time) and a stationary variance-covariance function in time. Although both the functional and stochastic models need to be pre-specified, their parameters (e.g., variance and correlation length of the deformation) are estimated from the InSAR time series.

Because of the stochastic modeling of deformation and APS, the uncertainty of their estimates can be quantified, which gives the precisions of the estimates.

The LSC method, however, has several limitations. First of all, it needs the nonlinear part of ground deformation to be stationary in time. A non-stationary deformation cannot be detected by the method and may result in biases (e.g., deformation leaking into APS) in the final ground deformation estimate. Secondly, similar to the window-based filtering method, it is only applicable to steady and progressive

ground deformation and assumes no temporal correlation of APS between adjacent acquisitions. Finally, the computational load of the method is significantly higher than the standard filter method, which is mainly the result of variance-covariance modeling of nonlinear deformation and APS. However, the modeling can be carried out per acquisition in parallel on multi-core CPUs to reduce the total computation time.

8.1.3 InSAR based water vapor mapping

The poor performance of weather models for simulating realistic water vapor distribution is largely due to the lack of high resolution water vapor observations. Such observations can only be obtained globally under all weather conditions by spaceborne InSAR. However, InSAR is only sensitive to the spatio-temporal variations of water vapor. To retrieve its spatial distributions at single SAR acquisitions from interferograms we develop a method that makes use of a temporal network of small baseline interferograms. The method is based on constrained least-squares and free network adjustment. It requires a sufficient number of SAR images from which semi-redundant interferograms can be formed. Under the assumption of no correlation between APS from different acquisitions, the lateral variations can be retrieved unambiguously and the redundancy helps to optimize the retrieval using free network adjustment. Unlike PSInSAR in which APS per acquisition is retrievable only from PS points our method can retrieve APS in 1-km resolution or better over the whole ground surface by forming small baseline interferograms to suppress phase decorrelation. We believe that the method will become widely applicable in the near future for the new generation of SAR satellites (such as Sentinel-1A/B) that have much shorter revisiting orbit (e.g., 6 days). The retrieved lateral distribution of water vapor may be assimilated by advanced weather models to improve the prediction of water vapor distribution at fine spatial scales. As a result, the improved modeling of water vapor can be used for mitigating APS in interferograms when separation of APS and deformation is difficult based on InSAR time series, e.g., earthquakes.

8.2 Contributions

Based on the conclusions in section 8.1, the contributions of this research are summarized as follows:

1. The feasibility of using numerical weather models for APS mitigation has been assessed. The mitigation can only be achieved in mountainous regions as the result of removing height dependent delay. The success rate of such mitigation is high (80%) but not always reliable. For flat regions the mitigation will often lead to deterioration of the original interferograms.

2. Statistics (lateral variation) of the simulated delay by WRF have been analyzed. The result shows that the model constantly underestimates the delay variation caused by turbulent mixing at all scales between 1 and 50 km.

3. A stochastic approach has been introduced for modeling ground deformation based on PSInSAR. The approach considers ground deformation as a stochastic process and models it via a variance-covariance model. It enables a systematic and simultaneous modeling of ground deformation together with other stochastic variables such as APS.

4. Separation of APS and ground deformation has been optimized for PSInSAR by taking into account the spatio-temporal stochastic characteristics of APS. In space, APS is correlated and modeled by a variance-covariance function from the Mátern-family. In time, APS is assumed uncorrelated and modeled by a diagonal variance-covariance matrix. The elements in the main diagonal correspond to the variances of APS during single SAR acquisitions.

5. A systematic way of assessing the precisions of the PSInSAR results has been introduced using least-squares collocation and the estimated variance-covariance matrices of ground deformation and APS.

6. The feasibility of mapping high resolution ($\sim 1\,\mathrm{km}$) water vapor distribution over land using InSAR has been demonstrated. The retrieved water vapor distribution has the potential to improve the prediction of water vapor distribution at fine scales using numerical weather simulations.

8.3 Outlook and recommendations

Two APS correction methods have been studied in this thesis. The weather model based method has a great potential (80% success rate) to remove height dependent delay but lacks the ability to correct the delay caused by turbulent mixing at fine spatial scales. The InSAR time series based method can estimate the fine scale lateral delay variations but relies on two assumptions: 1. temporal smoothness of ground deformation and 2. no correlation between APS at different acquisitions. It also requires a sufficient long time series of interferograms to allow a reliable estimation of APS statistics, i.e., the spatio-temporal variance-covariances. One way to get out of the dilemma is to improve the reliability of weather models.

8.3.1 Weather models

There are several possibilities to improve the reliability of weather models. One is to use better initial and boundary conditions, such as ECMWF (European Center for Medium-Range Weather Forecasts) data with 50 km resolution, as inputs for simulation. Another possibility is to use a so-called 4D-Var data assimilation scheme (Rabier and Courtier, 1992) which can utilize meteorological observations before and after SAR acquisitions to refine the forecast that only uses observations prior to the acquisitions. Moreover, satellite observations of water vapor (from e.g., MERIS, MODIS and GPS networks) can be included in the data assimilation to increase the spatial density of the input data.

Considering the high dynamic characteristics of turbulent mixing, simulating realistic water vapor distributions at the fine spatial scales may be difficult to achieve

in the next decades. Instead of simulating the distributions, weather models can be used to simulate the statistics (e.g., variograms) of the distributions. Then, the statistics can be used to construct variance-covariance functions of APS and allow an optimal separation of APS and deformation using InSAR time series for events in which ground deformation is progressive. For events like earthquakes and volcanic eruptions the variance-covariance functions and InSAR observations can be combined and incorporated into geophysical models and data inversion schemes.

8.3.2 InSAR meteorology

For weather models, the lack of the ability for simulating fine scale water vapor variations is largely due to the low spatial density ($> 50\,\text{km}$) of their input data. Until now, only satellite interferometry can provide fine scale mapping of water vapor over land globally under all weather conditions. We have demonstrated that it is possible to retrieve the spatial distributions of water vapor at single SAR acquisitions from interferograms. Therefore, space-borne InSAR can be used as an additional source for providing meteorological input data for weather models to improve their reliability. We expect the new generation of SAR satellites such as Sentinel-1A/B will be able to demonstrate the capability of InSAR for meteorological applications.

Addenda

Appendix A

Random process models

A spatial random field $Z(\mathbf{s})$ is called *homogeneous* if (Tatarski, 1961):

$$\mathbf{E}\{Z(\mathbf{s})\} = \mu, \tag{A.0.1}$$

and

$$\begin{aligned} Q(Z(\mathbf{s}), Z(\mathbf{s}+\mathbf{h})) &= E\{(Z(\mathbf{s}) - E\{Z(\mathbf{s})\})(Z(\mathbf{s}) - E\{Z(\mathbf{s})\})\} \\ &= Q(\mathbf{h}), \end{aligned} \tag{A.0.2}$$

where $\mathbf{E}\{.\}$ is the mathematical expectation, μ is a constant, $\mathbf{s}$ and $\mathbf{h}$ are spatial vectors and Q is the autocovariance function of Z. A random field is *isotropic* if it is homogeneous and $Q(\mathbf{h}) = Q(|\mathbf{h}|)$, where $|.|$ is the spatial distance operator. In addition, the *variogram* or *structure function* of Z is defined as:

$$\begin{aligned} \gamma(Z(\mathbf{s}), Z(\mathbf{s}+\mathbf{h})) &= \mathbf{E}\{|(Z(\mathbf{s}) - \mu) - (Z(\mathbf{s}+\mathbf{h}) - \mu)|^2\} \\ &= \gamma(\mathbf{h}). \end{aligned} \tag{A.0.3}$$

For an isotropic and ergodic random field we have:

$$Q(\mathbf{h}) = Q(0) - \frac{1}{2}\gamma(\mathbf{h}). \tag{A.0.4}$$

Spheric model. A spheric model has two parameters a and σ:

$$\gamma(\mathbf{h}) = \begin{cases} \sigma^2(1 - \frac{3}{2}\frac{\mathbf{h}}{a} + \frac{1}{2}\frac{\mathbf{h}^3}{a^3}) & \text{for } 0 \le \mathbf{h} \le a, \\ \sigma^2 & \text{for } \mathbf{h} > a, \end{cases} \tag{A.0.5}$$

$$Q(\mathbf{h}) = \begin{cases} \sigma^2(\frac{3}{2}\frac{\mathbf{h}}{a} - \frac{1}{2}\frac{\mathbf{h}^3}{a^3}) & \text{for } 0 \le \mathbf{h} \le a, \\ 0 & \text{for } \mathbf{h} > a, \end{cases} \tag{A.0.6}$$

Exponential model. Given the same parameters, the variogram of a exponential model has the form:

$$\gamma(\mathbf{h}) = \sigma^2(1 - \exp(-\frac{\mathbf{h}}{a})), \tag{A.0.7}$$

and the autocovariance reads:

$$Q(\mathbf{h}) = \sigma^2 \exp(-\frac{\mathbf{h}}{a}). \tag{A.0.8}$$

Gaussian model. Gaussian model has the same parameters:

$$\gamma(\mathbf{h}) = \sigma^2(1 - \exp(-\frac{\mathbf{h}^2}{a^2})), \tag{A.0.9}$$

and

$$Q(\mathbf{h}) = \sigma^2 \exp(-\frac{\mathbf{h}^2}{a^2}). \tag{A.0.10}$$

Hole-effect model. Hole-effect model is not a monotonic function of $\mathbf{h}$ and it is used to represent some type of pseudo-periodicity:

$$\gamma(\mathbf{h}) = \begin{cases} \sigma^2(1 - (1 - \frac{\mathbf{h}}{a})\exp(-\frac{\mathbf{h}}{a})) & \text{for } \mathbf{h} \leq a, \\ \sigma^2 & \text{for } \mathbf{h} > a, \end{cases} \tag{A.0.11}$$

and

$$Q(\mathbf{h}) = \begin{cases} \sigma^2(1 - \frac{\mathbf{h}}{a})\exp(-\frac{\mathbf{h}}{a}) & \text{for } \mathbf{h} \leq a, \\ 0 & \text{for } \mathbf{h} > a, \end{cases} \tag{A.0.12}$$

Mátern family. The models from Mátern family have one extra parameter τ which controls the spatial smoothness of Z:

$$\gamma(\mathbf{h}) = \sigma^2(1 - \frac{1}{2^{(\tau-1)}\Gamma(\tau)}(\frac{2\sqrt{\tau}\mathbf{h}}{a})^\tau K_\tau(\frac{2\sqrt{\tau}\mathbf{h}}{a})), \tag{A.0.13}$$

and

$$Q(\mathbf{h}) = \frac{\sigma^2}{2^{(\tau-1)}\Gamma(\tau)}(\frac{2\sqrt{\tau}\mathbf{h}}{a})^\tau K_\tau(\frac{2\sqrt{\tau}\mathbf{h}}{a}), \tag{A.0.14}$$

where Γ is the Gamma function and K is the modified Bessel function of the second kind.

Appendix B

Groningen: master APS and DEM inaccuracy estimation

This appendix provides the details of master APS and DEM inaccuracy estimation for the Groningen case study in section 6.4 of chapter 6.

The master APS and DEM (SRTM) inaccuracy are treated as deterministic variables. The estimates of the master APS and the DEM inaccuracy obtained from the collocation method (see chapter 4) are displayed in Fig. B.1 a and Fig. B.2 a respectively. The corresponding weighted least-squares solutions (see Eq. 6.1.8) are shown in Fig. B.1 b and Fig. B.2 b respectively for comparison. Moreover, the difference between the results from the two methods are visualized by histograms shown in Fig. B.3 a and b. The correlation between the two master APS estimates shown in Fig. B.1 a and b is 0.99. The mean and RMS of the difference between the two master APS estimates are 0.1 and 1.0 mm respectively.

Regarding the DEM inaccuracy the two methods again give quite similar results. The mean and RMS of the difference between the two DEM inaccuracy estimates are -0.05 and 0.2 m respectively. Therefore, we conclude that the collocation method does not give a significantly better result than WLS on estimating the deterministic variables for the Groningen case where the ground subsidence is steady in time and there are not significant gaps in the time series.

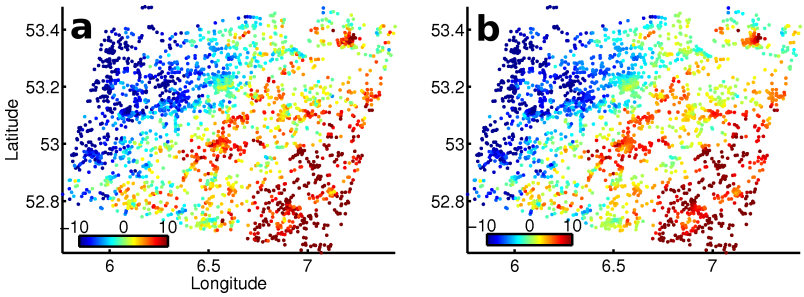

Fig. B.1. Master APS estimation. **a**) Master APS estimates (unit: mm) obtained from the collocation method. **b**) Master APS estimates (unit: mm) by WLS. In conclusion, the two methods give a comparable result

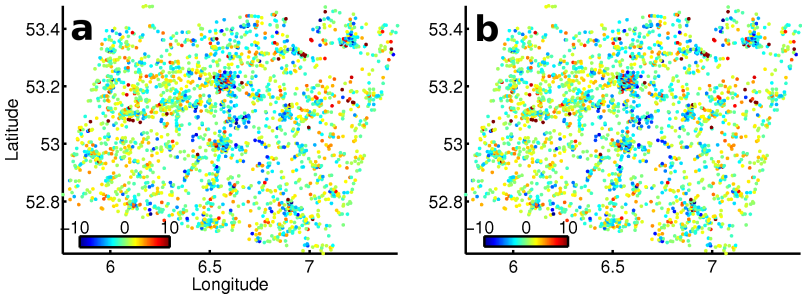

Fig. B.2. DEM inaccuracy estimation. **a**) DEM inaccuracy estimates (unit: m) obtained from the collocation method. **b**) DEM inaccuracy estimates (unit: m) by WLS. In conclusion, the two methods give a comparable result

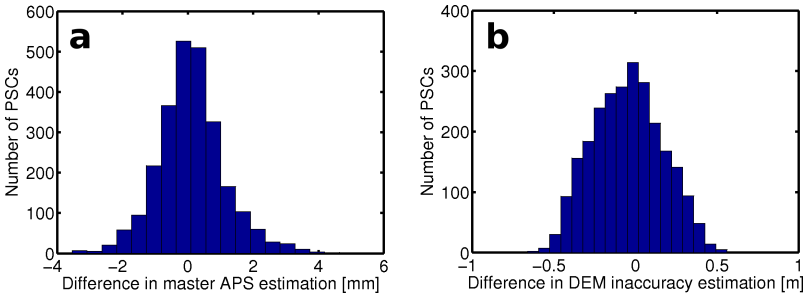

Fig. B.3. Result difference between the two methods. **a**) Histogram of the difference between the master APS estimates shown in Fig. B.1 a and b. **b**) Histogram of the difference between the DEM inaccuracy estimates shown in Fig. B.2 a and b.

Bibliography

Albert, P., R. Bennartz, and J. Fischer (2001). Remote sensing of atmospheric water vapour from backscattered sunlight in cloudy atmospheres. *Journal of Atmospheric and Oceanic Technology 18*(6), 865–874.

Amelung, F., S.-H. Yun, T. R. Walter, P. Segall, and S.-W. Kim (2007, May-18). Stress control of deep rift intrusion at mauna loa volcano, hawaii. *Science 316*, 1026–1030.

Arikan, M., F. van Leijen, L. Guang, and R. Hanssen (2008). Improved image alignment under the influence of elevation. In *Fifth International Workshop on ERS/Envisat SAR Interferometry, 'FRINGE07', Frascati, Italy, 26 Nov-30 Nov 2007*, pp. 4 pp.

Armstrong, M. (1984). Problems with universal kriging. *Mathematical Geology 16*(1), 101–108.

Baarda, W. (1968). *A testing procedure for use in geodetic networks* (2 ed.), Volume 5 of *Publications on Geodesy*. Delft: Netherlands Geodetic Commission.

Bamler, R. and P. Hartl (1998). Synthetic aperture radar interferometry. *Inverse Problems 14*, R1–R54.

Bean, B. R. and E. J. Dutton (1968). *Radio Meteorology*. New York: Dover.

Beauducel, F., P. Briole, and J.-L. Froger (2000, July). Volcano wide fringes in ERS synthetic aperture radar interferograms of Etna. *Journal of Geophysical Research 105*(B7), 16391–16402.

Bennartz, R. and J. Fischer (2001). Retrieval of column water vapour over land rom backscattered solar radiation using the medium resolution imaging spectrometer. *Remote Sens. Enviroment 78*, 274–283.

Berardino, P., G. Fornaro, R. Lanari, and E. Sansosti (2002). A new algorithm for surface deformation monitoring based on small baseline differential SAR interferograms. *IEEE Transactions on Geoscience and Remote Sensing 40*(11), 2375–2383.

Bevis, M., S. Businger, T. A. Herring, R. A. Anthes, C. Rocken, and R. H. Ware (1994). GPS meteorology: mapping zenith wet delays onto precipitable water. *Journal of Applied Meteorology 33*(3).

Bevis, M., S. Businger, T. A. Herring, C. Rocken, R. A. Anthes, and R. H. Ware (1992). GPS meteorology: Remote sensing of atmospheric water vapor using the Global Positioning System. *Journal of Geophysical Research 97*, 15,787–15,801.

Bevis, M., S. Chiswell, S. Businger, T. A. Herring, and Y. Bock (1996). Estimating

wet delays using numerical weather analysis and predictions. *Radio Science 31*(3), 477–487.

Bianchi, M. (2003, April). Phase ambiguity estimation on permanent scatterers in SAR interferometry: the integer least-squares approach. Master's thesis, Politecnico di Milano/Delft University of Technology.

Bowman, C. (2009). Moving from mm5 to wrf. (Last visit on 6 Nov. 2011), <http://yosemite.epa.gov/R10/airpage.nsf/smoke/09+meeting>.

Cassee, B. (2004, October). Selection of permanent scatterer candidates for deformation monitoring; amplitude calibration of ERS SLC SAR images. Master's thesis, Delft University of Technology.

Chen, C. W. and H. A. Zebker (2000, February). Two-dimensional phase unwrapping using statistical models for cost functions in nonlinear optimization. *Journal of the Optical Society of America A. 18*, 338–351.

Cimini, D., N. Pierdicca, E. Pichelli, R. Ferretti, V. Mattiolo, S. Bonafoni, M. Montopoli, and D. Perissin (2012). On the accuracy of integrated water vapor observations and the potential for mitigating electromagnetic path delay error in insar. *Atmospheric Measurement Techniques Discussion 5*, 839–880.

Colesanti, C., A. Ferretti, F. Novali, C. Prati, and F. Rocca (2003, July). SAR monitoring of progressive and seasonal ground deformation using the Permanent Scatterers Technique. *IEEE Transactions on Geoscience and Remote Sensing 41*(7), 1685–1701.

Counselman, C. C. and S. A. Gourevitch (1981). Miniature interferometer terminals for earth surveying: ambiguity and multipath with the Global Positioning System. *IEEE Transactions on Geoscience and Remote Sensing 19*(4), 244–252.

Cressie, N. (1985). Fitting variogram models by weighted least-squares. *Mathematical Geology 17*(5), 563–586.

Cressie, N. (1987). A nonparametric vieew of generalized covariances for kriging. *Mathematical Geology 19*(5), 425–449.

Crook, N. A. (1996). Sensitivity of moist convection forced by boundary layer processes to low-level thermodynamic fields. *Monthly Weather Review 124*, 1767–1785.

Crosetto, M., C. C. Tscherning, B. Crippa, and M. Castillo (2002). Subsidence monitoring using SAR interferometry: Reduction of the atmospheric effects using stochastic filtering. *Geophysical Research Letters 29*(9), xxx.

Davis, J., G. Elgered, A. Niell, and C. Kuehn (1991, November). Ground-based measurement of gradients in the "wet" radio refractivity of air. *Radio Science 28*, 1003–1018.

Davis, J. L., T. A. Herring, I. I. Shapiro, A. E. E. Rogers, and G. Elgered (1985). Geodesy by radio interferometry: Effects of atmospheric modelling errors on estimates of baseline length. *Radio Science 20*(6), 1593–1607.

De Zan, F. and F. Rocca (2005). Coherent processing of long series of SAR images. In *International Geoscience and Remote Sensing Symposium, Seoul, Korea, 25–29 July 2005*.

Delacourt, C., P. Briole, and J. Achache (1998, August). Tropospheric corrections of SAR interferograms with strong topography. application to Etna. *Geophysical Research Letters 25*(15), 2849–2852.

Di-Bisceglie, M., A. Fusco, C. Galdi, and E. Sansosti (2001). Stochastic modelling of atmospheric effects in sar differential interferometry. In *International Geoscience and Remote Sensing Symposium, Sydney, Australia, 9–13 July 2001*, pp. cdrom, 3 pages.

Dietrich, C. R. and G. N. Newsam (1993, August). A fast and exact method for multidimensional gaussian stochastic simulations. *Water Resources Research 29*(8), 2861–2869.

Dubai Meteorological Office (2011). Climate of dubai. (Last visit on 25 Oct 2011), <http://www.dia.ae/dubaimet/MET/Climate.aspx>.

Dudhia, M. and R. Ferretti (2010). personal communication.

Dupont, S., P. Nonin, L. Renouard, G. Pichon, and F. Bignone (1997). Atmospheric artifacts in ERS DTM. ISTAR's experience over multiple sites and large areas. In *Third ERS Symposium—Space at the Service of our Environment, Florence, Italy, 17–21 March 1997*.

Elgered, G. (1982). Tropospheric wet path-delay measurements. *IEEE Transactions on Antennas and Propagation AP-30*, 502–505.

Elosegui, P., A. Rius, J. L. Davis, G. Ruffini, S. J. Keihm, B. Burki, and L. P. Kruse (1998). An experiment for estimation of the spatial and temporal variations of water vapor using gps data. *Phys. Chem. Earth 23*, 125–130.

Emanuel, K., D. Raymond, A. Betts, L. Bosart, C. Bretherton, K. Droegemeier, B. Farrell, J. M. Fritsch, R. Houze, M. LeMone, D. Lilly, R. Rotunno, M. Shapiro, R. Smith, and A. Thorpe (1995). Report of the first prospectus development team of the u. s. weather research program to noaa and the nsf. *Bull. Amer. Meteor. Soc. 76*, 1194–1208.

Emardson, T. R., M. Simons, and F. H. Webb (2003). Neutral atmospheric delay in interferometric synthetic aperture radar applications: Statistical description and mitigation. *Journal of Geophysical Research 108*(B5), doi:10.1029/2002JB001781.

ESA (2006). Meris product handbook. Technical Report Issue2.1, European Space Agency.

Farr, T. G., S. Hensley, E. Rodriguez, J. Martin, and M. Kobrick (1999). The shuttle radar topography mission. In *CEOS SAR Workshop, ESA-CNES, Toulouse, France, 26-29 October 1999*, pp. 1–3.

Ferretti, A., C. Prati, and F. Rocca (1999, March). Multibaseline InSAR DEM reconstruction: The wavelet approach. *IEEE Transactions on Geoscience and Remote Sensing 37*(2), 705–715.

Ferretti, A., C. Prati, and F. Rocca (2000, September). Nonlinear subsidence rate estimation using permanent scatterers in differential SAR interferometry. *IEEE Transactions on Geoscience and Remote Sensing 38*(5), 2202–2212.

Ferretti, A., C. Prati, and F. Rocca (2001, January). Permanent scatterers in SAR interferometry. *IEEE Transactions on Geoscience and Remote Sensing 39*(1), 8–20.

Fischer, J. and R. Bennartz (1997). ATBD 2.4 retrieval of total water vapour content from MERIS measurements. Technical Report PO-TN- MEL-GS-0005, ESA.

Foster, J., B. Brooks, T. Cherubini, C. Shacat, S. Businger, and C. L. Werner (2006). Mitigating atmospheric noise for InSAR using a high resolution weather model. *Geophysical Research Letters 33*(L16304), doi:10.1029/2006GL026781.

Gatelli, F., A. Monti Guarnieri, F. Parizzi, P. Pasquali, C. Prati, and F. Rocca (1994, July). The wavenumber shift in SAR interferometry. *IEEE Transactions on Geoscience and Remote Sensing 32*(4), 855–865.

Goldstein, R. (1995, September). Atmospheric limitations to repeat-track radar interferometry. *Geophysical Research Letters 22*(18), 2517–2520.

Gong, W., F. Meyer, and S. Liu (2010). Performance analysis of atmospheric correction in insar data based on the weather research and forecasting model. In *International Geoscience and Remote Sensing Symposium, Honolulu, Hawaii, 25–30 July 2010*, pp. 5 pp.

Gong, W., F. Meyer, and S. Liu (2011). Numerical weather model assisted time series insar processing for geophysical application. In *Seventh International Workshop on ERS/Envisat SAR Interferometry, 'FRINGE2011', Frascati, Italy, 19-23 Sept 2011*, pp. 5 pp.

Grebenitcharsky, R. and R. Hanssen (2005, September-15). Spatial modeling of atmospheric delays for InSAR and GPS sensors. European Meteorological Society, 5th Annual Meeting, Utrecht, the Netherlands, 12–16 September 2005.

Hall, M. P. M., L. W. Barclay, and M. T. Hewitt (Eds.) (1996). *Propagation of Radiowaves*. London: The Institution of Electrical Engineers.

Handcock, M. S. and J. R. Wallis (1994, June). An approach to statistical spatial-temporal modeling of meteorological fields (with discussion). *Journal of the American Statistical Association 89*(426), 368–390.

Hanssen, R. (1998). *Atmospheric heterogeneities in ERS tandem SAR interferometry*. Delft, the Netherlands: Delft University Press.

Hanssen, R. and A. Feijt (1996). A first quantitative evaluation of atmospheric effects on SAR interferometry. In *'FRINGE 96' workshop on ERS SAR Interferometry, Zürich, Switzerland, 30 Sep–2 October 1996*, pp. 277–282. ESA SP-406.

Hanssen, R. and B. Kampes (2004). The use of synthetic aperture radar (SAR) interferometry to retrieve bio- and geo-physical variables. insar retrieval of atmospheric variables. Technical report, ENVEO, Innsbruck, Austria. European Space Agency Study Contract report ESA Contract Nr. 16366/02/NL/MM.

Hanssen, R. and R. Klees (1997, November-18). Land subsidence monitoring with SAR interferometry: Assessment of the atmospheric errors. *EOS Transactions, AGU 78*(46), F144.

Hanssen, R. and R. Klees (1999). An empirical model for the assessment of DEM accuracy degradation due to vertical atmospheric stratification. In *Second International Workshop on ERS SAR Interferometry, 'FRINGE99', Liège, Belgium, 10–12 Nov 1999*, pp. 1–5. ESA.

Hanssen, R., B. Vermeersen, R. Scharroo, B. Kampes, S. Usai, R. Gens, and R. Klees (2000, February). Deformatiepatroon van de aardbeving van 17 augustus 1999 in Turkije gemeten met satelliet radar interferometrie. *Remote Sensing Nieuwsbrief 90*, 42–44. In Dutch.

Hanssen, R., I. Weinreich, S. Lehner, and A. Stoffelen (2000, June-15). Tropospheric wind and humidity derived from spaceborne radar intensity and phase observations. *Geophysical Research Letters 27*(12), 1699–1702.

Hanssen, R., H. Zebker, R. Klees, and S. Barlag (1998). On the use of meteorological observations in SAR interferometry. In *International Geoscience and Remote*

Sensing Symposium, Seattle, Washington, USA, 6–10 July 1998, pp. 1644–1646.

Hanssen, R. F. (2001). *Radar Interferometry: Data Interpretation and Error Analysis*. Dordrecht: Kluwer Academic Publishers.

Hanssen, R. F., A. J. Feijt, and R. Klees (2001, May). Comparison of precipitable water vapor observations by spaceborne radar interferometry and Meteosat 6.7-μm radiometry. *Journal of Atmospheric and Oceanic Technology 18*(5), 756–764.

Hanssen, R. F., P. J. G. Teunissen, and P. Joosten (2001). Phase ambiguity resolution for stacked radar interferometric data. In *International Symposium on Kinematic Systems in Geodesy, Geomatics and Navigation, Banff, Canada, 5–8 June 2001*, pp. 317–320.

Hanssen, R. F., T. M. Weckwerth, H. A. Zebker, and R. Klees (1999, February-26). High-resolution water vapor mapping from interferometric radar measurements. *Science 283*, 1295–1297.

Heleno, S. I. N., C. Frischknecht, N. dÓreye, J. N. P. Lima, B. Faria, R. Wall, and F. Kervyn (2010). Seasonal tropospheric influence on SAR interferograms near the ITCZ the case of fogo volcano and mount cameroon. *Journal of African Earth Sciences 58*, 833–856.

Hobiger, T., Y. Kinoshita, S. Shimizu, R. Ichikawa, M. Furuya, T. Kondo, and Y. Koyama (2010, May). On the importance of accurately ray-traced troposphere corrections for interferometric SAR data. *Journal of Geodesy 84*(9), doi:10.1007/s00190–010–0393–3.

Hooper, A. (2006). *Persistent Scatterer Radar Interferometry for Crustal Deformation Studies and Modeling of Volcanic Deformation*. Ph. D. thesis, Stanford University.

Hooper, A., P. Segall, and H. Zebker (2007, July). Persistent scatterer interferometric synthetic aperture radar for crustal deformation analysis, with application to volcán alcedo, galápagos. *Journal of Geophysical Research 112*(B07407).

Jolivet, R., R. Grandin, C. Lasserre, M. P. Doin, and G. Peltzer (2011). Systematic insar tropospheric phase delay corrections from global meteorological reanalysis data. *Geophysical Research Letters 38*(L17311), doi:10.1029/2011GL048757.

Journel, A. G. and C. J. Huijbregts (1978). *Mining Geostatistics*. London: Academic Press.

Kampes, B. (1999). *Delft Object-Oriented Radar Interferometric Software: Users manual and Technical Documentation* (1.2 ed.). Delft: Delft University of Technology.

Kampes, B. and S. Usai (1999). Doris: the Delft Object-oriented Radar Interferometric Software. In *2nd International Symposium on Operationalization of Remote Sensing, Enschede, The Netherlands, 16–20 August, 1999*.

Kampes, B. M. (2005, September). *Displacement Parameter Estimation using Permanent Scatterer Interferometry*. Ph. D. thesis, Delft University of Technology, Delft, the Netherlands.

Kampes, B. M. and R. F. Hanssen (2004, November). Ambiguity resolution for permanent scatterer interferometry. *IEEE Transactions on Geoscience and Remote Sensing 42*(11), 2446–2453.

Ketelaar, V. B. H. (2008, September). *Monitoring surface deformation induced by hydrocarbon production using satellite radar interferometry*. Ph. D. thesis, Delft

University of Technology, Delft, the Netherlands.

Kitanidis, P. K. (1983, August). Statistical estimation of polynomial generalized covariance functions and hydrologic applications. *Water Resources Research 19*(4), 909–921.

Kitanidis, P. K. (1987, August). Parametric estimation of covariances of regionalized variables. *Water Resources Bulletin 23*(4), 557–567.

Kitanidis, P. K. (1993). Generalized covariance functions in estimation. *Mathematical Geology 25*(5), 525–540.

Kitanidis, P. K. (1997). *Introduction to Geostatistics: Application in Hydrogeology*. Cambridge: Cambridge University Press.

Kitanidis, P. K. and R. W. Lane (1985). Maximum likelihood parameter estimation of hydrologic spatial processes by the gauss-newton method. *Journal of Hydrology 79*, 53–71.

Kleijer, F. (2004, April). *Troposphere Modeling and Filtering for Precise GPS Leveling*. Ph. D. thesis, Delft University of Technology.

KNMI (2011). (Last visit on 6 Nov. 2011), <http://knmi.nl>.

Knospe, S. H. G. and S. Jonsson (2010, March). Covariance estimation for dinsar surface deformation measurements in the presence of anisotropic atmospheric noise. *IEEE Transactions on Geoscience and Remote Sensing 48*(4), 1–9.

Kolmogorov, A. N. (1941). Dissipation of energy in locally isotropic turbulence. *Doklady Akad. Nauk SSSR 32*(16). German translation in "Sammelband zur Statistischen Theorie der Turbulenz", Akademie Verlag, Berlin, 1958, p77.

Krarup, T. (1969). A contribution to the mathematical foundation of physical geodesy. Technical Report 44, Dan Geod Inst, Copenhagen.

Laur, H., P. Bally, P. Meadows, J. Sanchez, B. Schaettler, E. Lopinto, and D. Esteban (2002, September). Derivation of the backscattering coefficient σ^0 in ESA ERS SAR PRI products. Technical Report ES-TN-RS-PM-HL09, ESA. Issue 2, Rev. 5d.

Li, Z., E. Fielding, and P. Cross (2009). Integration of InSAR time series analysis and water vapour correction for mapping postseismic deformation after the 2003 bam, iran earthquake. *IEEE Transactions on Geoscience and Remote Sensing 47*, 3220–3230.

Li, Z., E. Fielding, P. Cross, and J.-P. Muller (2006). Interferometric synthetic aperture radar atmospheric correction: GPS topography-dependent turbulence model. *Journal of Geophysical Research 111*(B02404).

Li, Z., J.-P. Muller, P. Cross, P. Albert, J. Fischer, and R. Bennartz (2006). Assessment of the potential of MERIS near-infrared water vapour products to correct ASAR interferometric measurements. *International Journal of Remote Sensing 27*, 349–365.

Li, Z., J.-P. Muller, P. Cross, and E. J. Fielding (2005). Interferometric synthetic aperture radar (InSAR) atmospheric correction: GPS, moderate resolution imaging spectroradiometer (MODIS), and InSAR integration. *Journal of Geophysical Research 110*(B03410), doi:10.1029/2004JB003446.

Li, Z. W., X. L. Ding, and G. Liu (2004). Modeling atmospheric effects on InSAR with meteorological and continuous GPS observations: algorithms and some test results. *Journal of Atmospheric and Solar-Terrestrial*

Physics 66(doi:10.1016/j.jastp.2004.02.006), 907–917.

Lindenbergh, R., H. van der Marel, M. Keshin, and S. de Haan (2007). Towards sequential water vapor predictions based on time series of GPS and Meris. In *ESA ENVISAT Symposium, Montreux, Switzerland, 23–27 April 2007*, pp. 6 pp.

Liu, S., S. S. Esfahany, A. Hooper, and F. J. van Leijen (2011). Separating non-linear deformation and atmosperic phase screen for insar time series analysis using least-squares collocation. In *Seventh International Workshop on ERS/Envisat SAR Interferometry, 'FRINGE2011', Frascati, Italy, 19-23 Sept 2011*, pp. 5 pp.

Liu, S., R. F. Hanssen, and A. Mika (2009). Feasibility of retrieving spatial variations of atmospheric phase screen at epochs of SAR acquisitions from SAR interferometry. In *Sixth International Workshop on ERS/Envisat SAR Interferometry, 'FRINGE09', Frascati, Italy, 30 Nov-4 Dec 2009*, pp. 5 pp.

Liu, S., A. Mika, W. Gong, R. Hanssen, F. Meyer, D. Morton, and P. W. Webley (2011). The role of weather models in mitigation of tropospheric delay for SAR interferometry. In *International Geoscience and Remote Sensing Symposium, Vancouver, Canada, 24–29 July 2011*, pp. 4 pp.

Liu, S., A. Mika, and R. Hanssen (2009). On the value of high-resolution weather models for atmospheric mitigation in SAR interferometry. In *International Geoscience and Remote Sensing Symposium, Cape Town, South Africa, 12–17 July 2009*, pp. 4 pp.

Lopez-Quiroz, P., M. P. Doin, F. Tupin, P. Briole, and J. M. Nicolas (2009). Time series analysis of mexico city subsidence constrained by radar interferometry. *Journal of Applied Geophysics 69*(1), 1–15.

Lorenz, E. (1963, january). Deterministic nonperiodic flow. *Journal of the Atmospheric Sciences 20*, 130–141.

Massonnet, D. (1997, February). Satellite radar interferometry. *Scientific American*, 32–39.

Massonnet, D., P. Briole, and A. Arnaud (1995, June-15). Deflation of Mount Etna monitored by spaceborne radar interferometry. *Nature 375*, 567–570.

Massonnet, D. and K. L. Feigl (1995). Discrimination of geophysical phenomena in satellite radar interferograms. *Geophysical Research Letters 22*(12), 1537–1540.

Matheron, G. (1973). The intrinsic random functions and their applications. *Advances in Applied Probability 4*, 473–468.

Mattar, K. E., A. L. Gray, D. Geudtner, and P. W. Vachon (1999, March). Interferometry for DEM and terrain displacement: Effects of inhomogeneous propagation. *Canadian Journal of Remote Sensing 25*(1), 60–69.

Mendes, V. B. (1999). *Modeling the neutral-atmosphere propagation delay in radiometric space techniques*. Ph. D. thesis, University of New Brunswick.

Morgan, J. R. (1996). *Hawaii: A Unique Geography*. Honolulu, Hawaii: Bess Press.

Moritz, H. (1962). Interpolation and prediction of gravity and their accuracy. Technical Report 24, Inst Geod Phot Cart, Ohio State University, Columbus, USA.

Myers, D. E. (1989). To be or not to be ... stationary? that is the question. *Mathematical Geology 21*(3), 347–361.

Neuman, S. P. and E. A. Jacobson (1984). Analysis of nonintrinsic spatial variability by residual kriging with application to regional groundwater levels. *Mathematical Geology 16*(5), 499–521.

Nico, G., R. Tome, J. Catalao, and P. M. A. Miranda (2010). On the use of the wrf model to mitigate tropospheric phase delay effects in sar interferograms. *IEEE Transactions on Geoscience and Remote Sensing 58*, 833–856.

Nitti, D. O., R. F. Hanssen, A. Refice, F. Bovenga, and R. Nutricato (2011, March). Impact of dem-assisted coregistration on high-resolution sar interferometry. *IEEE Transactions on Geoscience and Remote Sensing 49*(3), 1127–1143.

Onn, F. and H. A. Zebker (2006). Correction for interferometric synthetic aperture radar atmospheric phase artifacts using time series of zenith wet delay observations from a GPS network. *Journal of Geophysical Research 111*(B09102), doi:10.1029/2005JB004012.

Osmanoglu, B., T. H. Dixon, S. Wdowinski, E. Cabral-Cano, and Y. Jiang (2011). Mexico city subsidence observed with persistent scatterer insar. *International Journal of Applied Earth Observation and Geoinformation 13*(1), 1–12.

Pepe, A., A. B. Ortiz, M. Bonano, R. Lanari, P. Lundgren, and P. A. Rosen (2010). Deformation in hawaii's volcanoes obtained from a scansar-to-stripmap small baseline subset technique. In *International Geoscience and Remote Sensing Symposium, Cape Town, South Africa, 12–17 July 2009*, pp. 4 pp.

Puyssegur, B., R. Michel, and J. P. Avouac (2007, May). Tropospheric phase delay in interferometric synthetic aperture radar estimated from meteorological model and multispectral imagery. *Journal of Geophysical Research 112*(B05419), doi:10.1029/2006JB004352.

Rabier, F. and P. Courtier (1992). Four dimensional assimilation in the presence of baroclinic instability. *Q. J. R. Meteorol. Soc. 118*, 649–672.

Rao, K. S. and S. M. Phalke (2001). Analysis of dem derived from SRTM for the assessment of geo-coding and height accuracy. In *International Geoscience and Remote Sensing Symposium, Sydney, Australia, 9–13 July 2001*, pp. cdrom, 4 pages.

Richardson, L. F. (2007). *Weather prediction by numerical process*. London: Cambridge university press.

Rind, D., E. W. Chiou, W. P. Chu, J. C. Larsen, S. Oltmans, J. Lerner, M. P. McCormick, and L. R. McMaser (1991). Positive water vapor feedback in climate models confirmed by satellite data. *Nature 349*, 7500–7503.

Rocca, F. (2007, October). Modeling interferogram stacks. *IEEE Transactions on Geoscience and Remote Sensing 45*(10), 3289–3299.

Rodriguez, E. and J. M. Martin (1992, April). Theory and design of interferometric synthetic aperture radars. *IEE Proceedings-F 139*(2), 147–159.

Rommen, B., L. Gale, R. Hanssen, S. Liu, C. Mätzler, A. Mika, J. Morland, M. Santoro, U. Wegmüller, C. Werner, and H. Zelle (2009, March). The ESA METAWAVE project—correcting for atmospheric water vapour effects in InSAR products. In *Third European Conference on Antennas and Propagation, Berlin, Germany, 23–27 March 2009*, pp. 1–5.

Rosen, P., S. Hensley, I. R. Joughin, F. K. Li, S. Madsen, E. Rodríguez, and R. Goldstein (2000, March). Synthetic aperture radar interferometry. *Proceedings of the IEEE 88*(3), 333–382.

Rosen, P. A., S. Hensley, E. Gurrola, F. Rogez, S. Chan, J. Martin, and E. Rodriguez (2001). SRTM C-band topographic data: Quality assessment and calibration

activities. In *International Geoscience and Remote Sensing Symposium, Sydney, Australia, 9–13 July 2001*, pp. 3 pages, cdrom.

Saastamoinen, J. (1972). Introduction to practical computation of astronomical refraction. *Bulletin Geodesique 106*, 383–397.

Samiei-Esfahany, S. (2008, July). Improving persistent scatterer interferometry results for deformation monitoring. Master's thesis, Delft University of Technology.

Sandwell, D. T. and E. J. Price (1998, December). Phase gradient approach to stacking interferograms. *Journal of Geophysical Research 103*(B12), 30183–30204.

Scharroo, R. and P. Visser (1998). Precise orbit determination and gravity field improvement for the ERS satellites. *Journal of Geophysical Research 103*(C4), 8113–8127.

Servicio Meteorologico Nacional (2011). (Last visit on 29 Oct 2011), <http://smn.cna.gob.mx>.

Seymour, M. S. and I. G. Cumming (1996). An iterative algorithm for ERS baseline estimation. In *'FRINGE 96' workshop on ERS SAR Interferometry, Zürich, Switzerland, 30 Sep–2 October 1996*. ESA.

Shimada, M., M. Minamisawa, and O. Isoguchi (2001). Correction of atmospheric excess path delay appeared in repeat-pass SAR interferometry using objective analysis data. In *International Geoscience and Remote Sensing Symposium, Sydney, Australia, 9–13 July 2001*, pp. cdrom, 3 pages.

Skamarock, W. C., J. B. Klemp, J. Dudhia, D. O. Gill, D. M. Barker, M. G. Duda, X.-Y. Huang, W. Wang, and J. G. Powers (2008, june). A description of the advanced research WRF version 3. NCAR Technical Note NCAR/TN-475+STR, NCAR.

Smith, Jr., E. K. and S. Weintraub (1953, August). The constants in the equation for atmospheric refractive index at radio frequencies. *Proceedings of the I.R.E. 41*, 1035–1037.

Solheim, F. S., J. Vivekanandan, R. H. Ware, and C. Rocken (1997). Propagation delays induced in GPS signals by dry air, water vapor, hydrometeors and other particulates. *draft for J. of Geoph. Res.*.

Solheim, F. S., J. Vivekanandan, R. H. Ware, and C. Rocken (1999). Propagation delays induced in GPS signals by dry air , water vapor, hydrometeors and other particulates. *Journal of Geophysical Research 104*, 9663–9670.

Starks, T. H. and J. H. Fang (1982). The effect of drift on experimental semivariogram. *Mathematical Geology 14*(4), 309–319.

Stein, M. L. (1986). A modification of minimum norm quadratic estimation of a generalized covariance function for use with large data sets. *Mathematical Geology 18*(7), 625–633.

Stein, M. L. (1999). *Interpolation of Spatial Data; Some Theory for Kriging*. Springer Series in Statistics. Springer.

Stein, M. L. (2005, March). Space-time covariance functions. *Journal of the American Statistical Association 100*(469), 310–321.

Strozzi, T., U. Wegmuller, C. L. Werner, A. Wiesmann, and V. Spreckels (2003, July). JERS SAR interferometry for land subsidence monitoring. *IEEE Transactions on Geoscience and Remote Sensing 41*(7), 1702– 1708.

Stull, R. B. (1995). *Meteorology Today For Scientists and Engineers*. St. Paul,

Minneapolis: West Publishing.

Tarayre, H. and D. Massonnet (1996, May). Atmospheric propagation heterogeneities revealed by ERS-1 interferometry. *Geophysical Research Letters 23*(9), 989–992.

Tatarski, V. I. (1961). *Wave propagation in a turbulent medium*. New York: McGraw-Hill. Translated from Russian.

Tatarskii, V. I. (1971). *The Effects of the Turbulent Atmosphere on Wave Propagation*. Jerusalem: Israel Program for Scientific Translations. translated from Russian.

Teunissen, P. J. G. (2000a). *Network quality control* (1 ed.). Delft: Delft University Press.

Teunissen, P. J. G. (2000b). *Testing theory; an introduction* (1 ed.). Delft: Delft University Press.

Teunissen, P. J. G. (2001). GNSS ambiguity bootstrapping: Theory and application. In *International Symposium on Kinematic Systems in Geodesy, Geomatics and Navigation, Banff, Canada, 5–8 June 2001*.

Teunissen, P. J. G. and A. R. Amiri-Simkooei (2006). Least-squares variance component estimation. *Journal of Geodesy xx*, submitted.

Teunissen, P. J. G., D. G. Simons, and C. C. J. M. Tiberius (2005). *Probability and observation theory*. Delft Institute of Earth Observation and Space Systems (DEOS), Delft University of Technology, The Netherlands.

Thayer, G. D. (1974). An improved equation for the radio refractive index of air. *Radio Science 9*, 803–807.

Tough, R. J. A., D. Blacknell, and S. Quegan (1995). A statistical description of polarimetric and interferometric synthetic aperture radar. *Proceeedings of the Royal Society London A 449*, 567–589.

Treuhaft, R. N. and G. E. Lanyi (1987, March). The effect of the dynamic wet troposphere on radio interferometric measurements. *Radio Science 22*(2), 251–265.

van der Hoeven, A., R. F. Hanssen, and B. Ambrosius (2002). Tropospheric delay estimation and analysis using GPS and SAR interferometry. *Physics and Chemistry of the Earth 27*, 385–390.

Wackernagel, H. (1995). *Multivariate Geostatistics: An Introduction with Applications*. Berlin: Springer-Verlag.

Wadge, G., P. W. Webley, I. N. James, R. Bingley, A. Dodson, S. Waugh, T. Veneboer, G. Puglisi, M. Mattia, D. Baker, S. C. Edwards, S. J. Edwards, and P. J. Clarke (2002, October). Atmospheric models, GPS and InSAR measurements of the tropospheric water vapour field over mount Etna. *Geophysical Research Letters 29*(19), 11/1–4.

Wang, W., C. Bruyere, M. Duda, J. Dudhia, D. Gill, H.-C. Lin, J. Michalakes, S. Rizvi, and X. Zhang (2009, july). *ARW Version 3 Modelling System User's Guide*. NCAR.

Webley, P. W., R. M. Bingley, A. H. Dodson, G. Wadge, S. J. Waugh, and I. N. James (2002). Atmospheric water vapour correction to insar surface motion measurements on mountains: results from a dense GPS network on Mount Etna. *Physics and Chemistry of the Earth, Parts A/B/C 29*(4-5), 363–370.

Williams, S., Y. Bock, and P. Fang (1998). Integrated satellite interferometry: Tropospheric noise, GPS estimates and implications for interferometric synthetic aperture radar products. *Journal of Geophysical Research 103*(B11), 27,051–27,067.

Yun, S. H., F. Webb, P. Lundgren, E. Fielding, S. Liu, Z. Liu, S. Hensley, P. Rosen, and J. Parker (2010). Quantitative assessment on the requirements of DESDYNI for crustal deformation study. In *International Geoscience and Remote Sensing Symposium, Honolulu, Hawaii, 25–30 July 2010*, pp. 5 pp.

Zebker, H. A., P. A. Rosen, R. M. Goldstein, A. Gabriel, and C. L. Werner (1994, October-10). On the derivation of coseismic displacement fields using differential radar interferometry: The Landers earthquake. *Journal of Geophysical Research 99*(B10), 19617–19634.

Zebker, H. A., P. A. Rosen, and S. Hensley (1997, April). Atmospheric effects in interferometric synthetic aperture radar surface deformation and topographic maps. *Journal of Geophysical Research 102*(B4), 7547–7563.

Zebker, H. A. and J. Villasenor (1992, September). Decorrelation in interferometric radar echoes. *IEEE Transactions on Geoscience and Remote Sensing 30*(5), 950–959.

About the Author

Shizhuo Liu was born in Wuhan, China, on 21st May 1982. He was a bachelor student at the Department of Photogrammetry and Geographic Information System, Wuhan University between 2000 and 2004. During the period between 2002 and 2004 he worked at the State Key Laboratory of Information Engineering in Surveying, Mapping and Remote Sensing as a student assistant supervised by Prof. Liangming Liu. In September 2004, he received the admission from Delft University of Technology (TUD), the Netherlands, to pursue his master degree in Earth Observation program at the Faculty of Aerospace Engineering. Between 2005 and 2006, he was offered a student assistantship by the Physical Space Geodesy (PSG) group (chaired by Prof. Roland Klees) in the Delft Institute of Earth Observation and Space Systems (DEOS). In 2006, he chose to work on satellite radar interferometry for his master project at the Mathematical Geodesy and Positioning (MGP) group (headed by Prof. Peter Teunissen), DEOS. His master project was supervised by Prof. Ramon Hanssen and Dr. Gini Ketelaar. In August, 2006 he received his mater degree with thesis title "*Spatial resolution enhancement for satellite SAR Interferometry*". Afterwards, he was hired by MGP as a researcher working on spatio-temporal signal modeling and estimation. In November 2007, he started his PhD study at MGP focusing on estimation of atmospheric delay in SAR interferometry for surface deformation monitoring and meteorological applications. Since November 2011, he has been working for Royal Dutch Shell at Rijswijk, the Netherlands as a geodesist.

Index

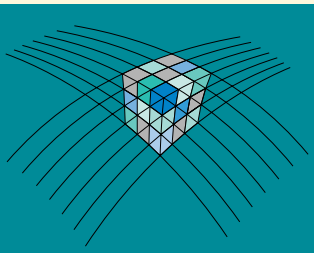

KONINKLIJKE NEDERLANDSE
AKADEMIE VAN WETENSCHAPPEN